Pharmacological Modulation and Functional Characterization of the Protein Kinase-Endoribonuclease IRE1α

Hannah C. Feldman

A dissertation
submitted in partial fulfillment of the
requirements for the degree of

Doctor of Philosophy

University of Washington

2019

Reading Committee:

Dustin J. Maly, Chair
Michael Gelb
Champak Chatterjee

Program authorized to offer degree:

Chemistry

University of Washington

Abstract

Pharmacological Modulation and Functional Characterization of the Protein Kinase-Endoribonuclease IRE1α

Hannah C. Feldman

Chair of Supervisory Committee:
Professor Dustin J. Maly
Department of Chemistry

Faithful folding of proteins in the endoplasmic reticulum (ER) is essential for cell survival and proper cellular function. Understandably, unfolded or misfolded proteins contribute to a myriad of human diseases. Numerous cellular perturbations can overwhelm the homeostatic capacity of the ER, causing the accumulation of unfolded proteins, and activation of the of the multi-domain protein sensor IRE1α as part of the unfolded protein response (UPR). Clustering of IRE1α lumenal domains in the presence of unfolded proteins promotes kinase trans-autophosphorylation in the cytosol and subsequent RNase domain activation. Depending on the duration and severity of ER stress, the kinase and RNase domains of IRE1α can have various outputs; exhibiting both adaptive/pro-survival and pro-apoptotic activities. IRE1α's role in cell fate decisions has consequently made it an attractive target for pharmacological modulation.

Interestingly, there is an allosteric relationship between the kinase and RNase domains of IRE1α, which allows ATP-competitive inhibitors to modulate the activity of the RNase domain. Here, we use kinase inhibitors to study how ATP-binding site conformation affects the activity of the RNase domain of IRE1α. In this study we find that diverse ATP-competitive inhibitors of IRE1α promote dimerization and activation of RNase activity despite blocking kinase autophosphorylation. In contrast, a subset of ATP-competitive ligands, which we call KIRAs, allosterically inactivate the RNase domain through the kinase domain by stabilizing monomeric IRE1α. Structural studies of IRE1α and integration of our extensive structure activity relationship (SAR) data has led us to formulate a model to rationalize how ATP-binding site ligands are able to control the IRE1α oligomeric state and subsequent RNase domain activity through conformational control of a motif known at the αC-helix. Furthermore we show that αC-helix conformation can be rheostatically tuned using ATP-competitive ligands, which led to the development of a new class of IRE1α kinase inhibitors known as partial KIRAs (pKIRAs). Unlike previously characterized RNase inhibitors, pKIRAs only partially weaken IRE1α dimerization and incompletely inhibit RNase activities. Most notably, pKIRAs are unique in their ability to selectively modulate the RNase functional outputs of IRE1α – preserving pro-survival outputs but preventing pro-apoptotic outputs in cells experiencing ER stress.

Table of Contents

List of Abbreviations

ACN	Acetonitrile
ADP	Adenosine diphosphate
Ala	Alanine
Alexa647	Alexa Fluor 647
Arg	Arginine
Asp	Aspartate
ATF6	Activating transcription factor 6
ATP	Adenosine triphosphate
BME	β-Mercaptoethanol
BFA	Brefeldin-A
BHQ	Black hole quencher
BiP	Binding immunoglobulin protein
BSA	Bovine serum albumin
CAM	S-carboxyamidomethylcysteine
CAS	Chemical abstracts service
cDNA	Complementary DNA
Cys	Cysteine
DCM	Dichloromethane
DFG	Aspartate-phenylalanine-glycine
DIEA	N,N-Diisopropylethylamine
DMAP	4-Dimethylaminopyridine
DMEDA	1,2-Dimethylethylenediamine
DMEM	Dubecco's modified eagle medium
DMF	Dimethylformamide
DMSO	Dimethyl sulfoxide
Dox	Doxycycline
Dp	Dephosphorylated
DSS	Disuccinimidyl suberate
DTT	Dithiothreitol
EC_{50}	Half maximal effective concentration
EDCI	1-Ethyl-3-(3-dimethylaminopropyl)carbodiimide
EDTA	Ethylenediaminetetraacetic acid
Eq.	Equivalents
ER	Endoplasmic reticulum
ERK	Extracellular regulated kinase
EtBr	Ethidium bromide
FBS	Fetal bovine serum
FDR	False discovery rate
FRET	Förster resonance energy transfer
FRT	Flippase recognition target
Glu	Glutamate
Gly	Glycine

HCT116	Human colorectal carcinoma cell
HEK293T	Human embryonic kidney 293T cells
HEPES	4-(2-hydroxyethyl)-1-piperazineethanesulfonic acid
His	Histidine
HPLC	High-performance liquid chromatography
IC_{50}	Half-maximal inhibitory concentration
Ile	Isoleucine
INS-1	Insulinoma cell line
IRE1α	Inositol-requiring enzyme 1 alpha
IRE1α*	Inositol-requiring enzyme 1 alpha residues 547-977
K_{DIMER}	Dimerization constant
KIRA	Kinase inhibitor RNase attenuator
LC	Liquid chromatography
LFQ	Label free quantification
Lys	Lysine
LysC	Lysyl endopeptidase
mAb	Monoclonal antibody
MBP	Myelin basic protein
MEK	Mitogen-activated protein kinase kinase
Met	Methionine
Mod. RIPA	Modified radioimmunoprecipitation buffer
mRNA	Messenger RNA
MS	Mass spectrometry
m/z	Mass to charge ratio
NIS	N-iodosuccinimide
NM-PP1	1-Tert-butyl-3-(naphthalen-1-ylmethyl)-1H-pyrazolo[3,4- d]pyrimidin-4-amine
NMR	Nuclear magnetic resonance
nt	Nucleotide
OE	Over expression
PAGE	Polyacrylamide gel electrophoresis
PBS	Phosphate buffered saline
PCR	Polymerase chain reaction
PDB	Protein data bank
PERK	Protein kinase R (PKR)-like endoplasmic reticulum kinase
Phe	Phenylalanine
PKD2	Polycystic kidney disease 2 protein
PKD3	Polycystic kidney disease 3 protein
pKIRA	Partial kinase inhibitor RNase attenuator
PMSF	Phenylmethylsulfonyl fluoride
PPase	Phosphatase
qPCR	Quantitative polymerase chain reaction
RAF	Rapidly accelerated fibrosarcoma kinase

RIDD	Regulated IRE1 dependent decay
RNase	Endoribonuclease
RPM	Rotations per minute
RPMI	Roswell Park Memorial Institute
RtcB	RNA 2',3'-cyclic phosphate And 5'-OH ligase
SAR	Structure activity relationship
SDS	Sodium dodecyl sulfide
SEM	Standard error of the mean
Ser	Serine
Sf9	Spodoptera frugiperda 9
Src	Proto-oncogene tyrosine-protein kinase Src
T-REx	Tetracycline regulated
TBS	Tris buffered saline
TBST	Tris buffered saline with Tween-20
TCEP	Tris (2-carboxyethyl) phosphine hydrochloride
TEA	Triethylamine
TEAB	Triethylammonium bicarbonate
TEMED	Tetramethylethylenediamine
TFA	Trifluoroacetic acid
THF	Tetrahydrofuran
Thr	Threonine
Tm	Tunicamycin
TO	Tetracycline operator
TPCK	6-(1-tosylamido-2-phenyl) ethyl chloromethyl ketone
Tris	Tris(hydroxymethyl)aminomethane
UPR	Unfolded protein response
UPLC	Ultra performance liquid chromatography
UT	Untreated
UV	Ultraviolet
v/v	Volume per volume
w/v	Weight per volume
XBP1	X-box binding protein 1
XBP1s	Spliced X-box binding protein 1
XBP1u	Unpliced X-box binding protein 1
yIRE1	Yeast IRE1

Units

A	Ampere
Å	Angstrom
C	Celsius
Ci	Curie
°	Degree
g	Gram
Hz	Hertz

hr	Hour
K	Kelvin
L	Liter
m	Meter
min	Minute
M	Molar
mol	Mole
s	Second
V	Volt

Prefixes

p	Pico
n	Nano
µ	Micro
m	Milli
c	Centi
k	Kilo
M	Mega

NMR

s	Singlet
d	Doublet
t	Triplet
q	Quartet
dd	Doublet of doublets
dt	Doublet of triplets
m	Multiplet
δ	Chemical shift in parts per million

List of Figures

Introduction:

Chapter 1:

Chapter 2:

List of Tables

Chapter 1:

Chapter 2:

Acknowledgments

This work would not have been possible without the support and guidance of my friends, family, colleagues, and mentors. To accurately express my gratitude to all of these individuals would be impossible, but I hope they know how deeply appreciative I am of them.

First I'd like to acknowledge my advisor, Dusty. I have come so far as a scientist since starting graduate school and it would not have been possible without his immense knowledge, patience, and unwavering support. To the Maly lab, I couldn't have dreamed of such wonderful, fun, and smart colleagues to surround myself with. To Zack and Linglan, my Michaelis-Menten mass spectrometry musketeers. To Sujata, my kinase queen. And of course Emily, Carrie, and Ames, who have been a constant source of laughter and friendship.

My best friends–Erin, Guinn, Madison, and Lauren–who are simply the best group of ladies and have encouraged me endlessly throughout graduate school. My siblings–Dan, Kristina, Nate, Jackie, and Doug–have always let me know how proud they were of me. My mom, who I can only hope to be as smart, kind, and successful as she is one day and has been my biggest cheerleader since starting grad school. My sweet Dad, I miss you more than I could ever express; you always pushed me to be inquisitive and passionate about life–and wish I could share this accomplishment with you.

Lastly, I'd like to thank Dan. I remember meeting you the first day I joined the lab and if I could have only known then what the future held for us. You imparted your passion for science and life onto me and have shown me true love and adventure. Going through grad school with you by my side has been such a joy and I can't wait for the road ahead.

Dedication

To my Dad, for always encouraging my pursuit of knowledge

Introduction

The endoplasmic reticulum (ER) is a netlike organelle consisting of interconnected sacs and branched tubules that extend throughout the cytosol of eukaryotic cells. This organelle plays important roles in lipid biosynthesis and is the cellular origin for almost all secreted and transmembrane proteins.[1] The ER maintains a distinct chemical environment characterized by a higher calcium concentration and a more oxidizing environment than the cytosol, which aids in the proper folding, post-translational modification, and maturation of proteins prior to their downstream trafficking.[2,3] However, the processing capacity of the ER is not unlimited, and a diversity of cellular perturbations can result in ER stress that overloads homeostatic folding capacity and results in the accumulation of misfolded proteins within the organelle. Professional secretory cells, such as plasma cells and β-cells of the endocrine pancreas, are especially sensitive to ER stress because they appear to operate at or near the limits of their secretory capacity.[4,5]

Under ER stress, the accumulation of unfolded proteins exceeds an excitatory threshold within the organelle causing the activation of an integrated intracellular signal transduction pathway called the unfolded protein response (UPR).[6] In mammals, the UPR contains three transmembrane sensor proteins inositol requiring enzyme 1 alpha (IRE1α), pancreatic endoplasmic reticulum kinase (PERK), and activating transcription factor 6 (ATF6) that monitor the protein folding status of the ER through their lumenal domains. When unfolded proteins

accumulate in the ER, these three arms of the UPR become activated and trigger specific downstream signaling cascades that affect cell fate.[7–10]

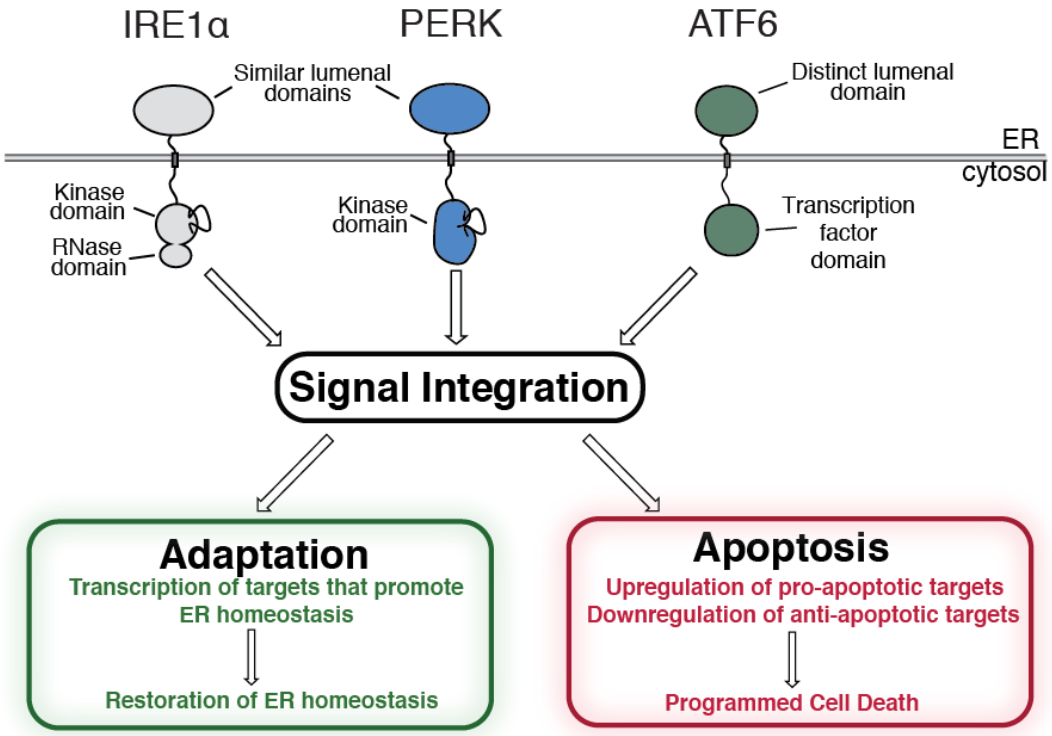

Figure I.1 Elements of the unfolded protein response[14]
In higher eukaryotes, the UPR is a three-arm pathway that consists two protein kinases: IRE1α and PERK, and the transcription factor ATF6. Under ER stress, the three UPR components leverage both transcriptional and translational responses that work to increase the ERs folding capacity and decrease the amount of proteins arriving in the ER. In cases where the UPR is unsuccessful in restoring protein-folding homeostasis, this initial adaptive response switches to a terminal–UPR that converges on sterile inflammation and programmed cell death.

Upon initial activation of the UPR, IRE1α, PERK, and ATF6 work to both reduce the amount of unfolded protein arriving at the ER, through a translational block, and expand folding capacity, by increasing the size of this organelle and upregulating ER chaperones, oxidoreductases, and biosynthetic enzymes.[11] However, in the event of severe and prolonged ER stress, the UPR switches from adaptive outputs to terminal signaling cascades that result in the

upregulation and activation of pro-inflammatory and pro-apoptotic regimes (**Figure I.1**).[12,13] Because the UPR has such profound effects on cellular fate, it is not surprising that dysregulated UPR signaling has been implicated in the etiology of numerous diseases. For example, certain types of cancer utilize adaptive-UPR outputs to promote their survival and proliferation; this is especially true of cancers of secretory cell origin that have a particularly high protein synthesis burden. Additionally, degenerative diseases are often hallmarked by chronic ER stress and premature cell loss through a terminal-UPR pathway.[14,15,16-26] Accordingly, there is widespread interest in the development of pharmacological agents that modulate IRE1α, PERK, and ATF6 function.[27,28]

The most ancient and well-conserved component of the UPR in mammals is the kinase/RNase IRE1α.[8,29] This multi-domain protein consists of an N-terminal lumenal domain sensor that is connected to cytosolic kinase and RNase domains through a transmembrane linker. In the absence of misfolded proteins in the ER IRE1α is monomeric and its N-terminal lumenal domain engages the protein chaperone BiP in what is thought of as an inhibitory or repressive complex. Under ER stress, BiP is sequestered away from IRE1α by unfolded proteins and IRE1α's lumenal domains oligomerize, which coincides with activation segment trans-autophosphorylation in the cytosolic kinase domains.[30] IRE1α activation segment phosphorylation results in enhanced dimerization and the stabilization of an RNase active dimeric state[31] commonly referred to as the back-to-back dimer that positions two RNase domains close to one another, facilitating the cleavage

of a 26-nucleotide intron from the XBP1 mRNA. The RNA ligase RtcB ligates the cleaved XBP1 mRNA,[32,33] yielding XBP1 spliced (XBP1s) mRNA, which is translated into an activated transcription factor that upregulates the expression of genes that help the ER adapt to stress.[34]

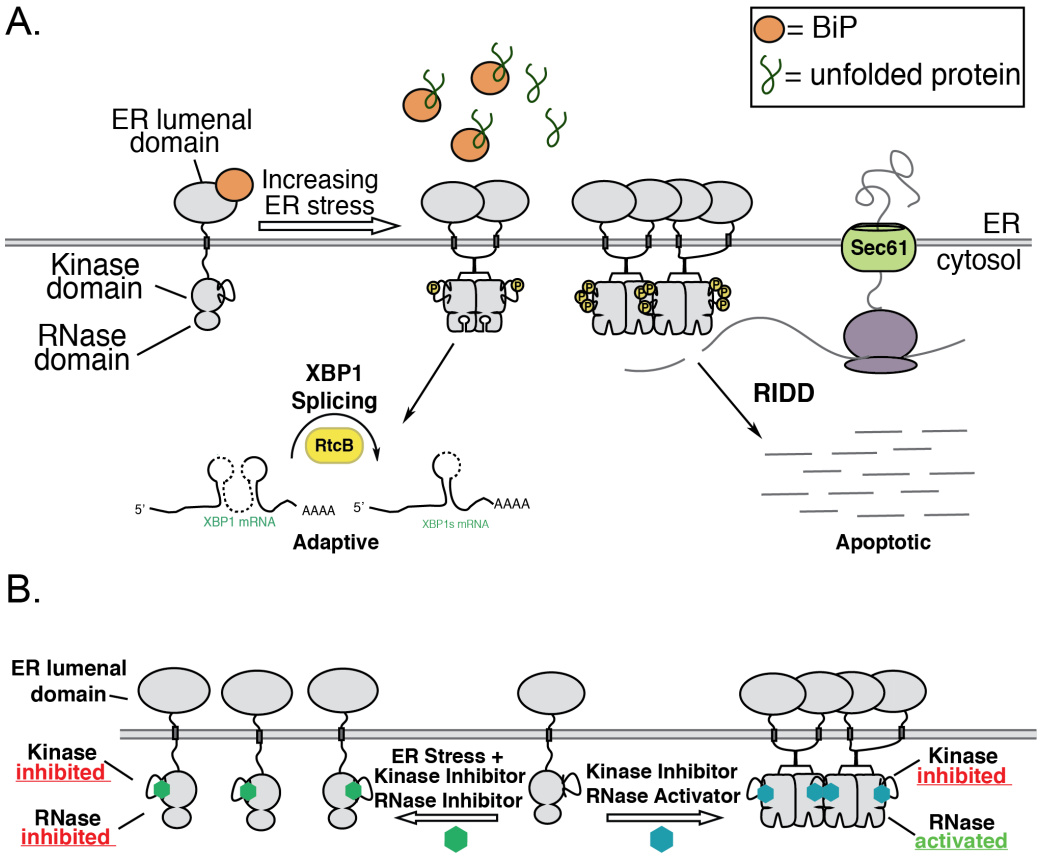

Figure I.2 IRE1α activation and divergent modulation by ATP-competitive inhibitors
(A) Model of IRE1α activation under ER stress. IRE1α contains a stress sensing lumenal domain linked to a cytosolic kinase and RNase domain by a transmembrane linker. In the presence of unfolded proteins in the ER, IRE1α is activated to initiate an adaptive response (XBP1 splicing). Prolonged ER stress leads to IRE1α oligomerization and endonucleolytic decay of ER-localized mRNAs (RIDD). (B) Allosteric inhibition of IRE1α's RNase activity with an ATP-competitive inhibitor under ER stress (left). Allosteric activation of IRE1α's RNase activity with an ATP-competitive inhibitor in the absence of ER stress (right).

However, if the initial adaptive response to ER stress is unsuccessful, IRE1α's RNase domain acts upon additional substrates, leading to extensive

endonucleolytic decay of hundreds of ER-localized mRNAs in a process known as regulated IRE1α dependent decay (RIDD).[13,35,36] The endonucleolytic decay activity of IRE1α's RNase domain further increases ER stress by inducing the activation of a number of pro-inflammatory and pro-apoptotic proteins and depleting mRNAs that encode for adaptive ER proteins (**Figure I.2A**).[37-38]

Previously it has been shown that the kinase and RNase domains of IRE1α are allosterically coupled. This allostery was first shown using a bump-hole engineered IRE1α construct whose gatekeeper residue was mutated from an isoleucine to a glycine (IRE1α I642G).[39] Mutation of gatekeeper residues to amino acids with small sides chains like glycines or alanines creates a "hole" in the active site of the kinase domain and allows for the binding of the "bumped" small molecule, NM-PP1. While the IRE1α I642G gatekeeper mutant was effectively kinase dead, binding of NM-PP1 activated the RNase domain of IRE1α I642G in the absence of both kinase phosphorylation and ER stress. This allosteric relationship between the kinase and RNase made targeting the kinase domain an additional possibility for pharmacological modulation of the RNase domain. Efforts to develop ATP-competitive inhibitors of IRE1α initially resulted in inhibitors that interacted with the kinase active site of IRE1α and activated RNase activity, similarly to IRE1α I642G and NM-PP1. Intriguingly, it was found that the allosteric relationship between the kinase and RNase domain is bi-directional in that ATP-competitive ligands can also decrease the activity of the RNase domain

(**Figure I.2B**). This thesis describes efforts to develop ATP-competitive pharmacological modulators of IRE1α as tools to better understand and characterize the allosteric network between the kinase and RNase domains. **Chapter One** details work to determine the structural and functional relationship between kinase active site conformation and RNase domain activity using ATP-competitive inhibitors. **Chapter Two** expands on the structural model described in **Chapter One** by further developing ATP-competitive inhibitors that function as rheostats of RNase activity and are able to selectively promote specific RNase functional outputs.

Chapter 1: Structural and Functional Analysis of the Allosteric Inhibition of IRE1α with ATP-Competitive Ligands[1]

I. Introduction

IRE1α's divergent effect on cellular fate has spurred widespread interest in the development of pharmacological modulators of this UPR sensor. As the ribonuclease activity of IRE1α appears to be the primary driver of IRE1α's roles in the adaptive and terminal UPR, most of these efforts have focused on modulating the RNase activity of this bifunctional enzyme. Toward this end, a number of aldehyde-containing small molecules that covalently modify and inhibit the RNase domain have been developed, although their use in cellular contexts or as therapeutics is limited.[14,40–43] The allosteric relationship between the kinase and RNase domains of IRE1α first characterized with yeast IRE1 (yIRE1) has also made it possible to modulate RNase activity with ATP-binding site ligands.[39] Ligands that interact with the ATP-binding site of IRE1α have the potential to either decrease or increase RNase activity. Indeed, all ligands that were first characterized to interact with the ATP-binding sites of yIRE1 and IRE1α activate RNase activity despite inhibiting the kinase domain. Recently, we have reported a series of ATP-competitive inhibitors based on an imidazopyrazine scaffold, called kinase inhibiting RNase attenuators (KIRAs), that inhibit RNase activity

[1] This chapter is reproduced with permission from: Feldman, H.C., Tong, M., Wang, L., Meza-Acevedo, R., Gobillot, T.A., Lebedev, I., Gliedt, M.J., Hari, S.B., Mitra, A.K., Backes, B.J., Papa, F.R., Seeliger, M.A., and Maly, D.J. (2016). Structural and Functional Analysis of the Allosteric Inhibition of IRE1α with ATP-Competitive Ligands. ACS Chemical Biology 11, 2195-2205. Copyright © 2016 American Chemical Society

through the kinase domain.[44] Here, a systematic study of how ATP-competitive inhibitor structure affects both the kinase and RNase activities of IRE1α is presented. By performing a structure–activity relationship (SAR) analysis, we find that all imidazopyrazine-based inhibitors of IRE1α's kinase domain also block RNase activity. However, the link between kinase and RNase domain inhibition does not appear to be a general feature of ATP-competitive ligands, as all inhibitors of IRE1α's kinase domain that were identified in an unbiased screen of a commercially available compound collection activate RNase activity rather than inactivate it. Further insight into how ATP-competitive inhibitors are able to divergently modulate the RNase domain through the kinase domain was gained by obtaining the first structure of apo human IRE1α in the RNase active back-to-back dimer conformation. Comparison of this structure with other existing structures of IRE1α and integration of our extensive SAR data has led us to formulate a structural model to rationalize how ATP-binding site ligands are able to control the IRE1α oligomeric state and subsequent RNase domain activity through kinase active site conformation.

II. Results and Discussion

A. Dual Enzymatic Activities of IRE1α

To better under-stand how specific inhibitor interactions with the ATP-binding site affect the RNase domain, a series of KIRAs based on an imidazopyrazine scaffold (**Figure 1.2A**) were tested for their effect on both enzymatic activities of IRE1α with in vitro assays.

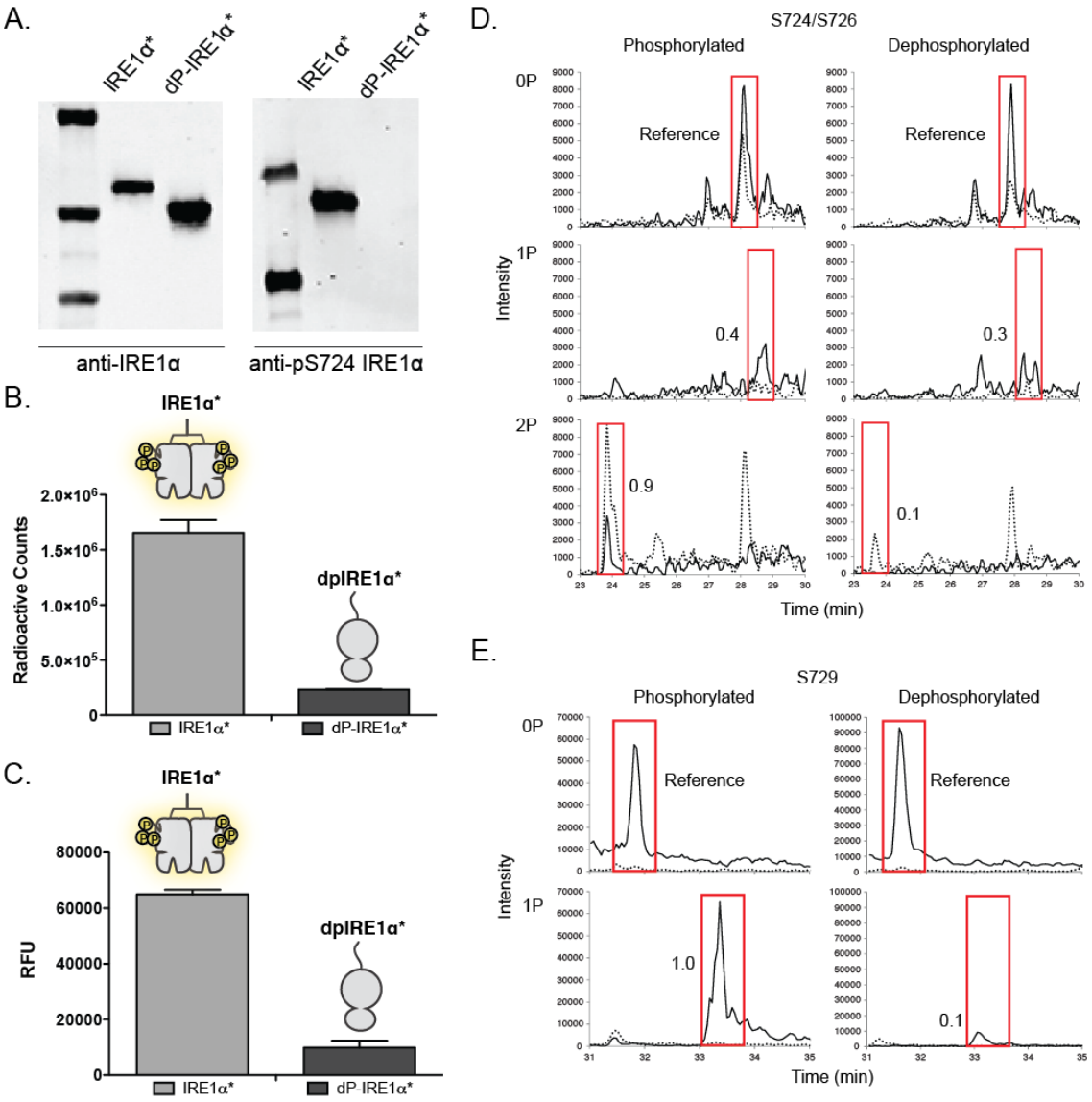

Figure 1.1 IRE1α* phosphorylation affects both kinase and RNase activity

(A) Western blot analysis of IRE1α* and dP-IRE1α* at four dilutions using a total and phosphospecific IRE1a primary antibody. (B) Comparative activity of IRE1α* and dP-IRE1α* in the kinase phosphorylation assay. Values are reported as radioactive counts/units (mean ± SEM; n=3). (C) Comparative activity of IRE1α* and dP-IRE1α* in the RNase activity assay. Values are reported as fluorescent units (mean ± SEM; n=3) (D) IRE1α* expressed and purified from baculovirus-infected insect cells is phosphorylated at Ser724, Ser726, and Ser729. Extracted ion chromatographs from LC/MS analyses of tryptic peptides of IRE1α* expressed and purified from baculovirus-infected insect cells either alone or treated with lambda phosphatase. Tryptic peptides analyzed were LAVGRHSFSRR (phosphorylated Ser724 and Ser726 underlined) and (E) SGVPGTEGWIAPEMLSEDCK (phosphorylated Ser729 underlined). Quantitated peak areas in red boxes are relative to those of unphosphorylated peptide for each sample.

Enzymatic assays were performed using an IRE1α construct, IRE1α*, that contains only the cytosolic kinase and RNase domains of this multidomain protein. Mass spectrometric analysis of this IRE1α* construct, which was expressed in baculovirus-infected insect cells and purified with immobilized metal ion affinity chromatography, revealed that this construct is phosphorylated on activation segment residues Ser724, Ser726, and Ser729 (**Figure 1.1D,E**).[45,46] Phosphorylation of these activation segment residues constitutively activates IRE1α*'s kinase and RNase domains (**Figure 1.B,C**).

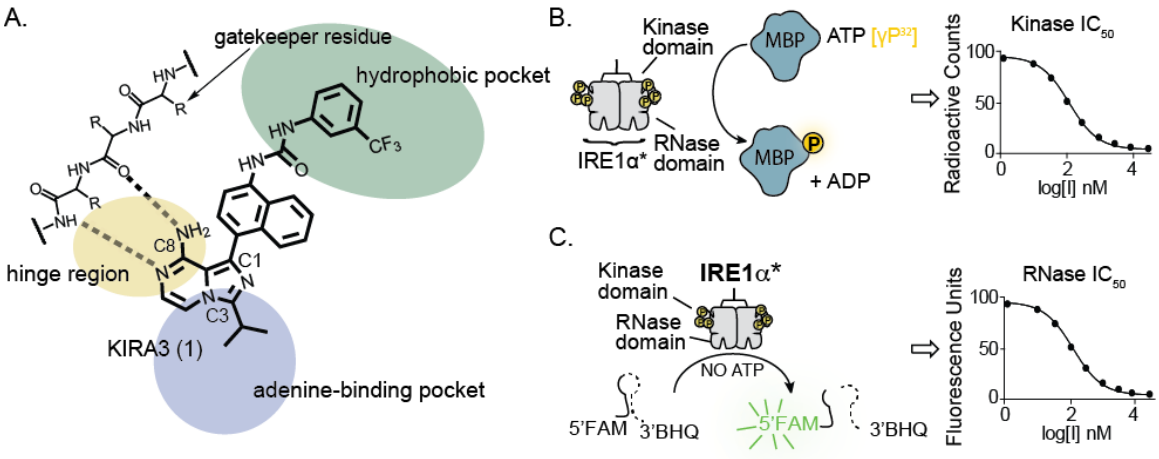

Figure 1.2 Determination of IRE1α's kinase activity and RNase activity in the presence of ATP-competitive inhibitors
(A) Structure and proposed binding mode of parent compound 1 (KIRA3). (B) Schematic of the activity assay used to screen inhibition of IRE1α's kinase activity. IRE1α* contains the cytosolic kinase and RNase domains of IRE1α. Kinase inhibition was determined by measuring the ability of KIRAs to block the phosphorylation of myelin basic protein (MBP). (C) RNase inhibition was determined by measuring the ability of KIRAs to block the cleavage of an XBP1 RNA mini-substrate. Cleavage of the 5′-FAM and 3′-BHQ labeled RNA substrate by IRE1α* results in release of fluorescein quenching, which can be monitored by fluorometric analysis

Kinase inhibition was determined by measuring the ability of a KIRA to block IRE1α*'s phosphorylation of an exogenous protein substrate (myelin basic protein, **Figure 1.2B**). RNase inhibition was determined with an assay that uses

an XBP1 mini-substrate labeled with a 5′-fluorescein and a 3′-black hole quencher (**Figure 1.2C**). KIRAs were tested for their ability to prevent mini-substrate cleavage, and the subsequent increase in fluorescence, by IRE1α.

B. SAR Analysis of KIRAs

To determine which structural elements allow KIRAs to inhibit the RNase activity of IRE1α through the ATP-binding site of the kinase domain, we performed a systematic SAR study using KIRA3 (1) as a benchmark (**Figure 1.2A**). The first series of analogs tested contain variable alkyl and cycloalkyl groups at the C-3 position (R_1) and a fixed naphthylurea-3-trifluoromethylphenyl moiety displayed from the C-1 position (R_2) of the imidazopyrazine scaffold (**Figure 1.3**). For this series, there is a 10-fold range in IC_{50} values for kinase and RNase activities, with the isopropyl analog (**1**) demonstrating the lowest potency and cyclo-propylmethyl (**3**) demonstrating the highest. Due to cyclo-propylmethyl appearing to be the most optimal R_1 substituent, this group was held constant for the remainder of the analogs tested in this study. Next, we determined how replacing the naphthyl R_2 group of **1** with different substituted aryl rings affects kinase and RNase inhibition. Previously, we found that inhibitors possessing a 4-naphthylamine R_2 group instead of a 4-anilino moiety are significantly more potent inhibitors of IRE1α*'s RNase activity.[44] Therefore, only analogs that contain substituted phenyl rings at the R_2 position were generated and tested. Of this series, only the 3-fluorophenyl (**7**) R_2 group confers sub-micromolar potency against the kinase and RNase activities of IRE1α*. Among mono-substituted

phenyl R_2 groups, 3-fluorophenyl (**7**) provides the most potent inhibition of IRE1α*'s kinase and RNase activities, with larger 3-chloro (**9**) or 3-methyl (**8**) substitutions proving to be less optimal.

Our original strategy to identify ATP-competitive inhibitors that allosterically inhibit the RNase activity of IRE1α was to screen compounds previously shown to stabilize an inactive conformation (DFG-Asp-out conformation) of the conserved Asp-Phe-Gly motif (DFG-motif) found at the base of the activation segment (type II inhibitors). Indeed, the original hit from this screen, and all subsequent potent KIRAs, contains an aryl-urea moiety, which is a known pharmacophore for a number of type II inhibitors that stabilize the DFG-out inactive conformation.[47-51] When type II inhibitors of this class are bound to the DFG-out form of protein kinases, the aryl group of the aryl-urea moiety occupies a hydrophobic pocket that is formed upon movement of the Phe side chain of the DFG motif, and the urea moiety serves as a linker that forms hydrogen bonds with a conserved glutamic acid on αC-helix, and with the backbone of the DFG motif. In order to test whether these canonical DFG-out-stabilizing interactions are necessary for allosteric inhibition of IRE1α's RNase domain, the aryl (R_3) and urea (R_4) moieties of **1** were systematically varied. As shown in Figure 1.3, diverse 3- and 4-substituted phenyl groups are tolerated at the R_3 position (**12–21**), with all but one phenylurea demonstrating IC_{50} values for RNase and kinase inhibition that are within 10-fold of the most potent KIRA, **3**. Notably, inhibitors **20** and **21**, which

contain the 4-methylpiperazin-1-yl group from the DFG-out-stabilizing, clinically approved drug imatinib, are potent inhibitors of the kinase and RNase activities of IRE1α*. Inhibitors that possess a benzyl (**23**) or phenethyl (**24**) R_3 group are poorer inhibitors of IRE1α*. Furthermore, inhibitors with heteroaryl (**22**) or cycloakyl (**25–28**) groups at the R_3 position also poorly inhibit IRE1α*'s enzymatic activities. Finally, we explored whether a urea linker at the R_4 position is absolutely necessary for allosteric inhibition of the RNase domain through the ATP-binding site of IRE1α. In this series, analogs that contain either an R_4 urea linkage that is not able to form a hydrogen bond donor and acceptor (**29** and **30**) or an ether linkage (**31** and **32**) are very poor inhibitors of IRE1α*. Thus, a urea linkage appears to be optimal for bridging the C-3 naphthyl group and the hydrophobic R_3 substituent. However, despite the low potencies of non-urea-containing analogs, all compounds that inhibit the kinase activity of IRE1α* show at least some degree of RNase inactivation. Therefore, a urea is not strictly necessary for linking kinase inhibition to inactivation of the RNase domain.

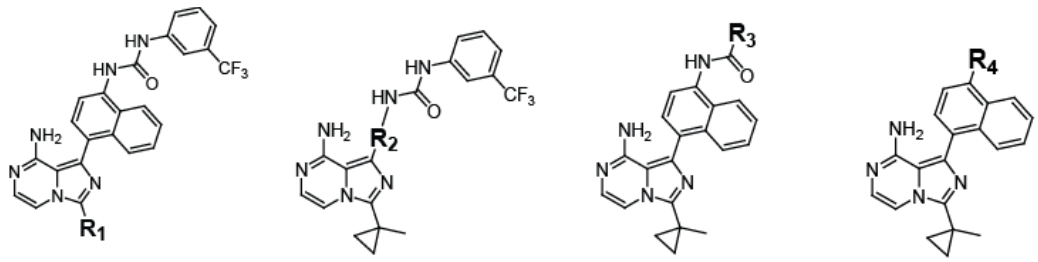

	R1	Kinase IC50 (μM)	RNase IC50 (μM)		R1	Kinase IC50 (μM)	RNase IC50 (μM)		R1	Kinase IC50 (μM)	RNase IC50 (μM)
1		1.3 ± 0.1	1.8 ± 0.1	3		0.14 ± 0.01	0.090 ± 0.01	5		0.26 ± 0.01	0.48 ± 0.02
2		0.17 ± 0.02	0.12 ± 0.01	4		0.51 ± 0.04	0.18 ± 0.04	6		0.68 ± 0.06	0.33 ± 0.01
	R2	Kinase IC50 (μM)	RNase IC50 (μM)		R2	Kinase IC50 (μM)	RNase IC50 (μM)		R2	Kinase IC50 (μM)	RNase IC50 (μM)
3		0.14 ± 0.01	0.09 ± 0.01	8		2.7 ± 0.5	1.5 ± 0.1	10		3.9 ± 0.2	1.2 ± 0.1
7		0.85 ± 0.05	0.39 ± 0.01	9		3.0 ± 0.2	2.4 ± 0.1	11		17 ± 1	20 ± 5
	R3	Kinase IC50 (μM)	RNase IC50 (μM)		R3	Kinase IC50 (μM)	RNase IC50 (μM)		R3	Kinase IC50 (μM)	RNase IC50 (μM)
3		0.14 ±0.01	0.09 ± 0.01	17		0.66 ± 0.08	0.29 ± 0.07	23		3.8 ± 0.8	3.6 ± 0.2
12		0.43± 0.07	0.19 ± 0.01	18		0.94 ± 0.06	0.61 ± 0.07	24		13 ± 1.7	4.1 ± 0.3
13		0.11 ± 0.01	0.22± 0.01	19		2.3 ± 0.7	1.6 ± 0.1	25		2.7 ± 0.4	2.2 ± 0.1
14		0.27 ± 0.03	0.26 ± 0.01	20		0.42 ± 0.14	0.19 ± 0.05	26		21 ± 2	~60
15		0.33 ± 0.08	0.31 ± 0.01	21		0.17 ± 0.07	0.34 ± 0.02	27		17± 1	~60
16		0.32 ± 0.02	0.14 ± 0.01	22		17 ± 5	7.1 ± 3.0	28		7.5 ± 0.6	6.3 ± 0.1
	R4	Kinase IC50 (μM)	RNase IC50 (μM)		R4	Kinase IC50 (μM)	RNase IC50 (μM)		R4	Kinase IC50 (μM)	RNase IC50 (μM)
3		0.14 ± 0.01	0.090 ± 0.01	30*		>60	>60	32		~50	~60
29		21 ± 3	19 ± 3	31		~50	~60				

Figure 1.3. SAR analysis of KIRA analogs (1–32)
Half maximum inhibitory concentration (IC_{50}) values for kinase and RNase activity (mean ± SEM, n = 3). *Compound 30 utilizes a tert-butyl group at the R_1 position rather than a cyclopropyl methyl moiety.

C. Correlation Between Kinase and RNase Inhibition

Throughout this SAR study, we observed that almost all inhibitors that block the kinase activity of IRE1α also inhibit RNase activity with a similar potency. Despite being based on an ATP-competitive inhibitor scaffold, we further confirmed that KIRAs do not directly inhibit the RNase domain by demonstrating that ATP is able to dose dependently restore RNase activity in the presence of an inhibitory concentration of **2** (**Figure 1.4A**). Furthermore, plotting the kinase and RNase IC_{50} values for the inhibitors shown in **Figure 1.3** shows strong correlation (R^2 = 0.88) that spans almost three orders of magnitude in potency (**Figure 1.4B**). Despite the correlation in inhibitory potencies, the fact that KIRAs allosterically modulate IRE1α's RNase activity through the kinase domain leaves open the possibility that only partial RNase inhibition may result from quantitative ATP-binding site occupancy by an inhibitor. Therefore, representative KIRAs were tested against IRE1α at a single concentration, and the residual amount of kinase and RNase activity was measured (**Figure 1.4C**). For a majority of the inhibitors tested, the observed residual RNase activity is within ± 5% of the residual kinase activity (**Figure 1.4C**). Therefore, the magnitude of kinase and RNase inhibition is tightly coupled for these compounds. In contrast, for compounds **26–28**, the amount of residual RNase activity is 30–50% greater than the remaining kinase activity. For example, in the presence of 60 μM of inhibitor **28**, IRE1α retains <2% of its kinase activity but ~35% of its RNase activity. A similar disparity in inhibition levels was observed for inhibitors **26** and **27**. This disparity does not appear to be

solely due to the lower potencies of **26–28**, as inhibitors **24, 29**, and **32** are also poor inhibitors of IRE1α's kinase activity but show similar levels of RNase inhibition. The common distinguishing feature of compounds **26–28** that differentiates them from the other KIRAs tested is that they possess smaller substituents at the R_3 position. Smaller substituents at this position may only lead to partial displacement of the structural element that is necessary for RNase inhibition.

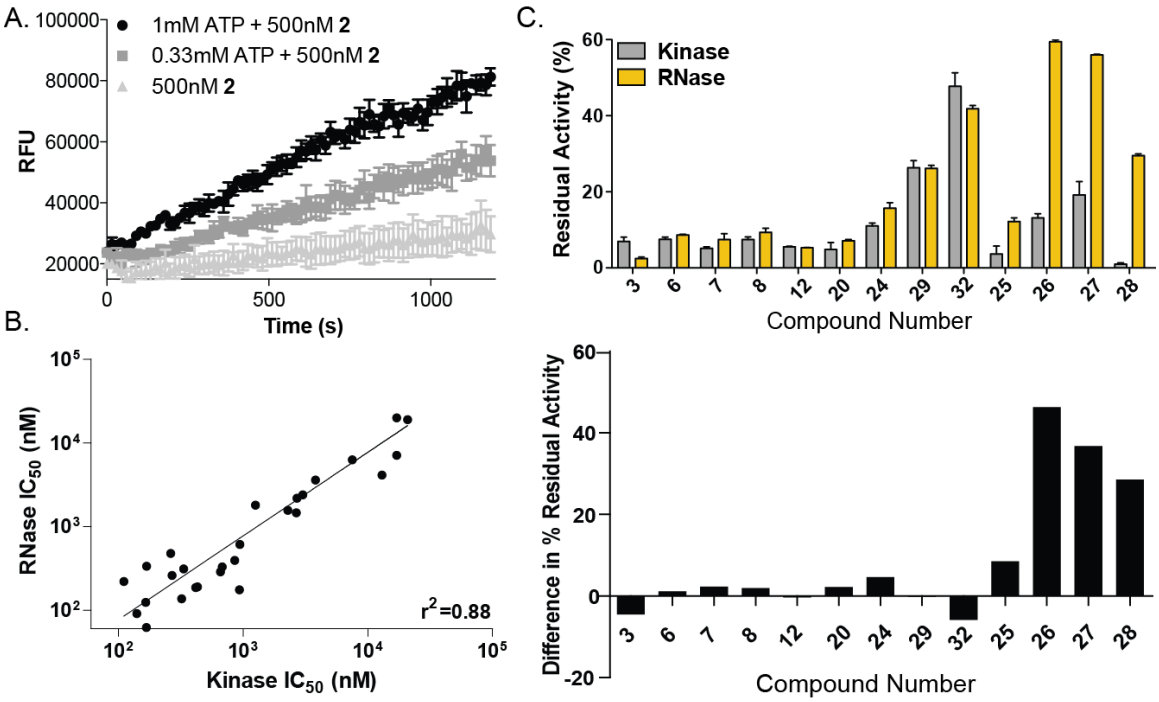

Figure 1.4. Inter-relationship between the kinase and RNase domains of IRE1α
(A) IRE1α* was incubated with 500 nM of KIRA **2**, a concentration that >95% inhibits RNase activity, in the absence or presence (0.5 or 1.0 mM) of ATP. B) Correlation plot of the kinase and RNase IC_{50} values for KIRAs. The R^2 value is 0.88. Inhibitors **26, 27**, and **30–32** were excluded from this analysis because kinase and RNase IC_{50} values could not be accurately determined. (C, *top)* Residual kinase and RNase activity of various inhibitors at a concentration in which the ATP-binding site is either >90% occupied (inhibitors **3, 6–8, 12, 20**, and **25**) or at a concentration of 60 μM* for less potent inhibitors (**24, 26–28, 29**, and **32**; mean ± SEM, n = 3). *A maximum inhibitor concentration of 60 μM was selected due to limits on inhibitor solubility. (C, *bottom*) Difference in percent residual RNase activity and kinase activity [value = (% residual RNase activity) – (% residual kinase activity)].

D. General Effects of Kinase Inhibitors on the RNase Domain

Above, we demonstrated that all KIRAs that interact with the ATP-binding site of IRE1α also provide at least some level of RNase inhibition. However, almost all other ligands that have been reported to interact with the ATP-binding site of IRE1α increase RNase activity rather than decrease it.[27,41,39,44,52,53]

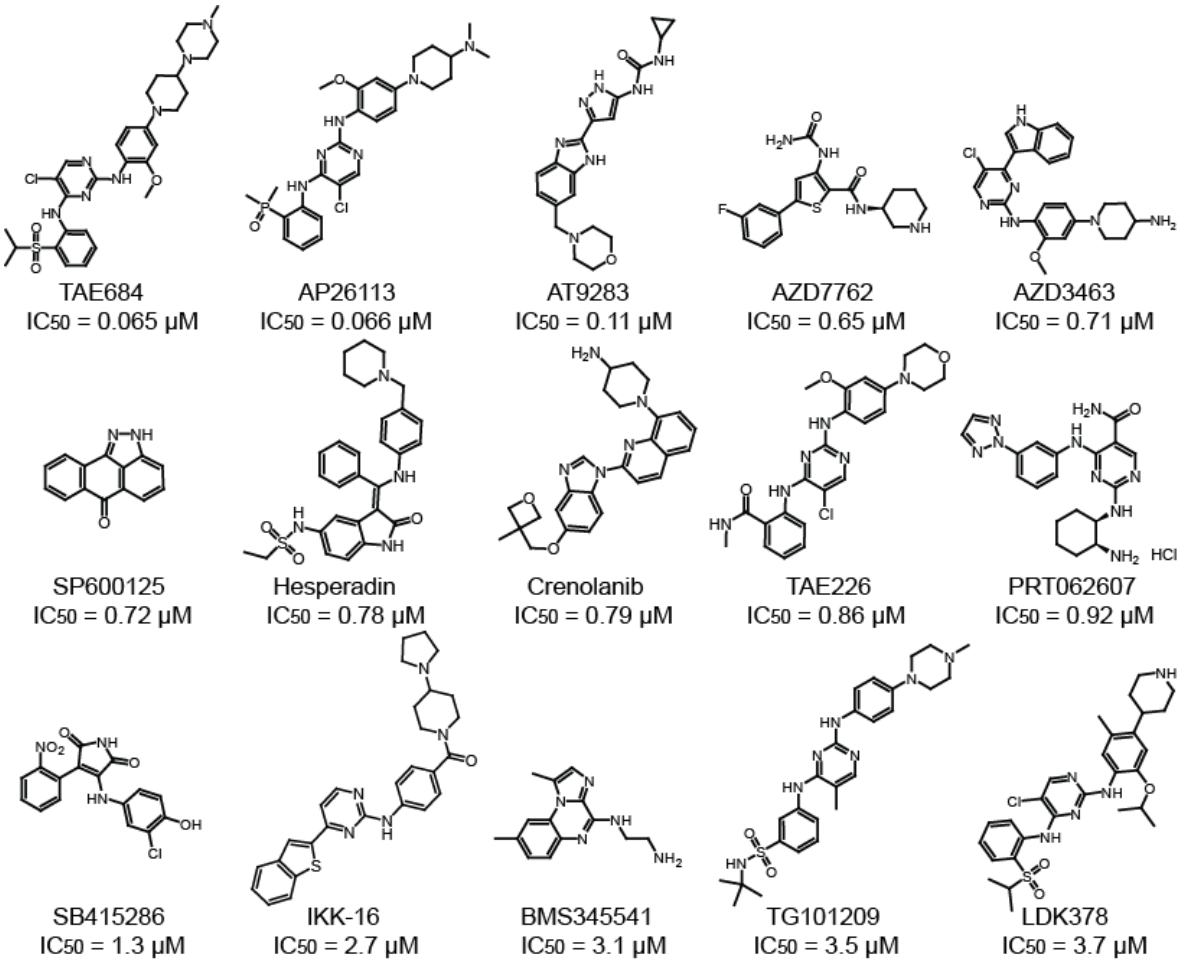

Figure 1.5. Structures and IC50 values for compounds from the Selleckchem kinase Inhibitor library
Screened inhibitors that inhibit the kinase activity of IRE1α > 50% at a concentration of 10 μM. Values shown are mean ± SEM (n = 3).

Therefore, we were curious whether the KIRAs are unique in their dual inhibitory properties or if there are other general classes of kinase inhibitors that are also

capable of blocking IRE1α's kinase and RNase activities. To address this question, a diverse panel of 378 commercially available kinase inhibitors (Selleckchem Kinase Inhibitor Library) containing both type I and II inhibitors was screened for their ability to block the kinase activity of IRE1α (**Figure 1.5**) Of the 378 compounds tested, 15 inhibited the kinase activity of IRE1α with an IC_{50} of less than 10 μM (**Figure 1.5**). The 13 most potent kinase inhibitors were then tested for their ability to inhibit the RNase activity of IRE1α*. In contrast to the KIRAs, none of the 13 IRE1α kinase inhibitors reduced the RNase activity of IRE1α* (**Figure 1.6A**). In the absence of any observed RNase inhibition of phosphorylated IRE1α*, the same 13 compounds were tested for their ability to activate the RNase domain of a minimally active IRE1α construct, dP-IRE1α*, which is quantitatively dephosphorylated and has low basal RNase activity (**Figure 1.1A,C**). Incubation of dP-IRE1α* with 10 μM of each inhibitor increased the cleavage of the XBP1 mini-substrate by 5–15-fold (**Figure 1.6B**). Thus, all of the IRE1α kinase inhibitors identified in this screen are activators, rather than inactivators, of dP-IRE1α*'s RNase domain. These results are consistent with the fact that all the inhibitors identified in this screen contain a type I pharmacophore, which binds to the active conformation of protein kinase ATP-binding sites. Indeed, co-crystal structures of eight of the inhibitors shown in **Figure 1.5** have been reported (**Table 1.1**), and in all cases the bound kinase target's ATP-binding site is in an active conformation.

Table 1.1

Inhibitor Name	PDB Accession Code	Protein Kinase	Lys-Glu Salt Bridge Distance (Å)
TAE684	4E93	c-Fes	2.8
AT9283	2W1I	JAK2	3.1
TAE226	2JKK	FAK	2.8
SP600125	1UKI	JNK1	2.9
AZD7762	2YDK	CHK1	2.4
LDK378	4MKC	ALK	2.9
TG101209	4JI9	JAK2	2.6
Hesperadin	4QMT	MST3	2.8

Table 1.1 Screened inhibitors bind kinase sites in an active conformation
For screened inhibitors with available crystal structures their mode of kinase target binding was assess by whether the catalytic Lys-Glu salt bridge is intact. Salt bridges with distances of under 4 Å were considered to be intact and in an active conformation.

As a truncated form of IRE1α was used for the in vitro studies described above, we next used a cell-based assay to determine whether activating kinase inhibitors have similar effects on the full-length IRE1α transmembrane protein (**Figure 1.6C**). To do this, INS-1 rat insulinoma cells, which are derived from insulin-producing pancreatic β-cell tumors, were treated with two concentrations (3 and 10 μM) of four of the most potent IRE1α-activating inhibitors (AT9283, AP26113, TAE684, and AZD7762). Consistent with the ability of type I kinase inhibitors to activate full-length IRE1α, treatment with each inhibitor led to an increase in spliced cellular XBP1 mRNA levels in the absence of ER stress. Strikingly, incubating INS-1 cells with AP26113 and AT9283 led to an equal or greater level of spliced XBP1 mRNA than treatment with 0.5 μg/mL of the ER stress agent tunicamycin (Tm), which is a protein glycosylation inhibitor that leads to acute ER stress.

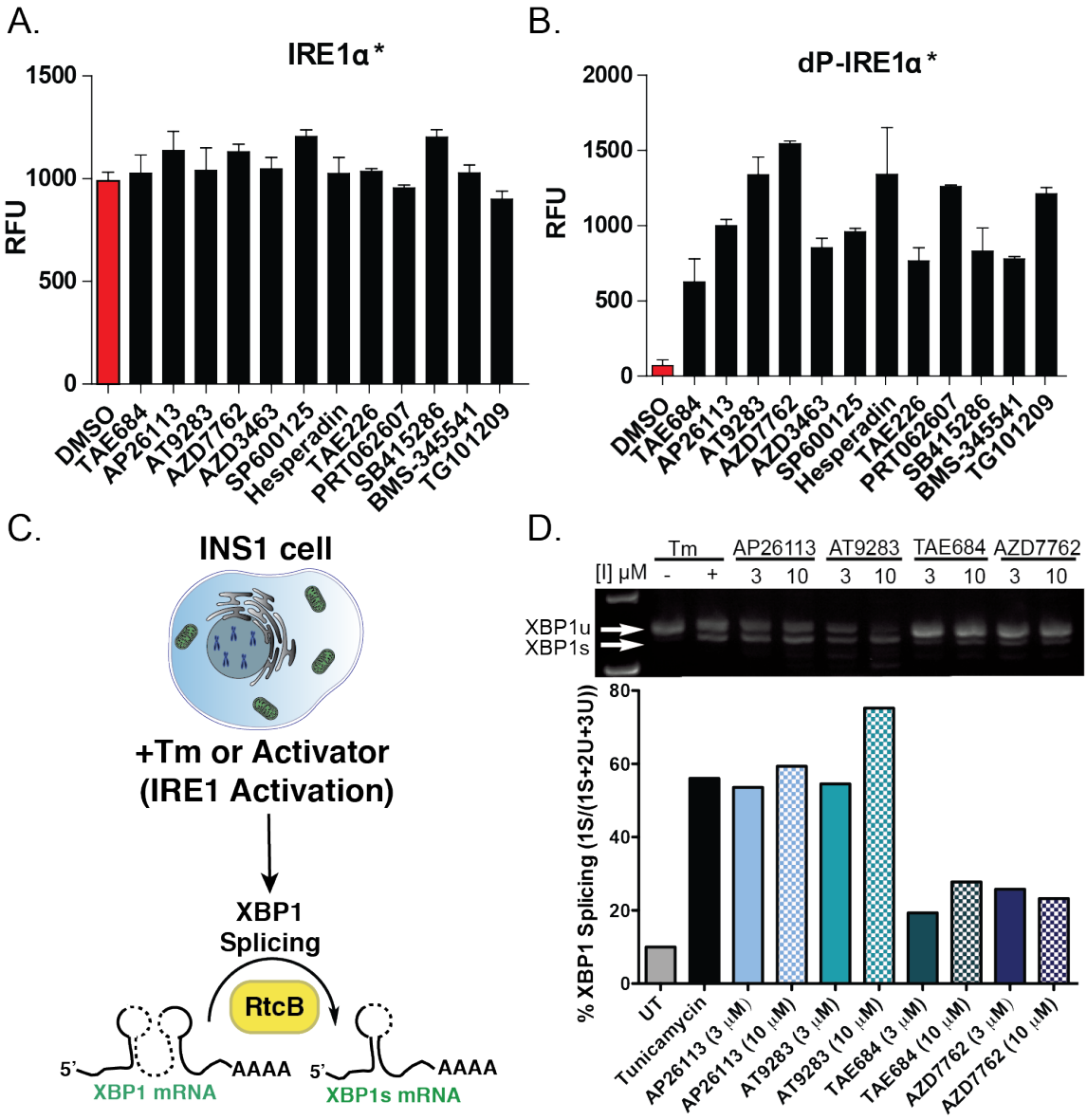

Figure 1.6 Diverse ATP-competitive inhibitors activate the RNase domain of dP-IRE1α*

(A) End point fluorescence of IRE1α*-catalyzed cleavage of the XBP1 mini-substrate in the presence of DMSO or 10 μM of the inhibitor listed. Values shown are mean ± SEM (n = 3). (B) End point fluorescence of dP-IRE1α*-catalyzed cleavage of the XBP1 mini-substrate in the presence of DMSO or 10 μM of the inhibitor listed. dP-IRE1α* was generated by treating IRE1α* with lambda phosphatase. Values shown are mean ± SEM (n = 3). (C) Cell-based assays were done using INS-1 cells treated with the ER stress agent Tunicamycin (Tm) or activator to look at XBP1 splicing RNase outputs. (D) Ethidium-bromide-stained agarose gel of XBP1 cDNA amplicons from INS-1 cells treated with inhibitors at the indicated concentrations for 2 h. For the positive control, INS-1 cells were treated with 500 ng/mL Tm for 4 hr. Ratiometric quantitation of XBP1s/(XBP1u + XBP1s) is shown at the bottom.

E. Structure of apo dP-IRE1α*

Crystal structures of IRE1α have been highly informative in determining which interactions are necessary for stabilizing RNase active IRE1α dimers and for providing insight into the conformational changes that occur in the kinase domain in transitioning from a monomeric to an RNase active dimeric state.[31,41,53–56] During our attempts to obtain a structure of a KIRA bound to IRE1α, we obtained the structure of human apo dP-IRE1α* to a resolution of 2.6 Å. Even though apo dP-IRE1α* is not phosphorylated, it forms an RNase active back-to-back dimer under the crystallization conditions used. The asymmetric unit of the crystal contains a dP-IRE1α* monomer, featuring a canonical bilobal kinase domain, and a globular α-helix rich RNase domain (**Figure 1.7A,B**). In the back-to-back dimer, the dP-IRE1α* kinase domain adopts an active kinase conformation: the aspartate (Asp711) of the DFG motif (Asp711-Phe712-Gly713) faces into the active site (DFG-in), and glutamate (Glu612) of αC-helix forms a salt bridge with the catalytic lysine (Lys599), typical of the αC-helix-in conformation (**Figure 1.7C**). Despite being dephosphorylated, the activation segment in dP-IRE1α* is completely resolved and adopts an extended active conformation. Interestingly, the beginning of the activation segment (Gly713, Cys715, Lys717) engages with αC-helix (Arg611, Glu618) and appears to anchor it in the αC-helix-in conformation (**Figure 1.7C**).

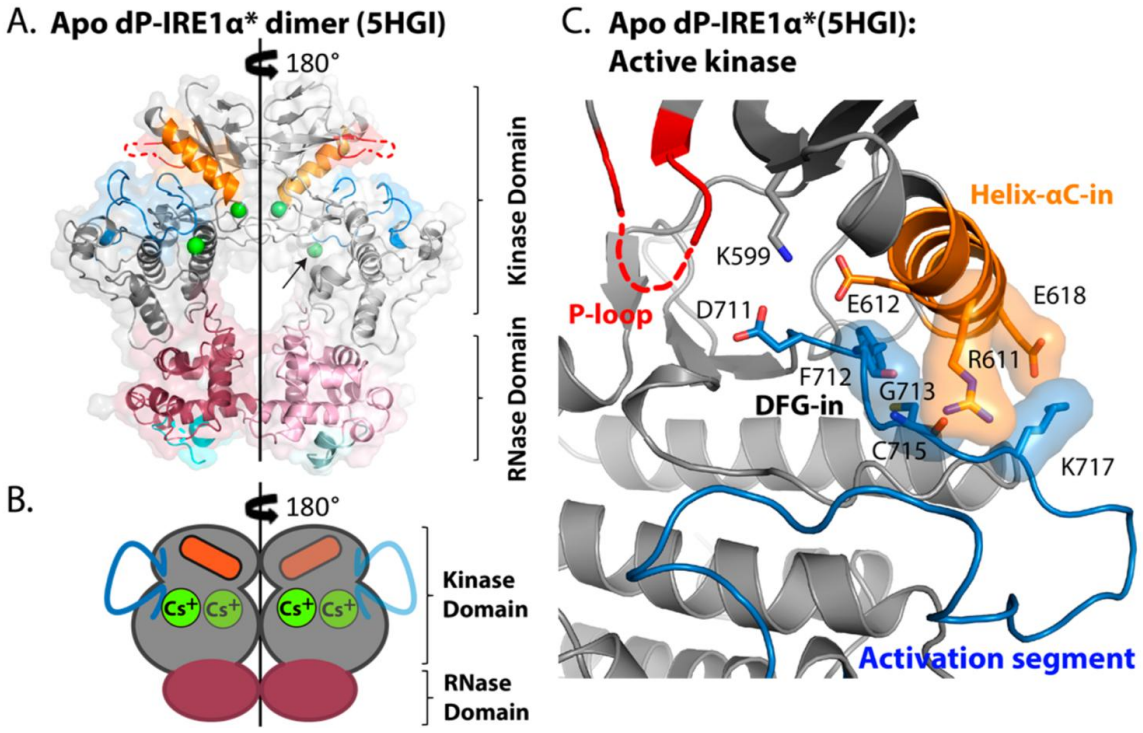

Figure 1.7 Apo human dP-IRE1α* adopts an RNase active back-to-back dimer promoted by cesium mediated stabilization of the active kinase conformation
(A) Two apo human dP-IRE1α* protomers (PDB: 5HGI) adopt an active kinase conformation that is stabilized by Cs^+ ions (green spheres), allowing the protomers to align parallel in a back-to-back dimer configuration comparable to the RNase active yIRE1 structure (PDB: 3FBV). Each protomer consists of a protein kinase domain (gray) and an RNase domain (purple). Protein kinase regulatory elements such as the P-loop (red), αC-helix (orange), and activation segment (blue) are highlighted. The helix-loop-element dubbed the HLE (cyan), a catalytic motif in the RNase domain is also shown. The arrow denotes that the position of helix-αE has been hidden in order to reveal one of the Cs^+ ions that stabilize the activation segment. A 2-fold symmetry axis is indicated by the black line. (B) Cartoon schematic illustrating that cesium and coupling between αC-helix and the activation segment helps mediate stabilization of the active kinase hallmarks (αC-helix-in, extended activation segment), which are associated with the RNase active back-to-back dimer. Cartoon features with reduced opacity denote those which are behind the dimer interface plane that is parallel to the 2-fold symmetry axis (black line). (C) A close-up view of the dP-IRE1α* kinase active site, presenting the canonical kinase active conformation hallmarks and key salt bridge interactions that couple the activation segment with αC-helix.

Because αC-helix is a major component of the back-to-back dimer interface, its stabilization in the αC-helix-in orientation promotes dimerization and RNase activation. Phosphorylation of the activation segment would further stabilize the

extended active conformation of this flexible structural element, resulting in enhanced dimerization and subsequent RNase activation. A novel feature of our dP-IRE1α* kinase domain structure is the presence of two cesium ion (Cs^+) binding sites, CsB1 and CsB2 (**Figure 1.7A,B**). These cesium ions stabilize the extended activation segment, and dimer interface residues near αC-helix, into conformations conducive to back-to-back dimerization. Our structure of dP-IRE1α* shows that activation segment phosphorylation is not absolutely necessary for adopting the active kinase conformation and the RNase active back-to-back dimer. Protomers of neighboring asymmetric units of apo dP-IRE1α* form a back-to-back dimer that is similar in overall orientation to the RNase active yeast IRE1 structure (PDB: 3FBV).[31,52] Analysis of the alignment of the protomers in dimeric IRE1α indicates that the dP-IRE1α* protomers align in a parallel and symmetrical fashion for both the kinase and RNase domains, like the active yIRE1 dimer, confirming that our dP-IRE1α* structure resembles a fully RNase active state. This contrasts with the pre-active dimer configuration of a recently reported human dP-IRE1α structure (PDB: 4Z7H)[54] in which the protomers are not aligned fully parallel, and the RNase domains do not complement to form the active conformation. While the overall quaternary structure is highly conserved between dP-IRE1α* and active yIRE1, sequence divergence and insertions cause secondary structure differences that change the details of stabilizing interactions for the activation segment and αC-helix.

Similarly, only three dimer interactions in the back-to-back dimer interface are conserved (**Figure 1.8**).

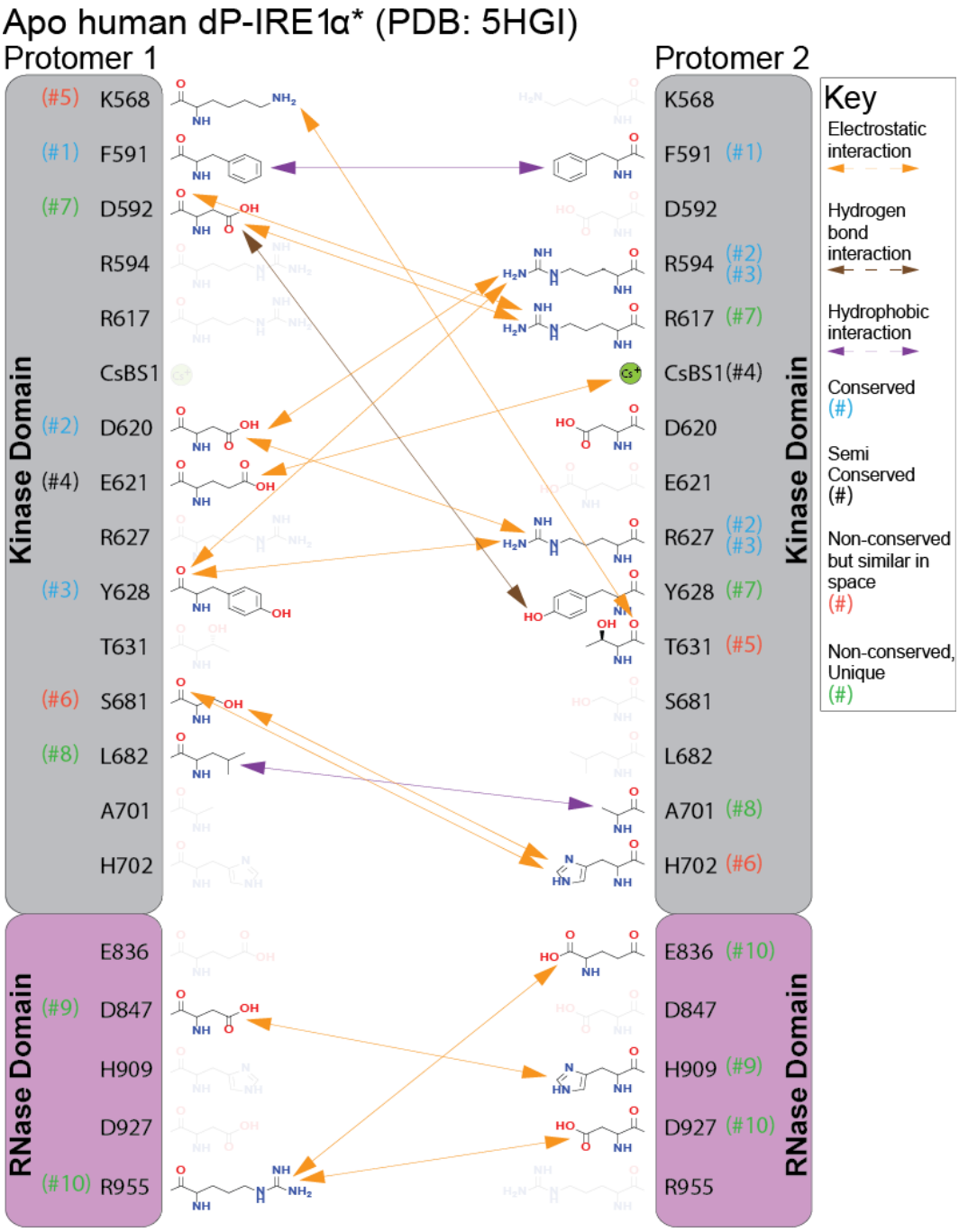

Figure 1.8 Structural comparison of the back-to-back dimer interface interactions in dP-IRE1α*

Schematic illustrations of the amino acid interactions found at the back-to-back dimer interface of dP-IRE1α* (PDB: 5HGI). In dP-IRE1α*, eight sets of interactions are mediated by the kinase domain and two by the RNase domain. Listed next to the residue

or CsBS1(Cs^+ binding site 1) is the number of the interaction denoted by: (# number), with the color corresponding to the degree of similarity for the interaction found in dP-IRE1α* compared to active yIRE1 (PDB: 3FBV; blue is conserved, black is partially conserved, orange is non-conserved but similar in space, and green is unique). The general nature of each interaction is defined in terms of: electrostatic (orange arrow), hydrogen bond (brown arrow), and hydrophobic (purple arrow). For clarity only one set of dimer interactions mediated by protomer A to protomer B is shown, hence some residues appear opaque.

F. ATP-Competitive Inhibitors Modulate RNase Activity by Affecting αC-Helix Conformation

To mechanistically rationalize how KIRAs are able to inhibit the RNase activity of IRE1α, we compared our active *apo* dP-IRE1α* structure to two different inactive mammalian IRE1α structures: (1) dephosphorylated IRE1α bound to ADP (PDB: 3P23)[30] and (2) dephosphorylated IRE1α bound to a KIRA recently developed by Amgen (compound **33**; PDB: 4U6R;[55] **Figure 1.9, Figure 1.10**). Analysis of these structures shows that the most direct mechanism to inhibit IRE1α's RNase activity is through the displacement of IRE1α's αC-helix from the active conformation (**Figure 1.9**). This movement of αC-helix would disrupt important contacts that contribute to the interface of the RNase active back-to-back dimer, likely resulting in monomeric IRE1α and subsequent loss of RNase activity (**Figure 1.10**).

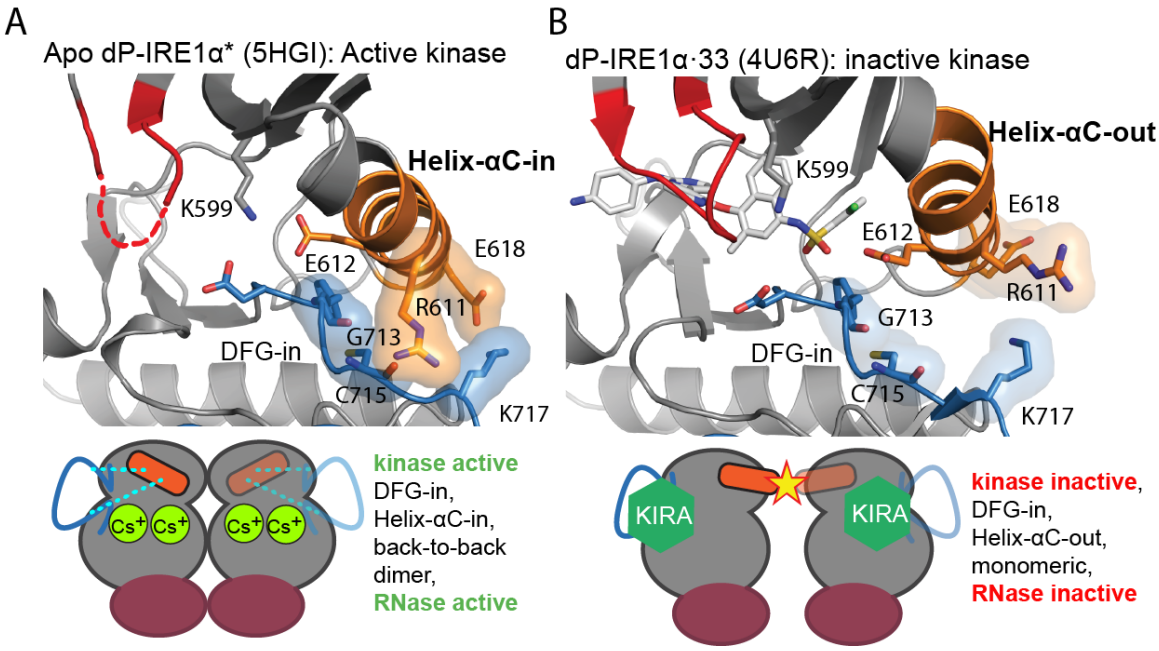

Figure 1.9 The conformation of αC-helix in the kinase domain affects the IRE1α oligomerization state and RNase domain activity
(A) The kinase domain active site of apo human dP-IRE1α* adopts an active conformation. Because αC-helix-in is a conformation conducive to dimerization, this allows the formation of RNase active back-to-back dimers as shown by the cartoon below. (B) In contrast, human IRE1α bound to the ATP-competitive Amgen KIRA (compound **33**; PDB: 4U6R) presents an inactive kinase conformation because the αC-helix-out conformation is adopted. The cartoon below indicates that back-to-back dimers are incompatible with this inactive kinase conformation due to αC-helix-out steric clashes at the dimer interface (see also Figure 1.10).

The ATP-competitive KIRA developed by Amgen (compound **33**) appears to exploit this mechanism of RNase inhibition (PDB: 4U6R)[55], Compound **33** projects an arylsulfonamide moiety toward IRE1α*'s αC-helix, which causes a ~2 Å displacement from the active conformation (**Figure 1.9B**). This shift of IRE1α*'s αC-helix from the active conformation disrupts part of the back-to-back dimer interface of the kinase domain and results in potent RNase inhibition (**Figure 1.10**).

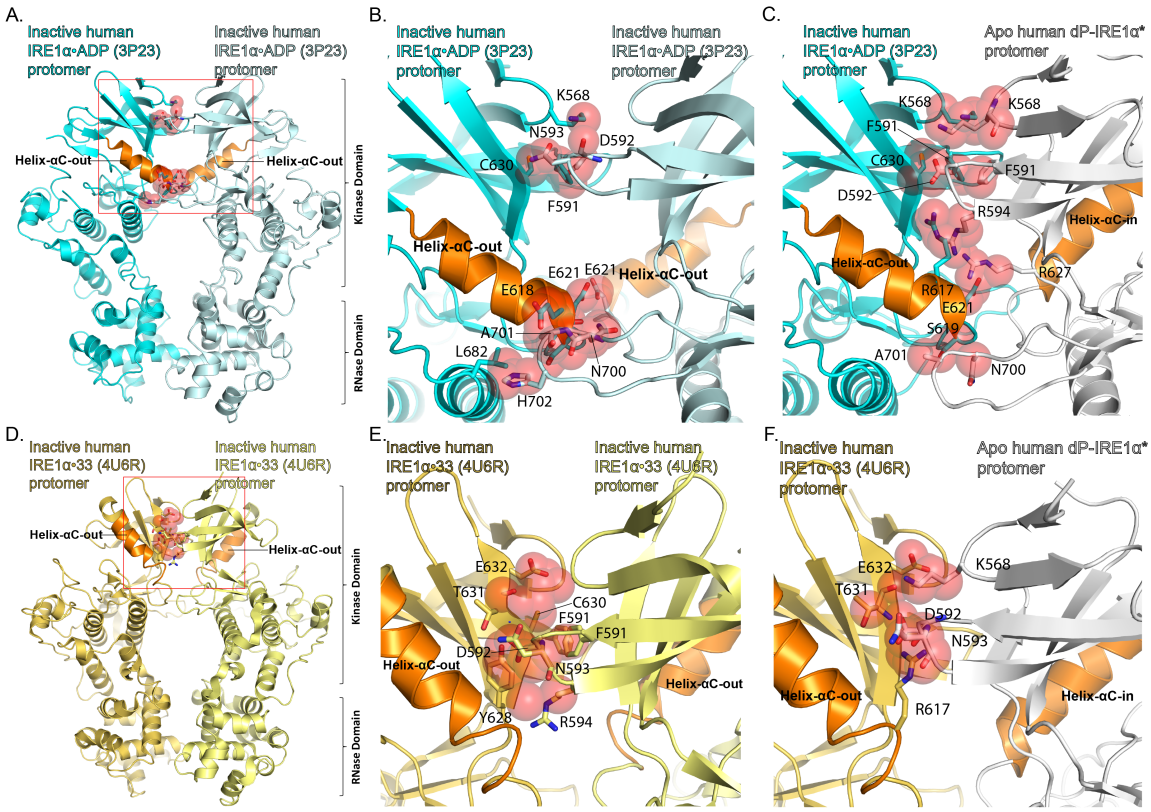

Figure 1.10 αC-Helix out is not conducive to forming the IRE1α RNase active back-to-back dimer

(A) Superimposition of two inactive IRE1α·ADP protomers (PDB: 3P23) onto the protomers of our RNase active dP-IRE1α* back-to-back dimer produces an incompatible back-to-back dimer model because of steric clashes when αC-helix-out is adopted. (B) A zoomed in view of the incompatible IRE1α·ADP back-to-back dimer model with steric clashed residues indicated. (D) Superimposition of two inactive IRE1α·KIRA protomers (PDB: 4U6R) onto our RNase active dP-IRE1α* back-to-back dimer also produces an incompatible back-to-back dimer model because of steric clashes resulting from the αC-helix-out conformation. (E) A zoomed in view of the incompatible IRE1α·KIRA back-to-back dimer model with steric clashed residues indicated. (C, F) Similarly, an incompatible dimer results when superimposing onto our RNase active dP-IRE1α* back-to-back dimer, one active dP-IRE1α* protomer in combination with one inactive IRE1α·ADP protomer, or one inactive IRE1α·KIRA protomer. Here, the hetero combination of one protomer with αC-helix-in, and the other with αC-helix-out, also creates steric clashes. Red spheres = steric clashes, inactive IRE1α·ADP protomer = cyan, inactive IRE1α·KIRA protomer = yellow, active apo dP-IRE1·KIRA protomer = gray, αC-helix = orange. The ADP and KIRA ligands have been omitted for clarity.

Furthermore, incubation of a saturating concentration of **33** with phosphorylated IRE1α* resulted in suppression of dimer formation in an in vitro cross-linking assay (**Figure 1.11C**). Although the KIRAs characterized in this study possess

aryl-urea moieties that are common in ligands that stabilize a flipped activation segment DFG-motif (DFG-out), it is likely they also stabilize IRE1α*'s αC-helix-out conformation based on their inhibition of dimer formation of phosphorylated IRE1α* in the same cross-linking assay (**Figure 1.11B**). For many of the KIRAs shown in Figure 1.3, this could be accomplished by directly displacing αC-helix from an active conformation like compound **33** although a larger movement than what is observed in structure 4U6R would likely be necessary to accommodate bulkier aryl-urea moieties. Consistent with this notion, a co-crystal structure of compound **1** bound to an off target kinase Src tyrosine kinase that we have determined shows this kinase in the αC-helix-out conformation, demonstrating that aryl-ureas are able to stabilize this inactive form (PDB: 5J5S). Overlay of Src·**1** with our active apo dP-IRE1α* structure reveals that the aryl-urea moiety of **1** is sterically incompatible with the αC-helix-in conformation (**Figure 1.12**). Thus, it is likely that our KIRAs and compound **33** lead to very similar conformational changes in the ATP-binding site of IRE1α and have a similar mechanism of RNase inhibition. On the basis of the observed interactions between IRE1α*'s αC-helix and the base of the activation segment in our dP-IRE1α* structure, we propose that inhibitors that stabilize the DFG-out conformation of the DFG-motif could also lead to αC-helix displacement and RNase inhibition by disrupting the interactions between the activation segment and αC-helix (**Figure 1.7C**). These interactions appear to anchor αC-helix in the active conformation, and the crankshaft rotation of the DFG motif that yields the DFG-out conformation would

collapse the activation segment into an inactive disordered conformation and destabilize the αC-helix-in conformation as exemplified in existing inactive IRE1α structures (PDB: 3P23, 4PL3).

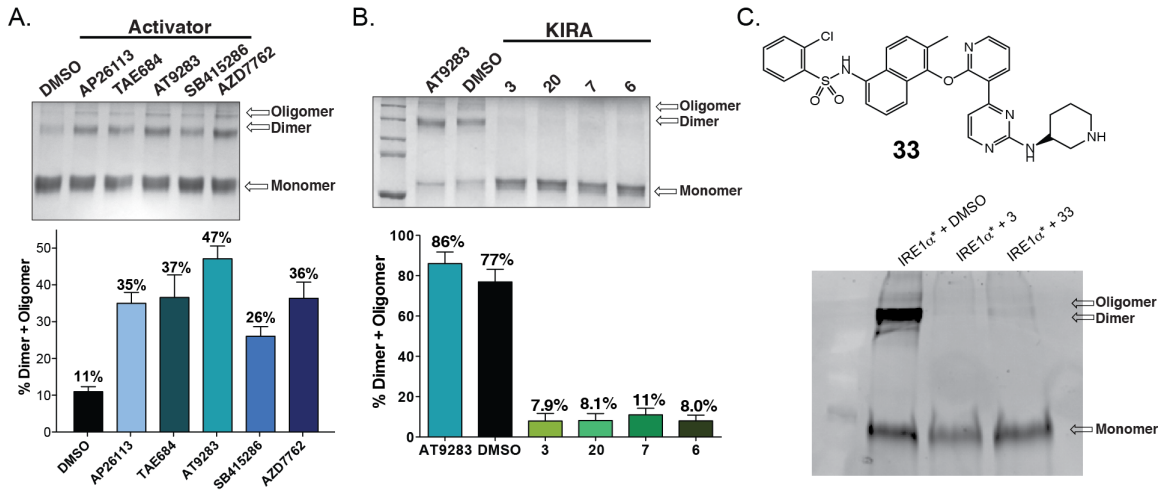

Figure 1.11 ATP-competitive inhibitors affect IRE1α oligomer formation
(A) Quantification of the ratios of dimeric/oligomeric to monomeric IRE1α* (mean ± SEM, n = 3). dP-IRE1α* (15 μM) was incubated with DMSO or the KIRA/Activator shown (100 μM) and then treated with 250 μM DSS. (B) Quantification of the ratios of dimeric/oligomeric to monomeric IRE1α* (mean ± SEM, n = 3). IRE1α* (15 μM) was incubated with DMSO or the KIRA shown (100 μM) and then treated with the chemical cross-linker disuccinimidyl suberate ([DSS] = 250 μM (C) SDS-PAGE gel of IRE1α* (7.5 μM) after incubation with DMSO, Compound **3** (100 μM), or previously characterized Amgen compound, **33**, (100 μM) and treated with chemical crosslinker disuccinimidyl suberate (DSS; 250 μM). The gel was visualized via SYPRO-Ruby Red Staining.

Indeed, in the structure of dephosphorylated IRE1α* bound to ADP (PDB: 3P23), which contains a αC-helix displaced 7.4 Å from the active conformation, the Glu618–Lys717 and Arg611–Gly713 and Cys715–backbone salt bridges are absent, and the activation segment is completely disordered (**Figure 1.10A**). Therefore, KIRAs may be able to prevent the RNase active back-to-back dimer and inhibit the RNase activity of IRE1α by displacing the activation segment, resulting in the disruption of contacts that anchor αC-helix in the active conformation. This model is especially appealing for KIRAs **20** and **21**, which

contain extended 4-methylpiperazin-1-yl aryl-urea substituents like the DFG-out-stabilizing inhibitor imatinib that are unlikely to be accommodated in the relatively confined pockets created by the movement of αC-helix in structures 4U6R and 3P23 (**Figure 1.9B, Figure 1.10A-F**). One caveat to this model is that any KIRAs that stabilize the DFG-out inactive conformation of IRE1α must lack the canonical hydrogen bond with Glu612 in αC-helix because this interaction would likely lead to increased dimer formation and subsequent RNase activation.

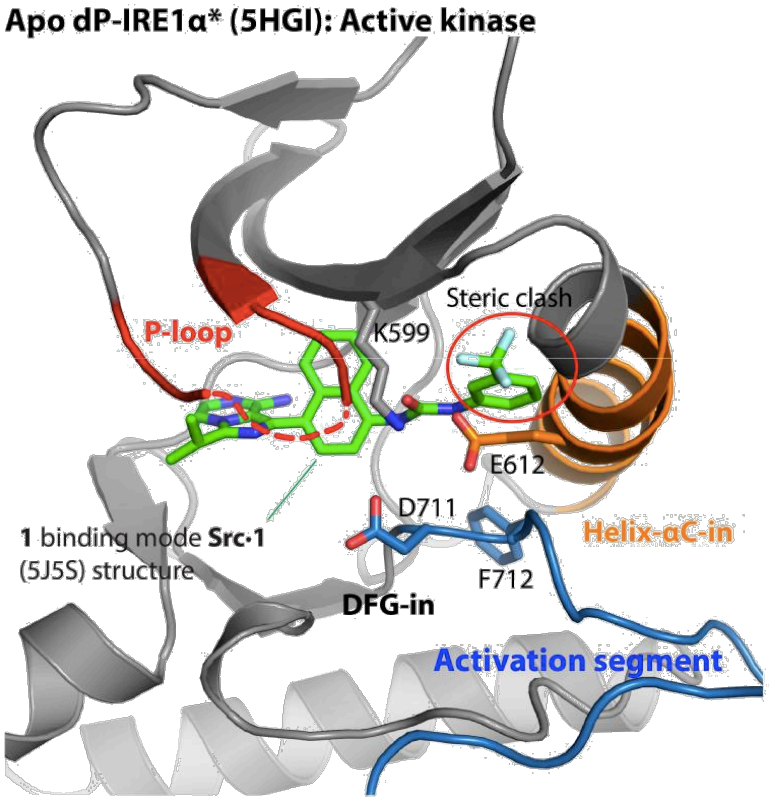

Figure 1.12. The binding mode of 1 in Src is incompatible with the *apo* dP-IRE1α* active kinase conformation
In complex with **1**, Src is stabilized in the αC-helix-out conformation (PDB: 5SJS). Superimposition of the binding mode of **1** (green) from the Src·**1** crystal structure onto the *apo* dP-IRE1α* ATP-binding site (PDB: 5HGI), produces a steric clash between the R_3 moiety of **1** and the αC-helix-in conformation. **1** was superimposed onto the *apo* dP-IRE1α* ATP-binding site by backbone alignment of the Src·**1** co-crystal structure with the *apo* dP-IRE1α* kinase domain structure.

Our data in **Figure 1.6** suggests that ATP-competitive kinase inhibitors activate the RNase domain unless they displace either αC-helix or the DFG-motif from the active conformation. For all IRE1α RNase activators (**Figure 1.5**) that co-crystal structures are available for, the bound kinase target is in the active, αC-helix-in conformation (**Table 1.1**). Similarly, these activators could be computationally docked to the active structure of dP-IRE1α* (data not shown), while aryl-ureas KIRAs cannot (**Figure 1.12**). Consistent with the RNase activators in **Figure 5** leading to stabilization of the αC-helix-in conformation, all compounds tested led to increased dimerization/oligomerization of dP-IRE1α* (**Figure 1.11A**). However, this stabilization does not appear to be through a direct interaction with either the DFG-motif or αC-helix, as none of the crystal structures or docked inhibitor structures show direct interactions with these structural motifs. Instead, binding of inhibitors to the ATP-binding site complements a cluster of hydrophobic amino acids ("catalytic spine") that promotes the closure of the active site between the kinase N-and C-lobes, which stabilizes the active αC-helix-in conformation.[57]

III. Conclusion

The ATP-binding sites of protein kinases are allosterically coupled to distal binding and regulatory sites in the kinase domain.[58] These allosteric networks allow communication between the ATP-binding and protein substrate-binding sites and are important for the regulation of kinase catalytic activity.[59,60] Biochemical and structural studies have defined how binding at allosteric regulatory sites and post-translational modifications are able to affect kinase

catalytic activity through the modulation of ATP-binding site conformation.[61] These kinase allosteric networks are bi-directional in that conformation-selective ATP-competitive inhibitors are able to influence distal sites in the kinase domain.[61–66] In this study, we have explored the allosteric relationship between the kinase and RNase domains of the ER sensor protein IRE1α. By screening a panel of commercially available kinase inhibitors, we find that most ATP-competitive inhibitors that interact with the kinase domain of IRE1α activate RNase activity rather than inactivate it. Diverse ATP-competitive ligands show variable levels of RNase activation of dephosphorylated IRE1α, which has very low basal RNase activity. Furthermore, these ATP-competitive IRE1α activators increase cellular XBP1 mRNA splicing in the absence of ER stress. All tested kinase inhibitors that increase the activity of the RNase domain also promote dimerization of the dephosphorylated form of IRE1α. Thus, most ATP-competitive kinase inhibitors strengthen the dimer interface that is necessary for RNase activity. The general characteristic of demonstrating enhanced dimerization in the presence of most ATP-competitive ligands is shared by RAF kinase.[67] For RAF, the propensity to dimerize in the presence of ATP-competitive inhibitors is believed to be responsible for the paradoxical activation of the RAF → MEK → Erk signaling pathway that is observed in certain cell lines. Interestingly, inhibitors that overcome paradoxical RAF pathway activation may prevent dimerization by enforcing a more pronounced adoption of the αC-helix-out conformation.[68]

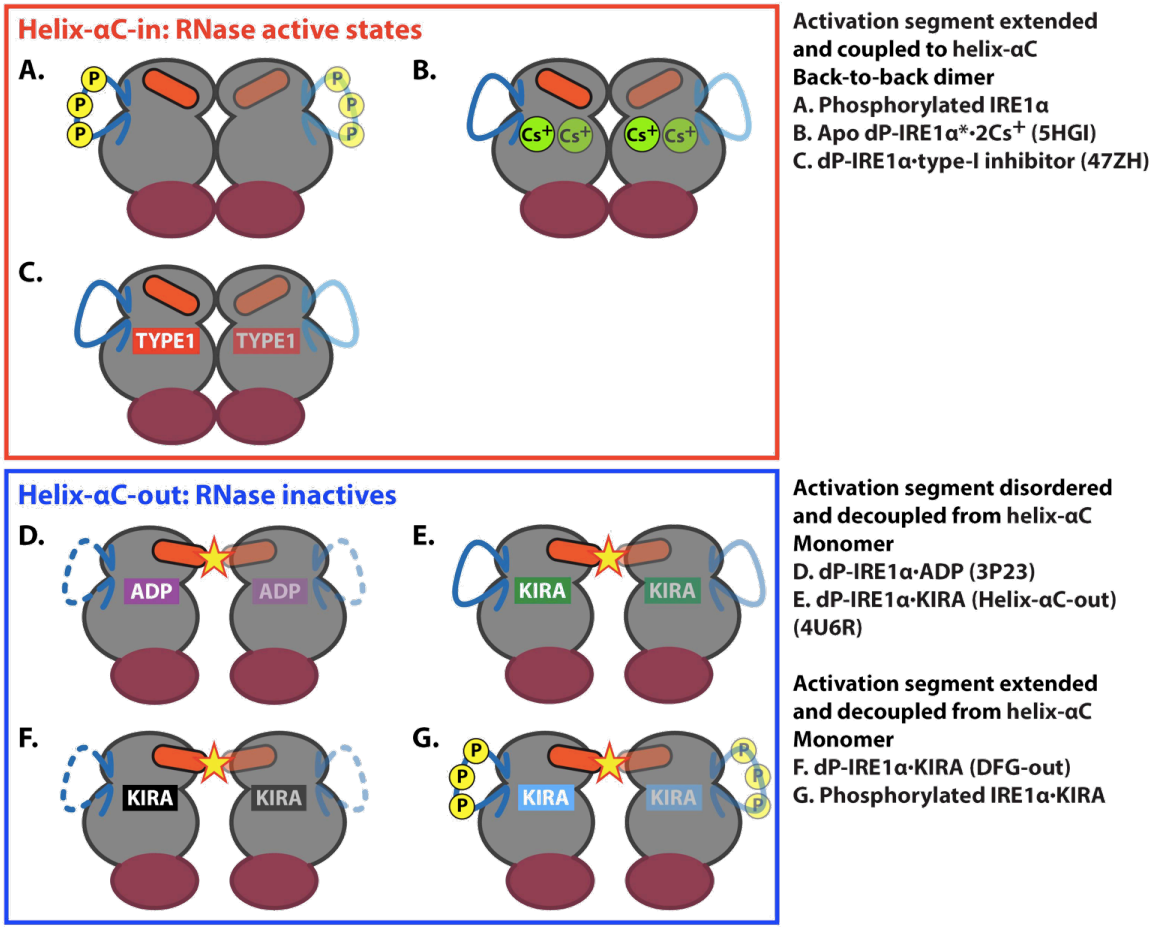

Figure 1.13 Schematic model summarizing the divergent modulation of IRE1α RNase activity

(A-G) IRE1α RNase activity depends on the conformation of αC-helix, because it regulates formation of the RNase active back-to-back dimer. AC-helix-in, and αC-helix-out, coincides with the RNase active back-to-back dimer (A-C), and RNase inactive monomer states (D-G), respectively. AC-helix-in can be stabilized through coupling with an extended activation segment which is stabilized by (A) phosphorylation, or (C) a type I inhibitor (PDB: 4Z7H). (B) AC-helix-in can also be stabilized directly by Cs^+ binding, and through coupling with the extended activation segment that is also stabilized by Cs^+ (PDB: 5HGI). Conversely, αC-helix-out can be stabilized through decoupling of αC-helix from the activation segment. This can occur when bound by (D) ADP (PDB: 3P23), (E, G) a KIRA that directly displaces αC-helix regardless of the extended activation segment, (PDB: 4U6R), (F) a KIRA that indirectly displaces αC-helix by stabilizing the DFG-out conformation and collapsing the activation segment.

In contrast to most inhibitors of IRE1α's kinase activity, a series of imidazopyrazine-based inhibitors that we have developed called KIRAs lead to allosteric inhibition of the RNase domain. For inhibitors based on the

imidazopyrazine KIRA scaffold, IC_{50}'s for kinase and RNase inhibition are highly correlated, highlighting the strong degree of coupling between both enzymatic activities of IRE1α. Furthermore, for all but a few of the KIRAs characterized, the level of ATP-binding site occupancy directly correlates with the degree of RNase inhibition, demonstrating that most KIRAs show complete rather than partial allosteric inhibition. The observed ability of KIRAs to block IRE1α dimerization/oligomerization, which is necessary for RNase activity, provides insight into the mechanism of allosteric inhibition. By stabilizing an ATP-binding site conformation that is incompatible with dimer formation, KIRAs are able to directly translate kinase domain interactions into RNase domain inhibition. This mechanism of allosteric RNase inhibition appears to be shared by the only other KIRA series that have been developed to date.[55] These KIRAs exemplified by inhibitor **33** are based on a completely different scaffold and contain an aryl sulfonamide instead of an aryl-urea yet still inhibit RNase activity through the kinase domain and suppress formation of IRE1α dimers/ oligomers.

We have resolved an apo dP-IRE1α* structure that adopts a back-to-back dimer resembling the active yIRE1 dimer. Furthermore, the dP-IRE1α* kinase domain contains the signatures of an active conformation, a prerequisite for IRE1α back-to-back dimerization and subsequent RNase activity. The active αC-helix-in conformation is critical for RNase domain activity because it allows IRE1α back-to-back dimerization to occur. Salt bridge interactions also exist between αC-helix

and the activation segment, indicating coupling between these regulatory elements. Because these regulatory elements are coupled, the destabilization/stabilization of either one can likely lead to destabilization/stabilization of the other, allowing for divergent modulation of RNase activity (**Figure 1.13**). As αC-helix is a dynamic element in the ATP-binding site that is a major component of the dimer interface, it is tempting to speculate that type I ATP-competitive RNase activators of IRE1α exert their influence by stabilizing the active conformation of αC-helix. None of the activators described in this study, for which kinase-bound structures are available directly interact with αC-helix, so this influence would have to be of an indirect nature. In contrast, KIRAs can inhibit the RNase activity of phosphorylated IRE1α by displacing αC-helix from an active conformation to an inactive conformation that is incompatible with back-to-back dimer formation. This displacement can either occur directly by inhibitors displaying substituents that would clash with the active αC-helix-in conformation, or indirectly, by stabilizing an inactive activation segment that disrupts the anchoring of αC-helix.

IV. Materials and Methods

A. Synthesis and Characterization of Intermediates

General Information

Unless noted, reagents were obtained from commercial sources and used without further purification. ^{1}H NMR spectra were obtained using a Bruker AV-300, AV-301, or 500 instrument at room temperature. Chemical shifts are

reported in ppm, and coupling constants are reported in Hertz. Mass spectrometry was performed on a Bruker Esquire Ion Trap MS instrument.

HPLC Preparatory Purification Conditions

Samples were injected onto a preparatory reverse-phase C18 column (250x21 mm) and separated using a Varian Pro-Star 210/325 HPLC instrument over 60 minutes at 8 mL/min (Acetonitrile/Water-0.05% TFA gradient: 1% B Phase to 100% B Phase). Purified products were detected using UV absorption at 254 nm and 220 nm.

HPLC Analytical Purification Conditions

Samples were injected onto an analytical reverse phase C18 column and separated using a Varian Pro-Star 210 HPLC instrument over 30 minutes at 1 mL/min (Acetonitrile/Water-0.05% TFA gradient 1%-100% B Phase). Purity of products was determined using UV absorption at 254 nm and 220 nm. Purity was determined by integrating the product peak and calculating its purity as a percentage of background subtracted total area.

$$\%\ Purity = \frac{Area\ of\ Compound\ Peak}{(Total\ Area\ of\ Compound\ Chromatogram - Total\ Area\ of\ Background\ Chromatogram)} * 100$$

Analytical chromatograms are shown as first the 220 nm channel followed by the 254 nm channel. Percent purity reported for the 220 nm channel of analytical chromatogram or via proton NMR.

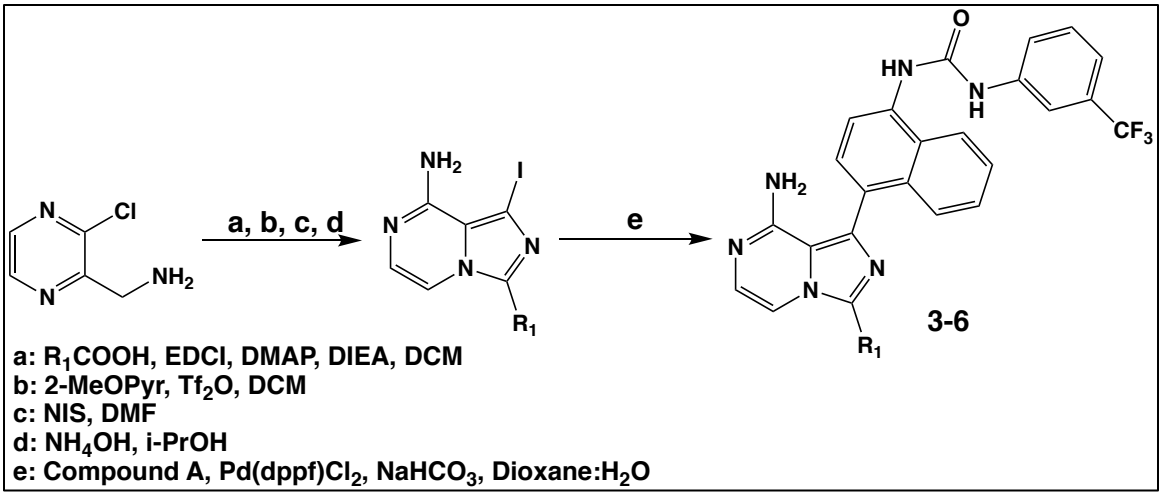

Figure S1.1 Synthetic Scheme 1
Synthesis of imidazopyrazine scaffolds (IA1- IA4) with variable R_1 groups from a commercially available pyrazine starting reagents. Imidazopyrazine scaffolds were further functionalized via Suzuki coupling with Compound A.

Table S1.1[69]

Intermediate Name and Structure:	Synthetic Method and Characterization:
IA1: 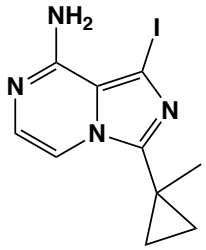	**IA1** was synthesized via **Scheme 1** and derivatized using commercially available 1-methylcyclopropanecarboxylic acid (CAS: 6914-76-7) ^{1}H NMR (300 MHz, MeOD) δ 7.71 (d, *J* = 5.1 Hz, 1H), 7.03 (d, *J* = 5.1 Hz, 1H), 1.42 (s, 3H), 1.03 (dd, *J* = 11.6, 7.6 Hz, 2H), 1.00 – 0.87 (m, 2H).
IA2: 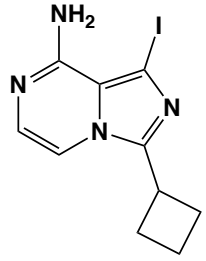	**IA2** was synthesized via **Scheme 1** and derivatized using commercially available cyclobutancecarboxylic acid (CAS: 3721-95-7) ^{1}H NMR (300 MHz, DMSO) δ 7.47 (d, *J* = 5.0 Hz, 1H), 6.96 (d, *J* = 5.0 Hz, 1H), 6.54 (s, 2H), 3.97 – 3.75 (m, 1H), 2.44 – 2.25 (m, 4H), 2.06 (ddd, *J* = 17.8, 10.7, 8.7 Hz, 1H), 1.98 – 1.81 (m, 1H).

IA3: 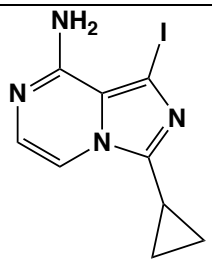	**IA3** was synthesized via **Scheme 1** and derivatized using cyclopropanecarboxylic acid (CAS: 1759-53-1) ^{1}H NMR (300 MHz, MeOD) δ 7.72 (d, *J* = 5.3 Hz, 1H), 6.98 (d, *J* = 5.3 Hz, 1H), 2.23 – 2.13 (m, 1H), 1.26 – 1.11 (m, 2H), 1.05 (dd, *J* = 12.9, 3.3 Hz, 2H).
IA4: 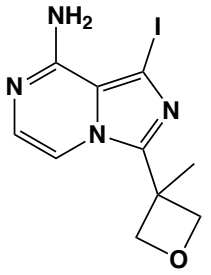	**IA4** was synthesized via **Scheme 1** and derivatized using commercially available 3-methyl-3-oxetanecarboxylic acid (CAS: 28562-68-7) ^{1}H NMR (300 MHz, MeOD) δ 7.25 (dd, *J* = 5.3, 1.9 Hz, 1H), 6.99 (d, *J* = 5.2 Hz, 1H), 5.17 (dd, *J* = 6.2, 1.9 Hz, 2H), 4.75 (dd, *J* = 6.0, 1.7 Hz, 2H), 1.82 – 1.73 (m, 3H).
Compound A: 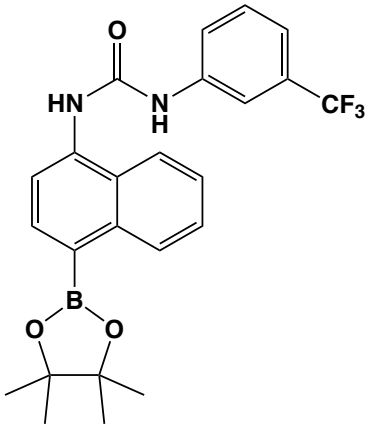	**Compound A** was synthesized and characterized via a previously published procedure.[44]

Table S1.1: Structure and characterization of Scheme 1 intermediates:[69]
(*right)* Chemical structure of intermediates IA1-IA4 and Compound A. *(left).* Synthetic procedure and structural characterization via proton NMR

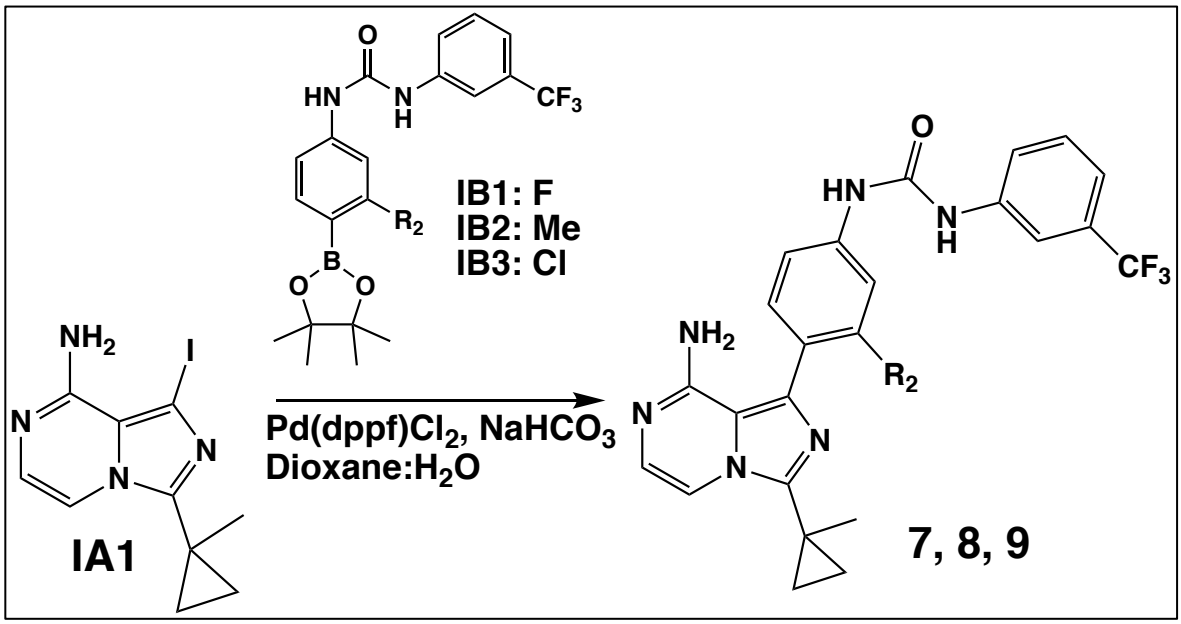

Figure S1.2 Synthetic Scheme 2
Synthesis of final compounds **7-9** using IA1 starting material and coupling of intermediates IB1-IB3 via Suzuki coupling.

Table S1.2

Intermediate Name and Structure:	Synthetic Method and Characterization:
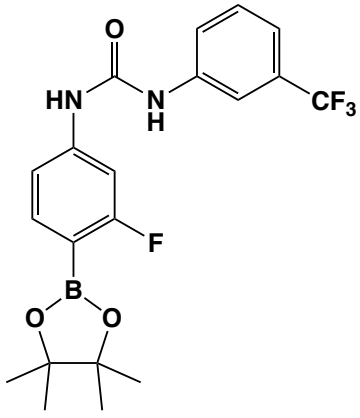 **IB1:**	**IB1:** 4-Amino-2-fluorophenylboronic acid pinacol ester (CAS: 819057-45-9) was dissolved in 0.1 M anhydrous THF at 0ºC. 3-(trifluoro)methylphenyl isocyanate was added dropwise to the reaction mixture. The mixture was brought to room temperature and allowed to stir overnight. The mixture was concentrated *in vacuo* and purified on silica. ^{1}H NMR (300 MHz, DMSO) δ 8.01 (s, 1H), 7.54 (dd, *J* = 15.2, 7.3 Hz, 3H), 7.42 (d, *J* = 12.1 Hz, 1H), 7.34 (d, *J* = 7.6 Hz, 1H), 7.18 (dd, *J* = 8.3, 1.9 Hz, 1H), 1.28 (s, 12H).

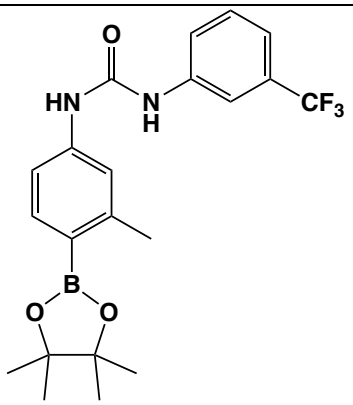 **IB2:**	**IB2:** 4-Amino-2-methylphenylboronic acid, pinacol ester (631911-01-8) was dissolved in 0.1 M anhydrous THF at 0ºC. 3-(trifluoro)methylphenyl isocyanate was added dropwise to the reaction mixture. The mixture was brought to room temperature and allowed to stir overnight. The mixture was concentrated *in vacuo* and purified on silica. ^{1}H NMR (300 MHz, DMSO) δ 8.03 (s, 1H), 7.54 (t, *J* = 9.4 Hz, 4H), 7.33 (s, 3H), 2.44 (s, 3H), 1.29 (s, 12H).
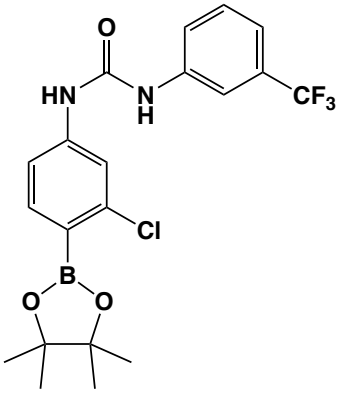 **IB3:**	**IB3:** 4-Amino-2-chlorophenylboronic acid, pinacol ester (CAS: 877160-63-9) was dissolved in 0.1 M anhydrous THF at 0ºC. 3-(trifluoro)methylphenyl isocyanate was added dropwise to the reaction mixture. The mixture was brought to room temperature and allowed to stir overnight. The mixture was concentrated *in vacuo* and purified on silica. ^{1}H NMR (300 MHz, DMSO) δ 8.01 (s, 1H), 7.67 (d, *J* = 1.9 Hz, 1H), 7.64 – 7.51 (m, 5H), 7.31 (d, *J* = 6.0 Hz, 1H), 1.28 (d, *J* = 5.2 Hz, 12H).

Table S1.2 Structure and characterization of Scheme 2 intermediates
(*right)* Chemical structure of intermediates IB1-IB3. *(left).* Synthetic procedure and structural characterization via proton NMR

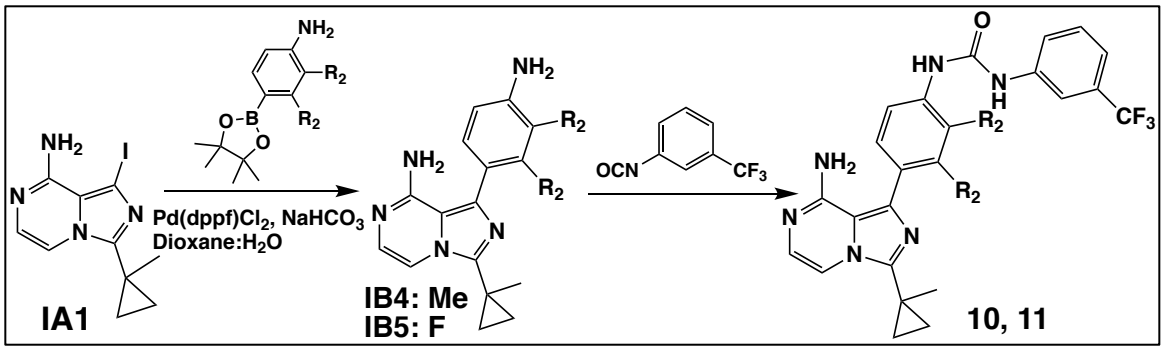

Figure S1.3 Synthetic Scheme 3
Synthesis of final compounds **10,11** using IA1 starting material and coupling of intermediates IB4, IB5 via Suzuki coupling, followed by urea bond formation using 3-(trifluoro)methyl phenyl isocyanate.

Table S1.3

Intermediate Name and Structure:	Synthetic Method and Characterization:
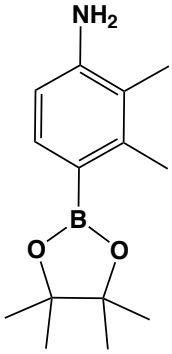 **Compound B:**	**Compound B:** 4-bromo-2,3-dimethylbenzenamine (CAS: 22364-25-6) was dissolved in dioxane (0.2 M) with Bis(pinacolato)diboron (2 eq.), K_2CO_3 (4 eq.), and 1,1'Bis(diphenylphosphino) ferrocene (0.05 eq.). The reaction was left to stir at 90ºC for 12 hr. Reaction was ran over a celite plug and extracted with DCM and H_2O. The organic layer was concentrated *in vacuo* and purified via flash chromatography (0-30% EtOAc in hexanes) and yielded 70% product. ^{1}H NMR (300 MHz, $CDCl_3$) δ 7.53 (d, *J* = 8.0 Hz, 1H), 6.60 – 6.55 (m, 1H), 2.53 (s, 3H), 2.10 (s, 3H), 1.35 (s, 12H).
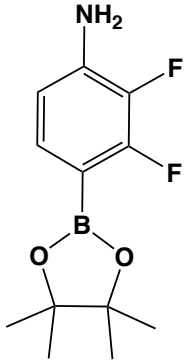 **Compound C:**	**Compound C:** Synthesized with the same procedure as **Compound B** using 4-bromo-2,3-difluorobenzenamine (CAS: 112279-72-8) ^{1}H NMR (300 MHz, $CDCl_3$) δ 6.93 – 6.86 (m, 1H), 6.59 (td, *J* = 8.4, 1.5 Hz, 1H), 1.29 (d, *J* = 1.5 Hz, 6H), 1.26 (s, 6H).
IB4: 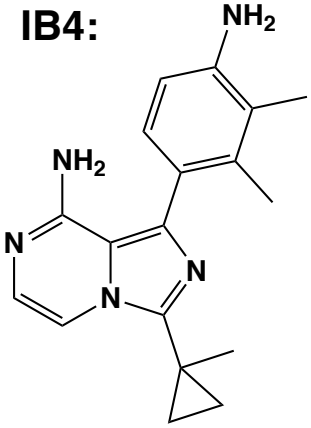	**IB4:** In a microwave vial, **Compound B** (1eq.) and **IA1** (2 eq.) and 0.1 M dioxane:water (3:1) were combined with $NaHCO_3$ (3.4 eq.) and $Pd(dppf)Cl_2$ (0.1 eq.) as described in **Scheme 3**. The vial was sealed and placed in a microwave reactor for 45 minutes at 120ºC. The resulting mixture was washed with DCM:Water, and the organic layers combined. The organic phase was purified via silica chromatography in EtOAc: Hex (0-100%). ^{1}H NMR (300 MHz, $CDCl_3$) δ 7.44 (d, *J* = 4.8 Hz, 1H), 7.02 (d, *J* = 7.9 Hz, 2H), 6.62 (d, *J* = 6.6 Hz, 1H), 3.48 (s, 3H), 2.13 (s, 3H), 1.48 (s, 3H), 1.14 (s, 2H), 0.88 (s, 2H).

IB5: 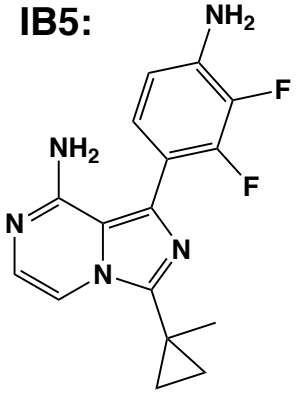	**IB5**: In a microwave vial, Compound C (1eq.) and IA1 (2 eq.) and 0.1M dioxane:water (3:1) were combined with $NaHCO_3$ (3.4 eq.) and $Pd(dppf)Cl_2$ (0.1 eq.) as described in **Scheme 3**. The vial was sealed and placed in a microwave reactor for 45 minutes at 120ºC. The resulting mixture was washed with DCM:Water, and the organic layers combined. The organic phase was purified via silica chromatography in EtOAc: Hex (0-100%). ^{1}H NMR (300 MHz, MeOD) δ 7.69 (d, *J* = 5.1 Hz, 1H), 7.06 (d, *J* = 5.1 Hz, 1H), 7.03 – 6.95 (m, 1H), 6.74 (td, *J* = 8.4, 1.8 Hz, 1H), 1.48 (s, 3H), 1.10 (t, *J* = 5.3 Hz, 2H), 0.96 (dd, *J* = 6.3, 4.6 Hz, 2H).

Table S1.3 Structure and characterization of Scheme 3 intermediates
(*right)* Chemical structure of intermediates Compounds B and C, IB4, and IB5. *(left).* Synthetic procedure and structural characterization via proton NMR

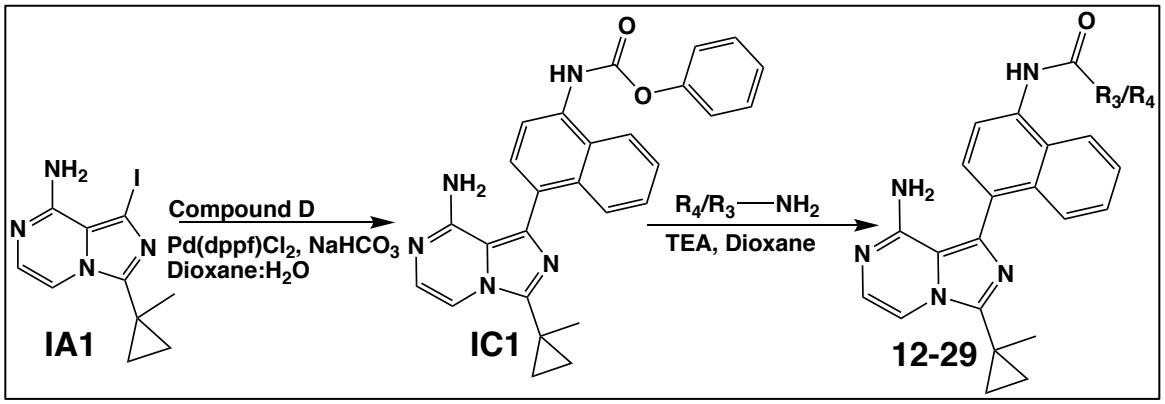

Figure S1.4 Synthetic Scheme 4
Synthesis of final compounds **12-29** using IA1 starting material and coupling of intermediate IC1 via Suzuki coupling, followed by urea bond formation using amine-functionalized reagents.

Table S1.4

Intermediate Name and Structure:	Synthetic Method and Characterization:
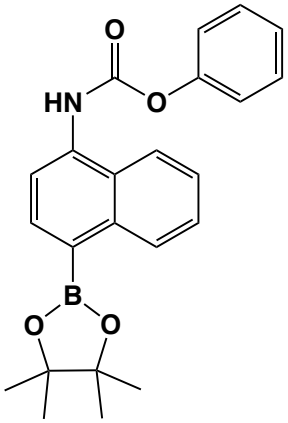 **Compound D:**	**Compound D**: 4-(4,4,5,5-tetramethyl-1,3,2-dioxaboroan-2-yl)-1-naphthalenamine (CAS: 1218790-22-7) (1 eq.) was dissolved in 0.1 M dioxane with TEA (2.4 eq.) followed with the addition of phenyl chloroformate (CAS: 1885-14-9) (2.4 eq.) added dropwise. The reaction was allowed to stir at room temperature overnight. The resulting micture was extracted with DCM:Water, and the organic layers concentrated *in vacuo*. The concentrated mixture was purified on silica. ^{1}H NMR (300 MHz, $CDCl_3$) δ 8.92 – 8.85 (m, 1H), 8.16 – 8.04 (m, 2H), 8.04 – 7.93 (m, 1H), 7.66 – 7.56 (m, 2H), 7.48 – 7.39 (m, 3H), 7.32 – 7.29 (m, 1H), 7.26 (d, *J* = 3.4 Hz, 1H), 1.44 (t, *J* = 0.5 Hz, 12H).
IC1: 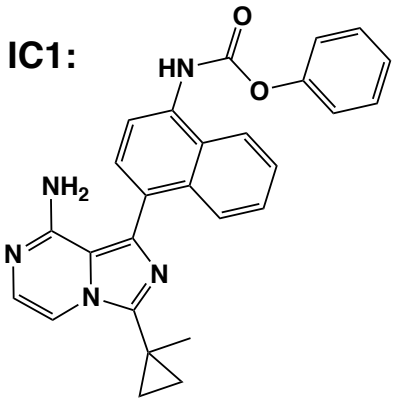	**Compound IC1**: In a microwave vial, **IA1** (1eq.) and **Compound D** (2 eq.) and 0.1 M dioxane:water (3:1) were combined with $NaHCO_3$ (3.4 eq.) and $PdCl_2(dppf)_2$ (0.1 eq.) as described in **Scheme 4**. The vial was sealed and placed in a microwave reactor for 45 minutes at 120ºC. The resulting mixture was washed with DCM:Water, and the organic layers combined. The organic phase was purified via silica chromatography in EtOAc: Hex (0-100%). ^{1}H NMR (300 MHz, $CDCl_3$) δ 8.05 (s, 1H), 7.85 (d, J = 8.3 Hz, 2H), 7.58 (d, J = 5.2 Hz, 1H), 7.47 (dd, J = 15.7, 7.9 Hz, 5H), 7.11 (d, J = 5.1 Hz, 2H), 1.57 (s, 3H), 1.26 (s, 2H), 0.98 (s, 2H).

Table S1.4 Structure and characterization of Scheme 4 intermediates
(*right)* Chemical structure of intermediates Compounds D and IC1. *(left).* Synthetic procedure and structural characterization via proton NMR

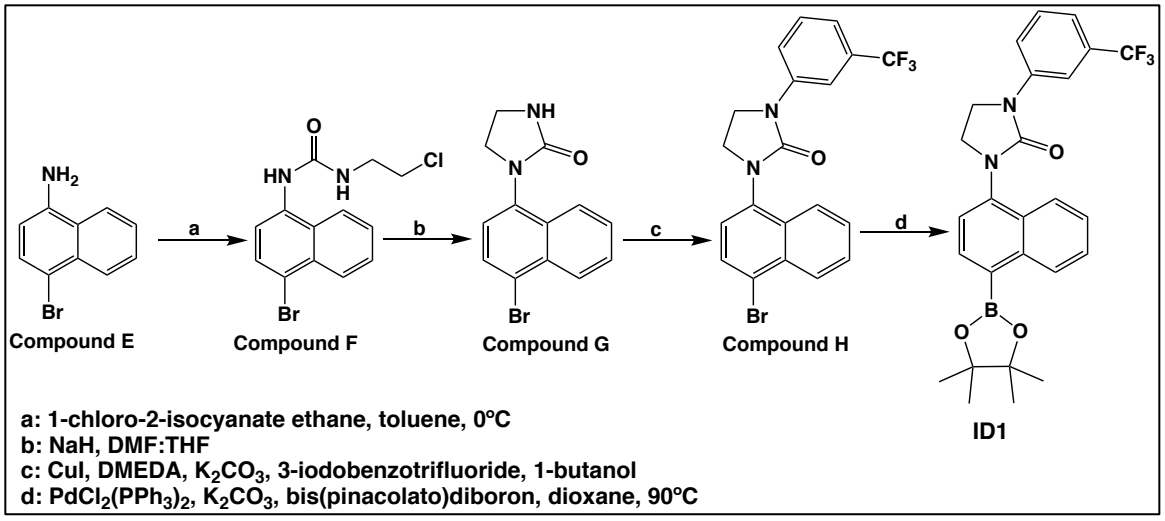

Figure S1.5 Synthetic Scheme 5
Synthesis of intermediates Compound E-H and ID1. In brief, 1-amino-4-bromo naphthalene was coupled with 1-chloro-2-isocyanate ethane to yield Compound F. Compound F was cyclized via NaH to yield Compound G. Copper mediated N-alkylation of the succinimide with 3-trifluoromethylbenzene gave Compound H. Compound H was functionalized with a Suzuki coupling compatible boronic ester.

Table S1.5

Intermediate Name and Structure:	Synthetic Method and Characterization:
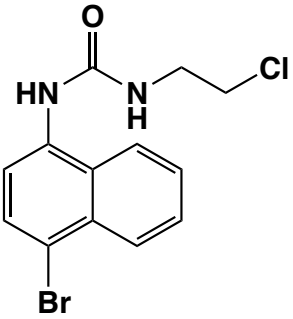 **Compound F**	**Compound F:** Dissolved 1-amino-4-bromonaphthalene (**Compound E**) (1g, 4.5 mmol, 1 eq.) in anhydrous Toluene (12 mL). The reaction was cooled to 0°C and then 1-chloro-2-isocyanate ethane (0.57 g, 5.4 mmol, 1.2 eq.) was dripped into the cooled solution. The reaction was allowed to warm to room temperature and then stirred for 18 hours. The reaction was diluted with ethyl acetate, washed with brine, dried over Na_2SO_4, filtered, and concentrated to yield **compound F** and taken into the next step without purification. ^{1}H NMR (400MHz, DMSO): d 8.8 (s, 1H), 8.2 (dd, 2H), 8.0 (d, 1H), 7.7 (d, 1H), 7.6 (m, 2H), 7.0 (m, 1H), 3.7 (t, 2H), 3.5 (m, 2H).

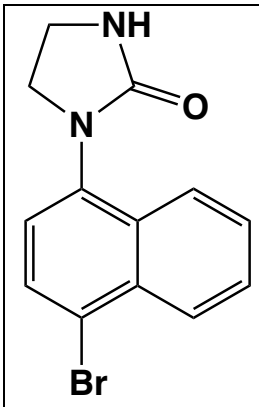 **Compound G**	Sodium Hydride (0.28 g, 6.9 mmol, 1.5 eq.) was suspended in THF (17 mL) and cooled to 0°C. **Compound F** (1.5 g, 4.6 mmol, 1eq.) was dissolved in DMF (17 mL) and dripped into the sodium hydride suspension. The reaction was stirred at 23ºC for 1 hour and then re-cooled to 0°C. The reaction was then quenched with methanol. The reaction was diluted with ethyl acetate, washed with brine, dried over Na_2SO_4, filtered, and concentrated to a solid. The solid was purified by column (0% to 100% ethyl acetate/hexane) to yield **compound G** (0.69 g, 52% yield) ^{1}H NMR (400MHz, DMSO): d 8.2 (d, 1H), 8.0 (d, 1H), 7.9 (d, 1H), 7.7 (m, 2H), 7.4 (d, 1H), 6.9 (s, 1H), 3.8 (m, 2H), 3.5 (m, 2H).
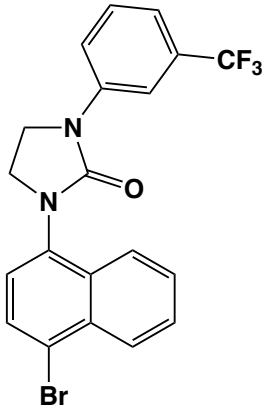 **Compound H**	**Compound G** (0.1 g, 0.35 mmol, 1 eq.), 3-Iodobenzotrifluoride (0.075 mL, 0.52 mmol, 1.5eq), Copper(I) Iodide (7mg, 0.035 mmol, 0.1 eq.), DMEDA (0.013 mL, 0.10 mmol, 0.3 eq.), and K_2CO_3 (0.14 g, 1.0 mmol, 3 eq.) were dissolved in n-butanol (1.4 mL). The reaction was heated at 100ºC for 2 hours. The reaction was diluted with ethyl acetate, washed with NH_4Cl and brine, dried over Na_2SO_4, filtered, and concentrated to yield crude **compound H** ^{1}H NMR (400MHz, DMSO): d 8.3 (m, 2H), 8.1 (d, 1H), 8.0 (d, 1H), 7.7-7.5 (m, 5H), 7.4 (d, 1H), 4.2 (m, 2H), 4.0 (m, 2H)
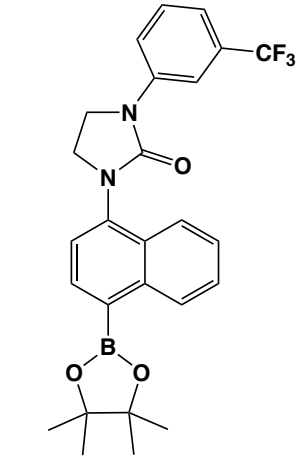 **ID1**	**Compound H** (0.15 g, 0.35 mmol, 1 eq.), Bis(pinacolato) diboron (0.13 g, 0.52 mmol, 1.5 eq.), Bis(triphenylphosphine) palladium(II) dichloride (0.012g, 0.017 mmol, 0.05 eq), and K_2CO_3 (0.19 g, 1.38 mmol, 4 eq.) in dioxane (1.7 mL). The reaction was heated at 90°C for 18 hours. The reaction was diluted with ethyl acetate, washed with brine, dried over Na_2SO_4, filtered, and concentrated to a solid. The solid was purified by column (0% to 35% ethyl acetate/hexane) to **ID1** (0.042g, 25% yield). ^{1}H NMR (400MHz, $CDCl_3$): d 8.8 (d, 1H), 8.2 (d. 1H), 7.9 (m, 3H), 7.5 (m, 4H), 7.4 (d, 1H), 4.2 (m, 2H), 4.1 (m, 2H), 1.4 (s, 12H)

Table S1.5 Structure and characterization of Scheme 5 intermediates
(*right)* Chemical structure of intermediates Compounds F-H and ID1. *(left).* Synthetic procedure and structural characterization via proton NMR

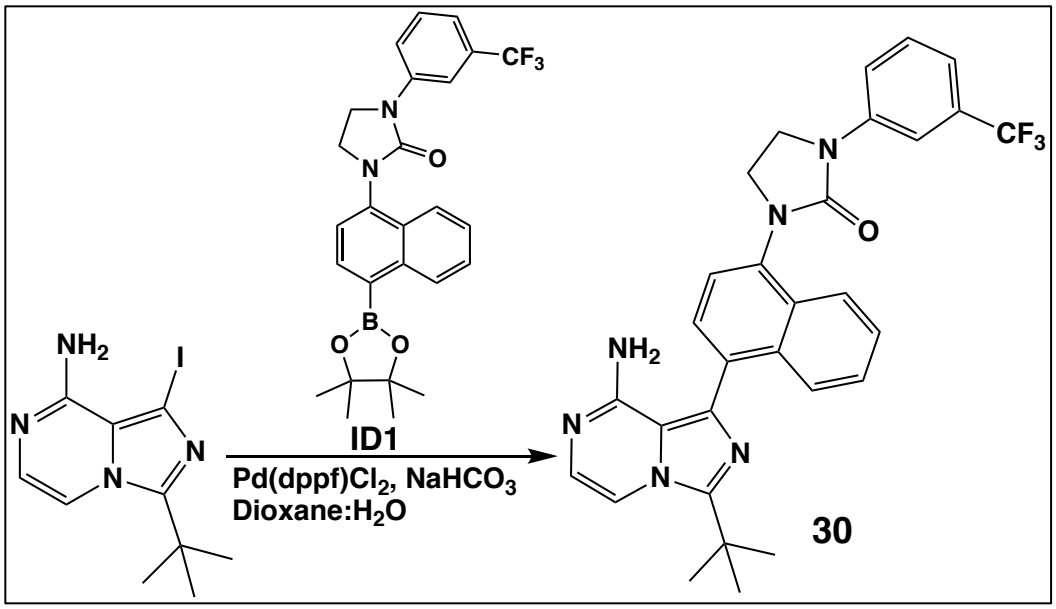

Figure S1.6 Synthetic Scheme 6
Synthesis of final compound **30** using a tert-butyl imidazopyrazine starting material and coupling of intermediate ID1 via Suzuki coupling.

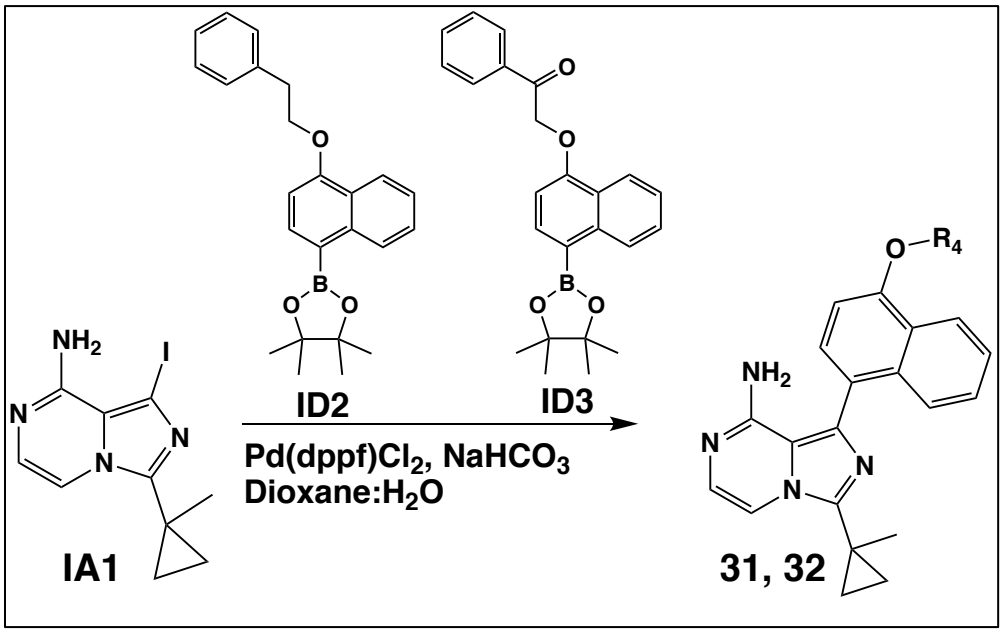

Figure S1.7 Synthetic Scheme 7
Synthesis of final compound **31** and **32** using a IA1 starting material and coupling of intermediate ID2 or ID3 via Suzuki coupling.

Table S1.6

Intermediate Name and Structure:	Synthetic Method and Characterization:
ID2: 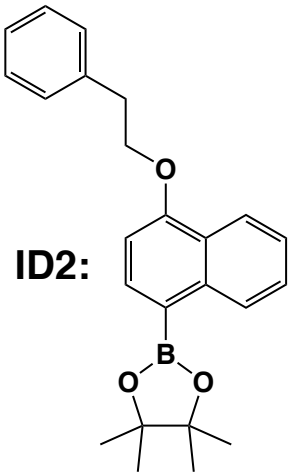	**ID2:** 4-bromo-1-naphthalenol (1 eq.) (CAS: 571-57-3) and (2-bromoethyl)-benzene (CAS:103-63-9) (2 eq.) were dissolved in DMF with K_2CO_3 (4 eq.) and stirred at 75ºC overnight. The resulting mixture was washed with DCM:Water and the organic phase concentrated *in vacuo*. The concentrated mixture was further purified on silica. ^{1}H NMR (300 MHz, $CDCl_3$) δ 8.79 (dd, *J* = 8.4, 0.6 Hz, 1H), 8.41 – 8.26 (m, 1H), 8.05 (d, *J* = 7.8 Hz, 1H), 7.54 (dddd, *J* = 25.6, 8.1, 6.8, 1.4 Hz, 2H), 7.43 – 7.25 (m, 5H), 6.84 (d, *J* = 7.8 Hz, 1H), 4.38 (dt, *J* = 11.6, 5.7 Hz, 2H), 3.29 (t, *J* = 6.9 Hz, 2H), 1.50 – 1.39 (m, 12H).
ID3: 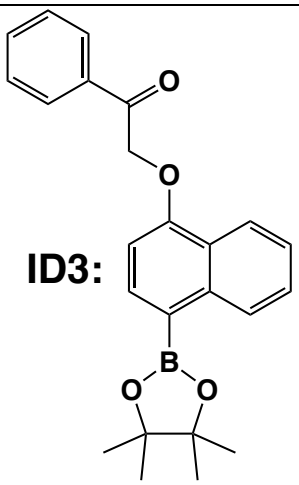	**ID3:** 4-bromo-1-naphthalenol (1 eq.) (CAS: 571-57-3) and 2-bromo-1-phenyl-ethanone (2 eq.) (CAS: 70-11-1) were dissolved in DMF with K_2CO_3 (4 eq.) and stirred at 75ºC overnight. The resulting mixture was washed with DCM:Water and the organic phase concentrated *in vacuo*. The concentrated mixture was further purified on silica. ^{1}H NMR (300 MHz, $CDCl_3$) δ 8.86 – 8.74 (m, 1H), 8.52 – 8.38 (m, 1H), 8.17 – 7.91 (m, 3H), 7.70 – 7.38 (m, 5H), 6.87 – 6.72 (m, 1H), 5.45 (t, *J* = 1.8 Hz, 2H), 1.43 (t, *J* = 1.9 Hz, 12H).

Table S1.6 Structure and characterization of Scheme 7 intermediates
(*right)* Chemical structure of intermediates ID2 and ID3. *(left).* Synthetic procedure and structural characterization via proton NMR

B. Synthesis and Characterization of Final Compounds

Compound 1 [44]: Previously published

Compound 2 [44]: Previously published

Compound 3: Synthesized via **Scheme 1** with **IA1** and **Compound A**. ^{1}H NMR (300 MHz, MeOD) δ 8.29 – 8.23 (m, 1H), 8.06 – 7.98 (m, 3H), 7.86 – 7.81 (m, 1H), 7.71 – 7.67 (m, 2H), 7.65 – 7.50 (m, 2H), 7.39 – 7.33 (m, 1H), 7.11 – 7.05

(m, 1H), 1.64 – 1.58 (m, 3H), 1.30 – 1.21 (m, 2H), 1.12 – 1.05 (m, 2H). Chemical Formula: $C_{28}H_{23}F_3N_6$/Exact Mass: 516.19. $[M+H]^+$ detected: 517.3 m/z. Retention Time: 15.0 minutes; Purity: 97.3%

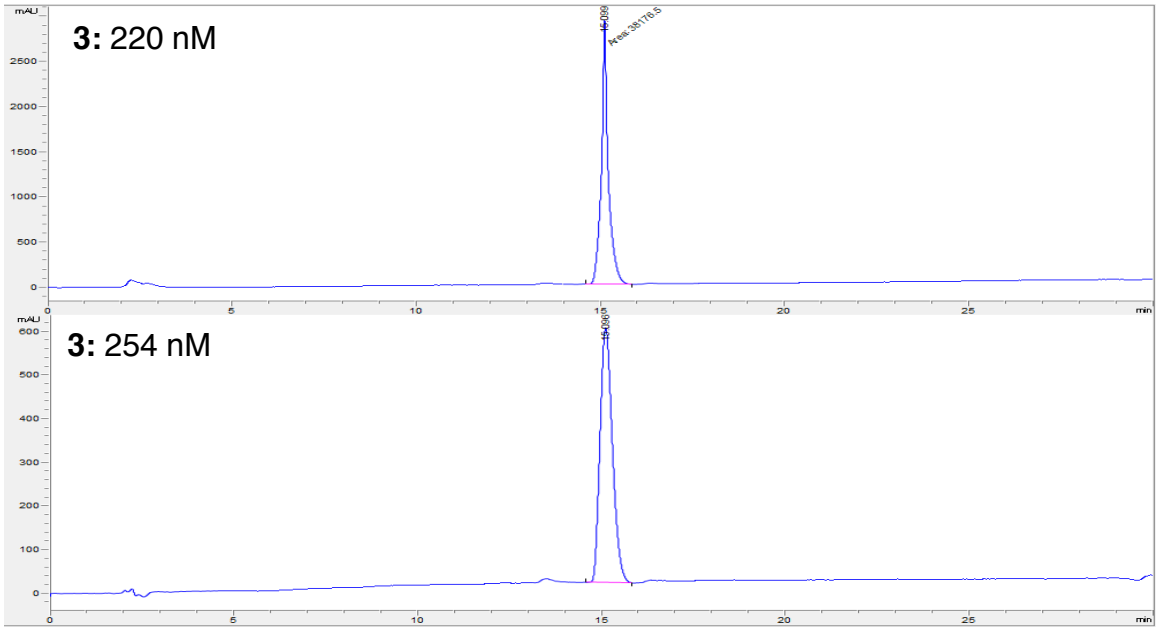

Compound 4: Synthesized via **Scheme 1** with **IA2** and **Compound A**. ^{1}H NMR (300 MHz, MeOD) δ 8.22 (d, *J* = 8.2 Hz, 1H), 8.05 – 7.97 (m, 2H), 7.77 (d, *J* = 8.4 Hz, 1H), 7.68 (dd, *J* = 14.8, 9.1 Hz, 3H), 7.59 – 7.51 (m, 2H), 7.49 (d, *J* = 5.2 Hz, 1H), 7.34 (d, *J* = 7.5 Hz, 1H), 7.02 (d, *J* = 5.2 Hz, 1H), 4.14 – 4.00 (m, 1H), 2.33 – 2.15 (m, 2H), 2.05 (s, 2H), 1.41 – 1.23 (m, 2H). Chemical Formula: $C_{28}H_{23}F_3N_6O$/Exact Mass: 516.19. $[M+H]^+$ detected: 517.3 m/z. Retention time: 14.8 minutes, purity: >99%

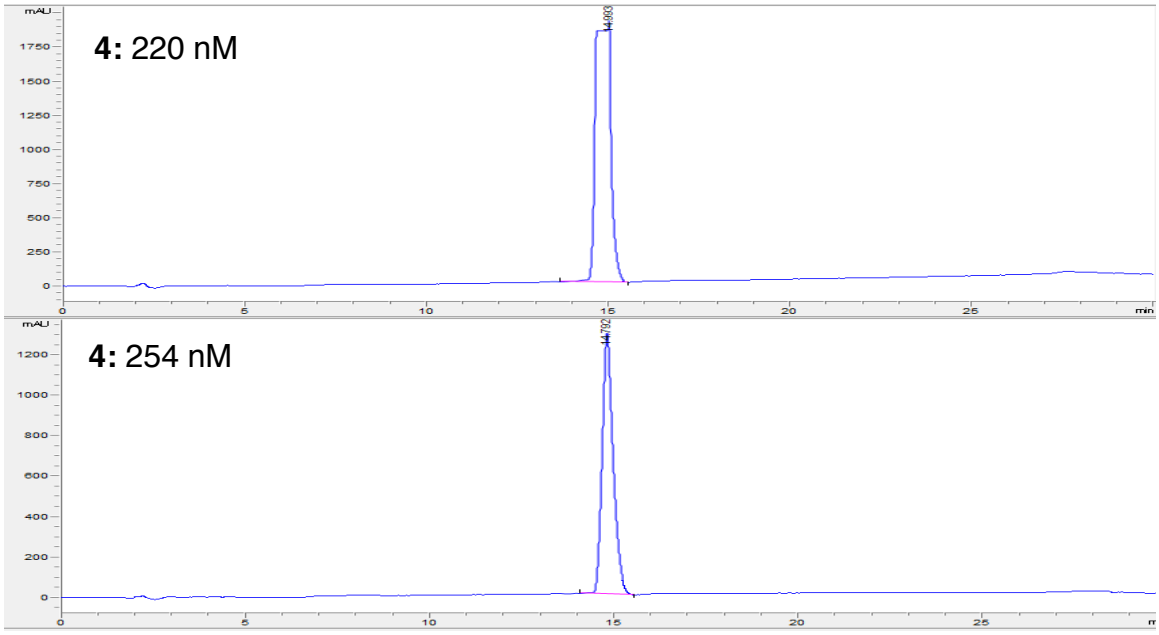

Compound 5: Synthesized via **Scheme 1** with **IA3** and **Compound A**. ^{1}H NMR (300 MHz, MeOD) δ 8.21 (d, *J* = 8.9 Hz, 34H), 8.01 (d, *J* = 7.7 Hz, 32H), 7.73 (d, *J* = 10.6 Hz, 45H), 7.69 (s, 10H), 7.65 (s, 18H), 7.57 (s, 5H), 7.36 (s, 4H), 7.08 (s, 10H), 2.40 – 2.25 (m, 1H), 1.22 (dd, *J* = 20.7, 11.7 Hz, 7H). Chemical Formula: $C_{27}H_{21}F_3N_6O$/Exact Mass: 502.17. $[M+H]^+$ detected: 503.3 m/z. Retention time: 15.2 minutes; purity: 99%

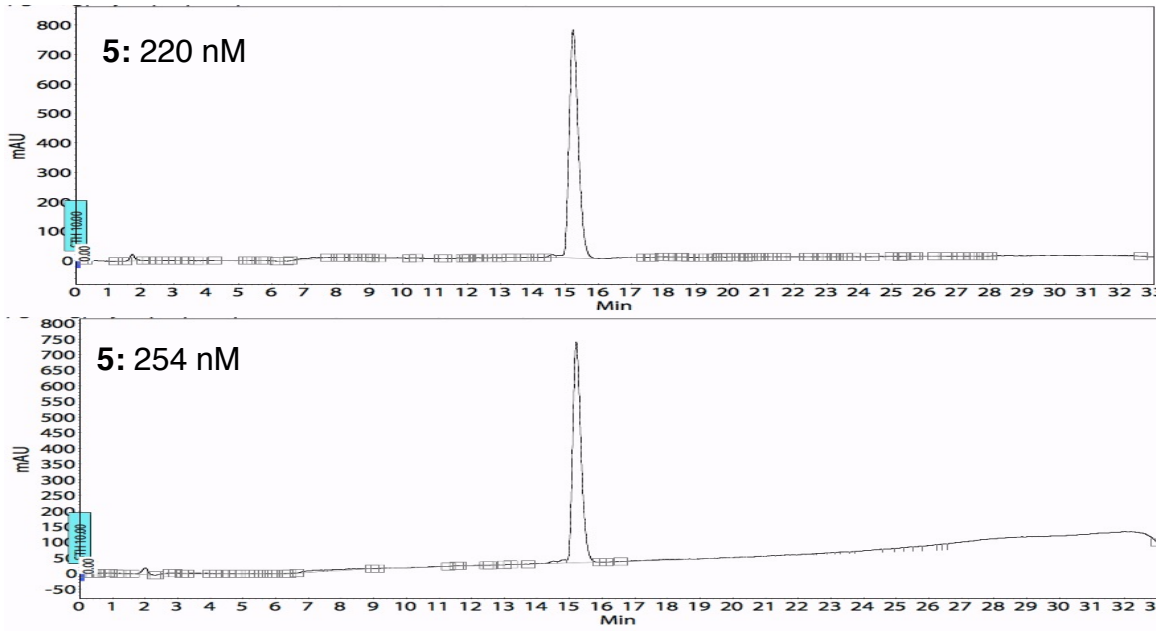

Compound 6: Synthesized via **Scheme 1** with **IA4** and **Compound A**. ^{1}H NMR (300 MHz, MeOD) δ 8.26 (s, 1H), 7.99 (s, 1H), 7.91 (d, *J* = 8.6 Hz, 1H), 7.73 (d, *J* = 3.1 Hz, 1H), 7.65 – 7.49 (m, 1H), 7.35 (d, *J* = 6.9 Hz, 1H), 7.03 (t, *J* = 3.4 Hz, 1H), 5.33 (s, 1H), 4.86 (d, *J* = 6.1 Hz, 1H), 1.95 (s, 1H). Chemical Formula: $C_{28}H_{23}F_3N_6O_2$/Exact Mass: 532.18. $[M+H]^+$ detected: 533.3 m/z. Retention time: 20.2 minutes; purity: 97%

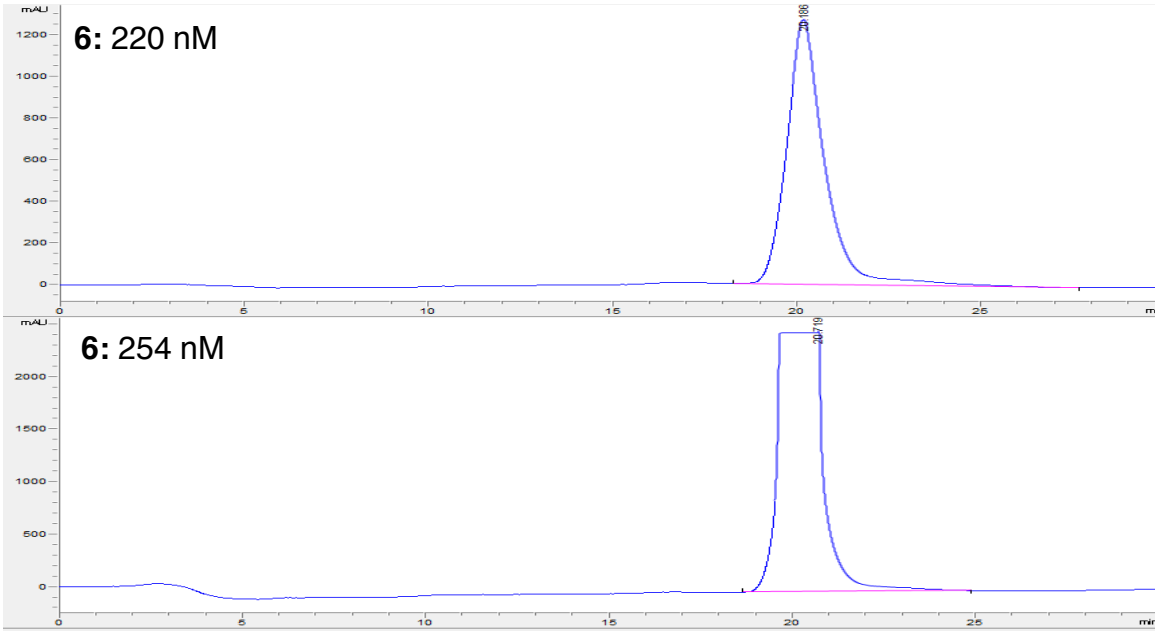

Compound 7: **IB1** (2 eq.) was dissolved with **IA1** (1 eq.) and 0.1 M dioxane:water (3:1) was combined with $NaHCO_3$ (3.4 eq.) and $Pd(dppf)Cl_2$ (0.1 eq.) as described in **Scheme 2**. The vial was sealed and placed in a microwave reactor for 45 minutes at 120ºC. The resulting mixture was washed with DCM:Water, and the organic layers combined. The organic layer was further purified using HPLC in an acetonitrile and water solvent system. ^{1}H NMR (300 MHz, MeOD) δ 7.97 – 7.89 (m, 2H), 7.72 (dd, *J* = 12.6, 2.1 Hz, 1H), 7.64 (d, *J* =

8.5 Hz, 1H), 7.55 – 7.47 (m, 2H), 7.36 – 7.30 (m, 2H), 7.04 – 7.01 (m, 1H), 1.51 (s, 3H), 1.16 (t, *J* = 5.6 Hz, 2H), 1.06 – 1.00 (m, 2H). Chemical Formula: $C_{24}H_{20}F_4N_6O$/Exact Mass: 484.16. Detected $[M+H]^+$= 485.2 m/z. Retention time: 14.7 minutes; purity: 96.8%

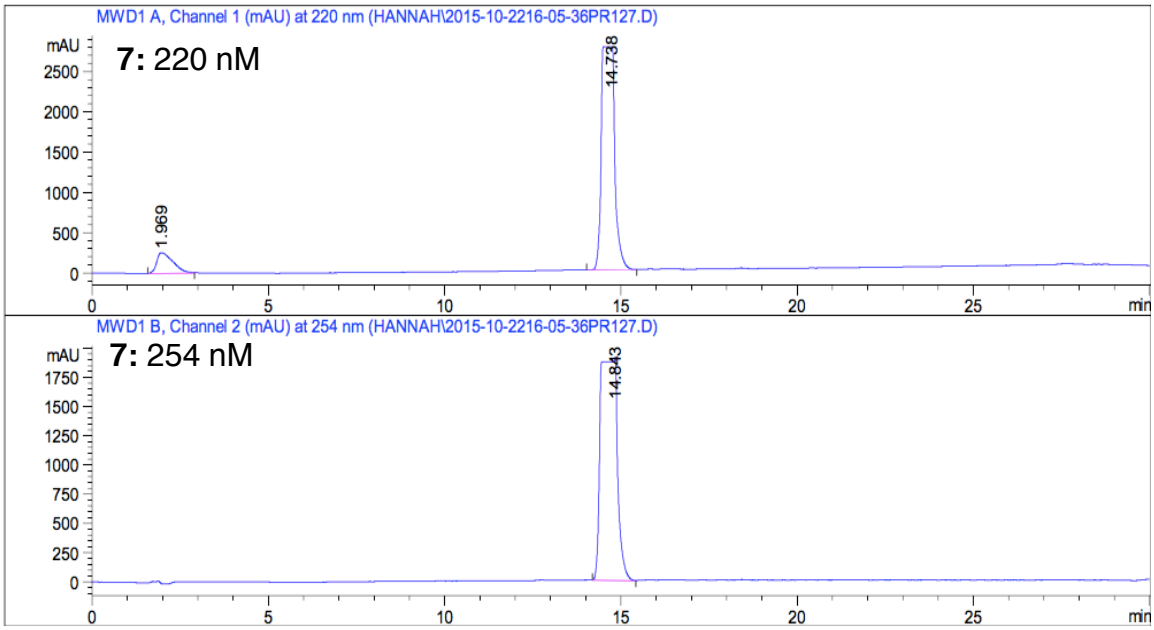

Compound 8: **IB2** (2 eq.) was dissolved with **IA1** (1 eq.) and 0.1 M dioxane:water (3:1) was combined with $NaHCO_3$ (3.4 eq.) and $Pd(dppf)Cl_2$ (0.1 eq.) as described in **Scheme 2**. The vial was sealed and placed in a microwave reactor for 45 minutes at 120ºC. The resulting mixture was washed with DCM:Water, and the organic layers combined. The organic layer was further purified using HPLC in an acetonitrile and water solvent system. ^{1}H NMR (300 MHz, MeOD) δ 8.01 – 7.89 (m, 3H), 7.72 – 7.61 (m, 1H), 7.62 – 7.46 (m, 3H), 7.34 (ddt, *J* = 7.8, 1.9, 1.0 Hz, 1H), 7.09 – 7.00 (m, 1H), 4.94 (d, *J* = 20.1 Hz, 13H), 1.53 (s, 3H), 1.23 – 1.12 (m, 2H), 1.04 (dd, *J* = 6.7, 4.6 Hz, 2H). Chemical

Formula: $C_{25}H_{23}F_3N_6O$/Exact Mass: 480.19. Detected $[M+H]^+$= 481.3 m/z. Retention time: 14.7 minutes; purity: 95.6%

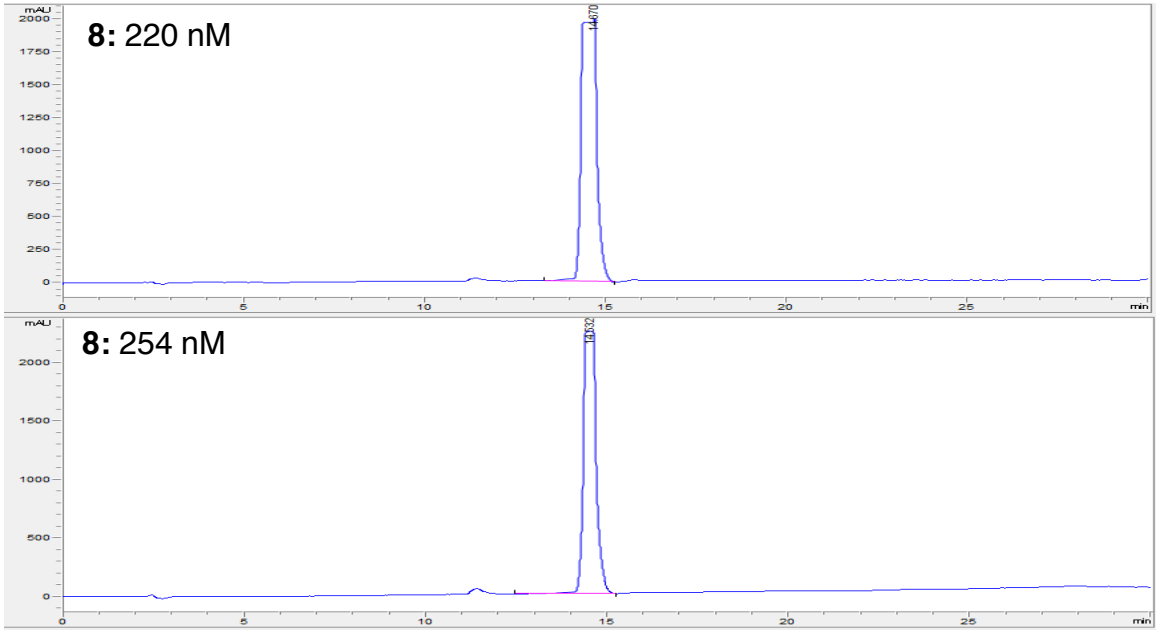

Compound 9: **IB3** (2 eq.) was dissolved with **IA1** (1 eq.) and 0.1 M dioxane:water (3:1) was combined with $NaHCO_3$ (3.4 eq.) and $Pd(dppf)Cl_2$ (0.1 eq.) as described in **Scheme 2**. The vial was sealed and placed in a microwave reactor for 45 minutes at 120°C. The resulting mixture was washed with DCM:Water, and the organic layers combined. The organic layer was further purified using HPLC in an acetonitrile and water solvent system. ^{1}H NMR (300 MHz, MeOD) δ 7.93 (dd, *J* = 8.4, 7.6 Hz, 2H), 7.69 – 7.57 (m, 1H), 7.57 – 7.43 (m, 3H), 7.33 (dd, *J* = 8.5, 3.7 Hz, 2H), 7.07 – 6.94 (m, 1H), 1.52 (d, *J* = 0.9 Hz, 3H), 1.19 – 1.06 (m, 2H), 1.02 (q, *J* = 4.2 Hz, 2H). Chemical Formula: $C_{24}H_{20}ClF_3N_6O$/Exact Mass: 500.13. Detected $[M+H]^+$= 501.4 m/z. Retention time: 17.9 minutes, purity: >99%

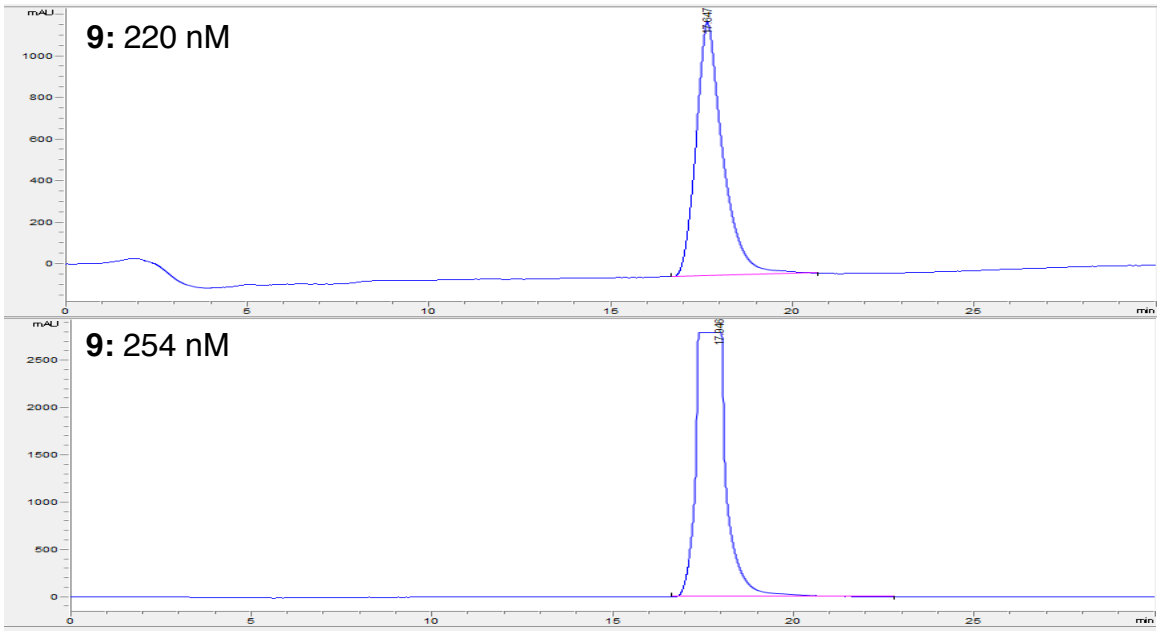

Compound 10: **IB4** dissolved in 0.1 M anhydrous THF at 0ºC. 3-(trifluoro)methyl phenyl isocyanate was added dropwise to the reaction mixture as described in **Scheme 3**. The mixture was brought to room temperature and allowed to stir overnight. The mixture was concentrated *in vacuo.* The concentration mixture was further purified using HPLC in an acetonitrile and water solvent system. ^{1}H NMR (300 MHz, MeOD) δ 7.98 (s, 1H), 7.92 (d, *J* = 6.0 Hz, 1H), 7.63 (d, *J* = 7.1 Hz, 1H), 7.56 – 7.46 (m, 2H), 7.32 (d, *J* = 8.3 Hz, 1H), 7.25 (d, *J* = 8.1 Hz, 1H), 7.03 (d, *J* = 6.0 Hz, 1H), 2.35 (s, 3H), 2.21 (s, 3H), 1.54 (s, 3H), 1.18 (s, 2H), 1.04 (s, 2H). Chemical Formula: $C_{26}H_{25}F_3N_6O$/Exact Mass: 494.20. $[M+H]^+$ detected: 495.4 m/z. Retention Time: 12.5 minutes; purity: >99%

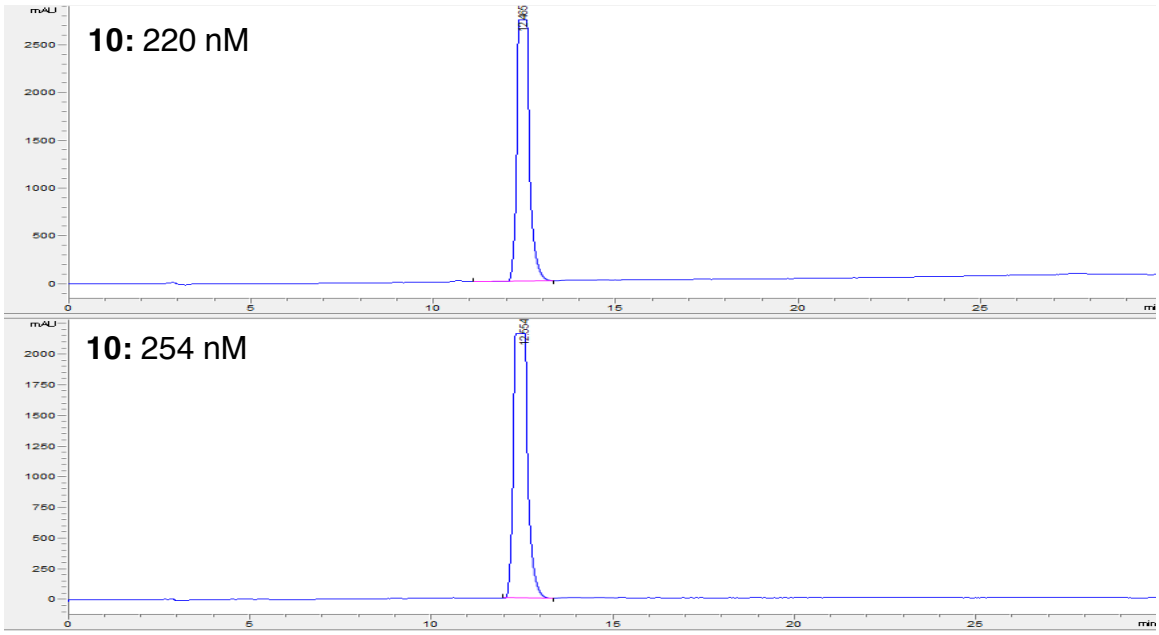

Compound 11: **IB5** dissolved in 0.1 M anhydrous THF at 0ºC. 3-(trifluoro)methyl phenyl isocyanate was added dropwise to the reaction mixture as described in **Scheme 3**. The mixture was brought to room temperature and allowed to stir overnight. The mixture was concentrated *in vacuo.* The concentration mixture was further purified using HPLC in an acetonitrile and water solvent system. ^{1}H NMR (300 MHz, MeOD) d 7.88 (s, 1H), 7.84 (d, J = 5.9 Hz, 1H), 7.65 (d, J = 12.6 Hz, 1H), 7.57 (d, J = 8.8 Hz, 1H), 7.45 – 7.38 (m, 1H), 7.26 (d, J = 8.2 Hz, 2H), 6.96 (d, J = 5.9 Hz, 1H), 1.46 – 1.43 (m, 3H), 1.12 – 1.07 (m, 2H), 0.96 (t, J = 3.1 Hz, 2H). Chemical Formula: $C_{24}H_{19}F_5N_6O$/Exact Mass: 502.15. $[M+H]^+$ detected: 503.1m/z. Retention Time: 11.8 minutes; purity: 93.5%

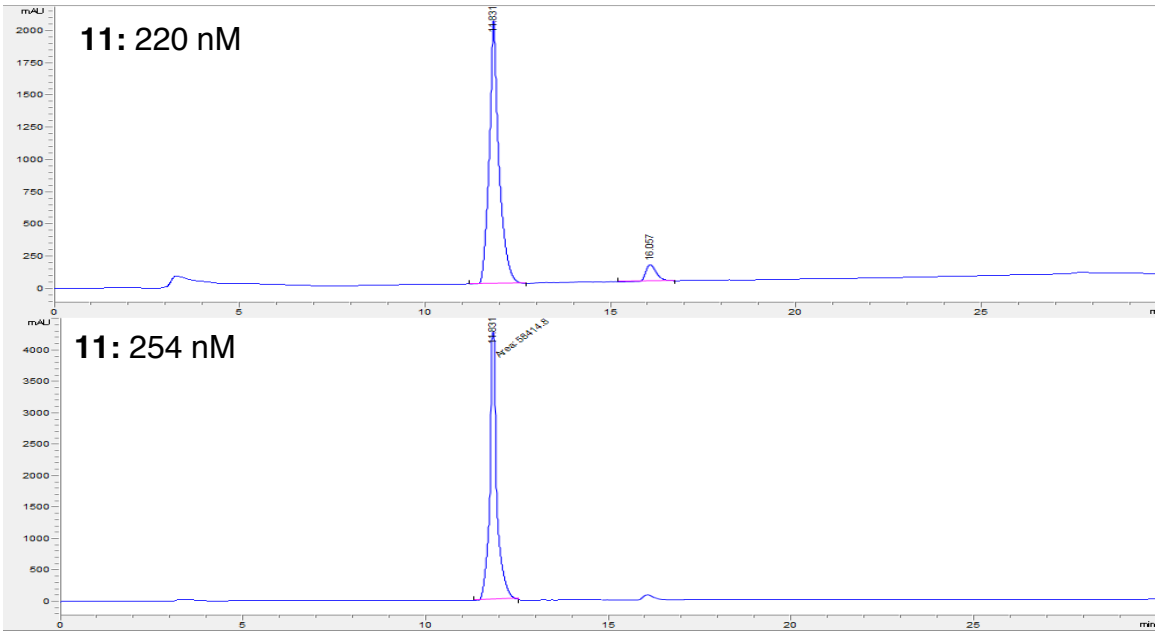

Compound 12: **IC1** and aniline (CAS: 62-53-3) (1.7 eq.) were dissolved in 0.1 M dioxane and TEA (1.7 eq.) and heated at 95ºC for 1.5 hours as described in **Scheme 4**. The reaction was washed in DCM:Water and the organic layer extracted and concentration. The organic layer was further purified using HPLC in an acetonitrile and water solvent system.^{1}H NMR (300 MHz, Methanol-d_4) δ 8.13 (ddd, J = 8.5, 1.3, 0.7 Hz, 1H), 7.93 – 7.82 (m, 2H), 7.70 (ddd, J = 8.4, 1.4, 0.7 Hz, 1H), 7.63 – 7.42 (m, 4H), 7.21 – 7.07 (m, 2H), 6.95 (d, J = 5.9 Hz, 1H), 6.86 (dt, J = 7.0, 1.9 Hz, 1H), 3.28 – 3.13 (m, 11H), 2.39 (s, 3H), 1.47 (s, 3H), 1.13 (d, J = 3.3 Hz, 2H), 0.95 (d, J = 2.1 Hz, 2H). Chemical Formula: $C_{27}H_{24}N_6O$/Exact Mass: 448.20; $[M+H]^+$ detected = 449.3m/z. Retention time: 12.3 minutes, purity: 97.8%

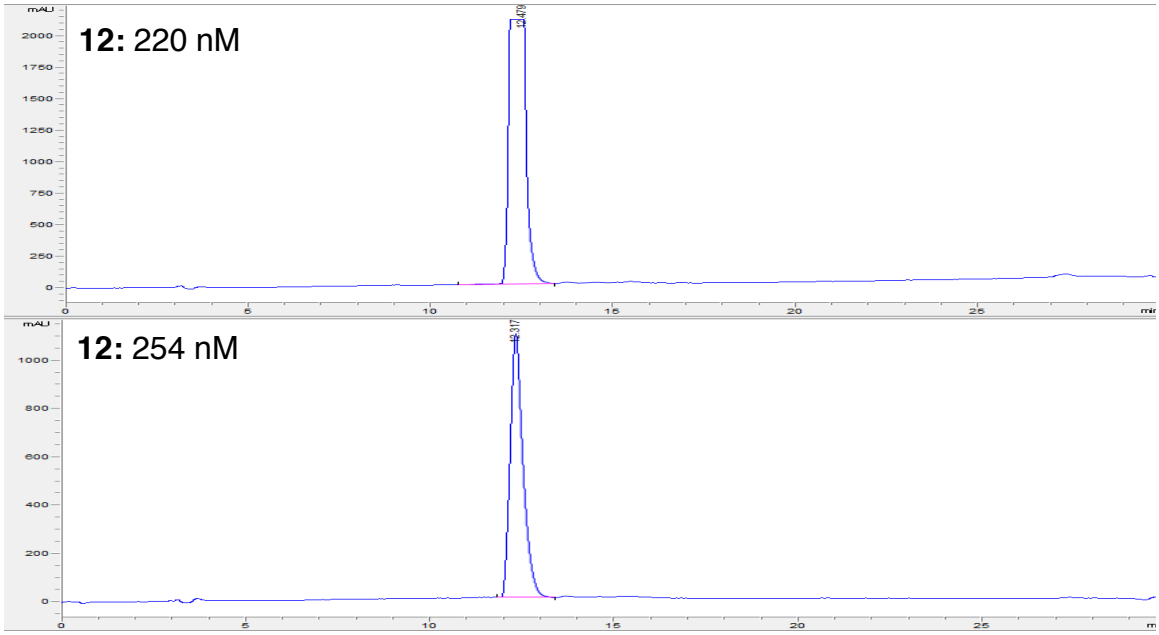

Compound 13: **IC1** and 3-fluoro benzenamine (CAS: 372-19-0) (1.7 eq.) were dissolved in 0.1 M dioxane and TEA (1.7 eq.) and heated at 95ºC for 1.5 hours as described in **Scheme 4**. The reaction was washed in DCM:Water and the organic layer extracted and concentration. The organic layer was further purified using HPLC in an acetonitrile and water solvent system ^{1}H NMR (300 MHz, $CDCl_3$) δ 8.08 – 8.01 (m, 1H), 7.97 – 7.85 (m, 3H), 7.70 (dt, *J* = 7.5, 4.2 Hz, 1H), 7.59 (t, *J* = 4.3 Hz, 1H), 7.49 (d, *J* = 7.8 Hz, 1H), 7.43 (d, *J* = 8.0 Hz, 1H), 7.23 – 7.14 (m, 1H), 6.99 (d, *J* = 8.1 Hz, 1H), 6.88 – 6.84 (m, 1H), 6.72 (dd, *J* = 9.8, 7.5 Hz, 1H), 1.59 (s, 3H), 1.25 (t, *J* = 5.5 Hz, 2H), 1.04 (t, *J* = 5.5 Hz, 2H). Chemical Formula: $C_{27}H_{23}FN_6O$/Exact Mass: 466.19. Detected $[M+H]^+$= 517.3 m/z. Retention Time: 12.5; Purity: 98.3%

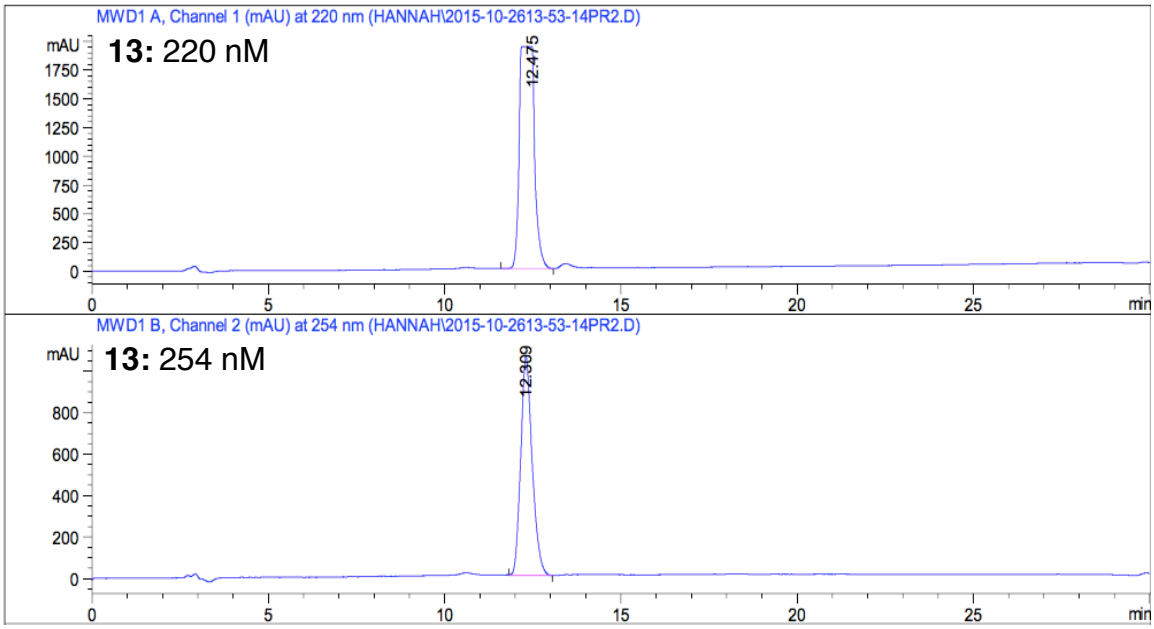

Compound 14: **IC1** and 3-methyl-benzamine 108-44-1(1.7 eq.) were dissolved in 0.1 M dioxane and TEA (1.7 eq.) and heated at 95ºC for 1.5 hours as described in **Scheme 4**. The reaction was washed in DCM:Water and the organic layer extracted and concentration. The organic layer was further purified using HPLC in an acetonitrile and water solvent system. ^{1}H NMR (300 MHz, Chloroform-*d*) δ 8.00 (t, *J* = 6.2 Hz, 1H), 7.83 – 7.66 (m, 1H), 7.63 – 7.45 (m, 2H), 7.33 – 7.14 (m, 3H), 6.92 (dd, *J* = 26.6, 6.4 Hz, 1H), 2.35 (s, 1H), 1.60 (s, 1H), 1.32 – 1.19 (m, 1H), 1.08 – 0.94 (m, 1H). Chemical Formula: $C_{28}H_{26}N_6O$/Exact Mass: 462.22. $[M+H]^+$ detected: 463.3m/z. Retention time: 12.1 minutes; purity: 98.7%

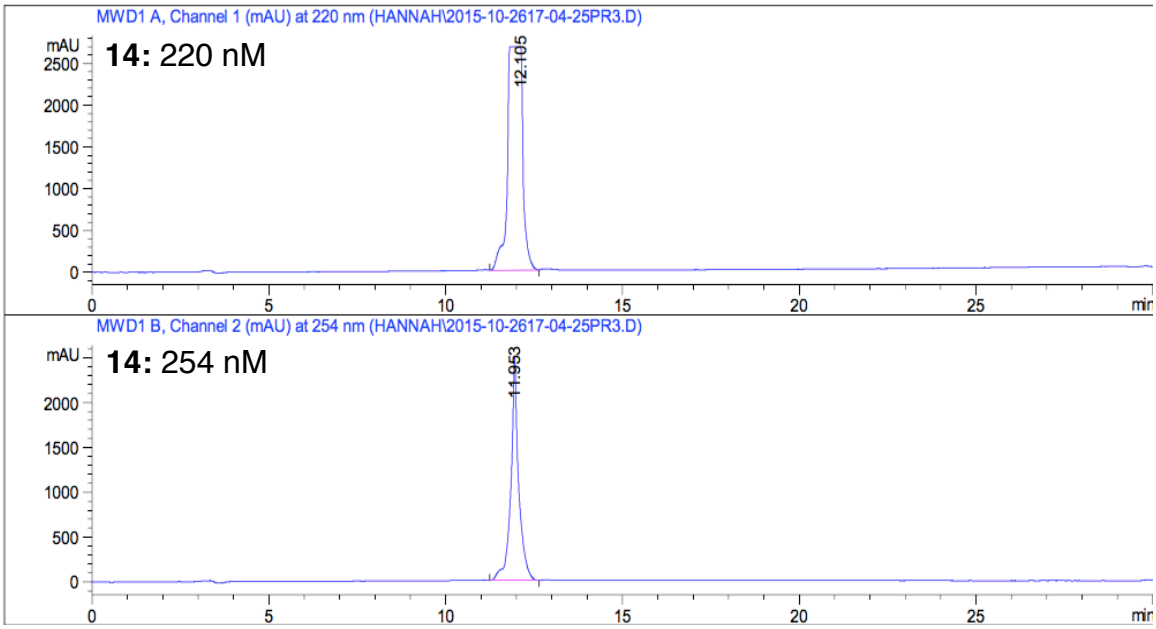

Compound 15: **IC1** and 3-methoxy aniline (CAS: 536-90-3) (1.7 eq.) were dissolved in 0.1 M dioxane and TEA (1.7 eq.) and heated at 95°C for 1.5 hours as described in **Scheme 4**. The reaction was washed in DCM:Water and the organic layer extracted and concentration. The organic layer was further purified using HPLC in an acetonitrile and water solvent system. ^{1}H NMR (300 MHz, Methanol-d_4) δ 8.17 – 8.08 (m, 1H), 7.92 – 7.83 (m, 2H), 7.74 – 7.67 (m, 1H), 7.62 – 7.45 (m, 3H), 7.19 – 7.08 (m, 2H), 6.95 (d, J = 5.9 Hz, 1H), 6.90 (ddd, J = 8.1, 2.0, 0.9 Hz, 1H), 6.54 (ddd, J = 8.3, 2.5, 0.9 Hz, 1H), 3.70 (s, 3H), 3.31 – 3.17 (m, 18H), 1.47 (s, 3H), 1.13 (d, J = 3.7 Hz, 2H), 1.01 – 0.91 (m, 2H). Chemical Formula: $C_{28}H_{26}N_6O_2$/Exact Mass: 478.21. $[M+H]^+$ detected 479.3m/z. Retention time: 13.5 minutes, purity: 95.6%

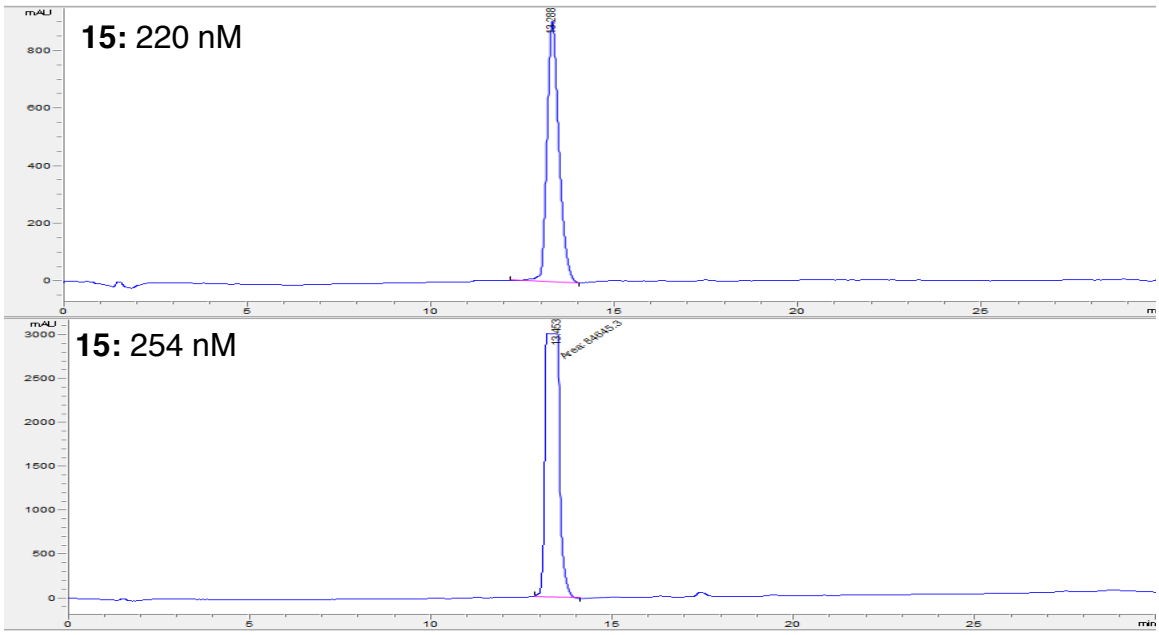

Compound 16: **IC1** and the 3-(methylthio)-aniline (CAS: 1783-81-9) (1.7 eq.) were dissolved in 0.1 M dioxane and TEA (1.7 eq.) and heated at 95ºC for 1.5 hours as described in **Scheme 4**. The reaction was washed in DCM:Water and the organic layer extracted and concentration. The organic layer was further purified using HPLC in an acetonitrile and water solvent system ^{1}H NMR (300 MHz, Methanol-d_4) δ 8.13 (ddd, J = 8.5, 1.3, 0.7 Hz, 1H), 7.93 – 7.82 (m, 2H), 7.70 (ddd, J = 8.4, 1.4, 0.7 Hz, 1H), 7.63 – 7.42 (m, 4H), 7.21 – 7.07 (m, 2H), 6.95 (d, J = 5.9 Hz, 1H), 6.86 (dt, J = 7.0, 1.9 Hz, 1H), 2.39 (s, 3H), 1.47 (s, 3H), 1.13 (d, J = 3.3 Hz, 2H), 0.95 (d, J = 2.1 Hz, 2H). Chemical Formula: $C_{28}H_{26}N_6OS$/Exact Mass: 494.19. Detected $[M+H]^+$= 495.3 m/z. Retention time: 13.5 minutes, purity: 94.9%

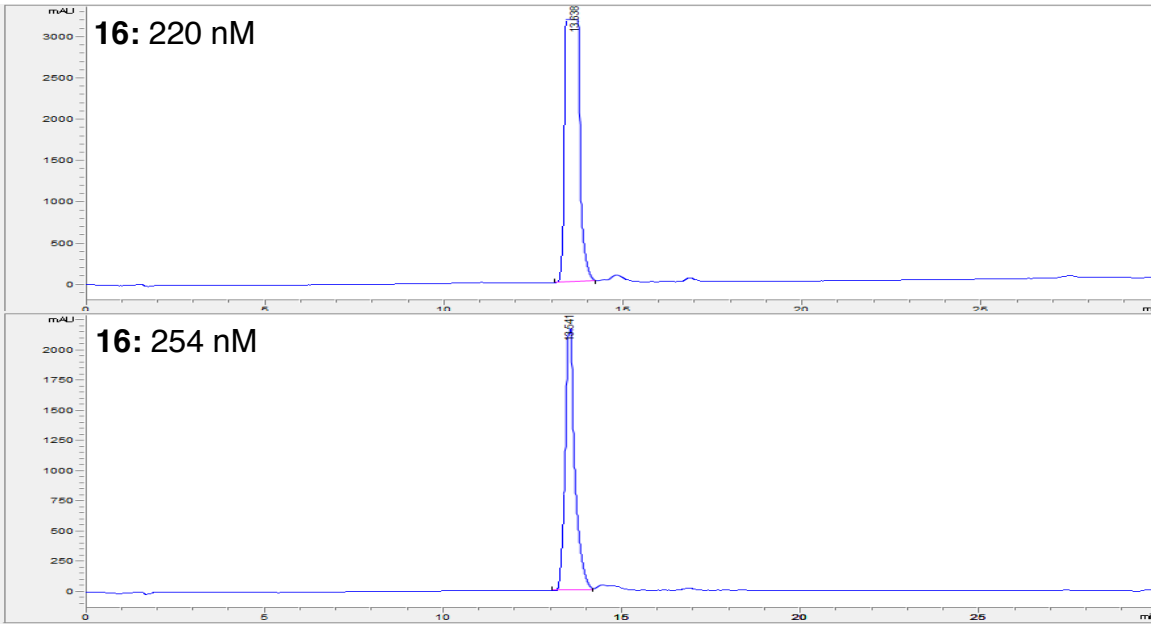

Compound 17: **IC1** and 3-(methoxy)-5-(trifluoro)methyl aniline)(CAS: 349-55-3) (1.7eq.) were dissolved in 0.1M dioxane and TEA (1.7 eq.) and heated at 95ºC for 1.5 hours as described in **Scheme 4**. The reaction was washed in DCM:Water and the organic layer extracted and concentration. The organic layer was further purified using HPLC in an acetonitrile and water solvent system. ^{1}H NMR (300 MHz, MeOD) δ 8.24 (d, *J* = 8.2 Hz, 1H), 7.98 (t, *J* = 6.8 Hz, 2H), 7.82 (d, *J* = 7.7 Hz, 1H), 7.75 – 7.54 (m, 3H), 7.44 (d, *J* = 13.8 Hz, 2H), 7.07 (d, *J* = 5.9 Hz, 1H), 6.88 (s, 1H), 3.88 (s, 3H), 1.59 (s, 3H), 1.24 (s, 2H), 1.07 (s, 2H). Chemical Formula: $C_{29}H_{25}F_3N_6O_2$/Exact Mass: 546.20. Found mass: $[M+H]^+$ 547.3 m/z. Retention time: 14.7 minutes, purity: 94.7%

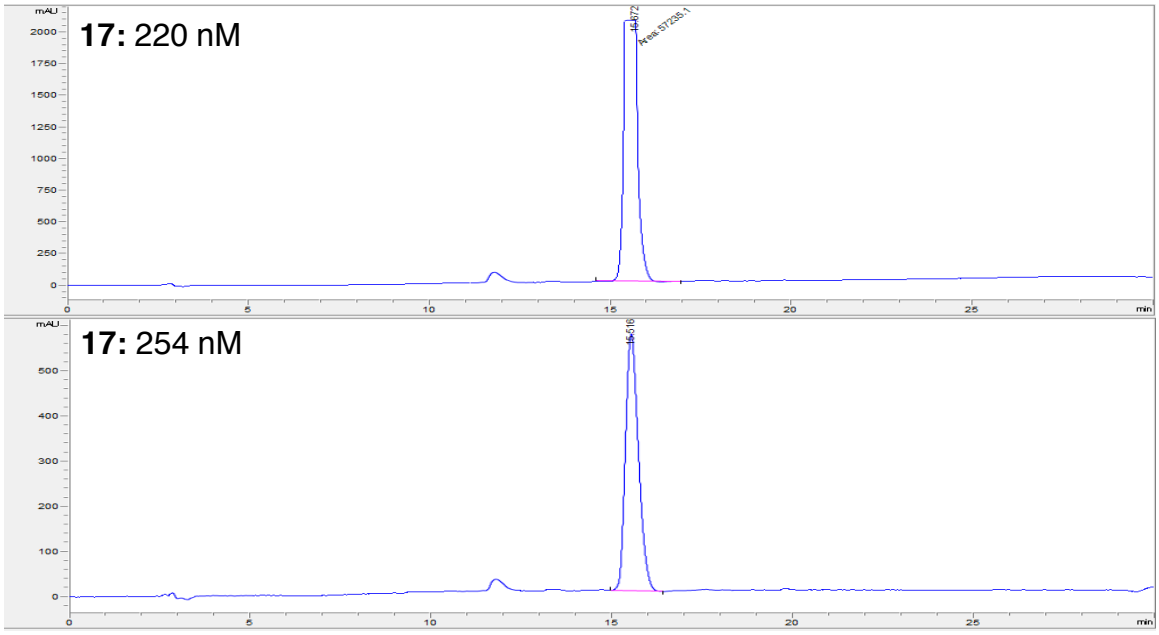

Compound 18: **IC1** and 3-fluoro-5-(trifluoro)methyl aniline (CAS: 454-67-1) (1.7 eq.) were dissolved in 0.1 M dioxane and TEA (1.7 eq.) and heated at 95ºC for 1.5 hours as described in **Scheme 4**. The reaction was washed in DCM:Water and the organic layer extracted and concentration. The organic layer was further purified using HPLC in an acetonitrile and water solvent system. ^{1}H NMR (300 MHz, MeOD) δ 8.26 – 8.20 (m, 1H), 7.98 (dd, *J* = 6.8, 4.0 Hz, 2H), 7.85 – 7.79 (m, 1H), 7.74 – 7.59 (m, 5H), 7.24 – 7.18 (m, 1H), 7.07 (d, *J* = 5.9 Hz, 1H), 1.59 (s, 3H), 1.24 (s, 2H), 1.07 (s, 2H). Chemical Formula: $C_{28}H_{22}F_4N_6O$/Exact Mass: 534.18. Detected $[M+H]^+$=534.3 m/z. Retention time: 13.2 minutes, purity: 96.4%

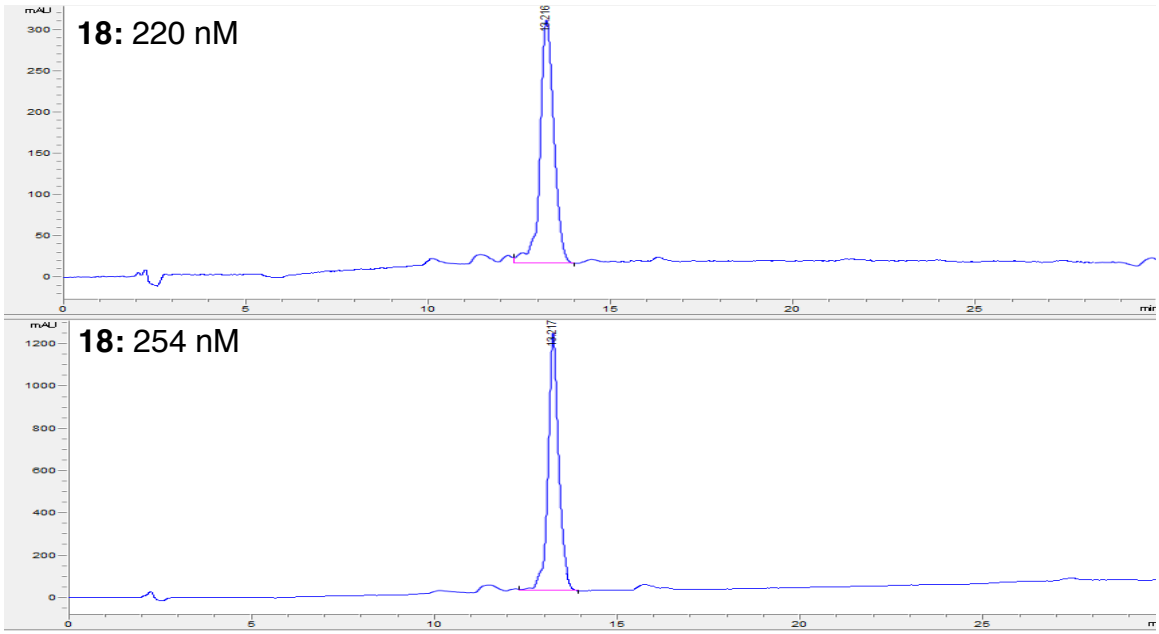

Compound 19: **IC1** and 2-amino-N-methylbenzenesulfonamide (CAS: 459434-40-3) (1.7 eq.) were dissolved in 0.1 M dioxane and TEA (1.7 eq.) and heated at 95ºC for 1.5 hours as described in **Scheme 4**. The reaction was washed in DCM:Water and the organic layer extracted and concentration. The organic layer was further purified using HPLC in an acetonitrile and water solvent system. ^{1}H NMR (300 MHz, MeOD) δ 8.23 (s, 1H), 8.18 (s, 1H), 7.98 (d, *J* = 6.6 Hz, 2H), 7.80 (s, 1H), 7.73 – 7.52 (m, 6H), 7.07 (d, *J* = 5.7 Hz, 1H), 2.58 (s, 3H), 1.59 (s, 3H), 1.24 (s, 2H), 1.07 (s, 2H). Chemical Formula: $C_{28}H_{27}N_7O_3S$/Exact Mass: 541.19. $[M+H]^+$ detected: 542.2 m/z. Retention time: 10.7 minutes; purity: 95.2%

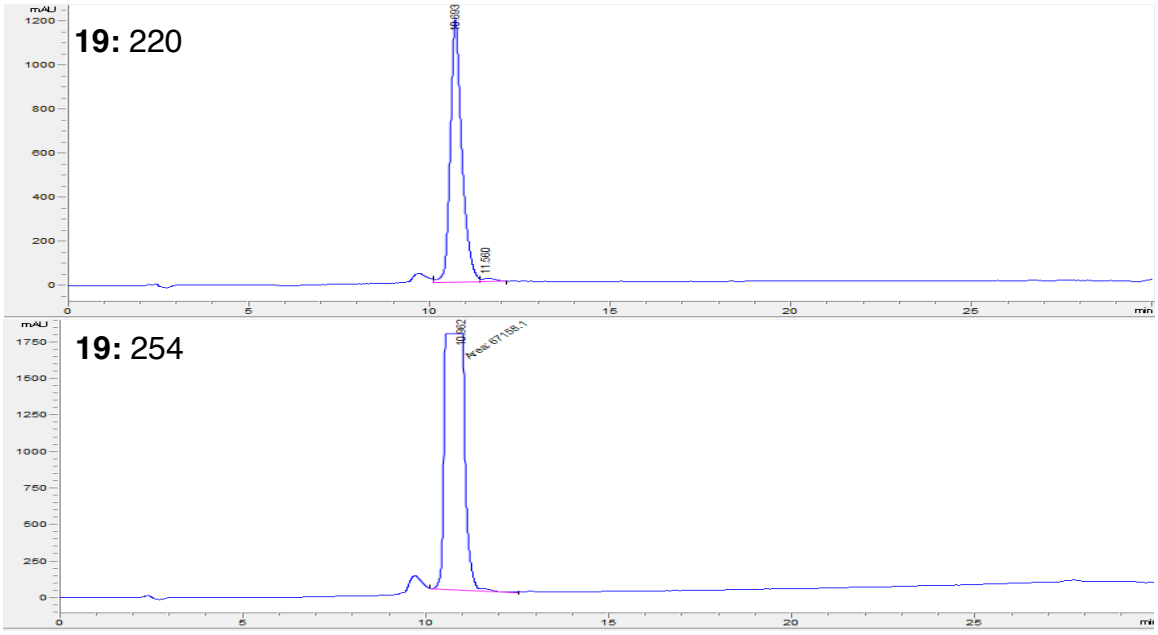

Compound 20: **IC1** and 4-(4-methylpiperazin-1-ylmethyl)-3-trifluoromethylaniline (1.7eq.) were were dissolved in 0.1M dioxane and TEA (1.7 eq.) and heated at 95ºC for 1.5 hours as described in **Scheme 4**. The reaction was washed in DCM:Water and the organic layer extracted and concentration. The organic layer was further purified using HPLC in an acetonitrile and water solvent system. ^{1}H NMR (300 MHz, MeOD) δ 8.25 (d, *J* = 7.8 Hz, 1H), 8.01-7.98 (m, 2H), 7.82 (d, *J* = 8.4 Hz, 1H), 7.73 (s, 2H), 7.64 (dd, *J* = 20.5, 7.3 Hz, 3H), 7.51-7.25 (m, 1H), 7.38 (dd, *J* = 4.2, 1.8 Hz, 1H), 7.08 (d, *J* = 5.9 Hz, 1H), 3.76 (s, 2H), 3.48 (s, 4H), 3.09 (s, 4H), 2.93 (s, 3H), 1.59 (s, 3H), 1.24 (s, 2H), 1.06, 2H). Chemical Formula: $C_{34}H_{35}F_3N_8O$/Exact Mass: 628.29. $[M+H]^+$ detected: 629.3 m/z. Retention time: 16.5 minutes, purity: >99%

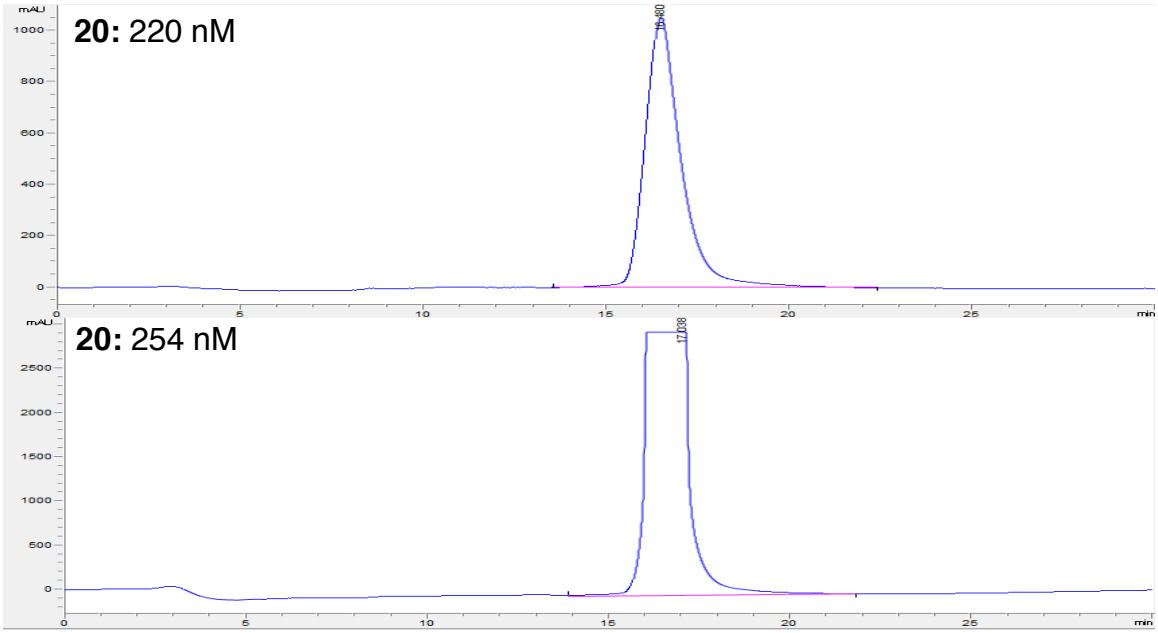

Compound 21: **IC1** and 4-[(4-methyl-1-piperazinyl)methyl] benzamine (1.7 eq.) were dissolved in 0.1 M dioxane and TEA (1.7 eq.) and heated at 95ºC for 1.5 hours as described in **Scheme 4**. The reaction was washed in DCM:Water and the organic layer extracted and concentration. The organic layer was further purified using HPLC in an acetonitrile and water solvent system. ^{1}H NMR (300 MHz, MeOD) δ 7.91 (d, *J* = 5.9 Hz, 1H), 7.73 (d, *J* = 12.6 Hz, 1H), 7.52 (t, *J* = 8.4 Hz, 4H), 7.46 – 7.24 (m, 4H), 7.04 (d, *J* = 5.9 Hz, 1H), 3.76 (s, 2H), 3.27 (s, 4H), 3.07 (d, *J* = 24.0 Hz, 3H), 2.85 (s, 2H), 1.53 (s, 3H), 1.18 (s, 2H), 1.04 (s, 2H). Chemical Formula: $C_{33}H_{36}N_8O$/ Exact Mass: 560.30. $[M+H]^+$ detected: 561.7 m/z. Retention time: 15.5 minutes, purity: 98.3%

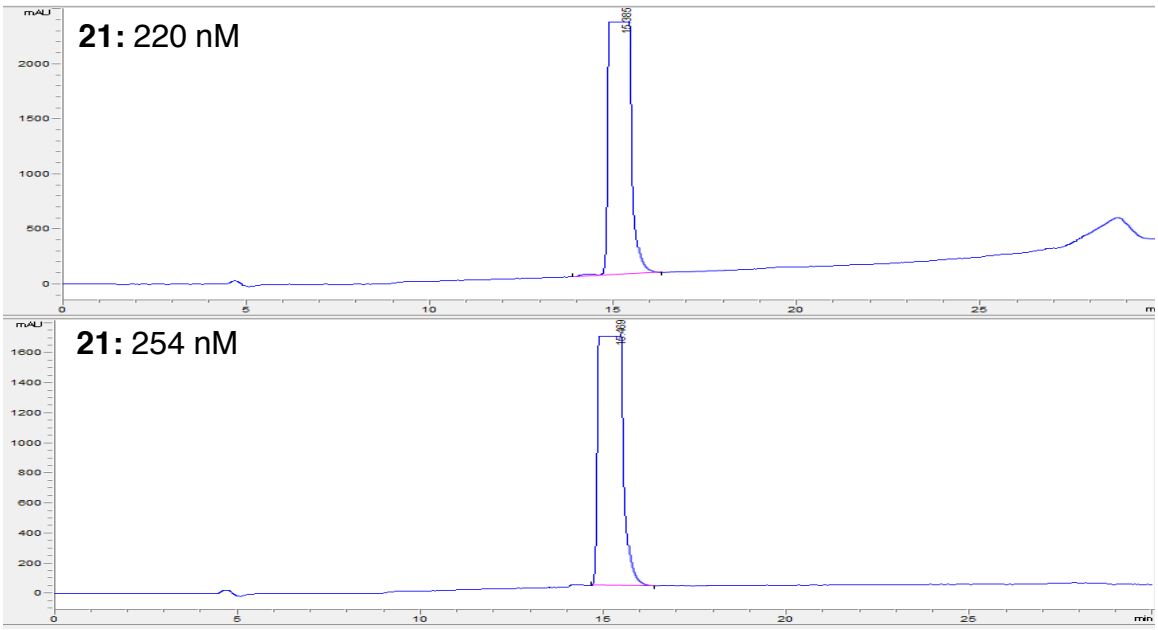

Compound 22: **IC1** and 5-methyl-1H-pyrzaol-3-amine (CAS: 31230-17-8) (1.7 eq.) were dissolved in 0.1 M dioxane and TEA (1.7 eq.) and heated at 95ºC for 1.5 hours as described in **Scheme 4**. The reaction was washed in DCM:Water and the organic layer extracted and concentration. The organic layer was further purified using HPLC in an acetonitrile and water solvent system. ^{1}H NMR (300 MHz, CD_3CN) δ 8.42 (d, *J* = 9.2 Hz, 2H), 7.91 (d, *J* = 8.7 Hz, 1H), 7.78 – 7.66 (m, 2H), 7.59 (s, 2H), 6.91 (d, *J* = 5.7 Hz, 1H), 5.82 (s, 1H), 2.53 (s, 3H), 1.54 (s, 3H), 1.16 (m, 2H), 0.99 (m, 2H). Chemical Formula: $C_{25}H_{24}N_8O$/Exact Mass: 452.21. Retention time: 12.6 minutes; Purity: >99%

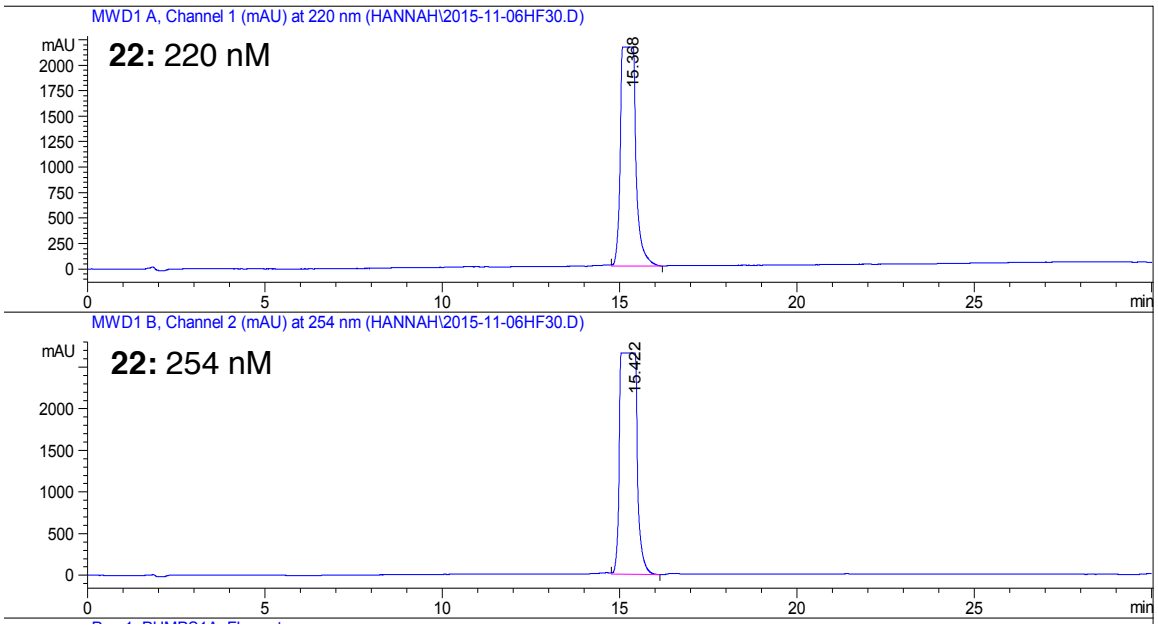

Compound 23: **IC1** and benzylamine (CAS: 100-46-9) (1.7 eq.) were dissolved in 0.1 M dioxane and TEA (1.7 eq.) and heated at 95ºC for 1.5 hours as described in **Scheme 4**. The reaction was washed in DCM:Water and the organic layer extracted and concentration. The organic layer was further purified using HPLC in an acetonitrile and water solvent system. ^{1}H NMR (300 MHz, CD_3CN) δ 8.20 (d, *J* = 8.3 Hz, 1H), 8.13 (d, *J* = 7.8 Hz, 1H), 7.88 (d, *J* = 8.4 Hz, 1H), 7.79 (s, 1H), 7.74 (d, *J* = 5.7 Hz, 1H), 7.63 (d, *J* = 7.2 Hz, 1H), 7.55 (d, *J* = 7.9 Hz, 2H), 7.43 – 7.38 (m, 3H), 7.31 (s, 1H), 6.91 (d, *J* = 6.0 Hz, 1H), 4.47 (d, *J* = 5.9 Hz, 2H), 1.53 (s, 3H), 1.15 (s, 2H), 0.99 (s, 2H). Chemical Formula: $C_{28}H_{26}N_6O$/Exact Mass: 462.22. $[M+H]^+$ detected: 463.3 m/z. Retention time: 12.4 minutes, purity: 96.1%

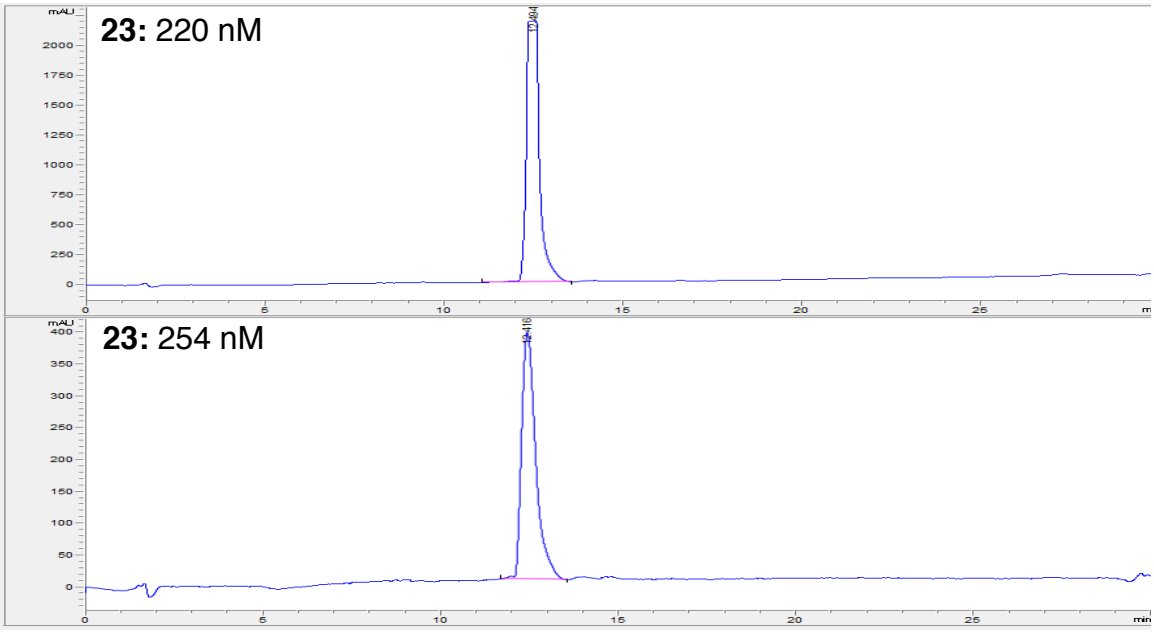

Compound 24: **IC1** and phenethylamine (CAS: 64-04-0) (1.7 eq.) were dissolved in 0.1 M dioxane and TEA (1.7 eq.) and heated at 95ºC for 1.5 hours as described in **Scheme 4**. The reaction was washed in DCM:Water and the organic layer extracted and concentration. The organic layer was further purified using HPLC in an acetonitrile and water solvent system. ^{1}H NMR (300 MHz, MeOD) δ 8.11 (d, *J* = 8.1 Hz, 1H), 7.97 (d, *J* = 5.9 Hz, 1H), 7.82 (d, *J* = 7.7 Hz, 1H), 7.77 (d, *J* = 7.6 Hz, 1H), 7.67 – 7.53 (m, 4H), 7.36 – 7.29 (m, 4H), 7.06 (d, *J* = 5.9 Hz, 1H), 3.56 (dd, *J* = 7.7, 5.8 Hz, 2H), 2.92 (dd, *J* = 10.8, 3.5 Hz, 2H), 1.62 – 1.54 (m, 3H), 1.23 (d, *J* = 0.9 Hz, 2H), 1.06 (d, *J* = 1.0 Hz, 2H). Chemical Formula: $C_{29}H_{28}N_6O$/Exact Mass: 476.23. $[M+H]^+$ detected: 477.4 m/z. Retention Time: 12.8 minutes, purity: 95.3%

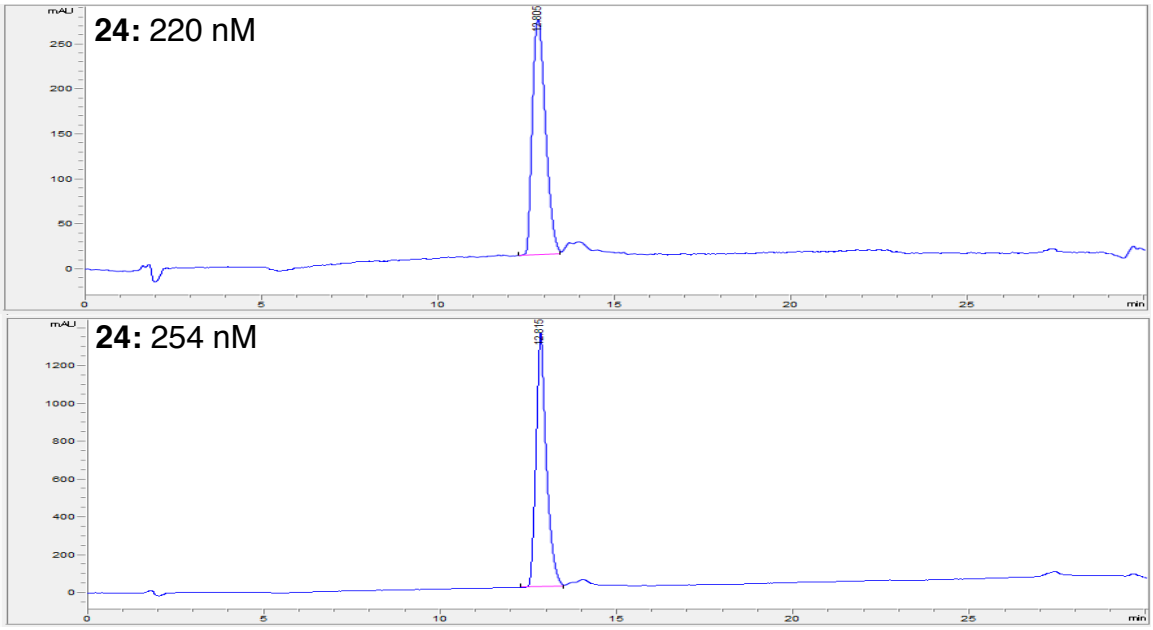

Compound 25: IC1 and cyclohexamine (CAS: 108-91-8) (1.7 eq.) were dissolved in 0.1 M dioxane and TEA (1.7 eq.) and heated at 95ºC for 1.5 hours as described in **Scheme 4**. The reaction was washed in DCM:Water and the organic layer extracted and concentration. The organic layer was further purified using HPLC in an acetonitrile and water solvent system. ^{1}H NMR (300 MHz, MeOD) δ 8.16 (d, *J* = 8.2 Hz, 1H), 7.98 (d, *J* = 6.1 Hz, 1H), 7.91 (d, *J* = 8.4 Hz, 1H), 7.78 (d, *J* = 8.4 Hz, 1H), 7.62 (d, *J* = 7.6 Hz, 3H), 7.06 (d, *J* = 6.1 Hz, 1H), 3.03 (s, 1H), 1.58 (s, 3H), 1.36 (s, 9H), 1.23 (s, 2H), 1.06 (s, 2H). Chemical Formula: $C_{27}H_{30}N_6O$/Exact Mass: 454.25. $[M+H]^+$ detected: 455.4 m/z. Retention time: 12.9 minutes, purity: >99%

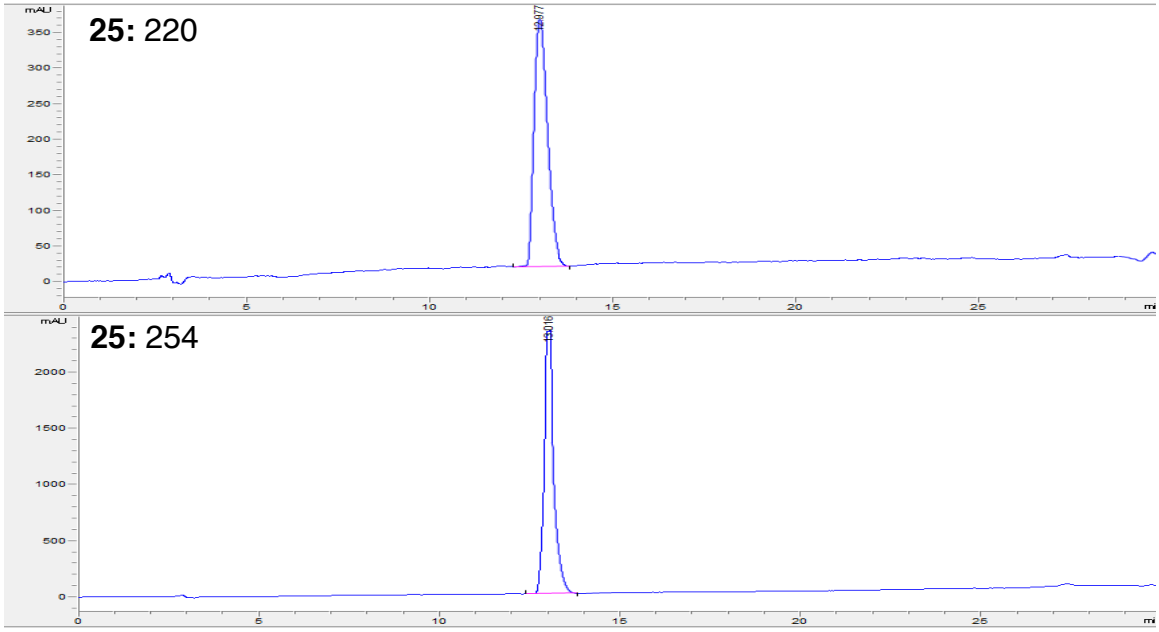

Compound 26: **IC1** and morpholine (CAS: 110-91-8) (1.7 eq.) were dissolved in 0.1 M dioxane and TEA (1.7 eq.) and heated at 95ºC for 1.5 hours as described in **Scheme 4**. The reaction was washed in DCM:Water and the organic layer extracted and concentration. The organic layer was further purified using HPLC in an acetonitrile and water solvent system. ^{1}H NMR (300 MHz, MeOD) δ 8.12 (d, J = 7.5 Hz, 1H), 7.97 - 7.87 (m, 1H), 7.75 (d, J = 7.8 Hz, 1H), 7.69 - 7.38 (m, 4H), 7.07 (d, J = 5.7 Hz, 1H), 3.89 (s, 2H), 3.83 (s, 2H), 3.67 (d, J = 4.9 Hz, 2H), 3.25 (d, J = 5.0 Hz, 2H), 1.57 (d, J = 6.2 Hz, 3H), 1.22 (s, 2H), 1.05 (s, 2H). Chemical Formula: $C_{25}H_{26}N_6O_2$/Exact Mass: 442.21. $[M+H]^+$ detected: 443.3 m/z. Retention time: 10.2 minutes, purity: 94.6%

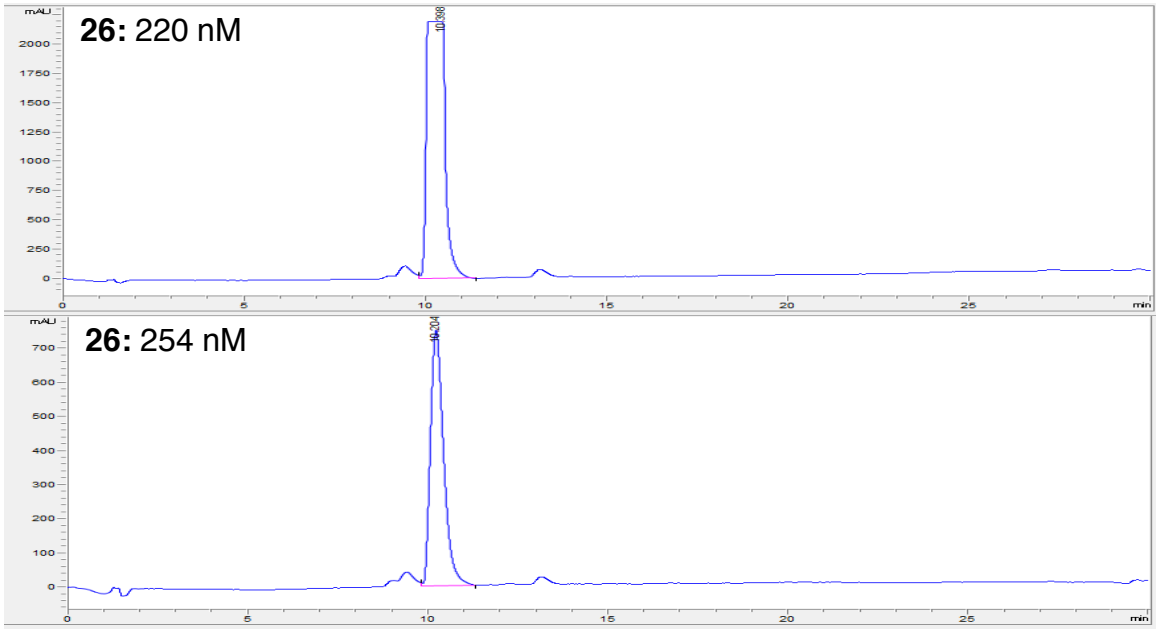

Compound 27: **IC1** and piperidine (CAS: 110-89-4) (1.7 eq.) were dissolved in 0.1 M dioxane and TEA (1.7 eq.) and heated at 95ºC for 1.5 hours as described in **Scheme 4**. The reaction was washed in DCM:Water and the organic layer extracted and concentration. The organic layer was further purified using HPLC in an acetonitrile and water solvent system. ^{1}H NMR (300 MHz, MeOD) δ 8.18 – 8.11 (m, 1H), 7.85 (d, *J* = 5.8 Hz, 1H), 7.61 (s, 1H), 7.49 (s, 2H), 7.40 (d, *J* = 7.5 Hz, 1H), 7.05 (s, 1H), 6.92 (d, *J* = 7.8 Hz, 1H), 3.15 (d, *J* = 5.5 Hz, 4H), 1.81 (s, 5H), 1.55 (s, 3H), 1.21 – 1.17 (m, 2H), 1.02 (s, 2H). Chemical Formula: $C_{26}H_{28}N_6O$/Exact Mass: 440.23. $[M+H]^+$ detected: 441.3 m/z. Retention time: 11.5 minutes, purity: 92.8%

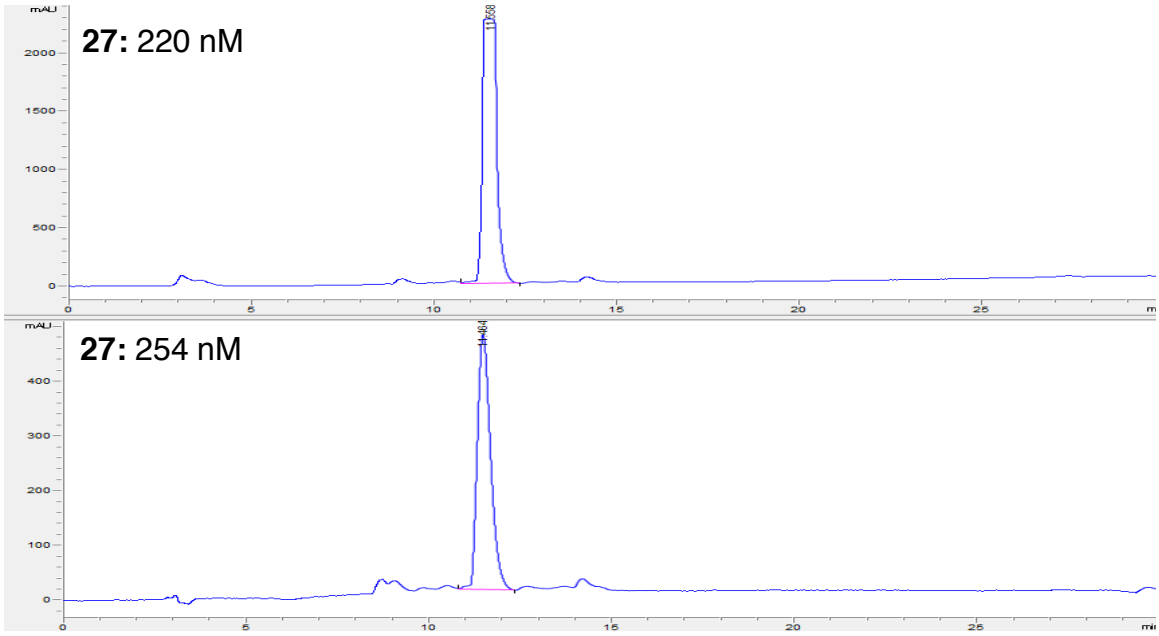

Compound 28: **IC1** and cyclopropylamine (CAS: 765-30-0) (1.7 eq.) were dissolved in 0.1 M dioxane and TEA (1.7 eq.) and heated at 95°C for 1.5 hours as described in **Scheme 4**. The reaction was washed in DCM:Water and the organic layer extracted and concentration. The organic layer was further purified using HPLC in an acetonitrile and water solvent system. ^{1}H NMR (300 MHz, CD_3CN) δ 8.15 (s, 2H), 7.89 (s, 1H), 7.73 (s, 1H), 7.63 (d, *J* = 7.0 Hz, 2H), 7.54 (s, 2H), 6.92 (s, 1H), 2.71 (s, 1H), 1.53 (s, 3H), 1.15 (s, 2H), 0.99 (s, 2H), 0.81 (s, 2H), 0.62 (s, 2H). Chemical Formula: $C_{24}H_{24}N_6O$/Exact Mass: 412.20. $[M+H]^+$ detected: 413.3 m/z. Retention time: 10.5 minutes, purity: 93.8%

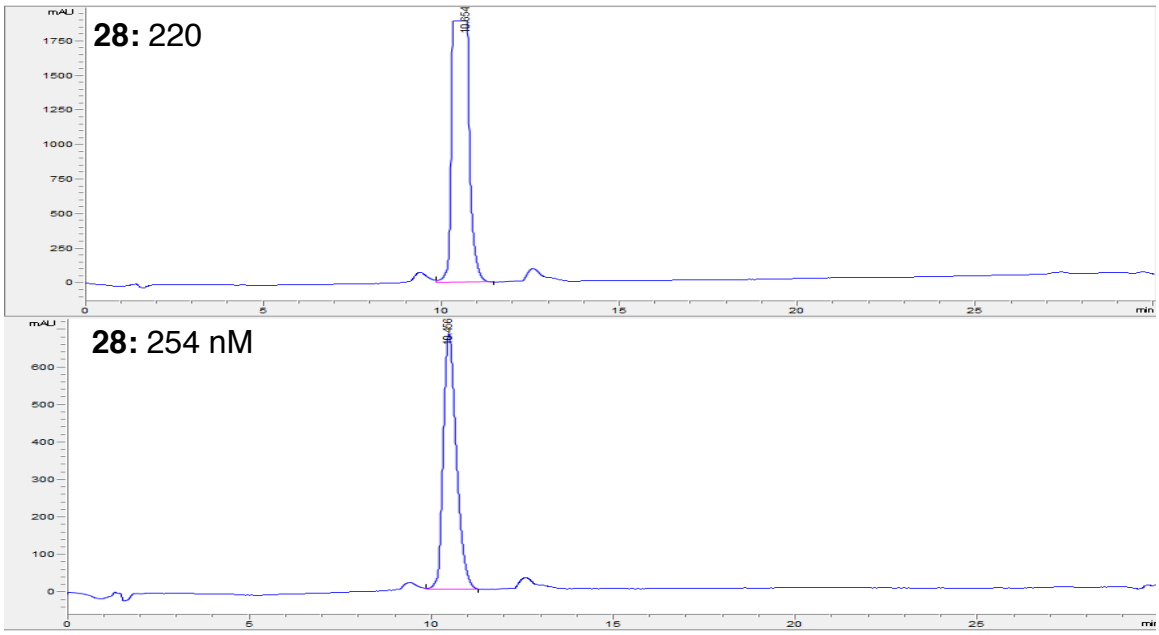

Compound 29: **IC1** and N-methyl-3-(trifluoromethyl)-benzenamine (CAS:2026-70-2) (1.7eq.) were dissolved in 0.1M dioxane and TEA (1.7 eq.) and heated at 95ºC for 1.5 hours as described in **Scheme 4**. The reaction was washed in DCM:Water and the organic layer extracted and concentration. The organic layer was further purified using HPLC in an acetonitrile and water solvent system. ^{1}H NMR (300 MHz, MeOD) δ 8.11 (d, J = 8.6 Hz, 1H), 7.98 (d, J = 5.9 Hz, 1H), 7.90 (s, 1H), 7.84 (d, J = 7.7 Hz, 1H), 7.75 (d, J = 9.1 Hz, 2H), 7.72 - 7.61 (m, 4H), 7.61 - 7.56 (m, 1H), 7.06 (d, J = 5.9 Hz, 1H), 3.55 - 3.50 (m, 3H), 1.58 (s, 3H), 1.23 (t, J = 2.7 Hz, 2H), 1.06 (t, J = 2.9 Hz, 2H). Chemical Formula: $C_{29}H_{25}F_3N_6O$/Exact Mass: 530.20. $[M+H]^+$ detected: 531.3 m/z. Retention Time: 14.6; Purity: 92.8%

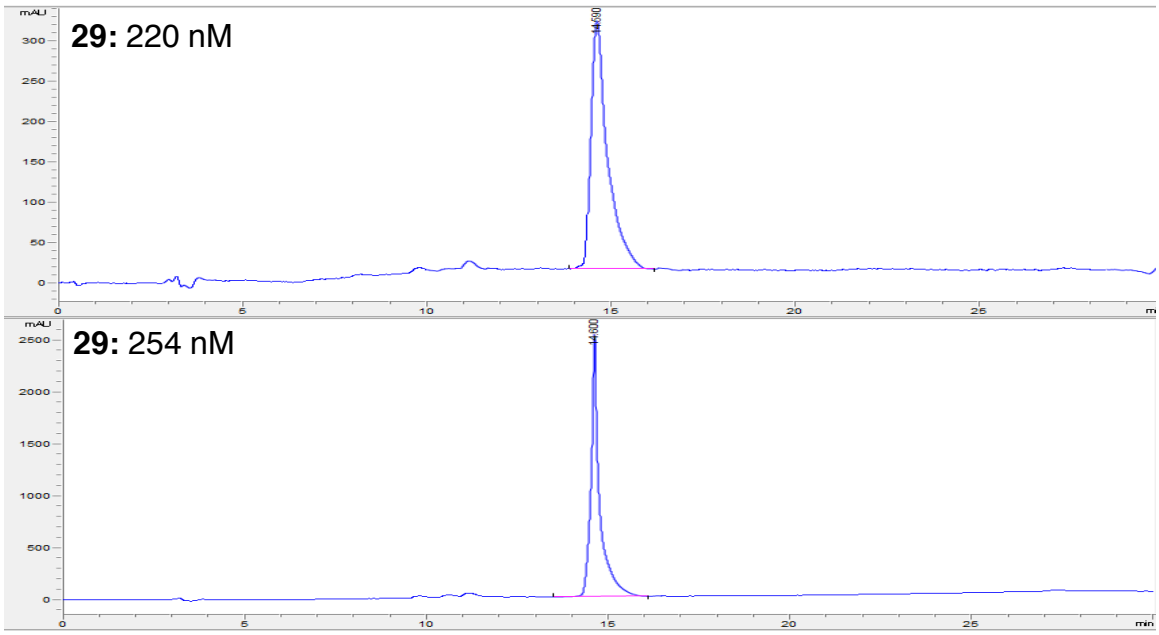

Compound 30: Both the water (0.2 mL) and dioxane (0.4 mL) were degassed with nitrogen for 10 minutes. Then 1-iodo-3-tertbutyl-imidazo[1,5-a]pyrazin-8-amine (0.04 g, 0.083 mmol, 1.2 eq.) was dissolved in the degassed water and dioxane. Next **ID1** (0.022 g, 0.070 mmol, 1 eq.), Bis(triphenylphosphine) palladium(II) dichloride (5 mg, 0.0070 mmol, 0.1 eq.), and K_2CO_3 (0.021 g, 0.15 mmol, 2.2 eq.) were added to the reaction. The reaction was heated at 80ºC for 3 hours. Then the reaction was diluted with ethyl acetate, washed with brine, dried over Na_2SO_4, filtered, and concentrated to a solid. The solid was purified by column (0% to 10% methanol/DCM) to yield **Compound 30** (0.028 g, 74% yield). ^{1}H NMR (400MHz, $CDCl_3$): d 8.1-7.8 (m, 3H), 7.6 (m, 2H), 7.55-7.4 (m, 5H), 7.3 (d, 1H), 7.0 (d, 1H), 4.2-3.9 (m, 4H), 1.7 (s, 9H). Chemical Formula:

$C_{30}H_{27}F_3N_6O$/Exact Mass: 544.22. $[M+H]^+$ detected: 545.3 m/z.

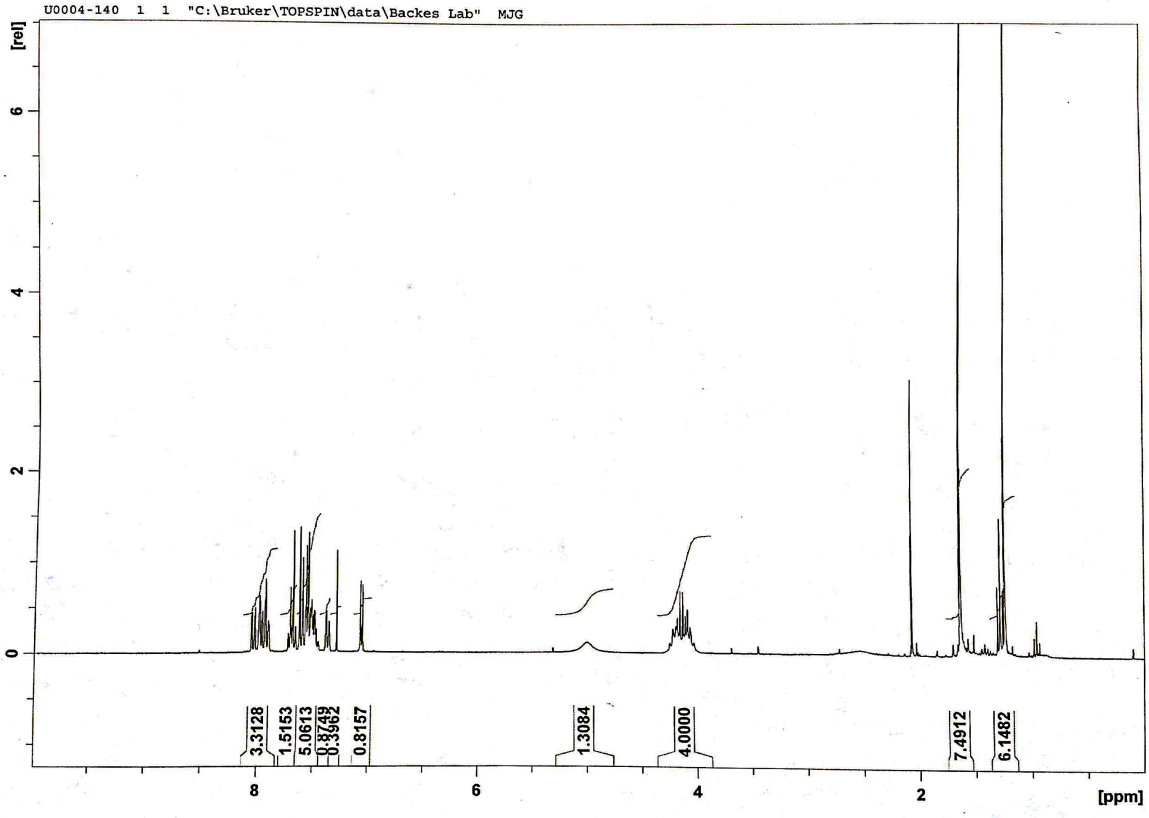

Compound 31: ID2 (2 eq.) was dissolved with IA1 (1 eq.) and 0.1 M dioxane:water (3:1) were combined with $NaHCO_3$ (3.4 eq.) and $PdCl_2(dppf)_2$ (0.1 eq.). The vial was sealed and placed in a microwave reactor for 45 minutes at 120°C. The resulting mixture was washed with DCM:Water, and the organic layers combined. The organic layer was further purified using HPLC in an acetonitrile and water solvent system. ^{1}H NMR (300 MHz, MeOD) δ 8.59 – 8.49 (m, 1H), 8.20 – 8.11 (m, 2H), 7.97 (d, *J* = 5.9 Hz, 1H), 7.71 (dd, *J* = 7.9, 5.8 Hz, 2H), 7.59 (ddd, *J* = 17.4, 10.5, 7.0 Hz, 6H), 7.04 (t, *J* = 6.7 Hz, 2H), 5.83 (s, 2H), 1.59 (d, *J* = 9.8 Hz, 3H), 1.21 (s, 2H), 1.05 (s, 2H). Chemical Formula: $C_{28}H_{26}N_4O$/Exact Mass: 434.21. $[M+H]^+$ detected: 435.4 m/z. Retention time: 13.8

minutes, purity: 97.9%

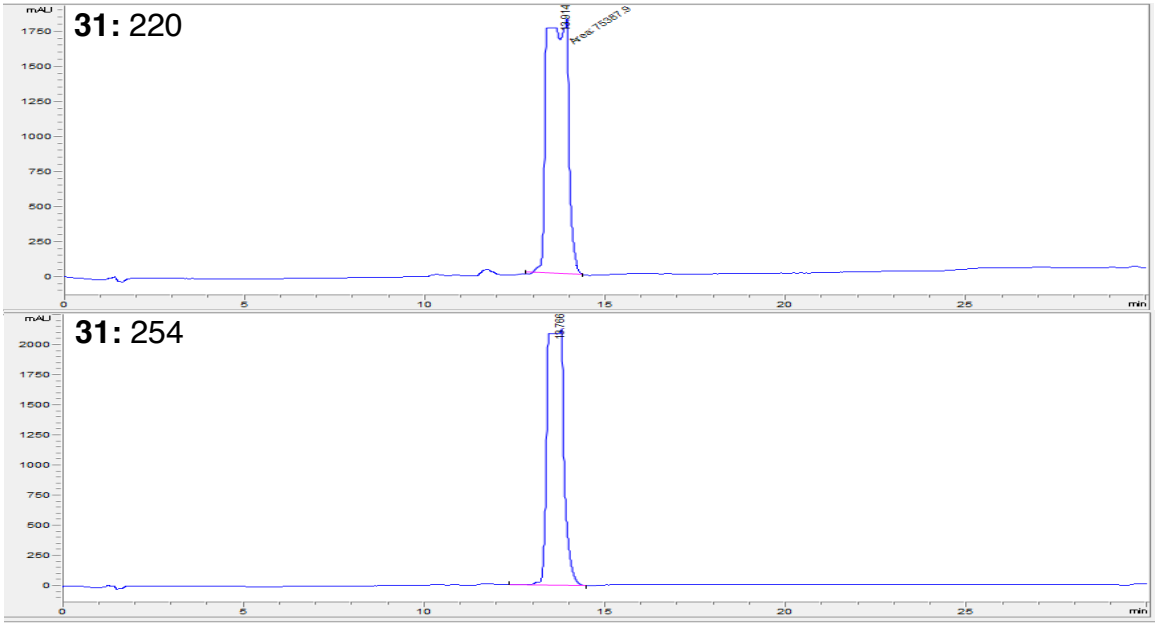

Compound 32: **ID3** (2 eq.) was dissolved with **IA1** (1 eq.) and 0.1 M dioxane:water (3:1) were combined with $NaHCO_3$ (3.4 eq.) and $PdCl_2(dppf)_2$ (0.1 eq.). The vial was sealed and placed in a microwave reactor for 45 minutes at 120°C. The resulting mixture was washed with DCM:Water, and the organic layers combined. The organic layer was further purified using HPLC in an acetonitrile and water solvent system. ^{1}H NMR (300 MHz, MeOD) δ 8.37 (d, *J* = 9.6 Hz, 1H), 7.97 (d, *J* = 5.9 Hz, 1H), 7.68 (d, *J* = 9.7 Hz, 1H), 7.56 (dd, *J* = 7.8, 6.0 Hz, 3H), 7.44 (d, *J* = 7.5 Hz, 2H), 7.34 (t, *J* = 7.5 Hz, 2H), 7.25 (d, *J* = 7.5 Hz, 1H), 7.08 (dd, *J* = 16.6, 7.0 Hz, 2H), 4.51 (t, *J* = 6.2 Hz, 2H), 3.29 (s, 2H), 1.57 (s, 3H), 1.21 (s, 2H), 1.05 (s, 2H). Chemical Formula: $C_{28}H_{24}N_4O_2$/Exact Mass: 448.19. $[M+H]^+$ detected: 449.3 m/z. Retention Time: 15.8 minutes; Purity: 97.2%

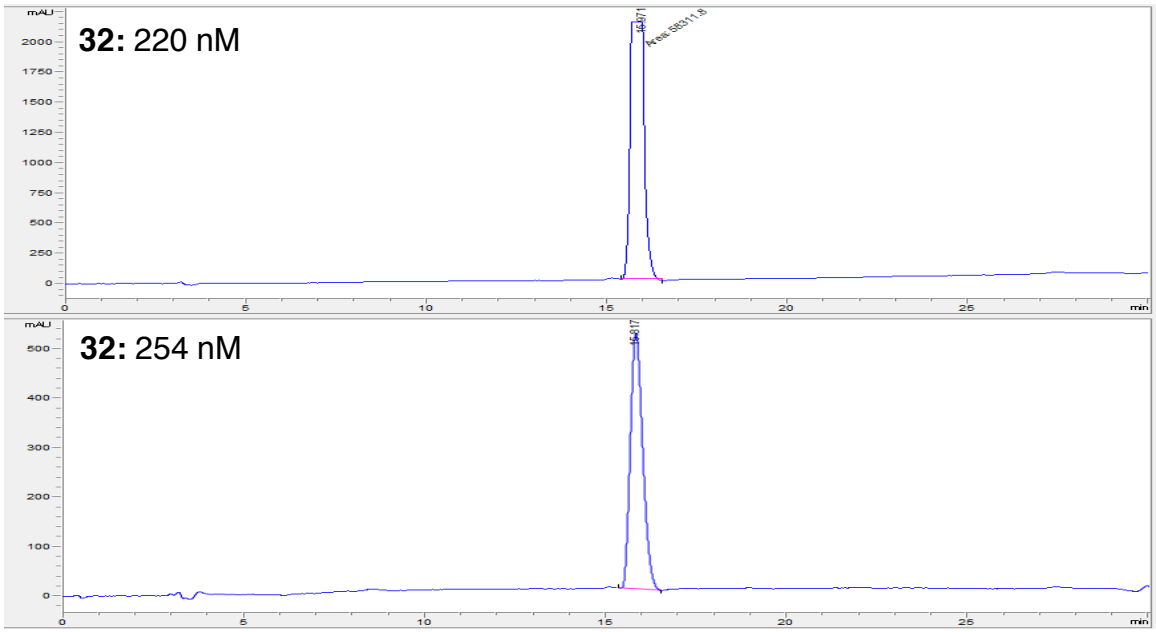

Compound 33 [55]: Previously published

C. Expression and Purification of IRE1α* and dP-IRE1α*

A construct containing the cytosolic kinase and RNase domains of human IRE1α (residues 547–977, IRE1α*) was expressed in SF9 insect cells by using the Bac-to-Bac baculovirus expression system (Invitrogen) with a His_6 tag at the N-terminus and purified with a nickel–nitriloacetic acid (Qiagen) column. To generate dP-IRE1α*, we removed basal phosphorylation sites by incubating IRE1α* with λ-PPase (New England Biolabs) at a molar ratio of 5:1 (IRE1α*: λ-PPase) in 50 mM HEPES pH 7.5, 100 mM NaCl, 1 mM $MnCl_2$, 2 mM dithiothreitol (DTT) and 0.01% Brij 35 detergent (v/v) for 40 min at 23°C. Dephosphorylation was verified by immunoblotting with an antibody specific for pS724-IRE1α (Abcam).

D. Western Blotting and Antibodies

Samples were prepared in loading buffer and boiled for 5 minutes at 95ºC prior to loading into an Any kD™ Mini-PROTEAN® TGX™ Precast protein gels (BioRad). Gels were then ran using Tris-Glycine running buffer (25 mM Tris pH 8.6, 192 mM glycine, 0.1% SDS) at 180 V. Gels were transferred to nitrocellulose paper using the TransBlot Turbo System (BioRad) at 25 V, 2.5 A for 15 minutes. Nitrocellulose blots were blocked for 30 minutes at room temperature with Odyssey blocking buffer (Li-Cor). Primary antibodies were diluted into blocking buffer (1:1000) and incubated over night at 4ºC. Blots were washed 2x with TBST (20 mM Tris pH 7.5, 150 mM NaCl, 0.1% Tween-20) and incubated with near-infrared-dye-conjugated secondary antibodies (Li-Cor) diluted in blocking buffer (1:10000) for 1 hour at room temperature. Blots were imaged using a Li-Cor Odyssey IR Imager and quantitated using ImageStudio.

Table S1.7

Antibody	Vendor	Product Number
IRE1α Rabbit mAb (14C10)	Cell Signaling	#3294
IRE1α pSer724 Rabbit	AbCam	#ab48187

Table S1.7 Western blotting antibodies
Primary antibodies used to detect IRE1α are listed with information about their reactivity, vendor source, and product number

E. *In Vitro* Enzymatic Assays

In Vitro Kinase Assay

Inhibitors (initial concentration of 10 or 60 μM, three-fold serial dilutions) were incubated with IRE1α* in cleavage buffer (20 mM HEPES at pH 7.5, 0.05% Triton X-100 (v/v), 50 mM potassium chloride, 1 mM magnesium chloride, 1 mM DTT) for 30 min, followed by incubation with 10 μCi [γ^{32}P] ATP(3,000 Ci mmol^{-1},

Perkin Elmer) at 23 °C for 3 hours. Samples were then spotted onto phosphocellulose paper and washed in triplicate with 0.5% phosphoric acid and autoradiographed. The percent inhibition was quantified by setting the background as 0 and standardizing to IRE1α* without compound treatment.

In Vitro RNase Assay

5′-Carboxyfluorescein (FAM)- and 3′-Black Hole Quencher (BHQ)-labeled XBP1 single stem-loop miniature substrate (5′FAM-CUGAGUCCGCAGCACUCAG-3′BHQ) were purchased from Dharmacon. We incubated 0.25 μM IRE1α* or dP-IRE1α* with inhibitors or DMSO for 30 min in assay buffer (20 mM Tris at pH 7.5, 50 mM sodium chloride, 1 mM magnesium chloride, 2 mM DTT, 0.05% Triton X-100 (v/v)), followed by incubation with 1 μM RNA substrate for 10 min. The reaction was quenched by adding urea to a final concentration of 4 M, and the fluorescence was detected on a SpectraMax M5 microplate reader (Molecular Devices) or a Perkin Elmer 2104 Envision microplate reader with excitation and emission wavelengths of 494 nm and 525 nm, respectively. The fluorescence intensities were normalized by setting the signal for the reaction without IRE1α* to 0.

F. IRE1α* Crosslinking to Determine Oligomer to Monomer Ratio

Concentration of IRE1α* or dpIRE1α at 15 μM were incubated with DMSO, KIRA, or Activator for 30 min and then crosslinked by adding 250 μM disuccinimidyl suberate (Pierce) for 1 hr at 23°C in the dark in crosslinking buffer (20 mM

HEPES at pH 7.5, 50mM sodium chloride). The reaction was quenched by addition of 100 mM Tris-HCl (pH 7.5). The samples were then boiled, resolved on SDS-PAGE and visualized via Coomassie stain via Alpha Innotech FluoroChem FC2 Gel Imager. Quantification of bands was done using ImageQuant.

G. Mammalian Tissue Culture

INS-1 cells were grown in RPMI, 10% FBS buffer (v/v), 1 mM sodium pyruvate, 10 mM HEPES, penicillin-streptomycin, 2 mM glutamine and 50 μM β-mercaptoethanol. T-REx 293 IRE1α were grown in DMEM H-21 with 10% FBS buffer (v/v) and penicillin-streptomycin.

H. *In Vivo* XBP1 Splicing Assay

After 1 hr incubation with compounds, INS-1 cells were treated with 6 nM tunicamycin for 4 h, and T-REx 293 IRE1α-expressing cells were treated with 1 μM Dox for 8 h. The RNA was then extracted using RNeasy Mini Kit (Qiagen) and reverse transcribed using the QuantiTect Reverse Transcription Kit (Qiagen). XBP1 splicing was performed as previously described[7]. Primers used: sense primer rXBP1.3S (5′- AAACAGAGTAGCAGCACAGACTGC-3′) and antisense primer rXBP1.2AS (5′- GGATCTCTAAGACTAGAGGCTTGGTG-3′) for the INS-1 cell line and sense primer mXBP1.3S (5′-AAACAGAGTAGCAGCGCAGACTGC-3′) and antisense primer mXBP1.2AS (5′-GGATCTCTAAAACTAGAGGCTTGGTG-3′) for the T-REx 293 cell line. PCR

products were resolved on 2.5% (w/v) agarose gels, stained with ethidium bromide and quantified by ImageJ.

I. Crystallization of apo dP-IRE1α* and Src•**1**$^{69-75}$

Buffer Composition

Purified dP-IRE1α* stock protein was stored in a default buffer composed of: 25 mM HEPES pH 7.5, 250 mM NaCl, 5% glycerol, 1 mM DTT, 1 mM EDTA. The dP-IRE1α*·KIRA3 complex was made to a final concentration of: 10 mg/ml (205 μM) of dP-IRE1α*, and 500 μM of KIRA3, (Protein to drug ratio of 1:2.4). In order to achieve these final protein concentrations and a final NaCl concentration of approximately 90 mM, the dP-IRE1α* stock protein was diluted with dilution buffer (25 mM HEPES pH7.5, 10 mM DTT, 1 mM EDTA) The final buffer composition of the dP-IRE1α*·KIRA3 complex was: 25 mM HEPES pH 7.5, 90 mM NaCl, 10 mM DTT, 1 mM EDTA, 1.8% glycerol, 5% DMSO, 500 μM KIRA3.

Protein-Drug Complex Procedure

The dP-IRE1α*·KIRA3 complex was made on ice according to the following steps: (i) Pipette the drug. (ii) Pipette the dilution buffer to the drug and add the appropriate amount of DMSO to maintain DMSO at 5% in the final protein drug complex. Pipette further to mix the drug and buffer mixture. (iii) Add the drug buffer mixture to the protein with further mixing by pipetting to make the final protein-drug complex. (iv) Spin down the protein-drug complex mixture at 14K RPM for 5 minutes at 4°C. Post spin precipitation was visible, which in hindsight of determining the apo dP-IRE1α* crystal structure, suggests that this is likely

insoluble KIRA3. (v) Use the supernatant to set up crystallization via the hanging drop method.

Crystallization Buffer and Procedure

The crystallization buffer condition was: 25 mM Bis-Tris Propane pH 9, 39% PEG 200, 250 mM CsCl, 10% glycerol, at 4°C, with a final concentration of 143 mM BME added into the reservoir mother liquor after setting up the protein-drug complex drop and crystallization drop mixture. The protein·drug complex drop and crystallization drop mixture were setup in a 1 µL:1 µL ratio using the liquid bridge method. Crystals appeared and continued to grow from overnight to a few days, forming long thick blades, and three dimensional hexagons. They were harvested and immersed in the crystallization buffer for cryoprotection because of the high percentage of PEG200.

X-ray Diffraction Data Collection and Processing

X-ray diffraction data was collected at 100 K, with a wavelength of 1.0 Å, using the beamline X29 at the National Synchrotron Light source (Brookhaven National Laboratories). Data were processed using HKL2000 and Xtriage in Phenix. The structure was determined by molecular replacement using the Src kinase domain (minus αC-helix residues: 298-317, and minus activation segment residues: 400-407, and 421-425) from the PDB entry: 2OIQ as a search model in PHASER. The structure was built using COOT and refined with PHENIX.

Data Collection and Refinement Statistics

Table S1.8

	Apo-hIRE1α (PDB: 5HGI)	**SrcKD·1 (PDB: 5J5S)**
PDB-entry	5HGI	5J5S
Space Group	C 2 2 21	P 1
Unit Cell		
a, b, c (Å)	68.04, 169.20, 104.14	42.21, 63.55, 73.66
α, β, γ (°)	90, 90, 90	100.60, 90.61, 90.96
Wavelength (Å)	1.00	1.00
Resolution Range (Å)	44.34 - 2.58 (2.676 - 2.584)	36.24 - 2.15 (2.23 - 2.15)
Total Reflections	123661 (11953)	156329 (15774)
Unique Reflections	19194 (1890)	38412 (3996)
Multiplicity	6.4 (6.3)	3.90 (3.90)
Completeness (%)	99.72 (99.68)	94.20 (87.38)
I/σI	20.47 (2.37)	36.44 (9.84)
B-factor	70.04	32.72
Rmerge	0.05432 (0.8543)	0.27 (0.50)
R-measurement	0.05925	0.31
CC1/2	0.999 (0.751)	0.92 (0.70)
CC*	1 (0.926)	0.98 (0.91)
Reflections used for R-free		
Rwork	0.2385 (0.4574)	0.191 (0.22)
Rfree	0.2679 (0.4828)	0.22 (0.28)
Number of non-hydrogen atoms	3010	4412
Macromolecules	2962	4121
Ligands	38	74
Water	10	217
Protein Residues	395	512
RMS (bonds)	0.005	0.003
RMS (angles)	0.76	0.8
Ramachandran favored (%)	95	98
Ramachandran allowed (%)	4.7	
Ramachandran outliers (%)	0.35	0.2
Clashscore	9.62	3.02
Average B-factor	82.51	48.00
Macromolecules	82.61	48.00
Ligands	110.90	56.80
Solvent	78.13	44.20

Table S1.8 Data collection and refinement statistics

Data collection and refinement statistics for apo dP-IRE1α* and Src. Statistics for the highest-resolution shell are shown in parentheses.

J. Phosphomapping of IRE1α* Activation Loop Serine Residues

IRE1α* (75 pmol) expressed from baculovirus was incubated either alone or with 400 Units lambda phosphatase (NEB) and 1 mM $MnCl_2$ for 1 hr at room temperature. Samples were then precipitated with 0.02% sodium deoxycholate and 10% trichloroacetic acid on ice for 10 min. Mixtures were centrifuged at 4°C for 15 min, and the pellets were washed once with cold acetone. After centrifugation, the pellets were re-suspended in 30 µL 200 mM Tris (pH 8.0), 8 M urea, and 2.4 mM iodoacetamide, and incubated in the dark for 30 min. Solutions were then diluted with 210 µL 200 mM Tris (pH 8.0), 5.7 mM CaCl2, and 1 µg/µL porcine trypsin (TPCK treated, Sigma), and incubated at 37 °C overnight. Samples (0.3 pmol) were injected onto a Thermo Scientific Dionex Acclaim Pepmap100 NanoLC capillary column (C18, 150 mm length, I.D. 75 µm, 3 µm particle size) connected inline to a Finnigan LTQ mass spectrometer. Peptides of interest were identified by MS/MS data (Thermo), and corresponding XIC peaks were integrated.

Chapter 2: Control of IRE1α RNase Functional Outputs Through Rheostatic Regulation of αC-Helix Conformation Using ATP-Competitive Inhibitors

I. Introduction

The use of ATP-competitive inhibitors has been paramount to understanding structural elements that control IRE1α RNase outputs. Interestingly, ATP-competitive inhibitors are divergent in their modulation of the RNase domain of IRE1α – with the ability to either activate or inhibit RNase function. Kinase inhibitors that attenuate RNase function (KIRAs) have been of particular interest because of their effectiveness as therapeutics in disease models of cell degeneration.[28,76] Structural studies of IRE1α and an extensive SAR of KIRAs were used to build a model of how KIRAs function to inhibit RNase activity. This model pointed to the αC-helix, a catalytically important and conserved motif shown previously to undergo conformational changes upon kinase phosphorylation and ligand binding.[45,58,59,60,77] Upon ER stress and subsequent activation of the UPR, IRE1α is phosphorylated and the αC-helix rotates into the kinase active site (αC-helix in) and promotes RNase function by making up a large interface of the back-to-back dimer, which is necessary for RNase activation (**Figure 2.1A,B**). KIRAs ability to inhibit RNase activity from the distal kinase active site therefore stems from the outward movement of the αC-helix (αC-helix out) due to steric hindrance, destabilizing back-to-back dimer formation and preventing RNase activity (**Figure 2.1C**).[78]

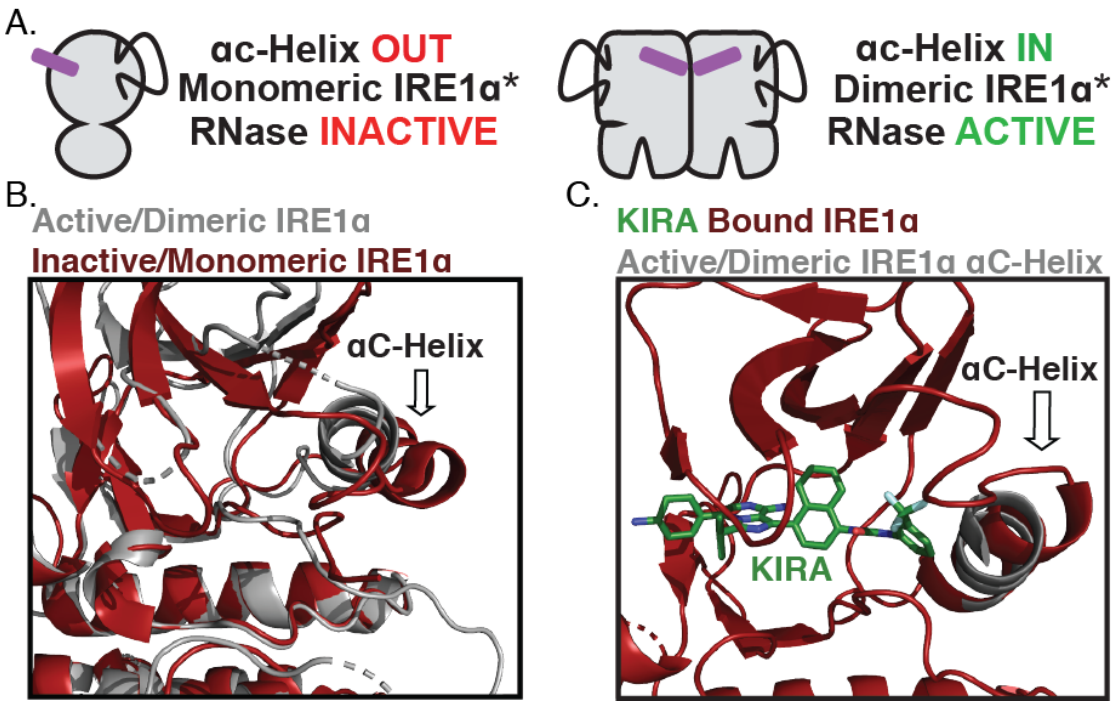

Figure 2.1 αC-helix conformation is important for IRE1α RNase activity
(A). Cartoon of how αC-helix conformation controls IRE1α RNase activity. In brief, when the αC-helix is in an "OUT" position, this causes a steric clashes in the back-to-back dimer interface and prevent RNase activity. When the αC-helix is in an "IN" position, dimerization is promoted and the RNase domain is active. (B). Superimposition of dimeric IRE1α* (gray, PDB: 5HGI) and monomeric IRE1α* (crimson, PDB: 3P23) reveal an 8 Å movement of the αC-helix. (C). Superimposition of the αC-helix of active IRE1α* (gray, PDB: 5HGI) show that KIRAs (green) stabilize an αC-helix-OUT conformation

The ability of ATP-competitive KIRAs to modulate IRE1α RNase activity through αC-helix conformation led us to hypothesize whether additional αC-helix conformations were possible. Here we present a new class of IRE1α kinase inhibitors called partial KIRAs (pKIRAs), named for their ability to only partially inhibit RNase activity. Through biochemical and structural characterization, we show that pKIRAs cause a subtle outward movement of the αC-helix and only attenuate IRE1α back-to-back dimer formation. This unique αC-helix conformation enforced by pKIRAs is able to uncouple RNase functional outputs

of IRE1α in cells – preserving pro-survival XBP1 splicing outputs but preventing pro-apoptotic RIDD outputs. Using chemical biology and proteomics, efforts are ongoing to better understand how signaling events change when only adaptive RNase outputs are preserved. Additionally, for pathologies that involve chronic ER stress, like type I diabetes, pKIRAs preservation of adaptive RNase outputs may prove beneficial therapeutically. Finally, rheostatic movement of the αC-helix by ATP-competitive inhibitors also reveals a potentially general method of allosteric regulation for other protein kinases.

II. Results and Discussion

A. Phosphorylation and ATP-Competitive Inhibitors Affect IRE1α Dimerization

IRE1α kinase phosphorylation is necessary for IRE1α back-to-back dimer formation and subsequent activation of IRE1α's RNase domain.[8,30,45,46] While this interdependence between the kinase and RNase domain has been well established, the effects of phosphorylation on IRE1α dimerization have not been robustly characterized. Due to the dependence of RNase activity on back-to-back dimer formation, IRE1α oligomerization can be measured by simply monitoring changes in the rate of RNase cleavage activity as a function of IRE1α concentration. *In vitro* enzymatic assays were preformed using a minimal IRE1α construct, IRE1α*, that includes both cytosolic kinase and RNase domains (residues 547-977). This construct was previously shown to be constitutively active via phosphorylation on three activation loop serine residues.[78] A quantitatively dephosphorylated IRE1α* construct, dpIRE1α*, that displays low

basal kinase and RNase activity was then generated by adding super-stoichiometric amounts of lambda phosphatase to IRE1α* (**Figure 2.2A**). IRE1α RNase cleavage activity was analyzed using an XBP1 mini-substrate labeled with a 5'-Alexa647 and a 3'-IowaBlack fluorescence quencher. IRE1α RNase activity leads to cleavage of the XBP1 mini-substrate and subsequent increase in fluorescence through disruption of FRET quenching (**Figure 2.2A**). IRE1α dimerization was reported as a second-order rate constant ($RFUs^{-1}M^{-1}$) and dimer curves resembled canonical dose-response plots, where plateaus represent 100% dimerization rather than substrate depletion. IRE1α* readily forms dimers at low concentrations, with a K_{DIMER} value of 135 ± 25 nM and a Hill Coefficient of 2.1 ± 0.2, which is consistent with formation of dimers rather than formation of high-order oligomers. In contrast, dpIRE1α* dimers could only be observed at near micro-molar concentrations and a K_{DIMER} value for dpIRE1α* could not be accurately determined due to limitations on protein concentration in the assay (**Figure 2.2B**). Between the two differentially phosphorylated constructs, a difference in K_{DIMER} of > 30-fold was observed, a result on par with the previously reported 39-fold improvement in RNase catalytic efficiency between dpIRE1α* and IRE1α*.[45] To assess how ATP-competitive inhibitors affect IRE1α dimerization, we tested two previously published inhibitors, AT9283 and KIRA8, in our K_{DIMER} assay. AT9283 has been established as an allosteric activator of IRE1α's RNase domain and was hypothesized to function by promoting back-to-back dimer formation even in the absence of

phosphorylation.[66] By treating dpIRE1α* with saturating amounts of AT9283, we can look specifically at the monomer-dimer equilibrium of dpIRE1α*•AT9283. The addition of AT9283 to dpIRE1α* shifts the monomer-dimer equilibrium in favor of dimer formation. Interestingly, the addition of AT9283 to dpIRE1α* improves the K_{DIMER} value to 51 ± 14 nM, a value similar to that seen with phosphorylated IRE1α*. A Hill Coefficient of 3.5 ± 0.2 was determined, suggesting that AT9283 binding leads to the formation of not just dimers, but high order oligomers as well (**Figure 2.2C**). KIRA8, an allosteric inhibitor of IRE1α's RNase domain was first published by Amgen and was later shown to prevent IRE1α dimerization in an *in vitro* chemical crosslinking assay and block all IRE1α RNase outputs in cells.[15,55,78] As expected based on previous chemical crosslinking results, treatment of IRE1α* with saturating concentrations of KIRA8 fully prevented dimerization up to 2 μM IRE1α* (**Figure 2.2D**). Altogether, these results highlight the importance of phosphorylation in IRE1α dimerization and RNase activation, and the ability of different classes of ATP-competitive inhibitors to phenocopy different IRE1α phosphorylation/activation states.

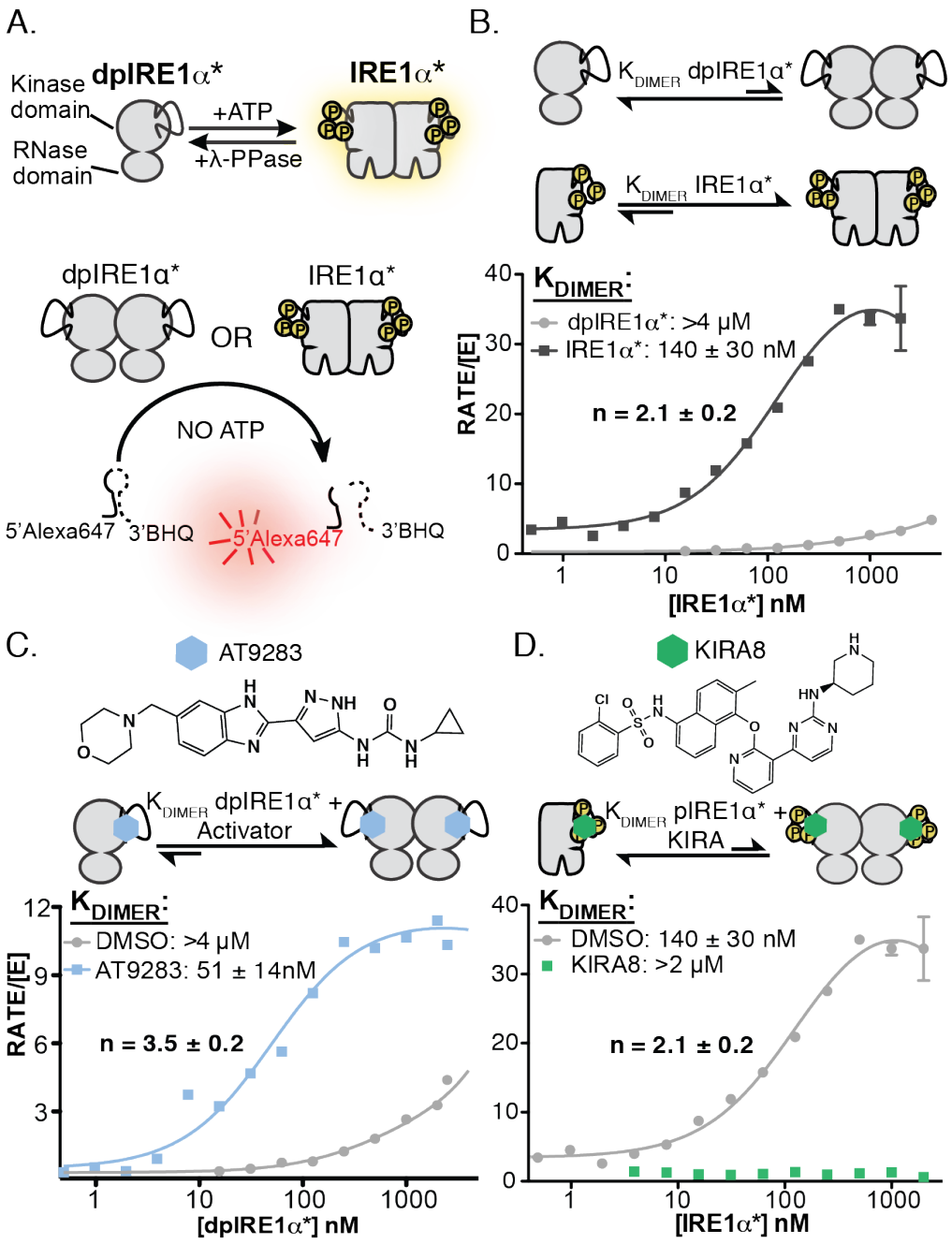

Figure 2.2 Phosphorylation and ATP-Competitive Inhibitors affect IRE1α dimerization

(A *top)* Recombinant constructs of IRE1α span residues 547-977, which includes the kinase and RNase domain. (A *bottom)* Schematic of the *in vitro* XBP1-mini substrate cleavage assay. In brief, IRE1α's RNase requires dimers to become active, and when active will cleave a FRET-quenched XBP1 substrate resulting in an increase in fluorescence. (B) Phosphorylation of IRE1α is important for dimerization. Phosphorylated IRE1α* (dark grey) has a K_{DIMER} of 140 ± 30 nM and a Hill Coeffiecient of 2.1 ± 0.2, while a K_{DIMER} for dephosphorylated dpIRE1α* could not be accurately determined. Data points shown are shown as the mean ± SEM, n=3. (C). dpIRE1α* was treated with 50 μM

AT9283 (light blue) in order to monitor the monomer-dimer equilibrium of dpIRE1α* when quantitatively occupied by AT9283. AT9283 promotes dimerization of dpIRE1α* with a K_{DIMER} value of 51 ± 14 nM and a Hill Coeffiecient of 3.5 ± 0.2. *Apo*-dpIRE1α* is shown as a comparison. Data points shown are shown as the mean ± SEM, n=3. (D). IRE1α* was treated with 50 μM KIRA8 (green) to monitor the monomer-dimer equilibrium of IRE1α* when quantitatively occupied by KIRA8. Binding of KIRA8 completely blocks dimerization of IRE1α* and a K_{DIMER} curve could not be fitted. Apo-IRE1α* (light gray) was plotted for comparison. Data points shown are shown as the mean ± SEM, n=3.

B. αC-helix of IRE1α is Responsible for Divergent RNase Modulation by ATP-Competitive Inhibitors

While the mode of binding and method of allosteric inhibition by KIRAs has been established through structural studies and an extensive structure-activity-relationship (SAR), known activators of the RNase domain are diverse and provide little detail on structural elements important to their allosteric activation of RNase activity.[55,78] Studies of KIRAs have pinpointed the αC-helix as the structural motif responsible for disruption of IRE1α dimer formation. To better understand the importance of the αC-helix in whether an ATP-competitive inhibitor functions as an allosteric activator or inhibitor of IRE1α's RNase domain, we performed a small SAR of inhibitors based on the pyridine-pyrimidine scaffold of KIRA8. Differing from KIRA8 in scaffold structure are the *trans*-hexanediamine motif as a replacement for the (S)-3-aminopiperidine as well as a 4-amino-3-fluorophenol in lieu of a methyl naphthyl moiety, both of which have insignificant affects on potency.[55] In this series, we modified only the amino substituent of the fluorophenol, R, located in a hydrophobic pocket proximal to the αC-helix. By limiting changes to just this motif, we aimed to isolate any conformational changes within the kinase active site of IRE1α to just the αC-helix. In our first series, we looked at three inhibitors of increasing size with respect to R-group.

Compound **1** is unmodified to give the free amine, while **2** and **3** contain trifluoroethylsulfonamide or trifluoropropylsulfonamide groups respectively (**Figure 2.3A**). The efficacy of these compounds as kinase inhibitors was assessed by their ability to block IRE1α*'s phosphorylation of the protein substrate myelin basic protein (MBP) using ATP[γ^{32}]. Compound **3** was the most potent in the series with a kinase IC_{50} of 50 ± 11 nM, while **1** and **2** were both ~6-fold less potent (**Figure 2.3A**). In a fluorescence assay using the same XBP1 mini-substrate described above, we show that **1** dose-dependently increases RNase activity with an EC_{50} of 610 ± 110 nM. Conversely, **2** and **3**, which contain larger substituents as their R-group, dose-dependently inhibit RNase activity (**Figure 2.3B**). From this result, we hypothesize that the threshold between activation and inhibition of RNase activity by ATP-competitive inhibitors stems directly from the conformation of the αC-helix. Compounds with small substituents in the αC-helix pocket, like **1,** are not sufficiently bulky to move the helix, promoting both dimerization and RNase activity. While, increasing the size of the substituent in the αC-helix pocket to a short chain alkylsulfonamide seen in **2** and **3** causes movement of the αC-helix through steric hinderance, preventing both dimerization and RNase activity. Compound **1** was tested in the K_{DIMER} assay to assess its ability to promote dimerization of dpIRE1α*. Similarly to AT9283, **1** promoted dimerization with a K_{DIMER} value of 210 ± 60 nM and a Hill Coefficient of 2.3 ± 0.1 (**Figure 2.3C**).

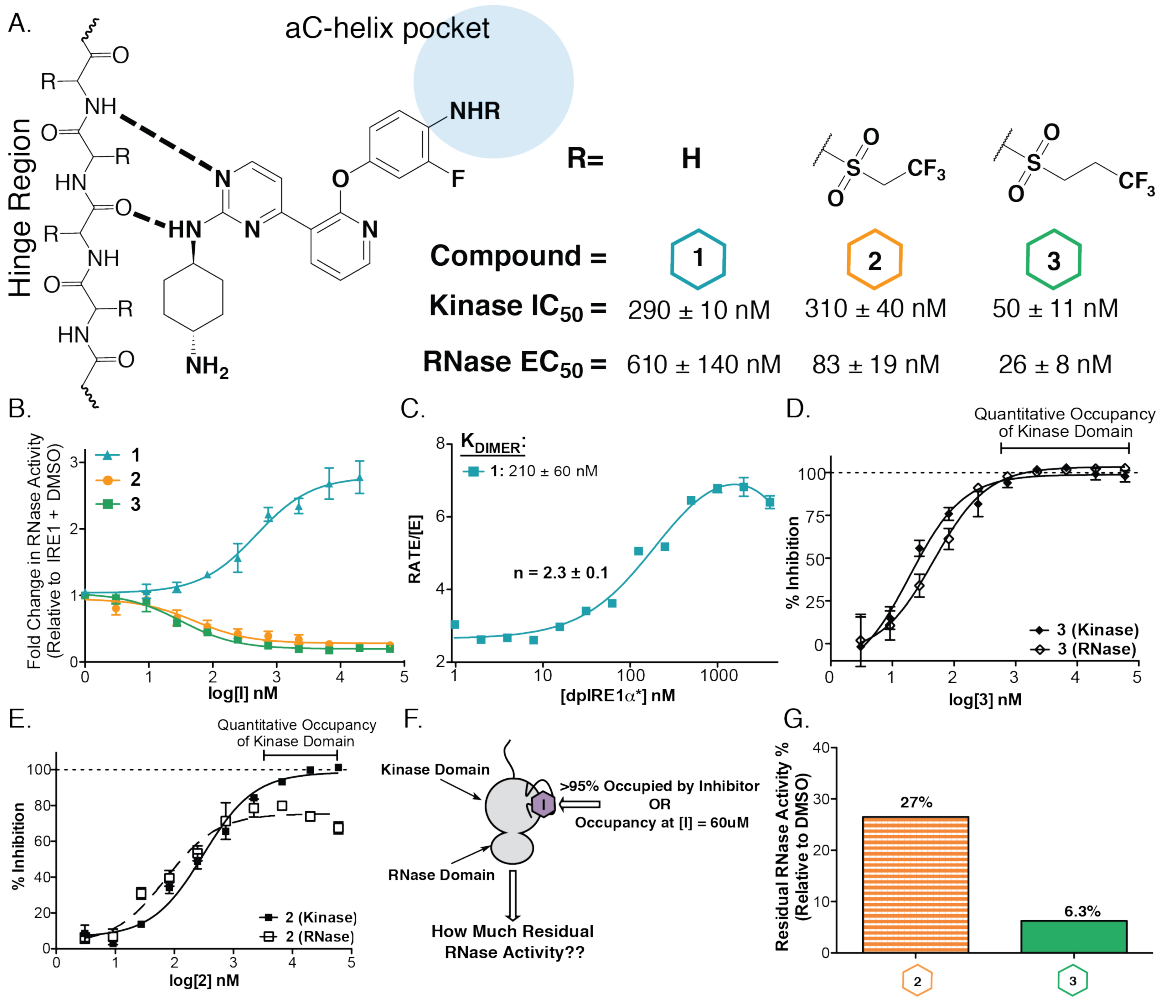

Figure 2.3 IRE1α's αC-Helix regulates the kinase-RNase allosteric network

(A) Proposed binding model of the parent scaffold for **1, 2, 3**. Varied substituents are localized to a pocket proximal to the αC-helix. R-groups and half maximal inhibitory values for the kinase and half maximal effective values for the RNase domain are shown (mean ± SEM, n=3). (B) Fold change in IRE1α* RNase activity relative by **1, 2,** and **3**. Compound **1** (blue) dose-dependently increases RNase activity relative to DMSO treated IRE1α*. Compounds **2** and **3** (orange and green) dose-dependently decrease RNase activity relative to DMSO treated IRE1α*. (C) dPIRE1α* treated with **1** has a K_{DIMER} of 210 ± 60 nM and a Hill Coefficient of 2.3 ± 0.1 (mean ± SEM, n=3). (D). Inhibitor titration of **3** in both kinase (closed diamonds) and RNase (open diamonds) *in vitro* activity assays. When **3** quantitatively occupies the kinase active site of IRE1α*, the RNase domain is completely inhibited (mean ± SEM, n=3). (E) Inhibitor titration of **2** in both kinase (closed squares) and RNase (open squares) *in vitro* activity assays. When **2** quantitatively occupies the kinase activity site, the RNase domain does not reach complete inhibition. (F). Residual RNase activity is determined as the amount of RNase activity remaining relative to DMSO treated IRE1α* when the kinase active site is quantitatively occupied. (E). IRE1α* residual RNase activity when treated with **2** is 27%, while treatment with **3** leaves only 6.3% residual RNase activity (mean ± SEM, n=3).

The Hill Coefficient of approximately two suggests that unlike AT9283, **1** allows primarily dimer formation and not the formation of higher order oligomers. This result suggests that ATP-competitive inhibitors that allosterically activate the RNase domain may have slightly different binding modes that can promote higher-order cooperativity. Interestingly for allosteric inhibitors of RNase activity, concentrations in which the kinase active site of IRE1α is quantitatively occupied by inhibitor **3,** lead to complete RNase inhibition, while **2** leads to only partial inhibition of the RNase domain even though these inhibitors differ by just a single methylene in their R-group (**Figure 2.3D,E**). Partial inhibition was further quantified as the percent residual RNase activity when the kinase domain was quantitatively inhibited and therefore occupied by a ligand (**Figure 2.3F**). Residual RNase of activity for **3** was 6.3% (or 94% inhibition of RNase activity), while **2** left 27% residual RNase activity (**Figure 2.3G**). Partial inhibition of RNase activity was seen previously with an imidazopyrazine-based ATP-competitive inhibitor containing a cyclopropyl urea motif in the hydrophobic pocket proximal to the αC-helix. At the time it was hypothesized that smaller substituents in this pocket may lead to only partial movement of the motif necessary for RNase inhibition.[78]

C. Partial KIRAs Do Not Fully Prevent RNase Activity and IRE1α Dimerization

To better assess whether partial inhibition of the RNase domain is a general consequence of small substituents in the αC-helix pocket or is specific to the two inhibitors mentioned above, we designed an additional series of inhibitors,

making small changes to the pyridine-pyrimidine scaffold. We varied the scaffold by exchanging the fluoroaniline for a naphthylamine motif and looked at both 1,4- and 1,5-substituted amine groups within the αC-helix pocket. For 1,4-substituted naphthyls a cyclopropyl urea and a cyclopropylsulfonamide R-group were used for compounds **4** and **5** respectively. Additionally, we made a 1,5 substituted cyclobutylsulfonamide inhibitor, **6** (**Figure 2.4A**).

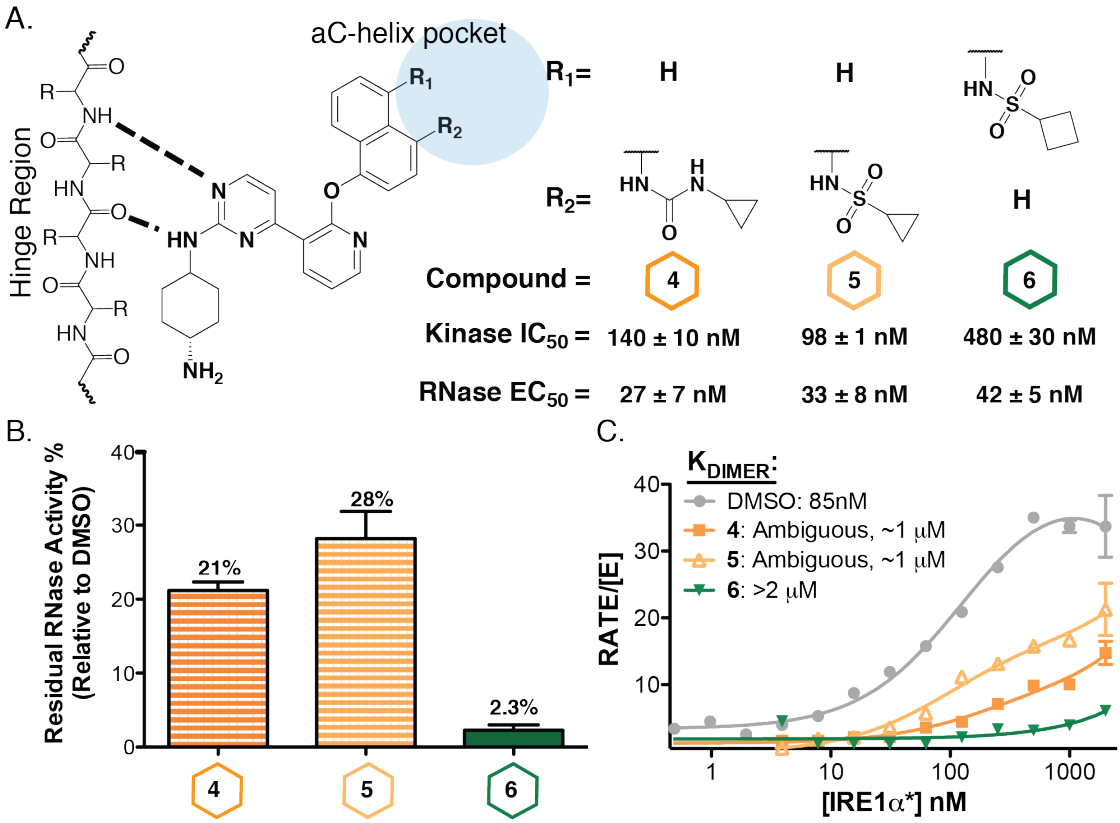

Figure 2.4 IRE1α's αC-helix is a rheostat of back-to-back dimer formation
(A). Proposed binding model of the parent scaffold for **4, 5, 6**. Varied substituents are localized to a pocket proximal to the αC-helix. R-groups and half maximal inhibitory values for the kinase and half maximal effective values for the RNase domain are shown (mean ± SEM, n=3). (B). Compounds **4** and **5** do not fully inhibit IRE1α* RNase activity, while **6** leads to <5% residual RNase activity (mean ± SEM, n=3). (C) Inhibitors that do not show any residual RNase activity, like **6**, completely block IRE1α* dimerization. Compounds **4** and **5** do not fully inhibit RNase activity and only partial attenuate IRE1α* dimerization with K_{DIMER}s of ~ 1 μM (mean ± SEM, n=3)

The least potent kinase inhibitor was **6** with a kinase IC_{50} of 490 ± 30 nM, 4-5-fold less potent than **4** and **5**. Despite its poor potency, **6** lead to >95% inhibition of the RNase domain and fully prevented IRE1α* dimerization (**Figure 2.4B,C**)**.** Compounds **3** and **4** contain smaller cyclopropyl groups within the αC-helix pocket, and leave 20-30% residual activity of the RNase domain (**Figure 2.4B**). When tested in our dimerization assay, unlike KIRAs that completely block dimerization, **3** and **4** only moderately attenuate IRE1α* dimerization with K_{DIMER}s = ~1 μM (**Figure 2.4C**). The pyrimidine-pyridine scaffold was further modified by exchanging the *trans*-hexanediamine for an (S)-3-aminopiperidine group and making modifications to the 1,4-substituted naphthylamine motif (**Figure 2.5A**). Trifluoroethylsulfonamide and trifluoropropylsulfonamide were again used as the R-groups for **7** and **8**, and these inhibitors behaved very similarly to their hexanediamine orthologs, **1** and **2**. Again, the difference of just a methylene in the alkyl chain of the R-group caused a change in residual RNase activity from 30% to 5.5%. As a comparison for how a large arylsulfonamide group in the αC-helix would affect residual RNase activity, KIRA8 was also tested and able to >94% inhibit RNase activity (**Figure 2.5B**). Much like the K_{DIMER} results above, **7,** with the smaller trifluoropropylsulfonamide R-group did not fully prevent IRE1α* dimerization with a K_{DIMER} of ~2 μM, while **8** fully blocked dimer formation (**Figure 2.5C**). For this new class of inhibitors, which includes **2, 4, 5,** and **7,** that display only partial inhibition of the RNase domain and lead to incomplete prevention of IRE1α* dimerization we've named them partial KIRAs, or pKIRAs.

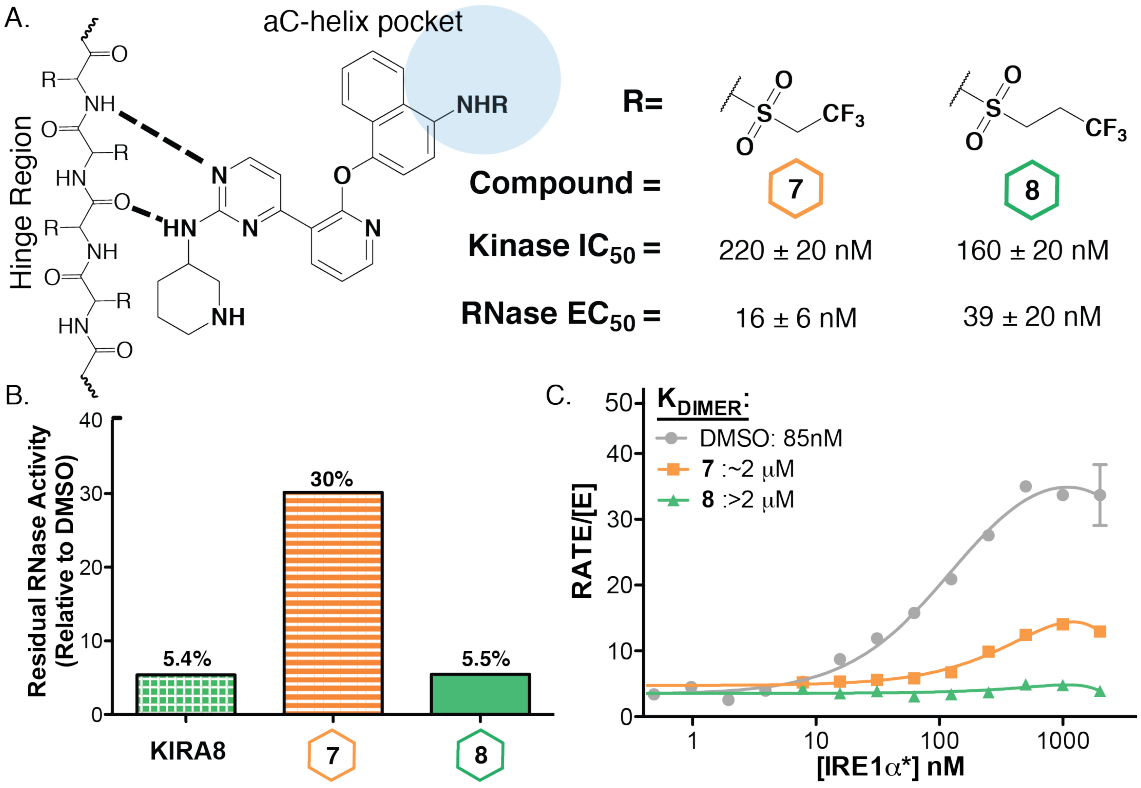

Figure 2.5 Partial inhibition is a general effect of small substituents in the αC-helix pocket

(A). Proposed binding model of the parent scaffold for **7** and **8**. Varied substituents are localized to a pocket proximal to the αC-helix. R-groups and half maximal inhibitory values for the kinase and half maximal effective values for the RNase domain are shown (mean ± SEM, n=3). (B). Compounds **7** leaves 30% residual RNase activity, while the addition of a single methylene with **8** leads to only 5.5% residual RNase activity. KIRA8 was plotted as a comparison to show how occupancy of the αC-helix pocket with large arylsulfonamides affects residual RNase activity (mean ± SEM, n=3). (C) Compound **8** fully prevents IRE1α* dimerization, **7** attenuates dimerization with a K_{DIMER} value of ~ 2 μM. (mean ± SEM, n=3)

D. pKIRAs Rheostatically Tune αC-Helix Conformation and Weaken Dimer Formation Through Movement of Key Dimer Interacting Residues

Crystal structures of IRE1α have been helpful in the past for building structural models of how kinase active site conformation affects RNase activity.[31,53-56] To better understand how our pKIRAs interact with the ATP-binding site of IRE1α, we obtained a 1.85 Å resolution co-crystal structure of **7** bound to IRE1α*. Ligand

density for **7** could be found in both protomers of IRE1α*, which crystallized as a back-to-back dimer. Crystallization in a back-to-back dimer is consistent with the K_{DIMER} of ~1 μM for **7** bound IRE1α* considering the high concentration of IRE1α* and **7** used to obtain crystals suitable for diffraction (**Figure 2.6A**). Looking at key interactions between **7** and the kinase active site of IRE1α*, the pyrimidine ring and amine linkage make two hydrogen bonding interactions with the backbone of Cys645 within the hinge region of the ATP-binding pocket. The piperidine ring nitrogen forms a salt bridge with Glu651 of the α-H helix. Additional interactions are made between the sulfonamide motif of the ligand and the backbone of Asp711 and Phe712 of the catalytically important DFG-motif (**Figure 2.6B**). These four main interactions are identical to those made in the co-crystal structure of the parent ligand KIRA8 bound to IRE1α* (PDB: 4U6R). Interestingly, although KIRA8 and **7** have near identical interactions with the kinase active site, KIRA8 bound IRE1α* crystallizes as a monomer. Next, we compared the ATP-binding sites of **7** bound IRE1α* and a crystal structure of apo-dpIRE1α* in an active kinase conformation (PDB: 5HGI). Specifically, by superimposing these two crystal structures, we can better understand how ligand binding affects the conformation of the αC-helix. Here we see that the αC-helix of pKIRA bound IRE1α* is rotated outward relative to the αC-helix of apo-dpIRE1α* in an active or αC-helix-in conformation. This overlay also reveals that the trifluoroethylsulfonamide R-group of **7** would cause a steric clash with Glu612 when the αC-helix is in an active conformation (**Figure 2.6C**). Next, to compare

the effects of different ATP-competitive ligands on αC-helix conformation we looked at differences in the movement of the αC-helix of IRE1α* when bound to either **7** or KIRA8. Superimposing crystal structures of both apo-dpIRE1α* (PDB: 5HGI) and KIRA8 bound IRE1α* (PDB: 4U6R) onto **7** bound IRE1α* show that while ligand binding of both **7** and KIRA8 cause αC-helix movement, **7** binding leads to a smaller movement of the αC-helix as compared to KIRA8 (**Figure 2.6D**). These slight differences in αC-helix conformation highlight its ability to be rheostatically modulated by ATP-competitive pharmacophores. We then looked for differences in key back-to-back dimer interface residues between active apo-dpIRE1α* and **7** bound IRE1α* to better understand how subtle movement of the αC-helix confers decreased dimer affinity. There are several key interactions between the two protomers of IRE1α* in the back-to-back dimer, and while intact upon pKIRA binding, are measurably farther apart.[78] One exception to this was residue Asp620 located in a flexible loop region directly C-terminal to the αC-helix. In our crystal structure, Asp620 shows density in two different conformations. In one conformation, Asp620-IN, the side-chain of Asp620 makes two favorable hydrogen bond interactions with the side-chains of Arg594 and Arg627 of the adjacent IRE1α* protomer. In the other conformation, Asp620-OUT, Asp620 is rotated 11.6 Å and can no longer make those favorable interactions (**Figure 2.6E**). Movement of this specific residue was previously described in crystal structure of mouse IRE1α* bound to ADP and OICR464 (PDB: 4PL4). Movement of Asp620 and disruption of the intermolecular salt

bridge between Asp620 and Arg594/627 of the opposite protomer was suggested to be essential for IRE1α dimerization.[41] Interestingly, the movement of Asp620 can be seen in another structure of ADP bound human IRE1α* (PDB: 3P23). In this structure, the αC-helix is rotated outwards and displaces Asp620 away from Arg594 and Arg627.[30] Mutation of this Asp620 residue to an alanine in murine IRE1α* retains kinase activity, but prevents RNase activation.[41] We propose that subtle outward movement of the αC-helix caused by pKIRA binding, leads to flexibility of the loop region directly C-terminal to the helix and this flexibility allows Asp620 to sample conformations both productive and non-productive to dimer formation, thus leading to an overall attenuation in dimer formation.

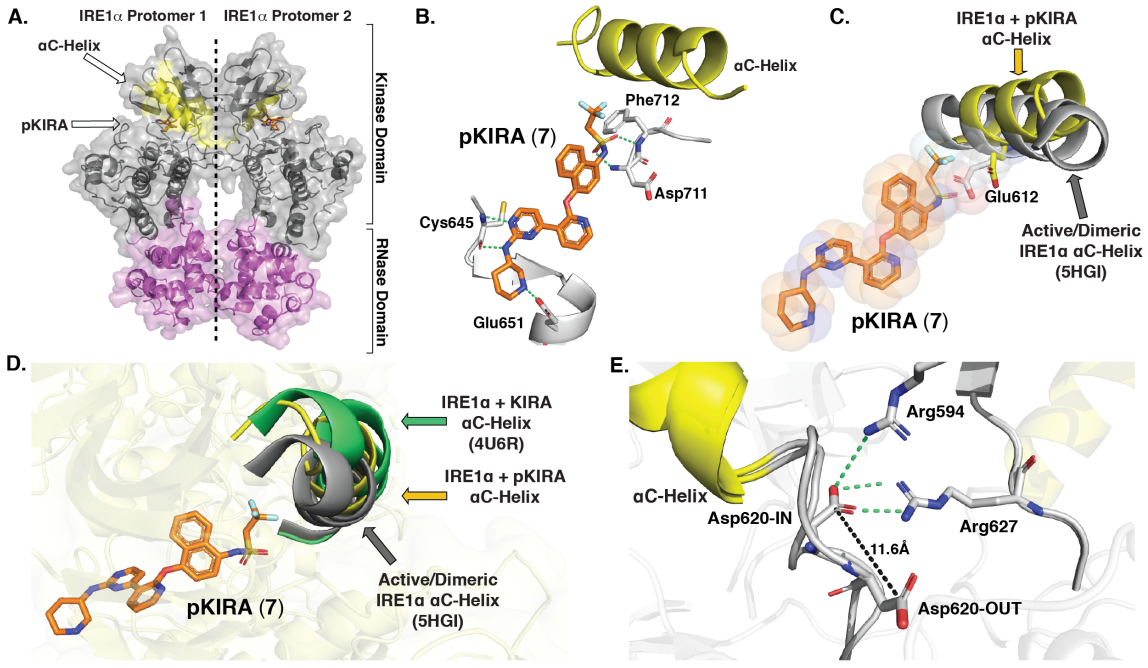

Figure 2.6 Crystal structure of pKIRA bound to IRE1α
(A). Co-crystal structure of **7** bound to IRE1α* crystallizes as a back-to-back dimer. Each protomer contains a kinase domain (shown in gray) and an RNase domain (shown in pink). The αC-helices located in the kinase active site are shown in yellow, and **7** is shown in orange sticks. Two-fold symmetry axis denoted by dashed line. (B). Zoom in of the ATP-binding site highlights contacts and key interactions (dashed green lines) mediating the binding between **7** (orange sticks) and IRE1α*. Residues involved in key

interactions are shown as grey sticks and the αC-helix is shown in yellow. (C). The αC-helix in an active conformation (gray cartoon, PDB: 5HGI) superimposed onto the structure of **7** bound to IRE1α*. The αC-helix of pKIRA bound IRE1α* is rotated outward relative to the αC-helix in an active conformation. Superimposition of an active αC-helix conformation produces a steric clashed between **7** and Glu612 (shown in sticks) (D). Superimposition of the αC-helix in an active conformation (gray, PDB: 5HGI), and an inactive conformation (green, PDB: 4U6R) shows rheostatic movement of the αC-helix. (E). Close-up of the dimer interface shows Asp620 (gray sticks) in two different conformations, Asp620-IN or rotated 11.6 Å to Asp620-OUT. In Asp620-IN, the carboxylate side chain makes contacts (dashed green lines) with the side chains of Arg594 and Arg627 (gray sticks) of the adjacent protomer. These contacts are disrupted in the Asp620-OUT conformation.

E. pKIRAs Preserve XBP1 Splicing but Prevent RIDD Outputs

To see if partial inhibition of the RNase domain was reproducible using the full length IRE1α transmembrane protein, we moved to cell-based assays. Before adding our inhibitors to cells, we first assessed their selectivity by preforming a comprehensive kinome profiling and selectivity experiment. This experiment helps confirm that any results are due to direct inhibition of IRE1α and not from engagement of off-targets. Endogenous kinases were profiled from HCT116 and HEK293 lysates using a kinase affinity reagent (Kinobead). Kinobeads contain a mixture of non-selective kinase inhibitors immobilized to the surface of a sepharose bead and enrich kinases from cell lysates through their ATP-binding sites. Kinobeads have been shown to interact with a majority of the kinome (over 300 kinases), and are a robust method for determining broad kinase selectivity of ATP-competitive inhibitors.[79] Lysates were spiked with recombinant IRE1α* and incubated with 10 μM of **4, 5, 6, 7, 8,** or DMSO prior to Kinobead incubation. Using mass spectrometry, inhibitor selectivity can be assessed by comparing

kinase enrichment in inhibitor treated as compared DMSO treated samples (**Figure 2.7A**).

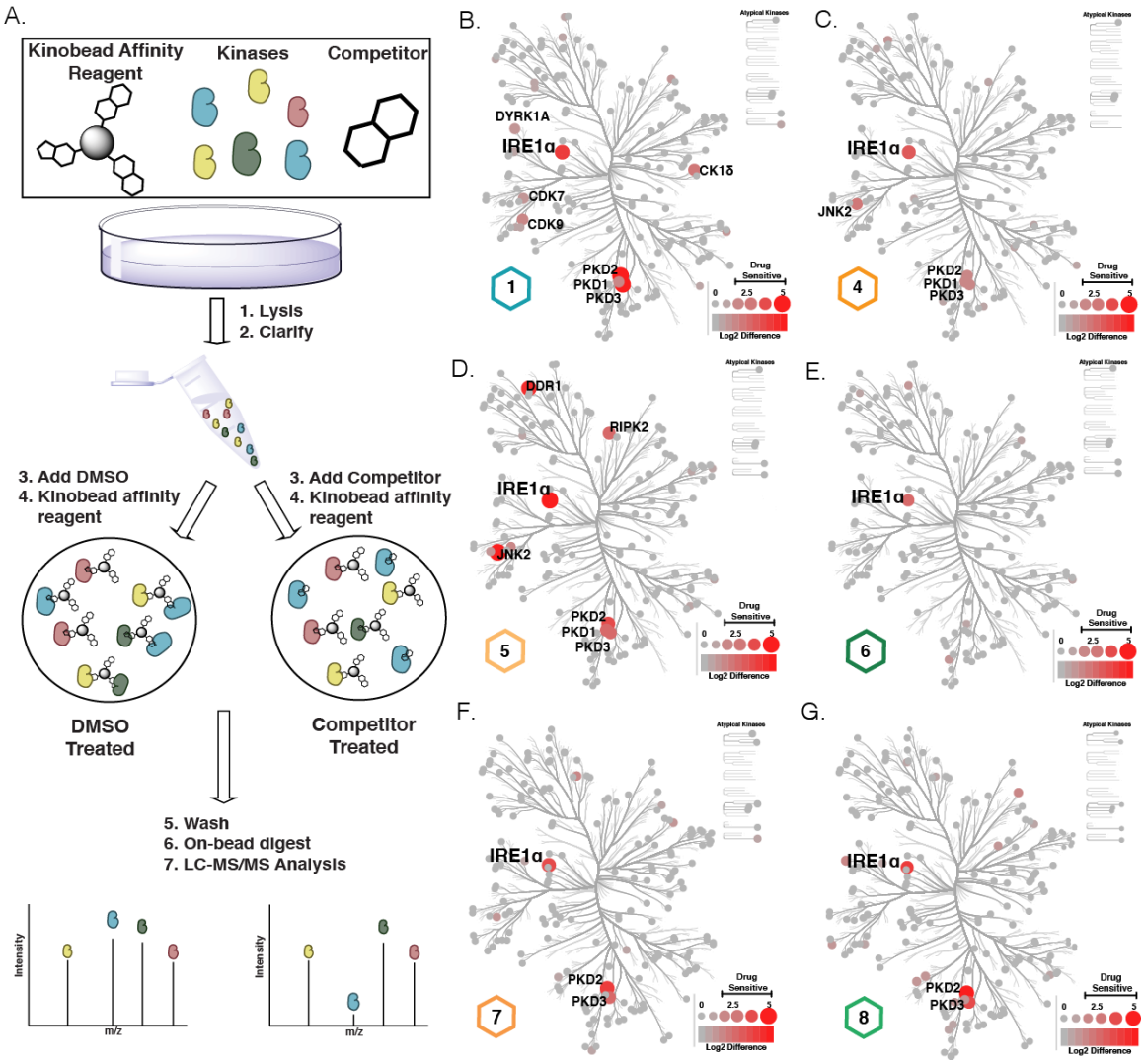

Figure 2.7 Analysis of kinases targeted by IRE1α ATP-Competitive Inhibitors
(A). Schematic of kinome profiling and selectivity assay. In brief, cells are lysed and incubated with either DMSO or inhibitor prior to kinobead incubation. Enriched kinases are trypsin digested and analyzed by LC-MS/MS. (B-G) Specificity of **1, 4, 5, 6, 7, 8** as determined by kinobead profiling. Kinases that were ID'd in the experiment are shown with gray circles. Circle size and color have been scaled to the log2 ratio (difference in LFQ intensity) between DMSO and treatment with 10 μM of inhibitor (mean of four replicates). Kinases reported as being drug-sensitive (Log2 Difference > 2) were also required to show significance from a two-sample T-test with FDR of 0.05. Heat maps show all kinase targets in the profiling experiments (see **Figure S2.2**).

All five inhibitors displayed selectivity for IRE1α* with minimal off-targets, but **7** and **8** were among the most selective, with the only two significant off-targets, PKD2 and PKD3, out of ~180 protein kinases profiled. Due to the high degree of similarity between **7** and **8** with respect to their structures, potencies, selectivities, and off-targets, these compounds were selected to move forward into our cell-based assays (**Figure 2.7B-G**). While the potencies of **7** and **8** against the kinase of IRE1α are very similar *in vitro*, we also confirmed this to be true in cells. Inhibitors ability to block the phosphotransferase activity of endogenous IRE1α was monitored using phostag-acrylamide gels, which resolve protein species based on their molecular weight and phosphorylation state. INS-1 cells, an insulin producing beta cell line derived from rat insulinomas, were pre-treated with a serial dilution of **7** or **8** for 1 hour followed by addition of the ER stress agent brefeldin-A (BFA).[80] Both **7** and **8** have cellular IC_{50} values of about 1 μM and showed >90% inhibition of IRE1α phosphorylation at concentrations at or above 7.5 μM (**Figure 2.8A,B**). To observe the effects of pKIRA (**7**) and KIRA (**8**) on XBP1 splicing outputs, INS-1s were pre-treated with 10 or 20 μM of drug followed by addition of BFA for 2 hours. Addition of BFA led to almost total (98%) splicing of XBP1. Treatment with **7** slightly decreased the amount of spliced XBP1 to 69% (10 μM) and 71% (20 μM), while treatment with either 10 or 20 μM **8** decreased XBP1 splicing to that of untreated cells (**Figure 2.8C**). An existing challenge of assaying IRE1α in cells is choosing the best method or reagent to activate the UPR and IRE1α. Several ER stress agents exist and while effective at promoting

ER stress, they also have tendency to be toxic to cells and induce extra-UPR signaling events that can be hard to uncouple from signaling events originating from the UPR.[81-84] A more direct and less pleiotropic method of IRE1α activation can be achieved through overexpression of IRE1α via stable integration or transient transfection of cells.

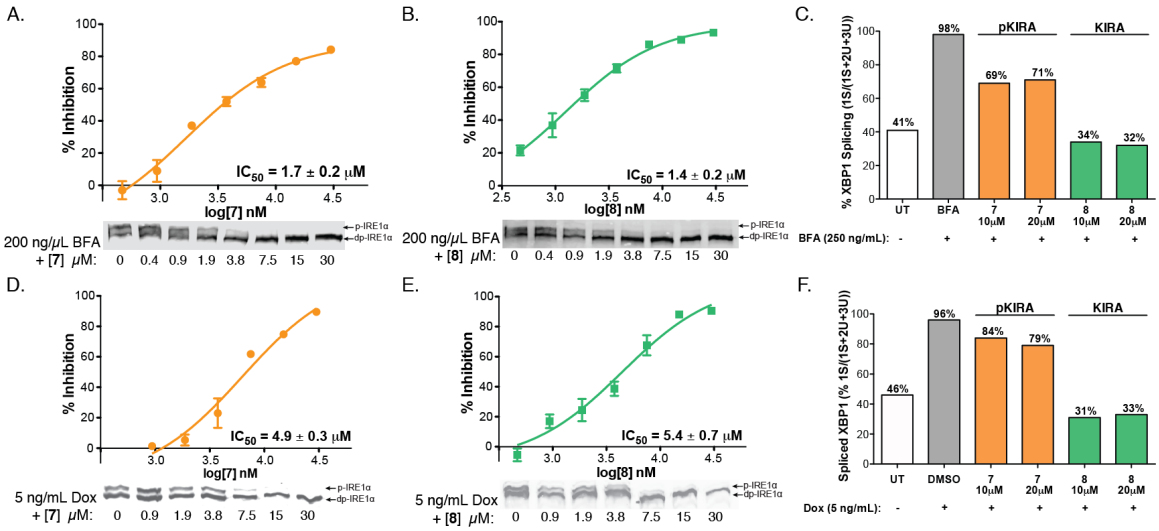

Figure 2.8 KIRAs and pKIRAs divergently affect XBP1 splicing outputs
(A, B). INS-1 cells were pre-treated with **7** or **8** followed by addition of 200 ng/μL Brefeldin-A for 2 hours. Engagement of IRE1α was determined through blockage of phosphotranferase ability. Phosphorylation of IRE1α is shown using phostag acrylamide gels and percent phosphorylation was determined by measuring the intensity of upper (phosphorylated IRE1α) bands as a percentage of total IRE1α intensity (mean ± SEM, n=3) (C). cDNA amplicons of XBP1 from INS-1s pre-treated with 10 and 20 μM of **7** and **8** followed by addition of 250 ng/mL BFA for 2 hours. (D, E). Isogenic INS-1s were pre-treated with **7** or **8** followed by addition of 5 ng/mL doxycycline for 6 hours. Engagement of IRE1α was determined through blockage of phosphotranferase ability. Phosphorylation of IRE1α was shown using phostag acrylamide gels and percent phosphorylation was determined by measuring the intensity of upper (phosphorylated IRE1α) bands as a percentage of total IRE1α intensity (mean ± SEM, n=3). (F). cDNA amplicons of XBP1 from isogenic INS-1-IRE1α cells pre-treated with 10 and 20 μM of **7** and **8** followed by addition of 5 ng/mL Dox for 6 hours.

IRE1α overexpression leads to spontaneous oligomerization of the lumenal domains and subsequent RNase activation.[8,29] To ensure that the results above were not specific to BFA-treatment, cellular engagement of IRE1α and XBP1

splicing was tested under IRE1α overexpression. Both **7** and **8** were able to quantitatively inhibit IRE1α even while being expressed at supra-physiological levels, with cellular IC_{50}s of ~5 μM (**Figure 2.8D,E**). Consistent with the results seen with BFA treatment, overexpression of IRE1α led to almost total splicing of cellular XBP1 (96%) and a 2.1-fold increase in in XBP1s as compared to untreated cells. Pre-treatment with pKIRA did not lead to significant decreases in XBP1s levels, while KIRAs treatment prevented overexpression induced XBP1 splicing events to levels at or below untreated cells (**Figure 2.8F**). To monitor RIDD RNase outputs, the levels of four different mRNAs were monitored: insulin precursors, Ins1 and Ins2, and the Golgi-localized glycosylating enzyme, Gytt1b.[13] ER stress (via IRE1α overexpression) led to decreased levels of all four mRNAs relative to untreated cells. Treatment with both pKIRA and KIRA blocked IRE1α-induced decreases in levels of these three mRNA substrates (**Figure 2.9**). Taken altogether, these results highlight the ability of pKIRAs to uncouple IRE1α's XBP1 splicing activity from its mRNA decay activity.

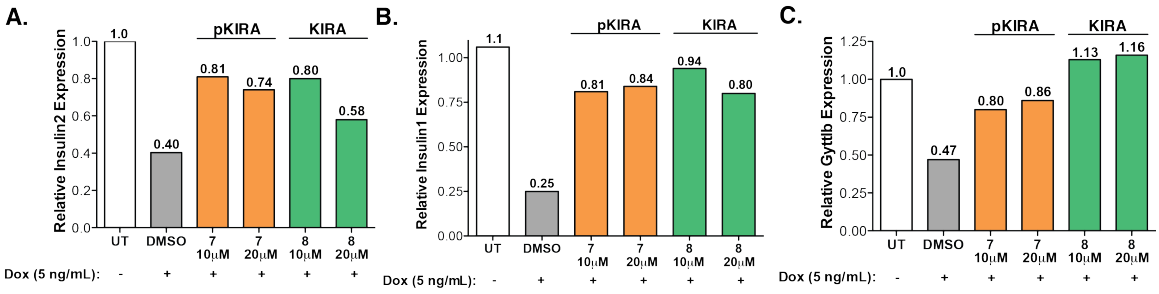

Figure 2.9 pKIRA and KIRAs block RIDD outputs in cells
qPCR of relative mRNAs from isogenic INS-1-IRE1α ± 10 and 20 μM of **7** and **8** followed by ± 5 ng/mL Dox for 24 hours. mRNA for four different targets were monitored. (A). Ins1 mRNA, (B). Ins2 mRNA, (C). Gyttlb mRNA

III. Conclusion

The role of IRE1α's RNase domain as a master regulator of cell fate decisions in cells experiencing ER stress has made it an attractive target for pharmacological modulation. Specifically, the inhibition of IRE1α has been shown to be a promising strategy for treatment of diseases of cell degeneration like type 1 and 2 diabetes, pulmonary fibrosis, and retinitis pigmentosa.[15,76,85,86] In the past, ATP-competitive inhibitors of IRE1α have not only emerged as attractive drug candidates, but have also been instrumental in the development of structural models of allostery between the kinase and RNase domains of IRE1α. These models have highlighted the importance of kinase active site conformation on IRE1α RNase activity through strengthening of the back-to-back dimer interface. This type of allosteric regulation through kinase active site conformation has been seen as a common mode of regulation for many other kinases.[45,58-60] Here, we sought to better characterize the allostery between the kinase and RNase by looking specifically at how αC-helix conformation affects IRE1α dimerization and thus RNase activity. Furthermore, we demonstrate that IRE1α αC-helix conformation can be rheostatic in nature, allowing for precise allosteric control over RNase functional outputs.

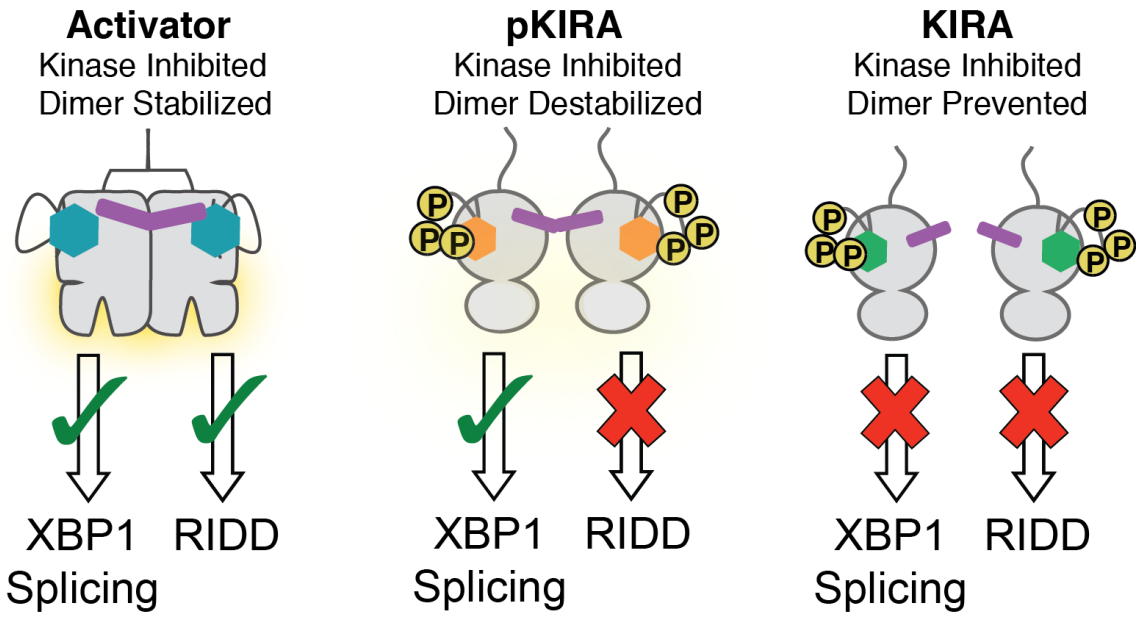

Figure 2.10 ATP-competitive inhibitors of IRE1α control RNase functional outputs through αC-helix conformation
Cartoon schematic summarizing the effect of different classes of ATP-competitive inhibitors on αC-helix conformation, IRE1α dimerization, XBP1-splicing, and RIDD outputs.

To demonstrate how kinase active site conformation can affect IRE1α dimerization we used two differentially phosphorylated IRE1α constructs – IRE1α* and dpIRE1α*. Phosphorylation state of IRE1α, and kinases in general, is known to cause conformational changes within their ATP-binding sites.[77,87] For IRE1α, the ability of its kinase to exert control over the RNase domain is reliant on αC-helix conformation.[31,56] Between IRE1α* and dpIRE1α* we see a ~30-fold change in IRE1α K_{DIMER} reflective of the change from an αC-helix in to αC-helix out conformation. We also looked at IRE1α dimerization using known inhibitors that stabilize either active (AT9283) or inactive (KIRA8) αC-helix conformations regardless of kinase phosphorylation state.[61-66] Treatment with AT9283 promoted

dpIRE1α* dimerization similar to that of IRE1α*, while KIRA8 treatment blocked the dimerization of IRE1α*.

Through an SAR of ATP-competitive inhibitors based on the pyrimidine-pyridine scaffold of KIRA8, we rationally varied substituents in a pocket proximal to the αC-helix within the kinase active site. For inhibitors in this SAR, we observed a close correlation between occupancy of the αC-helix pocket and IRE1α* K_{DIMER} values. Occupancy of the αC-helix pocket with small substituents stabilizes an αC-helix in conformation and promotes IRE1α dimerization, leading to RNase activation. Conversely, occupancy of this pocket by larger substituents that force an αC-helix out conformation due to steric bulk, prevent formation of IRE1α dimers and RNase activity. Interestingly, we show that inhibition of the RNase domain by ATP-competitive inhibitors seems to be rheostatic, where inhibitors with intermediate-sized substituents lack the ability to fully inhibit RNase activity and only attenuate IRE1α dimerization.[15,55,78]

Previously, crystal structures have been valuable in correlating SARs to structural models of IRE1α allostery.[31,53-56] A co-crystal structure of a pKIRA (**7**) bound to IRE1α* was resolved to better understand how αC-helix conformation is affected by increasing substituent size within the αC-helix binding pocket, and how this in turn can affect the back-to-back dimer interface. In this structure we confirmed that pKIRAs are ATP-competitive and that they function by modulating the αC-helix. Rheostatic movement of the αC-helix was also confirmed when we

compared pKIRA bound IRE1α* to crystal structures of IRE1α in active (PDB: 5HGI) and inactive (PDB: 4U6R) conformations.[55,78] Due to pKIRAs attenuation of IRE1α* K_{DIMER} values we looked at how pKIRA binding might cause attenuated affinity between two IRE1α* protomers. Here we see that pKIRA binding causes the flexibility of a loop C-terminal to the αC-helix that contains residues necessary for back-to-back dimer formation. We thus proposed that pKIRAs ability to attenuate dimerization is by producing a mixed population of IRE1α, in which only of subset is capable of back-to-back dimer formation.

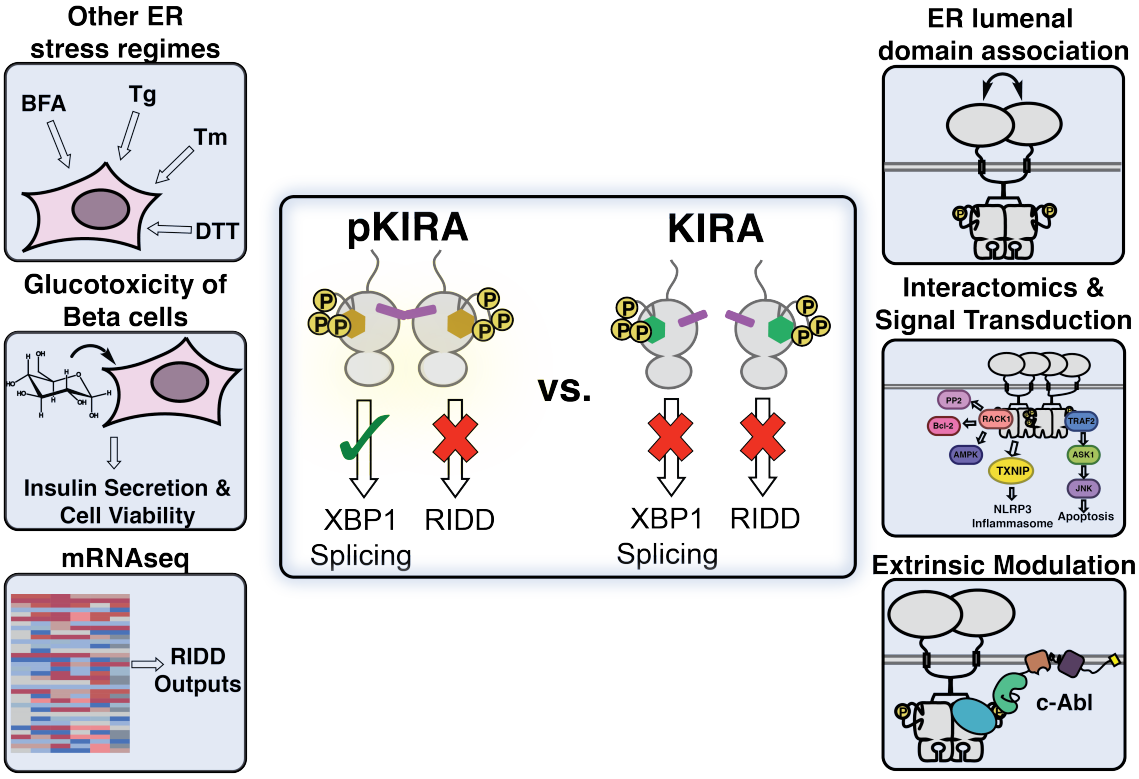

Figure 2.11 Benchmarking pKIRAs and KIRAs
Future work to determine how pKIRAs and KIRAs affect IRE1α regulation, signaling, and interaction networks under a myriad of different ER stress regimes.

Under ER stress, IRE1α is not limited to just dimer formation but has also been known to form high-order oligomers.[52,88-90] Previously, it has been suggested that

XBP1 splicing events are more sensitive to IRE1α dimerization, while RIDD outputs are more sensitive to high order oligomer formation.[13] To date, ATP-competitive inhibitors of IRE1α have been unable to uncouple RNase functional outputs, either promoting or inhibiting both XBP1 splicing and RIDD in tandem.[13,15,41,44,52,53,76,78] Interestingly, treatment of ER stressed cells with pKIRAs preserved XBP1 splicing functional outputs of IRE1α's RNase domain, but blocked RIDD outputs (**Figure 2.10**). We hypothesize that pKIRAs ability to divorce these two outputs stems directly from its affects on the IRE1α back-to-back dimer interface, which likely also influences the ability of IRE1α to form high-order oligomers. The ability of pKIRAs to distinguish the different functional outputs of IRE1α's RNase domain is an exciting result from both a therapeutic standpoint, but also for the future use of pKIRAs as biological tools. As tools, these pKIRAs provide a way to better understand how signal transduction from the ER or the IRE1α interactome changes when IRE1α is locked into a pro-survival regime. Additionally, we aim to benchmark pKIRAs against KIRAs by looking at how these two classes of inhibitors affect: IRE1α signaling under various ER stress regimes, RIDD targets, IRE1α lumenal domain association, and extrinsic modulation by scaffolding kinases, like the protein tyrosine kinase c-Abl (**Figure 2.11**). Therapeutically, we foresee the preservation of pro-survival outputs of IRE1α to be beneficial in the treatment of cell degenerative diseases that have already shown promising results with KIRAs.

III. Materials and Methods

A. Synthesis

General Information

Synthetic reagents are commercially available from the vendors listed below and were used without further purification. Proton and carbon NMR characterization was obtained using a Bruker AV-300 or 500 MHz instrument at room temperature. Chemical shifts are reported in ppm and coupling constants (J) are reported in Hz. Mass spectrometry on small molecules was preformed using a Bruker Esquire Ion Trap.

HPLC Preparatory Purification Conditions

Samples were suspended in methanol and injected onto a preparatory reverse-phase C18 column (250 x 21 mm) and separated using a Varian ProStar 210/325 HPLC instrument using a Methanol + 0.1% TFA: Water + 0.1% TFA solvent system from 1% Methanol + 0.1% TFA to 100% Methanol + 0.1% TFA over 60 minutes at a flow rate of 8 mL/min. Absorbance was detected via UV absorption at both 220 nm and 254 nm.

HPLC Analytical Conditions

Post preparatory purification, fractions were injected onto an analytical reverse phase C18 column and separated using a Varian Pro-Star 210 HPLC instrument over 30 minutes at 1 mL/min (Acetonitrile/Water-0.05% TFA gradient 1%-100% B Phase). Purity of products was determined using UV absorption at 254 nm and

220 nm. Purity was determined by integrating the product peak and calculating its purity as a percentage of background subtracted total area.

Reagent List

Table S2.1

Reagent	CAS#	Vendor	Product Number
4-Amino-1-naphthol	2834-90-4	Sigma	S57836
5-Amino-1-naphthol	83-55-6	Sigma	376469
4-amino-3-fluorophenol	399-95-1	Sigma	MAT047026697
N-Boc-trans-1,4-cyclohexanediamine	177906-48-8	Sigma	CDS007815
Cyclobutanesulfonyl chloride	338453-16-0	Sigma	ENA457508270
3,3,3-Trifluoropropane-1-sulfonyl chloride	845866-80-0	Sigma	680117
2,2,2-Trifluoroethanesulfonyl chloride	1648-99-3	Sigma	324787
Cyclopropanesulfonyl chloride	139631-62-2	Sigma	640573
Cyclopropyl isocyanate	4747-72-2	Sigma	ENA296274989
2-chloro-4-(2-fluoro-3-pyridinyl) pyrimidine	954216-54-7	Asta Tech	77359
(S)-tert-Butyl 3-((4-(2-fluoropyridin-3-yl)pyrimidin-2-yl)amino)piperidine-1-carboxylate	1630086-25-7	Sigma	COM497521364

Table S2.1 List of synthetic reagents
Reagent names, CAS numbers, vendors, and product numbers of synthetic materials used in the synthesis of intermediates and final compounds.

Synthesis and Characterization of Intermediates

Compound A

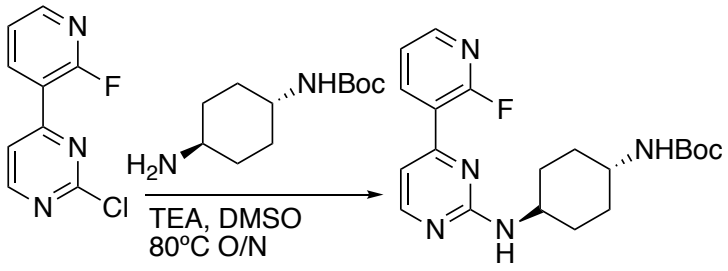

a

tert-butyl(1s,4s)-4-(4-(2-fluoropyridin-3-yl)pyrimidin-2-ylamino)

cyclohexylcarbamate*:* 2-chloro-4-(2-fluoro-3-pyridinyl)pyrimidine (1 mmol, 1 eq.,

CAS#: 954216-54-7) was added to N-Boc-trans-1,4-cyclohexanediamine (1mmol, 1 eq., CAS #: 177906-48-8) with triethylamine (1.5 mmol, 1.5 eq.) in 2 mL DMSO. Reaction was heated to 80ºC and stirred for 4 hours. After the 4 hours, the reaction was cooled to room temperature and diluted with 30 mL EtOAc. The diluted reaction mixture was then washed with 25 mL of water, followed by 25 mL of brine. After extraction the organic layer was dried over Na_2SO_4 and concentration via vacuum. The crude material was purified by column chromatography using a 0-20% EtOAc in hexanes over 60 minutes. ^{1}H NMR (500 MHz, $CDCl_3$) δ 8.50 (d, J = 7.7 Hz, 1H), 8.30 (d, J = 3.9 Hz, 1H), 8.22 (s, 1H), 7.27 (s, 1H), 7.06 (s, 1H), 5.05 – 4.96 (m, 1H), 4.42 – 4.30 (m, 1H), 3.83 – 3.72 (m, 1H), 2.12 (d, J = 10.1 Hz, 2H), 2.02 (t, J = 12.0 Hz, 2H), 1.38 (s, 9H), 1.32 – 1.18 (m, 5H). Exact Mass: 387.21, $[M+H]^+$ detected: 388.8 m/z.

Compound B

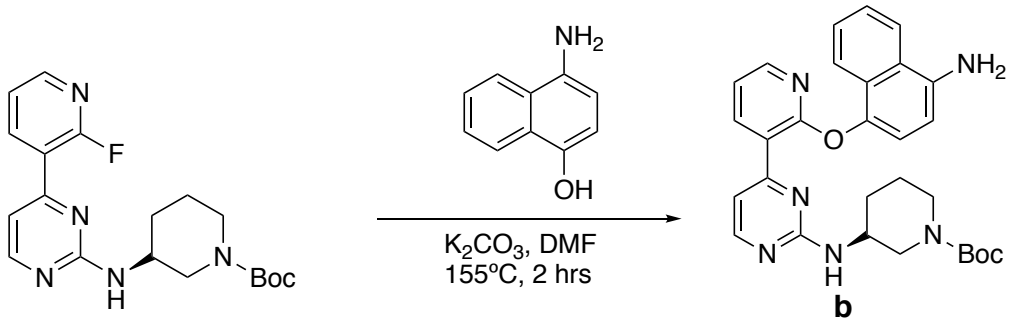

(3R)-tert-butyl 3-(4-(2-(4-aminonaphthalen-1-yloxy)pyridin-3-yl)pyrimidin-2-ylamino)piperidine-1-carboxylate: (S)-tert-Butyl 3-((4-(2-fluoropyridin-3-yl) pyrimidin-2-yl)amino)piperidine-1-carboxylate (1 mmol, 1 eq., CAS#: 1630086-25-7) was added to K_2CO_3 (1.5 mmol, 1.5 eq.) in 5 mL DMF in a microwave reaction vial and purged with N_2 for 5 minutes. 4-amino-naphthalen-1-ol (1 mmol,

1 eq., CAS #: 2834-90-4) was added to the reaction mixture and purged for another 3 minutes with N_2. The reaction vessel was then capped and microirradiated at 155ºC for 2 hours. After 2 hours, the reaction mixture was diluted with EtOAc and extracted with water followed by a brine solution. The organic layer was isolated and dried over Na_2SO_4 and concentration via vacuum. The crude material was purified by column chromatography using a 0-75% EtOAc in hexanes over 60 minutes. ^{1}H NMR (500 MHz, $CDCl_3$) δ 8.29 (d, *J* = 3.4 Hz, 1H), 8.09 – 8.02 (m, 1H), 7.80 (d, *J* = 8.5 Hz, 1H), 7.75 (d, *J* = 8.7 Hz, 1H), 7.59 (s, 1H), 7.42 (t, *J* = 7.4 Hz, 1H), 7.35 (t, *J* = 7.7 Hz, 1H), 7.20 (s, 2H), 7.03 (d, *J* = 6.9 Hz, 2H), 6.75 (d, *J* = 7.8 Hz, 1H), 4.11 – 4.00 (m, 2H), 3.58 – 3.45 (m, 1H), 1.97 (d, *J* = 15.4 Hz, 1H), 1.74 (dd, *J* = 13.3, 7.9 Hz, 1H), 1.62 – 1.49 (m, 7H), 1.35 (s, 9H). Exact Mass: 512.25, $[M+H]^+$ detected: 513.8 m/z.

Compound C

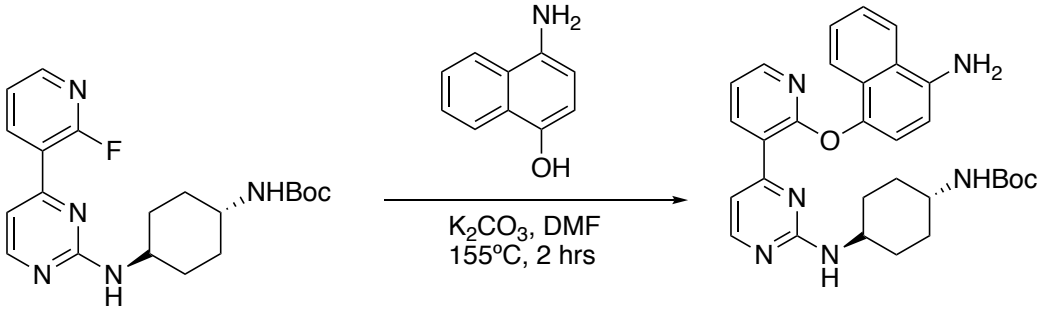

a **c**

tert-butyl (1s,4s)-4-(4-(2-(4-aminonaphthalen-1-yloxy)pyridin-3-yl)pyrimidin-2-ylamino)cyclohexylcarbamate: tert-butyl (1s,4s)-4-(4-(2-fluoropyridin-3-yl)pyrimidin-2-ylamino)cyclohexylcarbamate (1 mmol, 1 eq.) was added to K_2CO_3 (1.5 mmol, 1.5 eq.) in 5 mL DMF in a microwave reaction vial and purged with N_2 for 5 minutes. 4-amino-naphthalen-1-ol (1 mmol, 1eq., CAS #: 2834-90-4) was

added to the reaction mixture and purged for another 3 minutes with N_2. The reaction vessel was then capped and microirradiated at 155ºC for 2 hours. After 2 hours, the reaction mixture was diluted with EtOAc and extracted with water followed by a brine solution. The organic layer was isolated and dried over Na_2SO_4 and concentration via vacuum. The crude material was purified by column chromatography using a 0-75% EtOAc in hexanes over 60 minutes. ^{1}H NMR (500 MHz, CDCl3) δ 8.49 (d, J = 6.9 Hz, 1H), 8.33 (d, J = 4.5 Hz, 1H), 8.11 (d, J = 4.4 Hz, 1H), 7.84 (dd, J = 17.3, 8.4 Hz, 2H), 7.58 (d, J = 5.1 Hz, 1H), 7.47 (t, J = 7.6 Hz, 1H), 7.41 (t, J = 7.5 Hz, 1H), 7.08 (d, J = 7.6 Hz, 2H), 6.79 (d, J = 7.9 Hz, 1H), 4.43 (s, 1H), 3.90 (s, 1H), 3.49 (s, 1H), 2.21 (s, 2H), 2.07 (d, J = 9.0 Hz, 2H), 1.46 (s, 9H), 1.39 – 1.28 (m, 4H). Exact Mass: 526.27, $[M+H]^+$ detected: 527.5 m/z.

Compound D

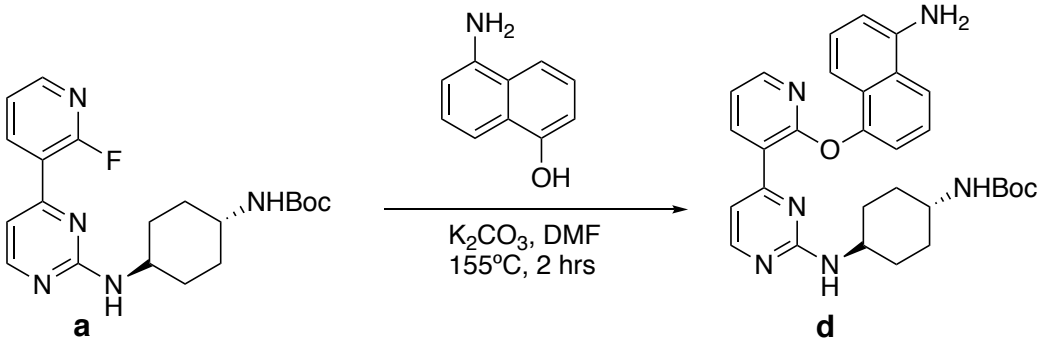

a **d**

tert-butyl (1s,4s)-4-(4-(2-(5-aminonaphthalen-1-yloxy)pyridin-3-yl)pyrimidin-2-ylamino)cyclohexylcarbamate*:* tert-butyl (1s,4s)-4-(4-(2-fluoropyridin-3-yl)pyrimidin-2-ylamino)cyclohexylcarbamate (1 mmol, 1 eq.) was added to K_2CO_3 (1.5 mmol, 1.5 eq.) in 5 mL DMF in a microwave reaction vial and purged with N_2 for 5 minutes. 5-amino-naphthalen-1-ol (1 mmol, 1 eq., CAS #: 83-55-6) was

added to the reaction mixture and purged for another 3 minutes with N_2. The reaction vessel was then capped and microirradiated at 155ºC for 2 hours. After 2 hours, the reaction mixture was diluted with EtOAc and extracted with water followed by a brine solution. The organic layer was isolated and dried over Na_2SO_4 and concentration via vacuum. The crude material was purified by column chromatography using a 0-75% EtOAc in hexanes over 60 minutes. ^{1}H NMR (500 MHz, MeOD) δ 8.42 (d, *J* = 4.7 Hz, 1H), 8.20 (d, *J* = 4.7 Hz, 1H), 8.02 (d, *J* = 4.4 Hz, 1H), 7.72 (s, 1H), 7.48 – 7.37 (m, 2H), 7.29 (d, *J* = 8.3 Hz, 1H), 7.17 (t, *J* = 7.9 Hz, 1H), 7.16 – 7.05 (m, 2H), 6.77 (d, *J* = 7.1 Hz, 1H), 3.77 (s, 1H), 3.35 (s, 1H), 2.11 (d, *J* = 11.9 Hz, 2H), 1.97 (d, *J* = 11.8 Hz, 2H), 1.38 (s, 10H), 1.36 – 1.15 (m, 5H). Exact Mass: 526.27, $[M+H]^+$ detected: 527.6 m/z.

Compound E

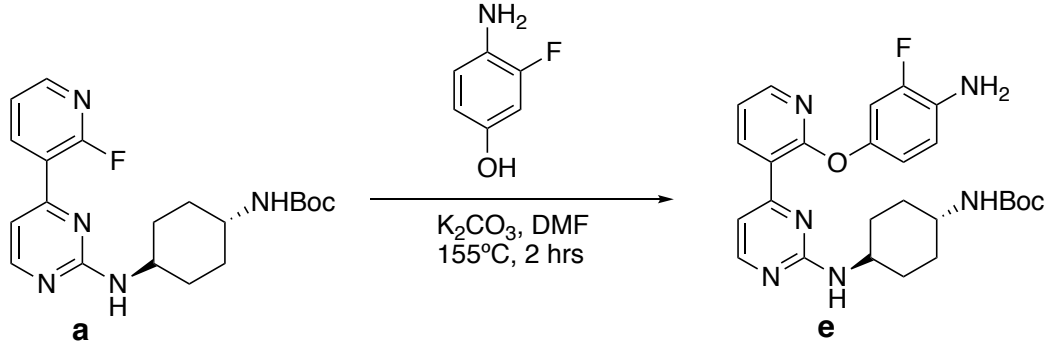

a **e**

tert-butyl (1s,4s)-4-(4-(2-(4-amino-3-fluorophenoxy)pyridin-3-yl)pyrimidin-2-ylamino)cyclohexylcarbamate*:* tert-butyl (1s,4s)-4-(4-(2-fluoropyridin-3-yl)pyrimidin-2-ylamino)cyclohexylcarbamate (1 mmol, 1eq.) was added to K_2CO_3 (1.5 mmol, 1.5 eq.) in 5 mL DMF in a microwave reaction vial and purged with N_2 for 5 minutes. 4-amino-3-fluorophenol (1 mmol, 1eq., CAS #: 399-95-1) was added to the reaction mixture and purged for another 3 minutes with N_2. The

reaction vessel was then capped and microirradiated at 155ºC for 2 hours. After 2 hours, the reaction mixture was diluted with EtOAc and extracted with water followed by a brine solution. The organic layer was isolated and dried over Na_2SO_4 and concentration via vacuum. The crude material was purified by column chromatography using a 0-75% EtOAc in hexanes over 60 minutes. ^{1}H NMR (500 MHz, $CDCl_3$) δ 8.76 (d, J = 6.9 Hz, 1H), 8.68 (d, J = 4.5 Hz, 1H), 8.56 (s, 1H), 7.70 (d, J = 4.8 Hz, 1H), 7.47 (d, J = 5.4 Hz, 1H), 7.27 – 7.06 (m, 3H), 4.78 (s, 1H), 4.22 (s, 1H), 3.84 (s, 1H), 2.56 (d, J = 11.3 Hz, 2H), 2.43 (d, J = 10.2 Hz, 2H), 1.81 (s, 9H), 1.67 (dt, J = 26.6, 13.3 Hz, 5H). Exact Mass: 494.24, $[M+H]^+$ detected: 495.2 m/z.

Synthesis and Characterization of Final Compounds

Compound **1**

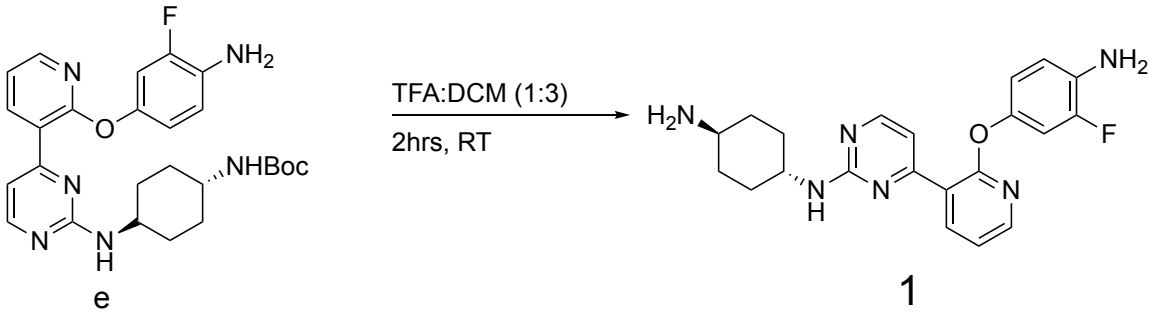

e 1

(1r,4r)-N1-(4-(2-(4-amino-3-fluorophenoxy)pyridin-3-yl)pyrimidin-2-yl) cyclohexane-1,4-diamine: tert-butyl (1s,4s)-4-(4-(2-(4-amino-3-fluorophenoxy) pyridin-3-yl)pyrimidin-2-ylamino)cyclohexylcarbamate (0.08 mmol, 1 eq.) was diluted into 1 mL TFA:DCM (1:3) and stirred at room temperature for 2 hours. The solvent was removed *in vacuo* and crude reaction mixture was re-suspended in MeOH for further purification using HPLC in a methanol and water solvent

system. ^{1}H NMR (700 MHz, MeOD) δ 8.51 (d, *J* = 7.0 Hz, 1H), 8.35 (s, 1H), 8.25 (d, *J* = 3.1 Hz, 1H), 7.51 (s, 1H), 7.30 (dd, *J* = 7.6, 4.8 Hz, 1H), 7.11 – 7.05 (m, 1H), 7.00 (dd, *J* = 11.5, 2.5 Hz, 1H), 6.88 (ddd, *J* = 8.7, 2.5, 1.1 Hz, 1H), 3.99 (s, 1H), 3.33 (s, 1H), 3.21 – 3.15 (m, 1H), 2.25 (d, *J* = 11.9 Hz, 2H), 2.14 (d, *J* = 12.2 Hz, 2H), 1.63 – 1.51 (m, 4H). ^{13}C NMR (176 MHz, MeOD) δ 161.52, 161.31, 161.07, 153.30, 151.93, 149.53, 147.15, 140.74, 120.92, 119.28, 119.04, 117.42, 109.79, 109.42, 109.30, 49.21, 48.98, 29.69, 29.09. Exact Mass: 394.19, $[M+H]^{+}$ detected: 395.3 m/z. Retention Time: 10.7 minutes Purity: >99%

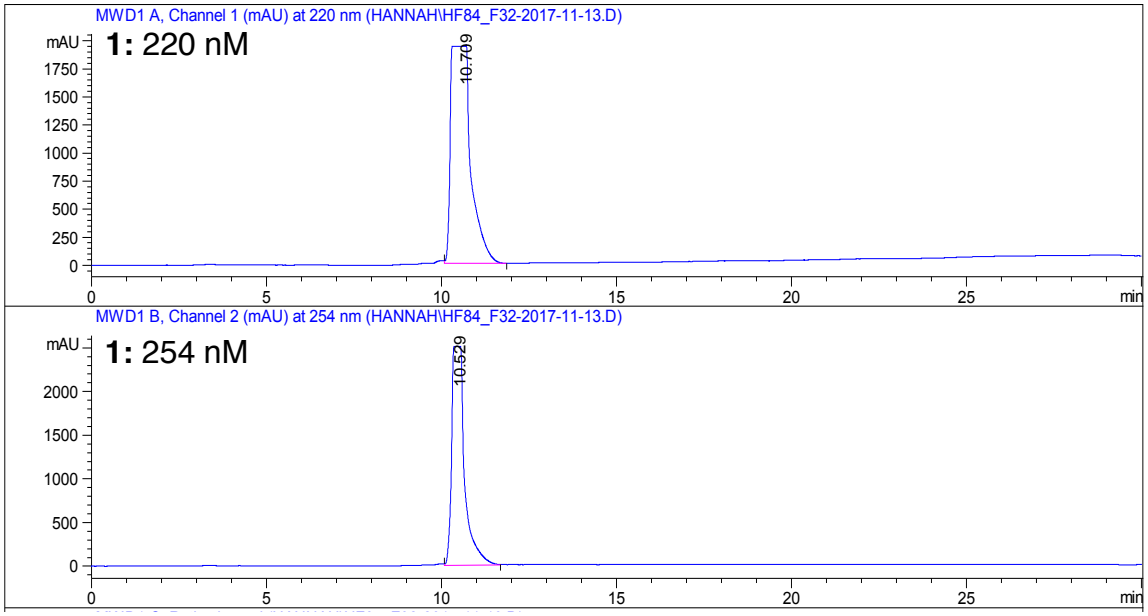

Compound **2**

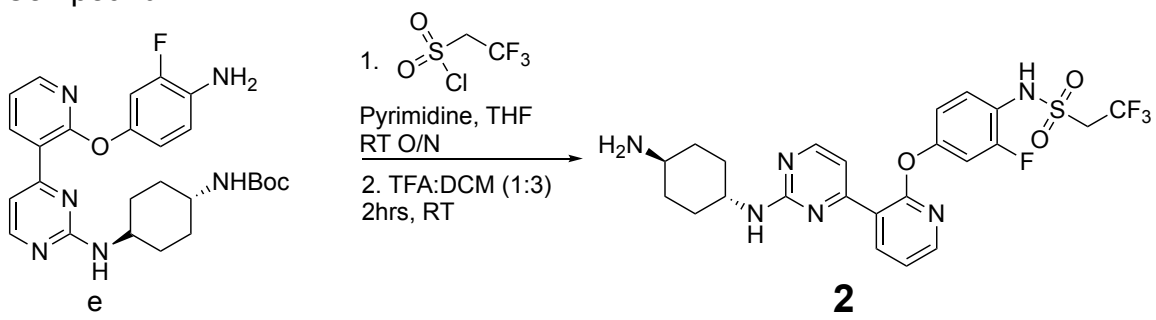

N-(4-(3-(2-((1r,4r)-4-aminocyclohexylamino)pyrimidin-4-yl)pyridin-2-yloxy)-2-fluorophenyl)-2,2,2-trifluoroethanesulfonamide: tert-butyl (1s,4s)-4-(4-(2-(4-amino-3-fluorophenoxy)pyridin-3-yl)pyrimidin-2-ylamino)cyclohexylcarbamate (0.04 mmol, 1 eq.) was dissolved in 1 mL THF and stirred for 1 minute before addition of pyridine (0.12 mmol, 3 eq.). The reaction mixture was stirred another 5 minutes before the dropwise addition of 2,2,2-Trifluoroethanesulfonyl chloride (0.06 mmol, 1.5 eq., CAS #: 1648-99-3). The reaction was then stirred at room temperature overnight. The reaction mixture was then concentrated *in vacuo* and purified via flash chromatography (0-50% EtOAc in hexanes). The product was then diluted into 1 mL TFA:DCM (1:3) and stirred at room temperature for 2 hours. The solvent was removed *in vacuo* and crude reaction mixture was re-suspended in MeOH for further purification using HPLC in a methanol and water solvent system. ^{1}H NMR (700 MHz, MeOD) δ 8.53 (d, *J* = 7.2 Hz, 2H), 8.36 (d, *J* = 5.9 Hz, 2H), 8.28 (d, *J* = 3.1 Hz, 2H), 7.56 (t, *J* = 8.8 Hz, 2H), 7.49 (s, 2H), 7.35 (dd, *J* = 7.5, 4.9 Hz, 2H), 7.16 (dd, *J* = 10.9, 2.5 Hz, 2H), 7.04 (dd, *J* = 8.8, 1.6 Hz, 2H), 4.22 (q, *J* = 9.4 Hz, 4H), 3.99 (s, 2H), 3.33 (dd, *J* = 3.3, 1.6 Hz, 3H), 3.18 (dd, *J* = 13.3, 9.5 Hz, 2H), 2.25 (d, *J* = 11.3 Hz, 4H), 2.14 (d, *J* = 11.9 Hz, 4H), 1.67 – 1.47 (m, 8H). ^{13}C NMR (176 MHz, MeOD) δ 161.19, 160.99, 160.53, 157.07, 155.66, 152.52, 149.53, 140.95, 127.46, 121.27, 120.72, 119.80, 117.52, 117.25, 115.59, 109.83, 109.73, 53.26, 53.09, 49.22, 48.99, 29.68, 29.10. Exact Mass: 540.16, $[M+H]^+$ detected: 541.3 m/z. Retention Time: 12.2 minutes Purity: >99%

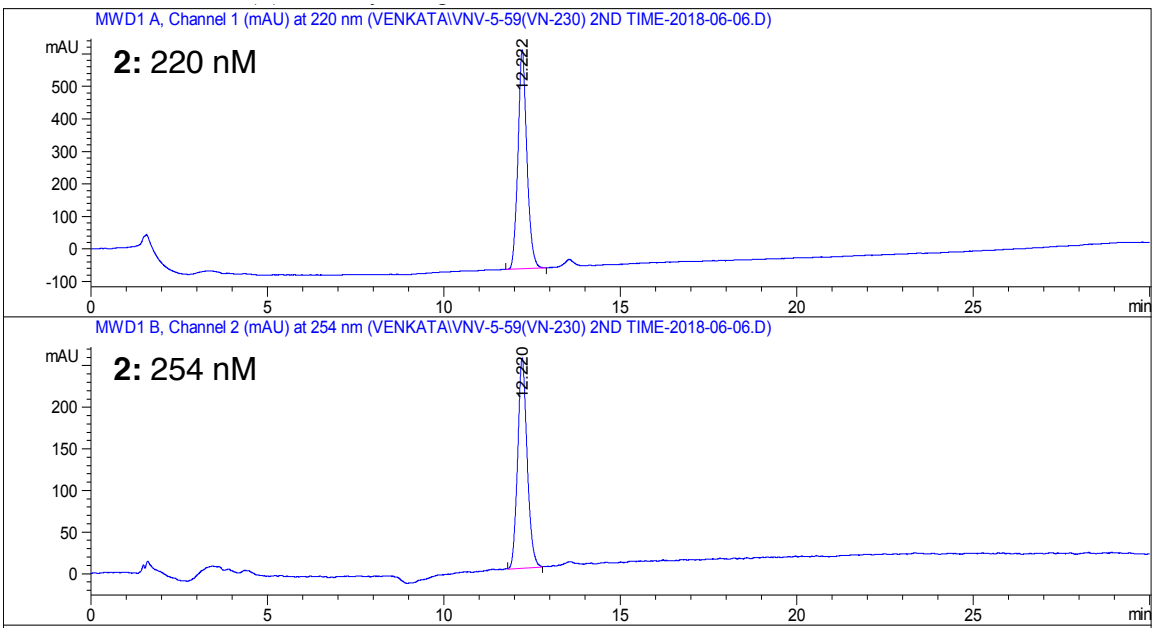

Compound **3**

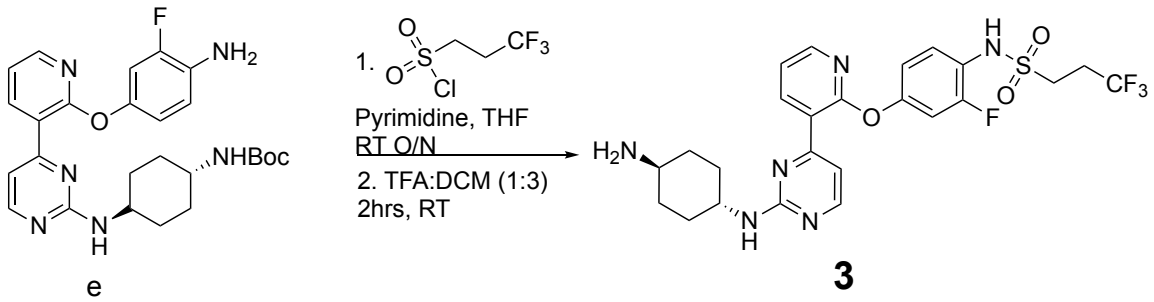

N-(4-(3-(2-((1r,4r)-4-aminocyclohexylamino)pyrimidin-4-yl)pyridin-2-yloxy)-2-fluorophenyl)-3,3,3-trifluoropropane-1-sulfonamide: : tert-butyl (1s,4s)-4-(4-(2-(4-amino-3-fluorophenoxy)pyridin-3-yl)pyrimidin-2-ylamino) cyclohexylcarbamate (0.03 mmol, 1 eq.) was dissolved in 1 mL THF and stirred for 1 minute before addition of pyridine (0.09 mmol, 3 eq.). The reaction mixture was stirred another 5 minutes before the dropwise addition of 3,3,3-Trifluoropropane-1-sulfonyl chloride (0.045 mmol, 1.5 eq., CAS #: 845866-80-0). The reaction was then stirred at room temperature overnight. The reaction

mixture was concentrated *in vacuo* and purified via flash chromatography (0-50% EtOAc in hexanes). The product was then diluted into 1 mL TFA:DCM (1:3) and stirred at room temperature for 2 hours. The solvent was removed *in vacuo* and crude reaction mixture was re-suspended in MeOH for further purification using HPLC in a methanol and water solvent system. ^{1}H NMR (500 MHz, MeOD) δ 8.30 (d, *J* = 7.4 Hz, 1H), 8.21 (d, *J* = 4.9 Hz, 1H), 8.16 (d, *J* = 4.6 Hz, 1H), 7.44 (t, *J* = 8.8 Hz, 1H), 7.22 – 7.14 (m, 1H), 7.11 (d, *J* = 5.2 Hz, 1H), 6.88 (dd, *J* = 21.2, 9.9 Hz, 2H), 3.70 (s, 1H), 3.28 (s, 1H), 3.23 – 3.18 (m, 2H), 2.77 – 2.58 (m, 3H), 2.06 (d, *J* = 9.4 Hz, 2H), 1.85 (d, *J* = 9.6 Hz, 2H), 1.28 – 1.17 (m, 5H). ^{13}C NMR (126 MHz, MeOD) δ 150.83, 142.23, 132.96, 130.63, 129.52, 128.42, 126.23, 125.39, 124.48, 123.39, Exact Mass: 554.17. $[M+H]^{+}$ detected: 555.6 m/z. Retention Time: 12.7 minutes Purity: >99%

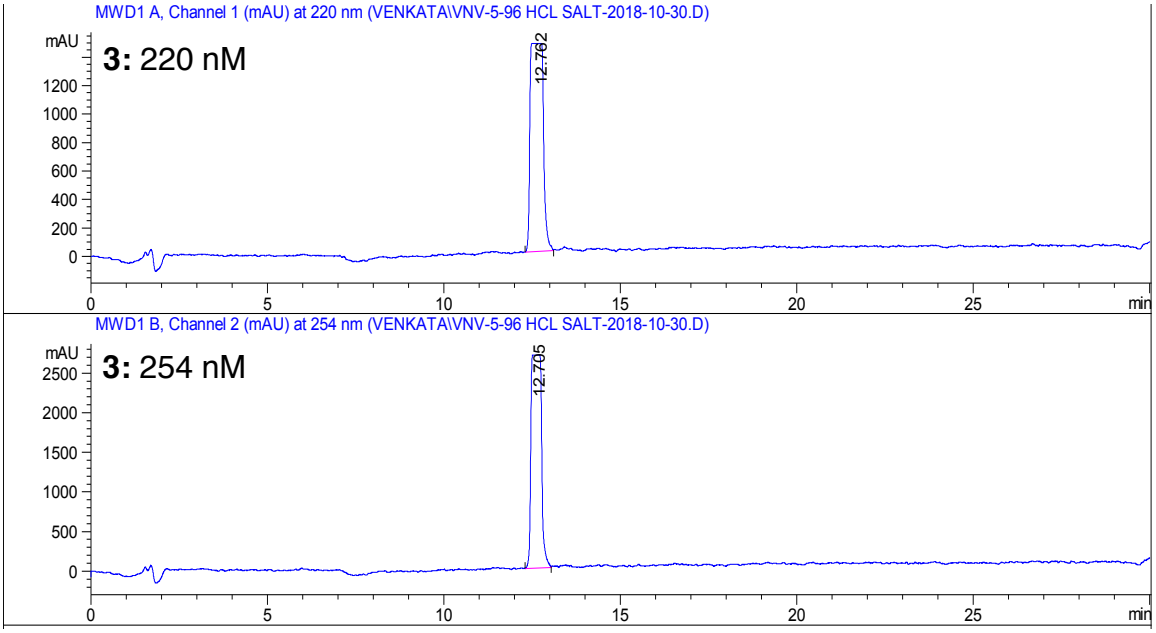

Compound **4**

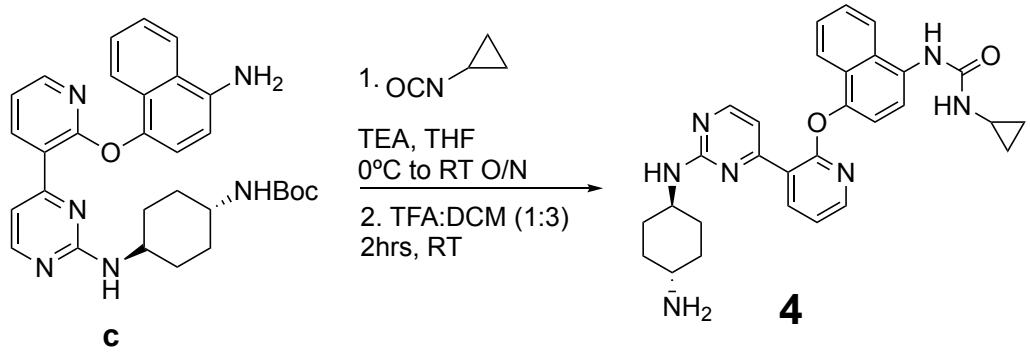

c **4**

1-(4-(3-(2-((1r,4r)-4-aminocyclohexylamino)pyrimidin-4-yl)pyridin-2-yloxy) naphthalen-1-yl)-3-cyclopropylurea: tert-butyl (1s,4s)-4-(4-(2-(4-aminonaphthalen-1-yloxy)pyridin-3-yl)pyrimidin-2-ylamino)cyclohexylcarbamate (0.03 mmol, 1 eq.) was dissolved in 1 mL THF and stirred for 1 minute at 0ºC before addition of triethylamine (0.09 mmol, 3 eq.). The reaction mixture was stirred another 5 minutes before the dropwise addition of cyclopropyl isocyanate (0.06 mmol, 2.0 eq., CAS #: 4747-72-2). The reaction was then brought to room temperature and stirred overnight. The reaction mixture was concentrated *in vacuo* and purified via flash chromatography (0-50% EtOAc in hexanes). The product was then diluted into 1 mL TFA:DCM (1:3) and stirred at room temperature for 2 hours. The solvent was removed *in vacuo* and crude reaction mixture was re-suspended in MeOH for further purification using HPLC in a methanol and water solvent system. ^{1}H NMR (500 MHz, MeOD) δ 8.34 (d, *J* = 6.0 Hz, 1H), 8.18 (d, *J* = 5.7 Hz, 1H), 7.99 (s, 1H), 7.88 (d, *J* = 8.5 Hz, 1H), 7.75 (d, *J* = 7.9 Hz, 1H), 7.49 – 7.34 (m, 3H), 7.31 (t, *J* = 7.6 Hz, 1H), 7.18 – 7.10 (m, 1H), 7.04 (d, *J* = 8.1 Hz, 1H), 3.65 (t, *J* = 11.0 Hz, 1H), 3.14 (d, *J* = 0.8 Hz, 1H), 2.86 (s, 1H), 2.52 – 2.45 (m, 1H), 1.93 (s, 2H), 1.77 (d, *J* = 6.6 Hz, 2H), 1.19 (dd,

J = 56.5, 15.7 Hz, 4H), 0.60 (d, *J* = 5.7 Hz, 2H), 0.41 (s, 2H). ^{13}C NMR (126 MHz, MeOD) δ 164.87, 162.74, 160.72, 150.29, 142.01, 132.19, 131.89, 129.06, 127.79, 127.42, 123.73, 123.28, 120.88, 119.31, 111.02, 50.81, 49.98, 31.27, 30.46, 23.56, 7.31. Exact Mass: 509.25. $[M+H]^+$ detected: 510.6 m/z. Retention Time: 11.9 minutes Purity: >99%

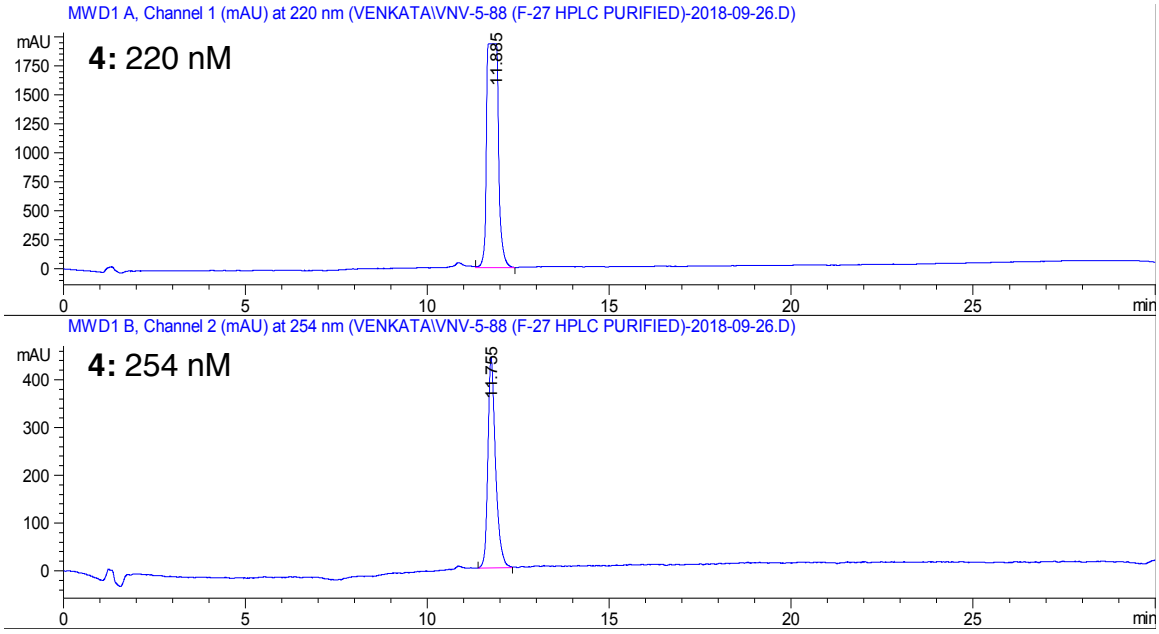

Compound **5**

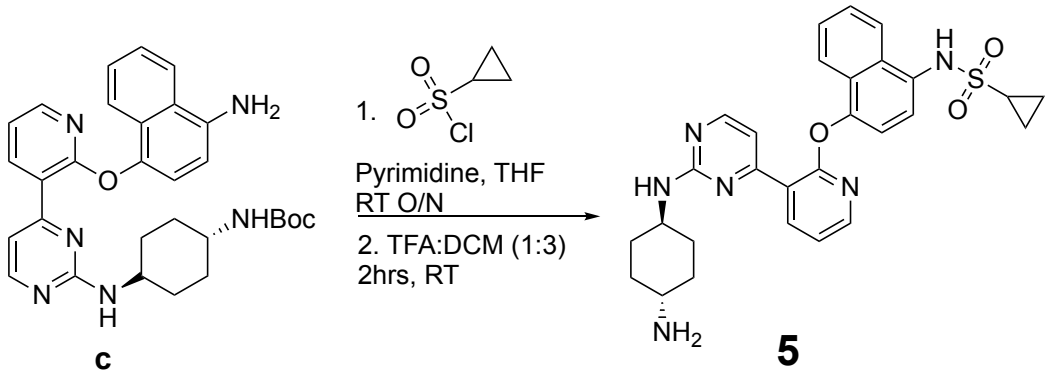

c **5**

N-(4-(3-(2-((1r,4r)-4-aminocyclohexylamino)pyrimidin-4-yl)pyridin-2-yloxy)naphthalen-1-yl)cyclopropanesulfonamide: tert-butyl (1s,4s)-4-(4-(2-(4-aminonaphthalen-1-yloxy)pyridin-3-yl)pyrimidin-2-ylamino)cyclohexylcarbamate

(0.1 mmol, 1 eq.) was dissolved in 1 mL THF and stirred for 1 minute before addition of pyridine (0.3 mmol, 3 eq.). The reaction mixture was stirred another 5 minutes before the dropwise addition of cyclopropanesulfonyl chloride (0.15 mmol, 1.5 eq., CAS #: 139631-62-2). The reaction was then stirred at room temperature overnight. The reaction mixture was concentrated *in vacuo* and purified via flash chromatography (0-50% EtOAc in hexanes). The product was then diluted into 1.5 mL TFA:DCM (1:3) and stirred at room temperature for 2 hours. The solvent was removed *in vacuo* and crude reaction mixture was re-suspended in MeOH for further purification using HPLC in a methanol and water solvent system. ^{1}H NMR (300 MHz, MeOD) δ 8.41 (d, *J* = 6.9 Hz, 1H), 8.23 (dd, *J* = 12.3, 6.9 Hz, 2H), 8.08 – 8.00 (m, 1H), 7.89 (d, *J* = 8.3 Hz, 1H), 7.54 (dd, *J* = 12.1, 8.0 Hz, 2H), 7.45 – 7.32 (m, 3H), 7.17 – 7.09 (m, 2H), 5.25 (s, 1H), 3.85 – 3.70 (m, 1H), 3.31 (s, 2H), 3.28 (s, 1H), 2.71 (s, 1H), 2.50 – 2.38 (m, 1H), 2.10 (s, 2H), 1.89 (s, 2H), 1.26 (dd, *J* = 26.7, 16.7 Hz, 5H), 1.08 – 1.00 (m, 2H), 0.88 – 0.80 (m, 2H). 13C NMR (126 MHz, MeOD) δ 161.59, 149.72, 149.01, 141.04, 132.06, 130.10, 128.16, 126.88, 126.60, 124.82, 123.79, 121.93, 119.70, 116.75, 110.00, 49.54, 49.16, 29.99, 29.81, 29.37, 5.02. Exact Mass: 530.21. $[M+H]^{+}$ detected: 531.3 m/z. Retention Time: 12.6 minutes Purity: >99%

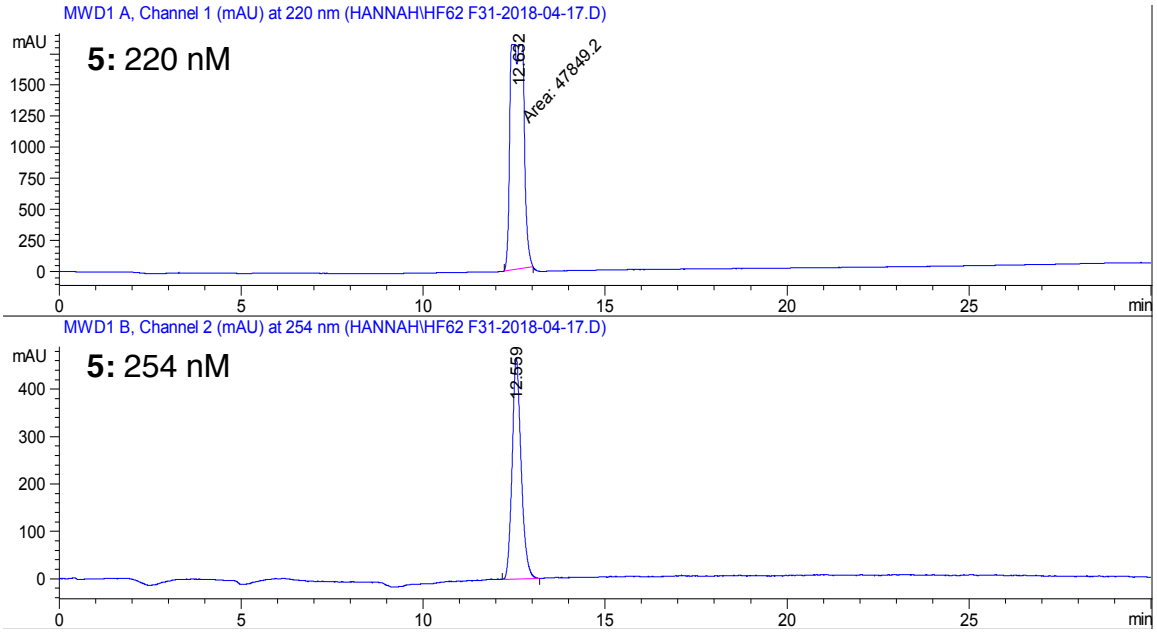

Compound **6**

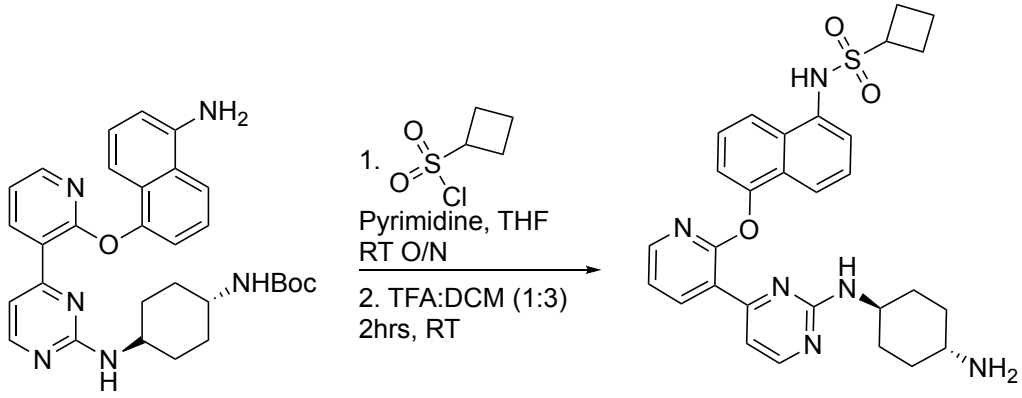

d **6**

N-(5-(3-(2-((1r,4r)-4-aminocyclohexylamino)pyrimidin-4-yl)pyridin-2-yloxy)naphthalen-1-yl) cyclobutanesulfonamide: tert-butyl (1s,4s)-4-(4-(2-(5-aminonaphthalen-1-yloxy) pyridin-3-yl)pyrimidin-2-ylamino)cyclohexylcarbamate (0.09 mmol, 1 eq.) was dissolved in 1 mL THF and stirred for 1 minute before addition of pyridine (0.27 mmol, 3 eq.). The reaction mixture was stirred another 5 minutes before the drop wise addition of cyclobutanesulfonyl chloride (0.14 mmol, 1.5 eq., CAS #: 338453-16-0). The reaction was then stirred at room

temperature overnight. The reaction mixture was concentrated *in vacuo* and purified via flash chromatography (0-50% EtOAc in hexanes). The product was then diluted into 1.5 mL TFA:DCM (1:3) and stirred at room temperature for 2 hours. The solvent was removed *in vacuo* and crude reaction mixture was re-suspended in MeOH for further purification using HPLC in a methanol and water solvent system. ^{1}H NMR (300 MHz, MeOD) δ 8.53 (dd, J = 7.9, 1.5 Hz, 1H), 8.35 (d, J = 5.3 Hz, 1H), 8.18 – 8.09 (m, 2H), 7.86 (d, J = 8.5 Hz, 1H), 7.66 – 7.57 (m, 2H), 7.46 (dd, J = 11.6, 6.5 Hz, 2H), 7.29 (t, J = 7.2 Hz, 2H), 3.95 (dt, J = 14.9, 7.5 Hz, 2H), 3.21 – 3.08 (m, 1H), 2.61 – 2.41 (m, 2H), 2.35 – 2.17 (m, 4H), 2.04 (dt, J = 17.5, 9.9 Hz, 4H), 1.51 (dd, J = 21.2, 10.7 Hz, 4H). ^{13}C NMR (126 MHz, MeOD) δ 163.02, 151.41, 151.16, 142.38, 134.47, 132.99, 129.91, 127.48, 127.24, 125.46, 121.83, 121.48, 120.92, 119.17, 111.26, 55.70, 50.78, 50.50, 31.24, 30.64, 25.15, 17.75. Exact Mass: 554.23. $[M+H]^{+}$ detected: 545.4 m/z. Retention Time: 11.8 minutes Purity: >99%

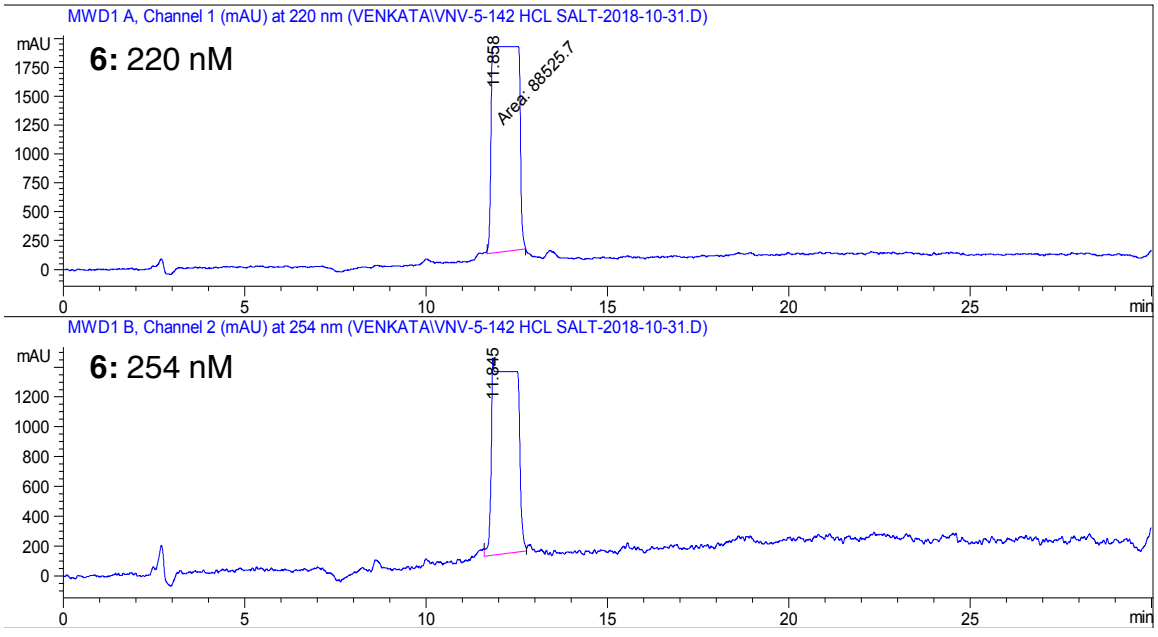

Compound **7**

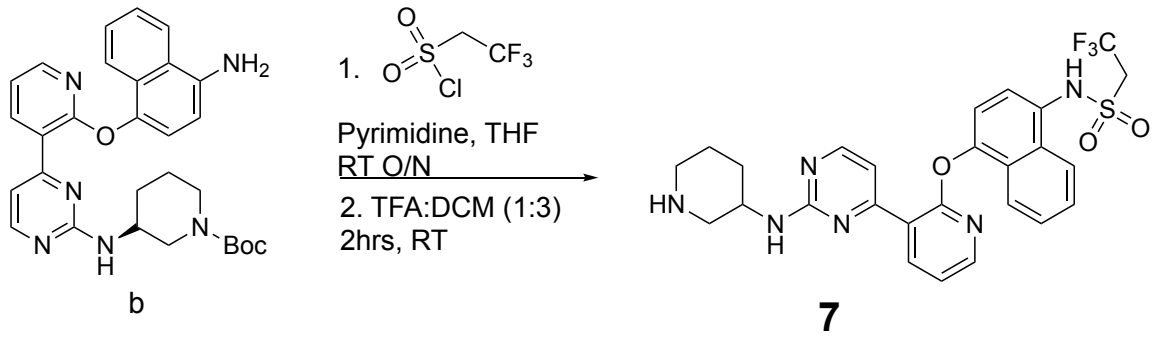

7

2,2,2-trifluoro-N-(4-(3-(2-(piperidin-3-ylamino)pyrimidin-4-yl)pyridin-2-yloxy)naphthalen-1-yl)ethanesulfonamide: (3R)-tert-butyl 3-(4-(2-(4-aminonaphthalen-1-yloxy)pyridin-3-yl)pyrimidin-2-ylamino)piperidine-1-carboxylate (0.03 mmol, 1 eq., CAS# 1630086-25-7) was dissolved in 1 mL THF and stirred for 1 minute before addition of pyridine (0.09 mmol, 3 eq.). The reaction mixture was stirred another 5 minutes before the drop wise addition of 2, 2,2-Trifluoroethanesulfonyl chloride (0.045 mmol, 1.5 eq., CAS #: 1648-99-3). The reaction was then stirred at room temperature overnight. The reaction mixture was then concentrated *in vacuo* and purified via flash chromatography (0-50% EtOAc in hexanes). The product was then diluted into 1 mL TFA:DCM (1:3) and stirred at room temperature for 2 hours. The solvent was removed *in vacuo* and crude reaction mixture was re-suspended in MeOH for further purification using HPLC in a methanol and water solvent system. ^{1}H NMR (500 MHz, MeOD) δ 8.53 (d, *J* = 7.1 Hz, 1H), 8.26 (s, 1H), 8.17 (d, *J* = 8.6 Hz, 1H), 8.03 (d, *J* = 4.2 Hz, 1H), 7.88 (d, *J* = 8.4 Hz, 1H), 7.60 – 7.49 (m, 3H), 7.44 (t, *J* = 7.6 Hz, 1H), 7.19 – 7.10 (m, 2H), 4.28 (s, 1H), 3.90 (q, *J* = 9.0 Hz, 2H), 3.48 (d, *J*

= 10.0 Hz, 1H), 3.31 (s, 1H), 3.20 (d, *J* = 12.7 Hz, 1H), 2.93 (dd, *J* = 20.1, 8.3 Hz, 2H), 2.06 (d, *J* = 12.5 Hz, 1H), 2.03 – 1.95 (m, 1H), 1.84 (dt, *J* = 14.2, 10.3 Hz, 1H), 1.67 (q, *J* = 9.7 Hz, 1H), 1.18 (s, 1H). ^{13}C NMR (126 MHz, MeOD) δ 163.07, 162.57, 159.83, 150.78, 149.87, 142.09, 133.02, 129.98, 129.51, 128.43, 127.98, 126.98, 125.60, 124.78, 124.59, 123.58, 123.26, 122.57, 120.94, 117.93, 112.40, 101.41, 49.56, 49.39, 49.22, 49.05, 48.88, 48.71, 48.54, 48.37, 46.60, 45.08, 29.28, 22.05. Exact Mass: 558.17. $[M+H]^+$ detected: 559.4 m/z. Retention Time: 13.6 minutes Purity: >99%

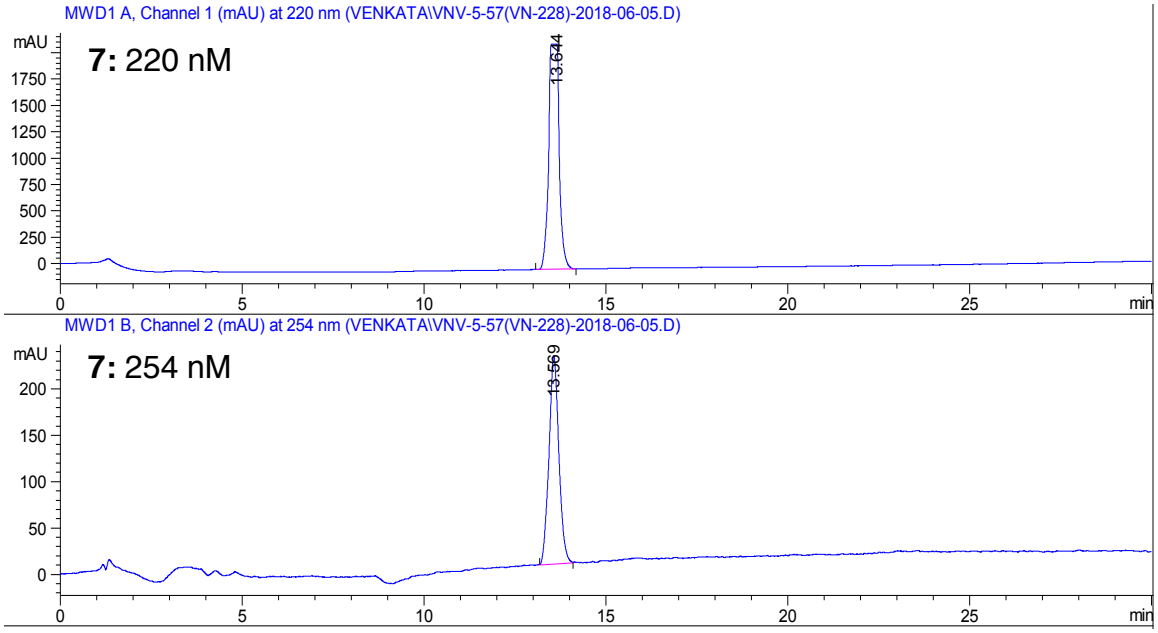

Compound **8**

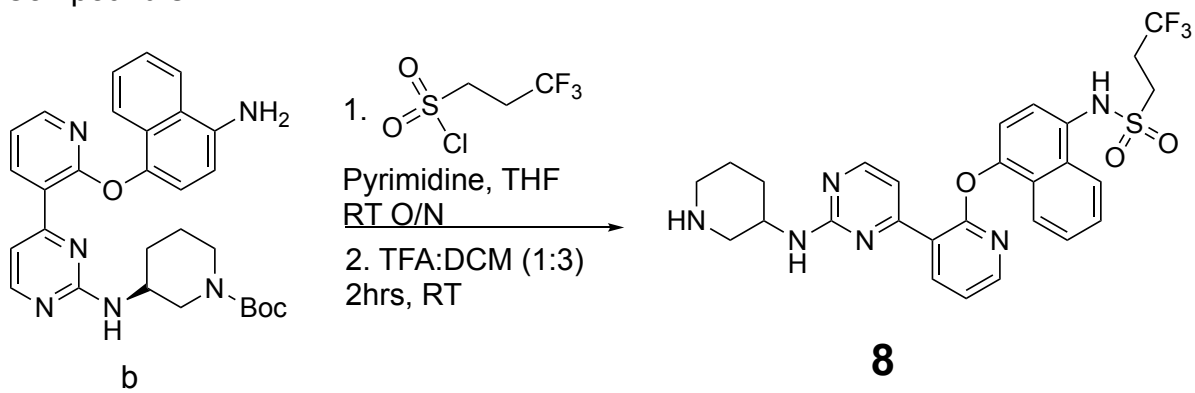

8

3,3,3-trifluoro-N-(4-(3-(2-(piperidin-3-ylamino)pyrimidin-4-yl)pyridin-2-yloxy)naphthalen-1-yl)propane-1-sulfonamide: (3R)-tert-butyl 3-(4-(2-(4-aminonaphthalen-1-yloxy)pyridin-3-yl)pyrimidin-2-ylamino)piperidine-1-carboxylate (0.03 mmol, 1 eq.) was dissolved in 1 mL THF and stirred for 1 minute before addition of pyridine (0.09 mmol, 3 eq., CAS# 1630086-25-7). The reaction mixture was stirred another 5 minutes before the drop wise addition of 3, 3,3-Trifluoropropane-1-sulfonyl chloride (0.045 mmol, 1.5 eq., CAS #: 845866-80-0). The reaction was then stirred at room temperature overnight. The reaction mixture was then concentrated *in vacuo* and purified via flash chromatography (0-50% EtOAc in hexanes). The product was then diluted into 1 mL TFA:DCM (1:3) and stirred at room temperature for 2 hours. The solvent was removed *in vacuo* and crude reaction mixture was re-suspended in MeOH for further purification using HPLC in a methanol and water solvent system. ^{1}H NMR (500 MHz, MeOD) δ 8.50 (d, *J* = 6.0 Hz, 2H), 8.23 (d, *J* = 5.2 Hz, 2H), 8.18 (t, *J* = 7.3 Hz, 2H), 8.03 (d, *J* = 3.6 Hz, 2H), 7.88 (t, *J* = 6.8 Hz, 2H), 7.59 – 7.49 (m, 4H), 7.45 (dd, *J* = 13.7, 6.5 Hz, 4H), 7.19 – 7.10 (m, 4H), 4.13 (s, 2H), 3.89 (q, *J* = 9.1 Hz, 1H), 3.39 – 3.32 (m, 2H), 3.27 (t, *J* = 8.1 Hz, 5H), 3.06 (d, *J* = 12.7 Hz, 2H), 2.83 – 2.69 (m, 4H), 2.69 – 2.57 (m, 3H), 2.05 (d, *J* = 12.3 Hz, 2H), 1.96 – 1.84 (m, 2H), 1.69 (dd, *J* = 13.6, 10.4 Hz, 2H), 1.60 (dd, *J* = 20.0, 9.8 Hz, 2H), 1.18 (s, 2H). ^{13}C NMR (126 MHz, MeOD) δ 162.53, 150.76, 150.02, 141.93, 132.99, 130.33, 129.50, 128.37, 127.91, 125.43, 124.42, 123.40, 120.89, 117.71, 111.37,

50.99, 50.07, 46.46, 31.44, 30.74, 30.12, 29.83. Exact Mass: 572.18. $[M+H]^+$ detected: 573.3 m/z. Retention Time: 14.6 minutes Purity: >99%

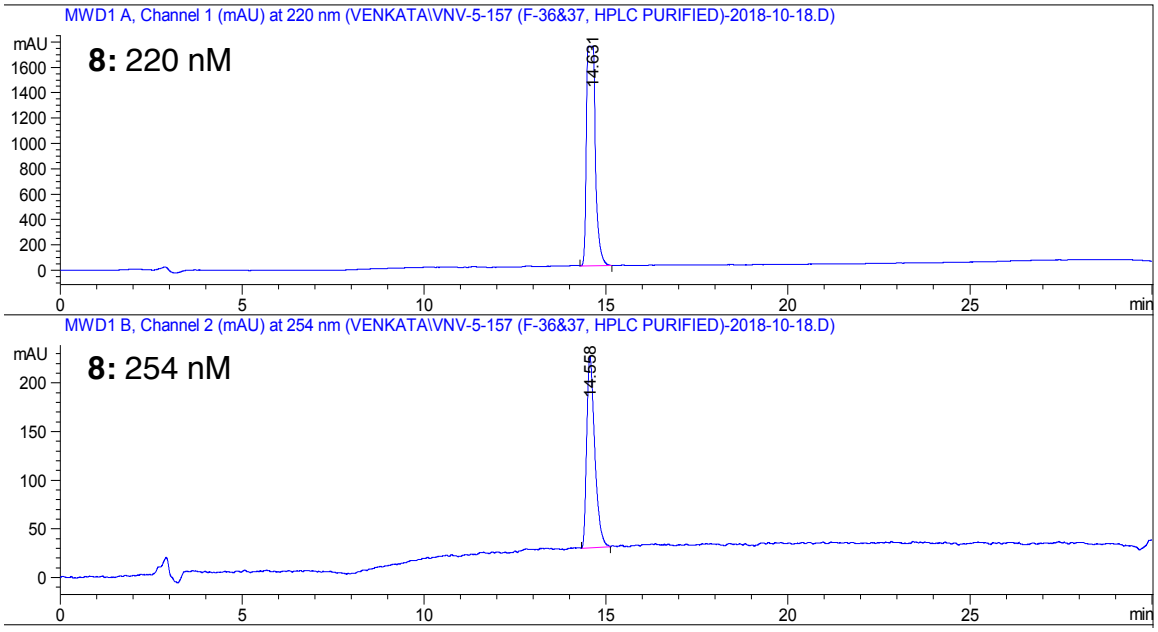

B. Western Blotting and Antibodies

Samples were prepared in loading buffer and boiled for 5 minutes at 95ºC prior to loading into an Any kD™ Mini-PROTEAN® TGX™ Precast protein gels (BioRad). Gels were then ran using Tris-Glycine running buffer (25 mM Tris pH 8.6, 192 mM glycine, 0.1% SDS) at 180 V. Gels were transferred to nitrocellulose paper using the TransBlot Turbo System (BioRad) at 25 V, 2.5 A for 15 minutes. Nitrocellulose blots were blocked for 30 minutes at room temperature with Odyssey blocking buffer (Li-Cor). Primary antibodies were diluted into blocking buffer and incubated over night at 4ºC. Blots were washed 2x with TBST (20 mM Tris pH 7.5, 150 mM NaCl, 0.1% Tween-20) and incubated with near-infrared-dye-conjugated secondary antibodies (Li-Cor) for 1 hour at room temperature.

Blots were imaged using a Li-Cor Odyssey IR Imager and quantitated using ImageStudio.

Table S2.2

Antibody	Vendor	Product Number
IRE1α Rabbit mAb (14C10)	Cell Signaling	#3294
FLAG (DYKDDDDK) Mouse mAb	Sigma	#F3165

Table S2.2 Western blotting antibody reagents
Primary antibodies used to detect IRE1α are listed with information about their reactivity, vendor source, and product number

C. Phostag Acrylamide Gels[91]

Phostag Gel Recipe

Table S2.3

Components	Resolving Layer	Stacking Gel
H_2O (mL)	8.3	3.71
30% 29:1 acrylamide (mL)	2.5	0.67
1.5 M Tris pH 8.8	3.75	-
1.5 M Tris pH 6.8	-	625
10% SDS (µL)	150	50
10% ammonia persulfate (µL)	150	50
5mM Phos-tag (µL)	75	-
10mM $MnCl_2$	75	-
TEMED	15	8

Table S2.3 Phostag gel recipe and reagents
Components, concentrations, and volumes used for pouring the resolving and stacking layers of phostag gels.

Phostag Acrylamide Gel Procedure

Resolving gels (poured using the recipe noted above) were allowed to solidify (~1.5 hr) before adding the stacking gel and comb and allowed to solidify (~1 hr).

Gels were run using Tris-Glycine-SDS running buffer at 100 V for 3-3.5 hours. After the gels have ran, they were transferred onto nitrocellulose paper via rapid transfer using a Transblot Turbo and premade transfer packs. Gels were transferred at 25 V, 2.5 A for 15 minutes. Once transferred onto nitrocellulose, proceed with western blotting procedure as normal.

D. Expression and Purification of IRE1α* and dP-IRE1α*

A construct containing the cytosolic kinase and RNase domains of human IRE1α (residues 547–977, IRE1α*) was expressed in SF9 insect cells by using the Bac-to-Bac baculovirus expression system (Invitrogen) with a His6 tag at the N-terminus and purified with a nickel–nitriloacetic acid (Qiagen) column. To generate dP-IRE1α*, we removed basal phosphorylation sites by incubating IRE1α* with λ-PPase (New England Biolabs) at a molar ratio of 5:1 (IRE1α*: λ-PPase) in 50 mM HEPES pH 7.5, 100 mM NaCl, 1 mM $MnCl_2$, 2 mM dithiothreitol (DTT) and 0.01% Brij 35 detergent (v/v) overnight at 4°C. Dephosphorylation was verified through western by using a universal phospho-protein detection agent. Blotting was performed with biotin-pIMAGO (Tymora Analytical Operations, Cat. No.: FL800) and imaged using a streptavidin-linked fluorophore. To ensure that dpIRE1α* was quantitatively dephosphorylated, concentrations of dpIRE1α* 1000x and 500x the detection limit of the pIMAGO reagent (12.5ng IRE1α*) were used (see below).

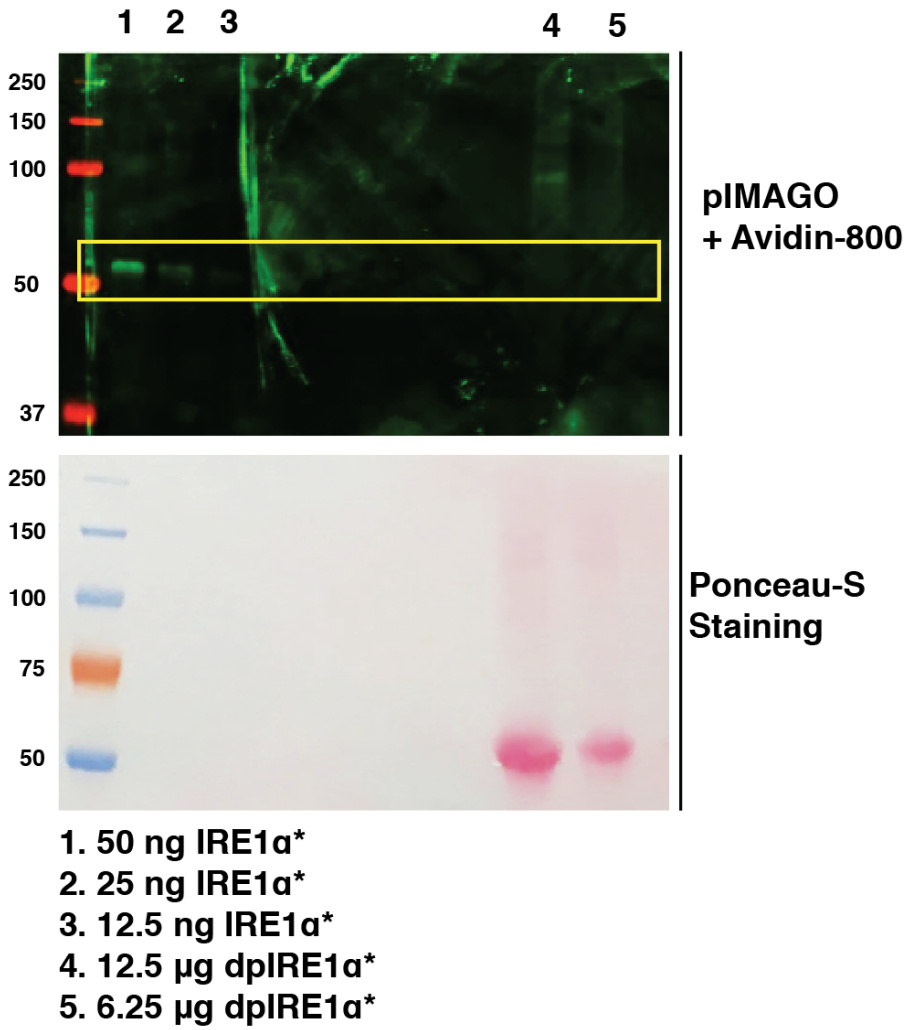

Figure S2.1 Western blot phospho-analysis of IRE1α* vs. dpIRE1α*
IRE1α* was titrated in 2x dilutions from 50 ng as a marker for phosphorylation detection limit (Lanes 1-3). dP-IRE1α* was loaded at 12.5 µg and 6.25 µg, concentrations 1000x and 500x the detection limit (Lanes 4 and 5). Gels were transferred to nitrocellulose paper and imaged using Ponceau-S staining and Tymora pIMAGO phosphor-protein detection stain.

E. *In Vitro* Enzymatic Assays

In Vitro Kinase Activity Assay

Inhibitors (initial concentration of 10 or 60 µM, three-fold serial dilutions) were incubated with IRE1α* in cleavage buffer (20 mM HEPES at pH 7.5, 0.05% Triton X-100 (v/v), 50 mM potassium chloride, 1 mM magnesium chloride, 1 mM DTT) for 30 min, followed by incubation with 10 µCi [γ^{32}P] ATP(3,000 Ci mmol^{-1},

PerkinElmer) at 23 °C for 3 hours. Samples were then spotted onto glass fiber paper (Easytab-C Glass Fiber Filter Paper, Perkin Elmer) and washed in twice with 0.5% phosphoric acid and autoradiographed using a GE Typhoon FLA 9000 Imager. Blots were quantitated using ImageQuant software. The percent inhibition was quantified by setting the background (no kinase well) as 0 and standardizing to IRE1α* without compound treatment (IRE1α* + DMSO). Dose-response curves were fit using “one-site fit logIC50” parameter using GraphPad Prism analysis software.

In Vitro RNase Activity Assay Inhibitor Titrations

50 nM IRE1α* was incubated with inhibitor (initial concentration of 10 or 60 μM, three-fold serial dilutions) or DMSO for 30 min in assay buffer (20 mM Tris at pH 7.5, 50 mM sodium chloride, 1 mM magnesium chloride, 2 mM DTT, 0.05% Triton X-100 (v/v)). Assays were initiated by adding 10 μL of XBP1-mini substrate (5’-Alex647-CAUGUCCGCAGCGCAUG-IowaBlack-FQ-3’; IDT) to the wells at a final concentration of 200 nM and a final well volume of 30 μL. Fluorescence was detected on a Perkin Elmer Envision Microplate Reader at excitation and emission wavelengths of 650 nm and 665 nm. Reaction process was monitored real time in 10-second intervals for at least 30 minutes. Dose-response curves were fit using “one-site fit logIC50” parameter using GraphPad Prism analysis software.

In Vitro K_{DIMER} Assay

IRE1α* or dpIRE1α* was titrated from either 2 μM or 4 μM in two-fold serial dilutions in assay buffer (20 mM Tris at pH 7.5, 50 mM sodium chloride, 1 mM magnesium chloride, 2 mM DTT, 0.05% Triton X-100 (v/v)) and incubated with 50 μM inhibitor for 30 minutes at room temperature. Assays were initiated by adding 10 μL of XBP1-mini substrate (5'-Alex647-CAUGUCCGCAGCGCAUG-IowaBlack-FQ-3'; IDT) to the wells at a final concentration of 6 μM and a final well volume of 30 μL. Fluorescence was detected on a Perkin Elmer Envision Microplate Reader at excitation and emission wavelengths of 650 nm and 665 nm. Reaction process was monitored real time in 10-second intervals for at least 30 minutes. Linear regions of the curves were fitted using the 'linear regression' parameter in GraphPad Prism analysis software to determine rate of XBP1-cleavage for each respective IRE1α* of dpIRE1α* concentration. Second order rate constants were then determined by dividing rate by the respective concentration of IRE1α* or dpIRE1α* used (Rate/[E]). K_{DIMER} values were determined by fitting these values using the non-linear regression 'one-site total' binding parameter in GraphPad Prism analysis software.

F. Crystallization of IRE1α* + Compound **7**

Data Collection and Processing

Suitable constructs for IRE1α* expression and crystallization had been previously established by PROTEROS. A cryo-protocol was established using PROTEROS Standard Protocols. Crystals have been flash-frozen and

measured at a temperature of 100 K. The X-ray diffraction data have been collected from complex crystals of IRE1α* with the ligand **7** at the SWISS LIGHT SOURCE (SLS, Villigen, Switzerland) using cryogenic conditions. The crystals belong to space group C2. Data were processed using the programs XDS and XSCALE.

*Data Collection and Processing Statistics for **7***

Table S2.4

Ligand	**7**
X-ray source	PXII/X10SA (SLS[1])
Wavelength [Å]	1.0000
Detector	PILATUS 6M
Temperature [K]	100
Space group	C 2
Cell: a; b; c; [Å]	164.91; 72.81; 119.24
α; β; γ; [◦]	90.0; 129.8; 90.0
Resolution [Å]	1.85 (2.10-1.85)
Unique reflections	91213 (28858)
Multiplicity	2.9 (2.9)
Completeness [%]	98.1 (98.6)
Rsym [%]	3.7 (43.1)
Rmeas [%]	4.5 (52.5)
Mean(I)/sd [3]	17.89 (2.71)

Table S2.4 Data collection and processing statistics
1. Swiss Light Source (SLS, Villigen, Switzerland)
2. Values in parenthesis refer to the highest resolution bin
3. Calculated from independent reflections

Structural Modeling and Refinement

The phase information necessary to determine and analyze the structure was obtained by molecular replacement. A previously solved structure of IRE1α was used as a search model. Subsequent model building and

refinement was performed according to standard protocols with the software packages CCP4 and COOT. For the calculation of the free R-factor, a measure to cross-validate the correctness of the final model, about 2.6% of measured reflections were excluded from the refinement procedure (see Table 3). TLS refinement (using REFMAC5, CCP4) has been carried out, which resulted in lower R-factors and higher quality of the electron density map. Automatically generated local NCS restraints have been applied (keyword "ncsr local" of newer REFMAC5 versions). The ligand parameterization and generation of the corresponding library files were carried out with CORINA.

The water model was built with the "Find waters"-algorithm of COOT by putting water molecules in peaks of the Fo-Fc map con-toured at 3.0 followed by refinement with REFMAC5 and checking all waters with the validation tool of COOT. The criteria for the list of suspicious waters were: B-factor greater 80 $Å^2$, 2Fo-Fc map less than 1.2, distance to closest contact less than 2.3 Å or more than 3.5 Å. The suspicious water molecules and those in the ligand-binding site (distance to ligand less than 10 Å) were checked manually. The Ramachandran Plot of the final model shows 92.6 % of all residues in the most favored region, 6.7 % in the additionally al-lowed region, and 0.4 % in the generously allowed region. The residues Met872 (A) and Met872 (B) are found in the disallowed region of the Ramachandran plot

(**Table 3**). They are either confirmed by the electron density map or could not be modeled in another sensible conformation. Statistics of the final structure and the refinement process are listed in **Table S2.5**.

Refinement Statistics for 7[a]

Table S2.5

Ligand	**7**
Resolution [Å]	91.59-1.85
Number of reflections (working /test)	88799 / 2411
Rcryst [%]	19.1
Rfree[%][b]	23.5
Total number of atoms:	
Protein	6680
Water	641
Ligand	78
Triethylene glycol	10
Glycerol	60
Di(hydroxyethyl)ether	28
1,2-Ethanediol	76
Deviation from ideal geometry: [c]	
Bond lengths [Å]	0.012
Bond angles [°]	1.62
Bonded B's [Å^2] [d]	4.7
Ramachandran plot: [e]	
Most favored regions [%]	92.6
Additional allowed regions [%]	6.7
Generously allowed regions [%]	0.4
Disallowed regions [%]	0.3

Table S2.5 Refinement statistics

Data collection and refinement statistics for IRE1α* and **7**

a. Values as defined in REFMAC5, without sigma cut-off
b. Test-set contains 2.6% of measured reflections
c. Root mean square deviations from geometric target values
d. Calculated with MOLEMAN
e. Calculated with PROCHECK

G. Mammalian Tissue Culture and Treatment of INS-1 cells

Tissue Culture

INS-1s (rat insulinoma beta cells) were grown in RPMI, 10% FBS buffer (v/v), 1 mM sodium pyruvate, 10 mM HEPES, 2 mM glutamine and 50 µM β-mercaptoethanol on Poly-D-Lysine coated tissue culture flasks. IRE1α (murine) was cloned into a pcDNA5/FRT/TO. INS-1 FRT/TO cells were grown following the protocol above. INS-1 FRT/TO cells were transfected with 2 µg IRE1α-pcDNA5/FRT/TO and 2 µg pOG44 using Lipofectamine 2000 (Thermo Fisher). Cell media was exchanged the next day and cells were allowed grow for another day before passaging. Selection was performed using 50 µg/mL Hygromycin-B (Thermo Fisher) over about two weeks until all un-transfected cells have died and colonies have appeared in transfected cells. Stably integrated cells were maintained in RPMI, 10% FBS buffer (v/v), 1 mM sodium pyruvate, 10 mM HEPES, 2 mM glutamine and 50 µM β-mercaptoethanol, 25 µg/mL Hygromycin-B. HEK293 cells were grown in DMEM High Glucose media (Gibco) supplemented with 10% FBS. HCT-116 cells were maintained in McCoy's 5A (Modified) media (Gibco) supplemented with 10% FBS. All cells lines were maintained at 37ºC with 5% CO_2

Treatment for Phostag Gels

INS-1 or INS-1-IRE1α cells were plated onto a 24-well Poly-D-Lysine coated tissue culture plate and grown for 48 hrs. Inhibitor or DMSO were added to the

media and incubated for 1 hour at 37ºC with 5% CO_2 prior to addition of ER stress agents. After the 1 hour inhibitor incubation, cells were treated 200 µg/mL BFA (Sigma, Prod. No.: B6542) for 2 hours or 5 ng/mL doxycycline (Sigma) for 6 hours, with care to ensure the total DMSO concentration in the media did not exceed 1% (v/v). Cells were lysed directly into SDS loading buffer.

Treatment for XBP1 Splicing and RIDD Outputs

INS-1 or INS-1-IRE1α cells were plated onto Poly-D-Lysine coated tissue culture plate and grown for 48 hrs. Inhibitors or DMSO were added to the media and incubated for 1 hour at 37ºC with 5% CO_2 prior to addition of ER stress agents. After the 1 hour inhibitor incubation, cells were treated 250 µg/mL BFA (Sigma, Prod. No.: B6542) for 2 hours or 5 ng/mL doxycycline (Sigma) for 6 or 24 hours, with care to ensure the total DMSO concentration in the media did not exceed 1% (v/v).

H. *In Vivo* XBP1 Splicing Assay

RNA was isolated from whole cells using either QIAGEN RNeasy Mini kits or Trizol (Invitrogen) and reverse transcribed as above to obtain total cDNA. Then, XBP-1 primers were used to amplify an XBP-1 amplicon spanning the 26 nt intron from the cDNA samples in a regular 3-step PCR. Thermal cycles were: 5 min at 95ºC, 30 cycles of 30 s at 95ºC, 30 s at 60ºC, and 1 min at 72ºC, followed by 72ºC for 15 min, and hold at 4ºC. Primers used for XBP-1 mRNA splicing were as follows: sense primer XBP1.3S (50-AAACAGAGTAGCACAGACTGC-30) and antisense primer XBP1.2AS (50-GGATCTCTAAGACTAGAGGCTTGGTG-30).

PCR fragments were then digested by PstI, resolved on 3% agarose gels, stained with EtBr and quantified by densitometry using ImageJ (NIH).

I. *In Vivo* RIDD Outputs Assay

RNA was isolated from whole cells using either QIAGEN RNeasy Mini kits or Trizol (Invitrogen). For standard mRNA detection, generally 1 mg total RNA was reverse transcribed using the QuantiTect Reverse Transcription Kit (QIAGEN). For qPCR, we used SYBR green (QIAGEN) and StepOnePlus Real-Time PCR System (Applied Biosystems). Thermal cycles were: 5 min at 95ºC, 40 cycles of 15 s at 95ºC, 30 s at 60ºC. Gene expression levels were normalized to Beta Actin or Hprt1. Primers used for qPCR were as follows: Rat Beta Actin: 50 -GCAAATGCTTCTAGGCGGAC-30 and 50 -AAGAAAGGGTGTAAAACGCAGC-30; Rat Ins1, 5'-GTCCTCTGGGAGCCCAAG-3' and 5'-ACAGAGCCTCCACCAGG-3'; Rat Ins2, 5'-ATCCTCTGGGAGCCCCGC-3' and 5'-AGAGAGCTTCCACCAAG-3'; Rat Gyltl1b, 5'-TCAACCAGCTCCGAAATGTG-3' and 5'-GGTAAGAAGTCAATATCACTGAGGAAGA-3'; Rat Galnt2, 5'-CAGACCACCAGGACATAGCTTTT-3' and 5'-CCGCAAAGTGTCCCAAGGT-3';

J. Kinome Profiling and Selectivity[79]

Kinobead Enrichment Protocol

HEK293 and HCT116 cells were plated on 15 cm plates until 90% confluent and lysed into 750 µL modified RIPA buffer (50 mM Tris, 150 mM NaCl, 10 mM NaF, 1% NP40, 0.25% sodium deoxycholate, 5% glycerol, pH 7.8) containing protease inhibitor (Pierce Protease Inhibitor Tablets and 1 mM PMSF) and phosphatase

inhibitor (Phosphatase inhibitor cocktail 2 and 3, Sigma Aldrich). Protein content was determined via Bradford assay. HEK293 and HCT116 lysates were combined in a 1:1 ratio and exogenous IRE1α* was added to the lysate at a final concentration of 33.3 nM (see note below). Lysate (300 µg per sample, 150 µL of 2 mg/mL lysate) was incubated and rotated end over end with 10 µM inhibitor or DMSO (1% v/v) for 1 hour at 4ºC. For kinase enrichment, 10 µL of 50% kinobead slurry (in 20% ethanol) was prepared by washing twice with 500 µL Mod. RIPA buffer. DMSO or inhibitor treated lysates were then added to the washed kinobeads and rotated end over end for 3 hours at 4ºC. After enrichment, the supernatant was aspirated off and the beads were washed twice with 500 µL ice cold Mod. RIPA buffer and three times with 500 µL ice cold TBS (50 mM Tris, 150 mM NaCl, pH = 7.8) to remove detergent. Beads were resuspended in 25 µL of denaturing buffer (6 M guanidinium chloride, 50 mM Tris containing 5 mM TCEP and 10 mM CAM, pH = 8.5). The bead slurries in denaturing buffer were then heated to 95°C for 5 min. After, the bead slurry was diluted 2-fold (add 25 µL) with 100 mM TEAB (triethylammonium bicarbonate buffer, pH 8.5). Then 0.4 µg of LysC (Wako) were added to the beads and. the pH adjusted to 8-9 with 1 N NaOH. The mixture was agitated on a Thermomixer (Eppendorf) at 37°C for 2 hr at 1400 rmp. After the samples were diluted 2-fold (50 µL) with 100mM TEAB and 0.4 µg of sequencing grade trypsin (Pierce) was added and the samples agitated for another 12 hr at 37°C at ~800 rpm in the Thermomixer. After the overnight trypsinization, samples were diluted 2-fold (100 µL) with Buffer A (5%

ACN, 0.1% TFA) containing 1% formic acid and the pH adjusted to 2-3 with formic acid if necessary. Homemade StageTips were prepared by running 50 µL of Buffer B (80% ACN, 0.1% TFA, H_2O) through them followed by 50 µL of Buffer A (5% ACN, 0.1% TFA, H_2O).[92] Beads were spun down and supernatant was added directly to StageTips. Following sample loading, StageTips were washed with 50 µL of Buffer A and eluted with 50 µL Buffer B. Samples were speed vacuumed until dry and re-suspend in Buffer A for injection onto LC-MS.

Note: Determination of Exogenous IRE1 Added to Lysates[93]
-Average HEK293/HCT116 cell volume = 2000 μM^3 (2 pL).

-Number of cells on a 15 cm plate at 80% confluency = ~ 13 million cells.

-13 million cells have an approximate total volume of 26 million pL or 26 µL.

-Cells are lysed in 750 µL of Mod. RIPA, giving a dilution factor of 30x.

-A highly expressed protein (ERK) has a concentration of 1 µM in a HEK cell

-Under these dilution conditions, ERK has a concentration of 33.3 nM in the lysate.

LC-MS and Data Analysis

Tryptic peptides were separated using a nanoAcquity UPLC instrument with 10 cm fused silica capillary columns made in house and packed with 5 µm 120 Å reverse-phase C18 beads (ReproSil-Pur®, Maisch). Liquid chromatography was performed over 120 minutes using and initial 20 minute isocratic trapping of 3% Buffer B and a flow rate of 700 nL/minute followed by a 100 minute gradient of 35% Buffer B to 80% Buffer B gradient at 350 nL/minute. LC Buffer A solvent is

0.1% Acetic acid and LC Buffer B is 99.9% ACN, 0.1% Acetic Acid. MS data was analyzed using a Thermo Orbitrap Fusion Tribrid with the settings in **Table S2.6**.

Table S2.6

Thermo Orbitrap Fusion Tribrid Settings	
Ion Source Type	NSI
Spray Voltage	Static
Positive Ion (V)	2100
Negative Ion (V)	600
Sweep Gas (Arb)	0
Ion Transfer Tube Temperature (ºC)	350
Detector Type	Orbitrap
Orbitrap Resolution	120000
Mass Range	Normal
Quadrapole Isolation	ON
Scan Range (m/z)	380-1500
RF Lens (%)	65
AGC Target	40000
Maximum Injection Time (ms)	50
Microscans	1
Data Type	Centroid
Polarity	Positive

Table S2.6 LC-MS/MS instrument settings
Kinobead samples were analyzed on a Thermo Oribtrap Fusion Tribrid instrument using the listed settings.

Table S2.7

Global Parameters: Identification	
Peptide Spectrum Match FDR	0.01
Protein FDR	0.01
Site decoy fraction	0.01
Min. score for modified peptides	40
Min. delta score for un-modified peptides	0
Min. delta score for modified peptides	6
Main search maximum combinations	200
Global Parameters: Sequence	
Database search	UniProt Human Database
Fixed modification	Carbamidomethyl (Cys)
Min. peptide length	7
Max. peptide mass [Da]	4600

Min. peptide length for unspecific search	8
Max. peptide length for unspecific search	25
Global Parameters: Protein Quantification	
Variable modifications	Oxidation (Met), Acetyl (N-terminus)
Label min. ratio count	2
Global Parameters: MS/MS-FTMS	
Match tolerance	20 ppm
Global Parameters: MS/MS-ITMS	
Match tolerance	0.5 Da
Group-specific parameters: Instrument	
First search peptide tolerance	20
Main search peptide tolerance	4.5
Centroid match tolerance	8
Centroid half width	35
Time valley factor	1.4
Group-specific parameters: Label-free quantification	
Label-free quantification	LFQ ON

Table S2.7 MaxQuant search parameters
Raw files were analyzed using MaxQuant (Andromeda) Version 1.6.0.16 using the listed search parameters.

Files were analyzed further using Perseus (Version 1.6.0.7) by filtering LFQ intensity values only identified by site, reverse, or potential contaminant. Missing LFQ intensity values were imputed in Perseus from a standard distribution downshifted by 1.4 and having a width of 0.5. To determine kinases that were significantly competed by treatment with 10 μM of inhibitor we applied a two-tailed two-sample t-test in Perseus with an FDR of 0.05. Kinases were reported as being non-competed by an inhibitor if it had a Log2 LFQ ratio (Log2 Difference) <1.0. Kinome tree visualization plots were created using CORAL and heat maps were made using GraphPad Prism v.8.

Heat Map of All Kinase Targets Profiled

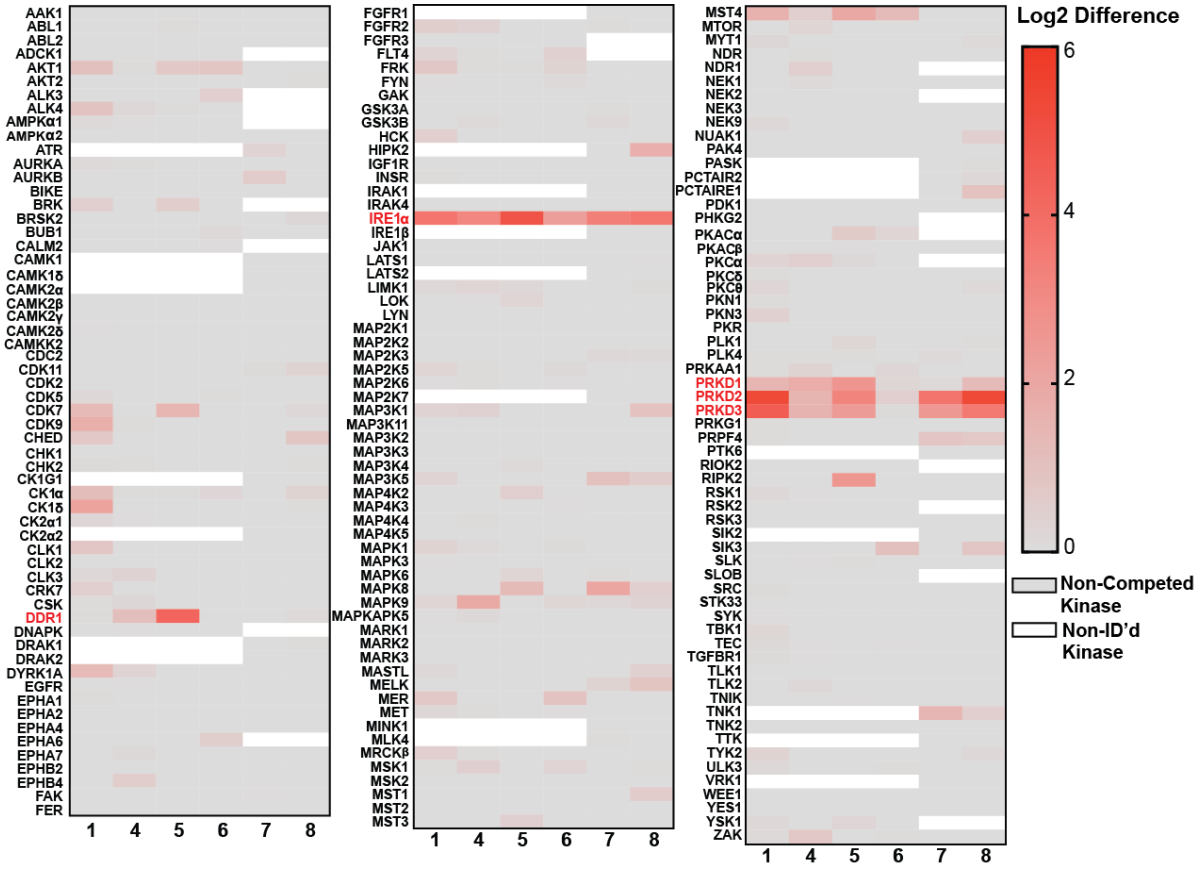

Figure S2.2 Heat map of all kinase targets profiled

Heat maps show all kinase identified in the profiling experiments and all drug-kinase interactions. Panels color scale shows the log2 difference between DMSO treated and drug treated samples from four LFQ replicates. Kinases reported as being drug-sensitive (Log2 Difference > 2) were also required to show significance from a two-sample T-test with FDR of 0.05.

REFERENCES

1. Anelli, T., and Sitia, R. (2008) Protein quality control in the early secretory pathway. EMBO J. 27, 315–327.

2. van Anken, E., and Braakman, I. (2005) Versatility of the endoplasmic reticulum protein folding factory. Crit. Rev. Biochem. Mol. Biol. 40, 191–228.

3. Merksamer, P. I., Trusina, A., and Papa, F. R. (2008) Real-time redox measurements during endoplasmic reticulum stress reveal interlinked protein folding functions. Cell 135, 933–947.

4. Scheuner, D., and Kaufman, R. J. (2008) The unfolded protein response: a pathway that links insulin demand with beta-cell failure and diabetes. Endocr. Rev. 29, 317–333.

5. van Anken, E., Pena, F., Hafkemeijer, N., Christis, C., Romijn, E. P., Grauschopf, U., Oorschot, V. M., Pertel, T., Engels, S., Ora, A., Lastun, V., Glockshuber, R., Klumperman, J., Heck, A. J., Luban, J., and Braakman, I. (2009) Efficient IgM assembly and secretion require the plasma cell induced endoplasmic reticulum protein pERp1. Proc. Natl. Acad. Sci. U. S. A. 106, 17019–17024.

6. Walter, P., and Ron, D. (2011) The unfolded protein response: from stress pathway to homeostatic regulation. Science 334, 1081– 1086.

7. Hetz, C., Chevet, E., and Oakes, S. A. (2015) Proteostasis control by the unfolded protein response. Nat. Cell Biol. 17, 829–838.

8. Tirasophon, W., Welihinda, A. A., and Kaufman, R. J. (1998) A stress response pathway from the endoplasmic reticulum to the nucleus requires a novel bifunctional protein kinase/endoribonuclease (Ire1p) in mammalian cells. Genes Dev. 12, 1812–1824.

9. Harding, H. P., Zhang, Y., and Ron, D. (1999) Protein translation and folding are coupled by an endoplasmic-reticulum-resident kinase. Nature 397, 271–274.

10. Haze, K., Yoshida, H., Yanagi, H., Yura, T., and Mori, K. (1999) Mammalian transcription factor ATF6 is synthesized as a trans-membrane protein and activated by proteolysis in response to endoplasmic reticulum stress. Mol. Biol. Cell 10, 3787–3799.

11. Travers, K. J., Patil, C. K., Wodicka, L., Lockhart, D. J., Weissman, J. S., and Walter, P. (2000) Functional and genomic analyses reveal an essential

coordination between the unfolded protein response and ER-associated degradation. Cell 101, 249–258.

12. Shore, G. C., Papa, F. R., and Oakes, S. A. (2011) Signaling cell death from the endoplasmic reticulum stress response. Curr. Opin. Cell Biol. 23, 143–149.

13. Han, D., Lerner, A. G., Vande Walle, L., Upton, J. P., Xu, W., Hagen, A., Backes, B. J., Oakes, S. A., and Papa, F. R. (2009) IRE1alpha kinase activation modes control alternate endoribonuclease outputs to determine divergent cell fates. Cell 138, 562–575.

14. Papandreou, I., Denko, N. C., Olson, M., Van Melckebeke, H., Lust, S., Tam, A., Solow-Cordero, D. E., Bouley, D. M., Offner, F., Niwa, M., and Koong, A. C. (2011) Identification of an Ire1alpha endonuclease specific inhibitor with cytotoxic activity against human multiple myeloma. Blood 117, 1311–1314.

15. Morita, S. et al. (2017) Targeting ABL-IRE1α Signaling Spares ER-Stressed Pancreatic β Cells to Reverse Autoimmune Diabetes. Cell Metabolism 25, 883–897

16. G. Auf, A. Jabouille, S. Guérit, R. Pineau, M. Delugin, M. Bouchecareilh, N. Magnin, A. Favereaux, M. Maitre, T. Gaiser, et al. (2010) Inositol-requiring enzyme 1alpha is a key regulator of angiogenesis and invasion in malignant glioma. Proc. Natl. Acad. Sci. USA. 107, 15553–15558.

17. S.J. Healy, A.M. Gorman, P. Mousavi-Shafaei, S. Gupta, A. Samali. (2009) Targeting the endoplasmic reticulum-stress response as an anticancer strategy. Eur. J. Pharmacol. 625, 234–246

18. Laybutt, D. R. et al. (2007) Endoplasmic reticulum stress contributes to beta cell apoptosis in type 2 diabetes. Diabetologia 50, 752–763

19.F. Allagnat, F. Christulia, F. Ortis, P. Pirot, S. Lortz, S. Lenzen, D.L. Eizirik,,A.K. Cardozo. (2010) Sustained production of spliced X-box binding protein 1 (XBP1) induces pancreatic beta cell dysfunction and apoptosis.Diabetologia. 53, 1120–1130.

20. A. Hayashi, T. Kasahara, K. Iwamoto, M. Ishiwata, M. Kametani, C. Kakiuchi, T. Furuichi, T. Kato. (2007) The role of brain-derived neurotrophic factor (BDNF)-induced XBP1 splicing during brain development. J. Biol. Chem. 282, 34525–34534.

21. K.M. Doyle, D. Kennedy, A.M. Gorman, S. Gupta, S.J. Healy, A. Samali. (2011) Unfolded proteins and endoplasmic reticulum stress in neurodegenerative disorders. J. Cell. Mol. Med. 15, 2025–2039.

22. A. Gow, L. Wrabetz. (2009) CHOP and the endoplasmic reticulum stress response in myelinating glia. Curr. Opin. Neurobiol. 19, 505–510.

23. C.A. Hetz, C. Soto. (2006) Stressing out the ER: a role of the unfolded protein response in prion-related disorders. Curr. Mol. Med. 6, 37–43.

25. C. Hetz, P. Thielen, S. Matus, M. Nassif, F. Court, R. Kiffin, G. Martinez, A.M. Cuervo, R.H. Brown, L.H. Glimcher. (2009) XBP-1 deficiency in the nervous system protects against amyotrophic lateral sclerosis by increasing autophagy. Genes Dev. 23, 2294–2306.

25. Zhang, S. X., Sanders, E., Fliesler, S. J. & Wang, J. J. (2014) Endoplasmic reticulum stress and the unfolded protein responses in retinal degeneration. Experimental Eye Research 125, 30–40

26. Back, S. H. & Kaufman, R. J. Endoplasmic Reticulum Stress and Type 2 Diabetes. (2012) Annual Review of Biochemistry 81, 767–793

27. Maly, D. J., and Papa, F. R. (2014) Druggable sensors of the unfolded protein response. Nat. Chem. Biol. 10, 892–901.

28. Hetz, C., Chevet, E., and Harding, H. P. (2013) Targeting the unfolded protein response in disease. Nat. Rev. Drug Discovery 12, 703–719.

29. Wang, X. Z., Harding, H. P., Zhang, Y., Jolicoeur, E. M., Kuroda, M., and Ron, D. (1998) Cloning of mammalian Ire1 reveals diversity in the ER stress responses. EMBO J. 17, 5708–5717.

30. Ali, M. M., Bagratuni, T., Davenport, E. L., Nowak, P. R., Silva-Santisteban, M. C., Hardcastle, A., McAndrews, C., Rowlands, M. G., Morgan, G. J., Aherne, W., Collins, I., Davies, F. E., and Pearl, L. H. (2011) Structure of the Ire1 autophosphorylation complex and implications for the unfolded protein response. EMBO J. 30, 894–905.

31. Lee, K. P., Dey, M., Neculai, D., Cao, C., Dever, T. E., and Sicheri, F. (2008) Structure of the dual enzyme Ire1 reveals the basis for catalysis and regulation in nonconventional RNA splicing. Cell 132, 89–100.

32. Lu, Y., Liang, F. X., and Wang, X. (2014) A synthetic biology approach identifies the mammalian UPR RNA ligase RtcB. Mol. Cell 55, 758–770.

33.Kosmaczewski, S. G., Edwards, T. J., Han, S. M., Eckwahl, M. J., Meyer, B. I., Peach, S., Hesselberth, J. R., Wolin, S. L., and Hammarlund, M. (2014) The RtcB RNA ligase is an essential component of the metazoan unfolded protein response. EMBO Rep. 15, 1278–1285.

34. Calfon, M., Zeng, H., Urano, F., Till, J. H., Hubbard, S. R., Harding, H. P., Clark, S. G., and Ron, D. (2002) IRE1 couples endoplasmic reticulum load to secretory capacity by processing the XBP-1 mRNA. Nature 415, 92–96.

35. Hollien, J., Lin, J. H., Li, H., Stevens, N., Walter, P., and Weissman, J. S. (2009) Regulated Ire1-dependent decay of messenger RNAs in mammalian cells. J. Cell Biol. 186, 323–331.

36. Hollien, J., and Weissman, J. S. (2006) Decay of endoplasmic reticulum-localized mRNAs during the unfolded protein response.Science 313, 104–107.

37. Lerner, A. G., Upton, J. P., Praveen, P. V., Ghosh, R., Nakagawa, Y., Igbaria, A., Shen, S., Nguyen, V., Backes, B. J., Heiman, M., Heintz, N., Greengard, P., Hui, S., Tang, Q., Trusina, A., Oakes, S. A., and Papa, F. R. (2012) IRE1alpha induces thioredoxin-interacting protein to activate the NLRP3 inflammasome and promote programmed cell death under irremediable ER stress. Cell Metab. 16, 250–264.

38. Upton, J. P., Wang, L., Han, D., Wang, E. S., Huskey, N. E., Lim, L., Truitt, M., McManus, M. T., Ruggero, D., Goga, A., Papa, F. R., and Oakes, S. A. (2012) IRE1alpha cleaves select microRNAs during ER stress to derepress translation of proapoptotic Caspase-2. Science 338, 818–822.

39. Papa, F. R., Zhang, C., Shokat, K., and Walter, P. (2003) Bypassing a kinase activity with an ATP-competitive drug. Science 302, 1533–1537.

40. Mimura, N., Fulciniti, M., Gorgun, G., Tai, Y. T., Cirstea, D., Santo, L., Hu, Y., Fabre, C., Minami, J., Ohguchi, H., Kiziltepe, T., Ikeda, H., Kawano, Y., French, M., Blumenthal, M., Tam, V., Kertesz, N. L., Malyankar, U. M., Hokenson, M., Pham, T., Zeng, Q., Patterson, J. B., Richardson, P. G., Munshi, N. C., and Anderson, K. C. (2012) Blockade of XBP1 splicing by inhibition of IRE1alpha is a promising therapeutic option in multiple myeloma. Blood 119, 5772–5781.

41. Sanches, M., Duffy, N. M., Talukdar, M., Thevakumaran, N., Chiovitti, D., Canny, M. D., Lee, K., Kurinov, I., Uehling, D., Al-awar, R., Poda, G., Prakesch, M., Wilson, B., Tam, V., Schweitzer, C., Toro, A., Lucas, J. L., Vuga, D., Lehmann, L., Durocher, D., Zeng, Q., Patterson, J. B., and Sicheri, F. (2014) Structure and mechanism of action of the hydroxy-aryl-aldehyde class of IRE1 endoribonuclease inhibitors. Nat. Commun. 5, 4202.

42. Volkmann, K., Lucas, J. L., Vuga, D., Wang, X., Brumm, D., Stiles, C., Kriebel, D., Der-Sarkissian, A., Krishnan, K., Schweitzer, C., Liu, Z., Malyankar, U. M., Chiovitti, D., Canny, M., Durocher, D., Sicheri, F., and Patterson, J. B. (2011) Potent and selective inhibitors of the inositol-requiring enzyme 1 endoribonuclease. J. Biol. Chem. 286, 12743–12755.

43. Cross, B. C., Bond, P. J., Sadowski, P. G., Jha, B. K., Zak, J., Goodman, J. M., Silverman, R. H., Neubert, T. A., Baxendale, I. R., Ron, D., and Harding, H. P. (2012) The molecular basis for selective inhibition of unconventional mRNA splicing by an IRE1-binding small molecule. Proc. Natl. Acad. Sci. U. S. A. 109, E869–878.

44. Wang, L., Perera, B. G., Hari, S. B., Bhhatarai, B., Backes, B. J., Seeliger, M. A., Schurer, S. C., Oakes, S. A., Papa, F. R., and Maly, D. J. (2012) Divergent allosteric control of the IRE1alpha endoribonuclease using kinase inhibitors. Nat. Chem. Biol. 8, 982–989.

45. Prischi, F., Nowak, P. R., Carrara, M., and Ali, M. M. (2014) Phosphoregulation of Ire1 RNase splicing activity. Nat. Commun. 5, 3554.

46. Itzhak, D., Bright, M., McAndrew, P., Mirza, A., Newbatt, Y., Strover, J., Widya, M., Thompson, A., Morgan, G., Collins, I., and Davies, F. (2014) Multiple autophosphorylations significantly enhance the endoribonuclease activity of human inositol requiring enzyme 1alpha. BMC Biochem 15, 3.

47. Pargellis, C., Tong, L., Churchill, L., Cirillo, P. F., Gilmore, T., Graham, A. G., Grob, P. M., Hickey, E. R., Moss, N., Pav, S., and Regan, J. (2002) Inhibition of p38 MAP kinase by utilizing a novel allosteric binding site. Nat. Struct. Biol. 9, 268–272.

48. Hari, S. B., Perera, B. G., Ranjitkar, P., Seeliger, M. A., and Maly, D. J. (2013) Conformation-selective inhibitors reveal differences in the activation and phosphate-binding loops of the tyrosine kinases Abl and Src. ACS Chem. Biol. 8, 2734–2743.

49. Seeliger, M. A., Ranjitkar, P., Kasap, C., Shan, Y., Shaw, D. E., Shah, N. P., Kuriyan, J., and Maly, D. J. (2009) Equally potent inhibition of c-Src and Abl by compounds that recognize inactive kinase conformations. Cancer Res. 69, 2384–2392.

50. Ranjitkar, P., Brock, A. M., and Maly, D. J. (2010) Affinity reagents that target a specific inactive form of protein kinases. Chem. Biol. 17, 195–206.

51. Okram, B., Nagle, A., Adrian, F. J., Lee, C., Ren, P., Wang, X., Sim, T., Xie, Y., Wang, X., Xia, G., Spraggon, G., Warmuth, M., Liu, Y., and Gray, N. S. (2006) A general strategy for creating ″inactive-conformation″ Abl inhibitors. Chem. Biol. 13, 779–786.

52. Korennykh, A. V., Egea, P. F., Korostelev, A. A., Finer-Moore, J., Zhang, C., Shokat, K. M., Stroud, R. M., and Walter, P. (2009) The unfolded protein response signals through high-order assembly of Ire1. Nature. 457, 687–693.

53. Korennykh, A. V., Egea, P. F., Korostelev, A. A., Finer-Moore, J., Stroud, R. M., Zhang, C., Shokat, K. M., and Walter, P. (2011) Cofactor-mediated conformational control in the bifunctional kinase/ RNase Ire1. BMC Biol. 9, 48.

54. Joshi, A., Newbatt, Y., McAndrew, P. C., Stubbs, M., Burke, R., Richards, M. W., Bhatia, C., Caldwell, J. J., McHardy, T., Collins, I., and Bayliss, R. (2015) Molecular mechanisms of human IRE1 activation through dimerization and ligand binding. Oncotarget. 6, 13019–13035.

55. Harrington, P. E., Biswas, K., Malwitz, D., Tasker, A. S., Mohr, C., Andrews, K. L., Dellamaggiore, K., Kendall, R., Beckmann, H., Jaeckel, P., Materna-Reichelt, S., Allen, J. R., and Lipford, J. R. (2015) Unfolded Protein Response in Cancer: IRE1alpha Inhibition by Selective Kinase Ligands Does Not Impair Tumor Cell Viability. ACS Med. Chem. Lett. 6, 68–72.

56. Korennykh, A. V., Korostelev, A. A., Egea, P. F., Finer-Moore, J., Stroud, R. M., Zhang, C., Shokat, K. M., and Walter, P. (2011) Structural and functional basis for RNA cleavage by Ire1. BMC Biol. 9, 47.

57. Taylor, S. S., and Kornev, A. P. (2011) Protein kinases: evolution of dynamic regulatory proteins. Trends Biochem. Sci. 36, 65–77.

58. Tong, M., and Seeliger, M. A. (2015) Targeting conformational plasticity of protein kinases. ACS Chem. Biol. 10, 190–200.

59. Foda, Z. H., Shan, Y., Kim, E. T., Shaw, D. E., and Seeliger, M. A. (2015) A dynamically coupled allosteric network underlies binding cooperativity in Src kinase. Nat. Commun. 6, 5939.

60. Jura, N., Zhang, X., Endres, N. F., Seeliger, M. A., Schindler, T., and Kuriyan, J. (2011) Catalytic control in the EGF receptor and its connection to general kinase regulatory mechanisms. Mol. Cell 42, 9–22.

61. Agius, M. P., and Soellner, M. B. (2014) Modulating noncatalytic function with kinase inhibitors. Chem. Biol. 21, 569–571.

62. Krishnamurty, R., Brigham, J. L., Leonard, S. E., Ranjitkar, P., Larson, E. T., Dale, E. J., Merritt, E. A., and Maly, D. J. (2013) Active site profiling reveals coupling between domains in SRC-family kinases. Nat. Chem. Biol. 9, 43–50.

63. Register, A. C., Leonard, S. E., and Maly, D. J. (2014) SH2-catalytic domain linker heterogeneity influences allosteric coupling across the SFK family. Biochemistry 53, 6910–6923.

64. Leonard, S. E., Register, A. C., Krishnamurty, R., Brighty, G. J., and Maly, D. J. (2014) Divergent modulation of Src-family kinase regulatory interactions with ATP-competitive inhibitors. ACS Chem. Biol. 9, 1894–1905.

65. Hari, S. B., Merritt, E. A., and Maly, D. J. (2014) Conformation-selective ATP-competitive inhibitors control regulatory interactions and noncatalytic functions of mitogen-activated protein kinases. Chem. Biol. 21, 628–635.

66. Kung, J. E., and Jura, N. (2016) Structural Basis for the Non-catalytic Functions of Protein Kinases. Structure 24, 7–24.

67. Holderfield, M., Nagel, T. E., and Stuart, D. D. (2014) Mechanism and consequences of RAF kinase activation by small-molecule inhibitors. Br. J. Cancer 111, 640–645.

68. Zhang, C., Spevak, W., Zhang, Y., Burton, E. A., Ma, Y., Habets, G., Zhang, J., Lin, J., Ewing, T., Matusow, B., Tsang, G., Marimuthu, A., Cho, H., Wu, G., Wang, W., Fong, D., Nguyen, H., Shi, S., Womack, P., Nespi, M., Shellooe, R., Carias, H., Powell, B., Light, E., Sanftner, L., Walters, J., Tsai, J., West, B. L., Visor, G., Rezaei, H., Lin, P. S., Nolop, K., Ibrahim, P. N., Hirth, P., and Bollag, G. (2015) RAF inhibitors that evade paradoxical MAPK pathway activation. Nature 526, 583–586.

69. Van Voorhis, W.C.V. et al. Compositions and methods for treating toxoplasmosis. cryptosporidiosis and other apicomplexan protozoan related diseases. (2011) PCT Int. Appl., WO/2011/094628

70. Kabsch, W. (2010) Xds. Acta Crystallogr. Sect. D, Biol. Crystallogr., 66, 125–132.

71. Evans, P.R. and Murshudov, G.N. (2013) How good are my data and what is the resolution? Acta Crystallogr. Sect. D, Biol. Crystallogr., 69, 1204–1214.

72. Vonrhein, C., Flensburg, C., Keller, P., Sharff, A., Smart, O., Paciorek, W., Womack, T. and Bricogne, G. (2011) Data processing and analysis with the autoPROC toolbox. Acta Crystallogr. Sect. D, Biol. Crystallogr., 67, 293–302.

73. McCoy, A.J., Grosse-Kunstleve, R.W., Storoni, L.C. & Read, R.J. (2005) Likelihood-enhanced fast translation functions. Acta Crystallogr. D Biol. Crystallogr. 61, 458–464

74. Adams, P.D. et al. (2002) PHENIX: building new software for automated crystallographic structure determination. Acta Crystallogr. D Biol. Crystallogr. 58, 1948–1954

75. Emsley, P. & Cowtan, K. (2004) Coot: model-building tools for molecular graphics. Acta Crystallogr. D Biol. Crystallogr. 60, 2126–2132

76. Ghosh, R. et al. Allosteric Inhibition of the IRE1α RNase Preserves Cell Viability and Function during Endoplasmic Reticulum Stress. (2014) Cell 158, 534–548

77. Steichen, J. M., Iyer, G. H., Li, S., Saldanha, S. A., Deal, M. S., Woods, V. L., Jr., and Taylor, S. S. (2010) Global consequences of activation loop phosphorylation on protein kinase A J. Biol. Chem. 285, 3825– 383

78. Feldman, H. C. et al. (2016) Structural and Functional Analysis of the Allosteric Inhibition of IRE1α with ATP-Competitive Ligands. ACS Chemical Biology 11, 2195–2205

79. Golkowski, M. et al. (2017) Kinobead and Single-Shot LC-MS Profiling Identifies Selective PKD Inhibitors. Journal of Proteome Research 16, 1216–1227

80. Asfari M, Janjic D, Meda P, Li G, Halban PA, Wollheim CB (1992) Establishment of 2-mercaptoethanol-dependent differentiated insulin-secreting cell lines. Endocrinology 130:167–178

81. Lodish, H. F. & Kong, N. (1993) The secretory pathway is normal in dithiothreitol-treated cells, but disulfide-bonded proteins are reduced and reversibly retained in the endoplasmic reticulum. Journal of Biological Chemistry 268, 20598–20605

82. Thastrup, O., Cullen, P. J., Drobak, B. K., Hanley, M. R. & Dawson, A. P. (1990) Thapsigargin, a tumor promoter, discharges intracellular Ca2 stores by specific inhibition of the endoplasmic reticulum Ca2+ ATPase. Proceedings of the National Academy of Sciences 87, 2466–2470

83. Fujiwara, T., Oda, K., Yokota, S., Takatsuki, A. & Ikehara, Y. (1988) Brefeldin A causes disassembly of the Golgi complex and accumulation of secretory

proteins in the endoplasmic reticulum. Journal of Biological Chemistry 263, 18545–18552

84. Oslowski, C. M. & Urano, F. (2011) Measuring ER Stress and the Unfolded Protein Response Using Mammalian Tissue Culture System. The Unfolded Protein Response and Cellular Stress, Part B Methods in Enzymology 71–92

85. Amin, A. et al. (2012) Chronic inhibition of endoplasmic reticulum stress and inflammation prevents ischaemia-induced vascular pathology in type II diabetic mice. The Journal of Pathology 227, 165–174

86. Thamsen, M. et al. (2019) Small molecule inhibition of IRE1α kinase/RNase has anti-fibrotic effects in the lung. PLOS One 14(1)

87. Steichen, J. M., Kuchinskas, M., Keshwani, M. M., Yang, J., Adams, J. A., and Taylor, S. S. (2012) Structural basis for the regulation of protein kinase A by activation loop phosphorylation J. Biol. Chem. 287, 14672– 14680

88. Shamu, C. E. & Walter, P. (1996). Oligomerization and phosphorylation of the Ire1p kinase during intracellular signaling from the endoplasmic reticulum to the nucleus. The EMBO Journal15, 3028–3039

89. Kimata, Y. et al. (2007). Two regulatory steps of ER-stress sensor Ire1 involving its cluster formation and interaction with unfolded proteins. The Journal of Cell Biology 179, 75–86

90. Li, H., Korennykh, A. V., Behrman, S. L. & Walter, P. (2010). Mammalian endoplasmic reticulum stress sensor IRE1 signals by dynamic clustering. Proceedings of the National Academy of Sciences 107, 16113–16118

91. Qi, L., Yang, L. & Chen, H. (2011). Detecting and Quantitating Physiological Endoplasmic Reticulum Stress. The Unfolded Protein Response and Cellular Stress, Part B Methods in Enzymology 137–146

92. Yu, Y., Smith, M. & Pieper, R. (2014). A spinnable and automatable StageTip for high throughput peptide desalting and proteomics. Protocol Exchange

93. Fujioka A, Terai K, Itoh RE, Aoki K, Nakamura T, Kuroda S, Nishida E, Matsuda M. (2006) Dynamics of the Ras/ERK MAPK cascade as monitored by fluorescent probes. J Biol. Chem. 281, 8917-26 p.8919